9th Numerical Towing Tank Symposium

1. October 2006 - 3. October 2006

Le Croisic / France

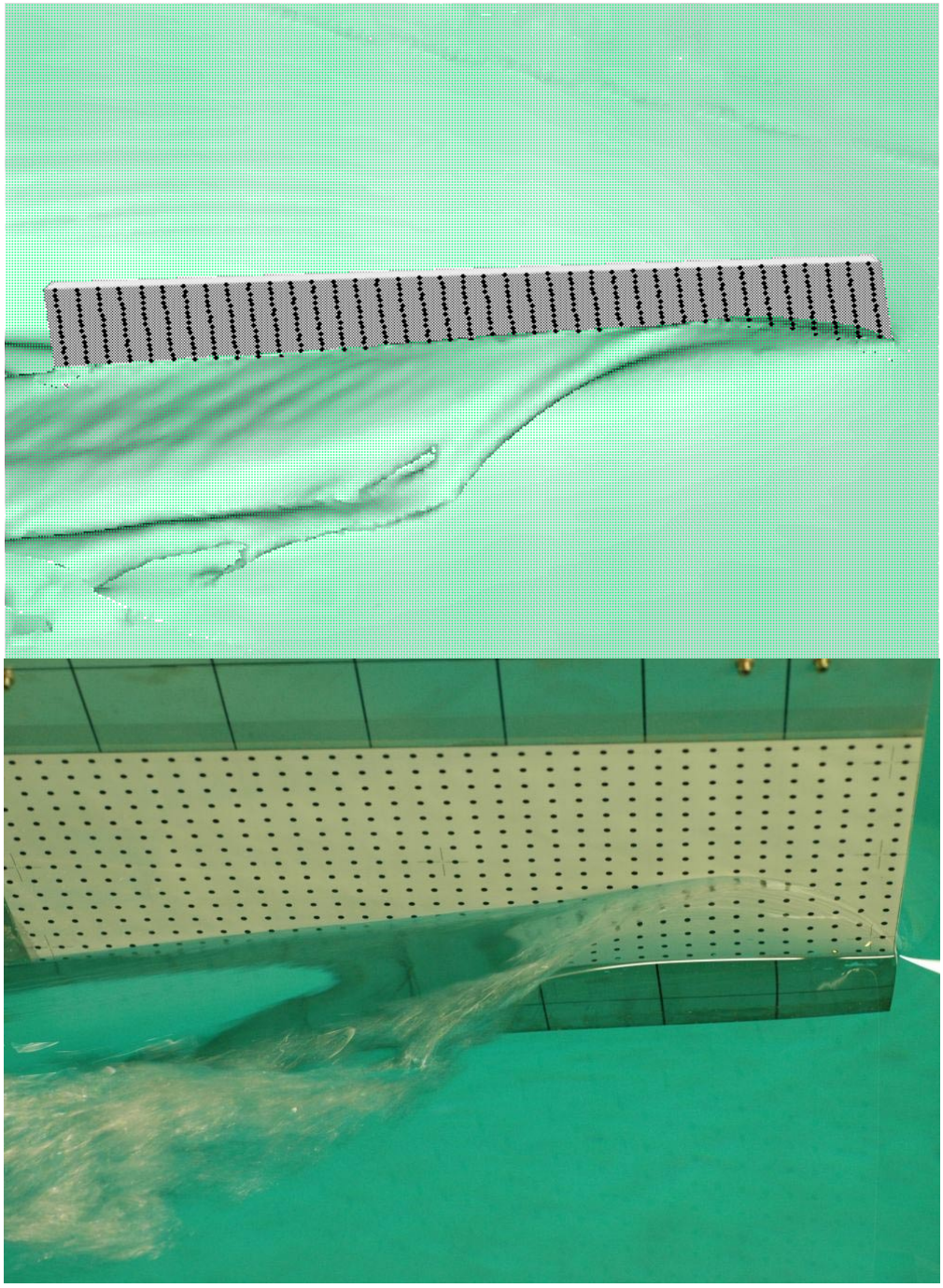

Gerard Delhommeau, Michel Visonneau (Ed.)

LABORATOIRE DE MECANIQUE DES FLUIDES-UMR 6598 DU CNRS
ECOLE CENTRALE DE NANTES
BP 92101
44321 NANTES CEDEX 3, FRANCE

Sponsored by

Centre National de la Recherche Scientifique

C.N.R.S.

NUMECA

ECOLE CENTRALE DE NANTES

8th Numerical Towing Tank Symposium, 1. October – 3. October 2006, Le Croisic, France

Papers are ordered in alphetical order of first author :

Bensow, R.E.; Larson, M.G.
Towards a Novel Residual Based Subgrid Modelling Based on Multiscale Techniques

Berton, M.; Alessandrini, B.; Barre, S. ; Kobus, J.M.
Hydrodynamic analysis of the performance of Rowing boats with unsteady motions

Bertram, V.; Söding H.; Graf, K.
PDSTRIP – A Strip Method for Ship and Yacht Seakeeping

Bugalski, T.;Kraskowski, M.
Validation of the RANSE wake computations for the training vessel Nawigator XXI and the dredger Uilenspiegel

Ciortan, C.; Wanderley, J.; Guedes Soares, C.
Free Surface Flow around Ship Hulls Using the Slightly Compressible Flow Formulation

Delhommeau, G.. Guilbaud, M.; Noblesse, F.
A simple analytical criterion to predict if a ship in steady motion generates unnsteady bow waves

Dymarski, P.; Kraskowski, M.
Numerical Computation of Propeller Characteristics with the Use of Periodic Non-Matching Boundary Condition

El Moctar, B.; Muzaferija, S.; Peric, M.
Effects of Gas Bubbles and Their Compressibility on Slamming Loads

Fabbri, L.; Benedetti, L.; Boucasse, B.; La Gala, F.; Lugni, C.
An experimental study of the manoeuvrability of a blunt ship : the effect of water depth

Godderidge, B.; Tan, M.; Earl, C.; Turnock, S.
Multiphase CFD Modelling of a Lateral Sloshing Tank

Hu, C.; Kashiwagi, M.
Wave-Body Interaction Experiments for Validation of CFD method on Strongly Nonlinear Problems

Jahanbakhsh, E.; Panahi, R.; Seif, M.S.
Ship Dynamic Simulation, Based on a Three-Dimensional Viscous freee Surface Flow Solver

Kraskowski, M.
Simplified RANSE simulation of the side launching

Kyulevcheliev, S.
A Procedure for Hydrodynamic Shape Optimization Using RANSE Solver

Lewis, S.G.; Hudson, D.A., Turnock, S.
Visualisation Techniques for Interpreting Performance of High Speed Craft

Lugni, C.; Colicchio, G.; Colagrosssi, A.
Investigation of sloshing phenomena near the critical filling depth through the Hilbert-Huang Transformation

Mueller, S.B.; Steden, M.; Neugebauer, J.; El-Haddad, M.F.; Abdel Maksoud, M.
Comparing a Propeller Model with a Rotating Propeller in a CFD-Simulation of the Viscous Flow around a Ship

Palladino, F.; Lugni, C. ; Bertram, V.
Validation of Ship Motions Functions of PDSTRIP for Some Standard Test Cases

Panahi, R.; Jahanbakhsh, E.; Seif, M.S.
Numerical Investigation on the Effect of baffle Arrangement in Tanker Sloshing

Persson, T.; Bark, B.; Bensow, R.; Berchiche, N.;Fureby C.
Modelling the Cavitating Flow around a 3-dimensional Wing Section Using Large Eddy Simulation

Pinto, A.; Broglia, R.; Campana, E.F. ; Di Mascio, A.; Peri, D.
RANS analysis of the interference effect in catamarans

Quérard, A.; Temarel, P.; Turnock, S.R.
Developments On Hydroelasticity Of Ships Using RANS

Schmode, D.; Henning Günther, J.; Kaufmann, J.; Rung, T.; Hafermann, D.
Investigation of Scale Effects in Exhaust-Gas Tests using RANS Solver FreSCo

Stück, A.; Rung, T.
Obvious techniques towards adjoint CFD

Sueyoshi, M.
Validation Study of a particle Method for Violent Free Surface Flow

Viviani, M.; Savio, L.; Brizzolara, S.
Evaluation of slamming loads on V-shape ship sections with different numerical methods

Vorhölter, H., Schmode, D.; Rung,T.
Implementation of Cavitation Modelling in FreSCo

Werner, S. Pistidda, A., Larsson, L.; Regnström B.
CFD validation for a yacht keel

Towards a Novel Residual Based Subgrid Modelling Based on Multiscale Techniques

Rickard E. Bensow[1] and Mats G. Larson[2]
[1]Dep. of Shipping and Marine Technology, Chalmers, S-41296 Göteborg, Sweden
rickard.bensow@chalmers.se
[2]Dep. of Mathematics, Umeå University, S-90187 Umeå, Sweden
mats_larson@yahoo.com

This paper uses the idea of computing the effect of the small, unresolved scales in an LES using 1) a variational approach to exactly split the problem into coarse (resolved) and fine (subgrid) scales and 2) the residuals as data for the approximated fine scale problem. Using a vorticity-strain formulation we are able to identify interesting subgrid scale dynamics. As a starting demonstration of the approach we use very crude approximations leading not to a full subgrid scale model, rather additional terms in a fashion similar to the vorticity confinement approach by Steinhoff *et al.*[4]. Realizing the potential in the achieved results, we have work in progress to advance the technique to full subgrid modeling.

The Variational Multi Scale (VMS) framework used here was introduced by Hughes *et al.*[5] and has previously been applied to fluid problems [6][7]. New in this work is that we express the non-linear term in the Navier-Stokes equations using the vorticity and strain which makes it possible to successfully find relevant approximations of the fine scales as well as our use of the residuals in the modeling. The fine scale approximations are easily computed and we show, by numerical computations, that they contain relevant information on the unresolved flow. Especially, some terms are driving the resolved flow instead of damping it leading, e.g., to better preservation of vortices in the flow. This is despite the very crude simplifications introduced at this stage.

We start by describing the VMS approach in general term, before replacing the non-linear term with vorticity and strain. Then, we derive approximate expressions for the fine scale vorticity and strain and show their action on the coarse scales by computing a wing tip vortex.

The basis of the variational multiscale approach is that we do not use the standard LES formulation based on filtering of the Navier-Stokes equations (NSE), instead a split (based on large and small scales) is introduced in a variational formulation of NSE. We start with the incompressible NSE in a domain $\Omega \subset \mathbf{R}^3$: find the velocity $\boldsymbol{u} : \Omega \to \mathbf{R}^3$ and pressure $p : \Omega \to \mathbf{R}$ such that

$$\frac{\partial \boldsymbol{u}}{\partial t} + \boldsymbol{u} \cdot \nabla \boldsymbol{u} + \nabla p - \nabla \cdot (\nu \nabla \boldsymbol{u}) = \boldsymbol{f}, \tag{1}$$

$$\nabla \cdot \boldsymbol{u} = 0, \tag{2}$$

together with boundary conditions on the boundary $\partial\Omega$.

Integrating (1) and applying Gauss' theorem leads to the integral formulation that the finite volume method is based on. To instead reach a variational formulation, we multiply the equation with test functions for velocity $\boldsymbol{v}$ and pressure q before integration, leading to an equivalent integral equation if we choose the set of test functions properly. We thus seek the velocity $\boldsymbol{u} : \Omega \to \mathbf{R}^3$ and pressure $p : \Omega \to \mathbf{R}$ such that

$$\int_\Omega \frac{\partial \boldsymbol{u}}{\partial t} \cdot \boldsymbol{v} d\Omega + \int_\Omega (\boldsymbol{u} \cdot \nabla \boldsymbol{u}) \cdot \boldsymbol{v} d\Omega - \int_\Omega p \nabla \cdot \boldsymbol{v} d\Omega + \int_\Omega \nabla \cdot \boldsymbol{u} q d\Omega + \int_\Omega \nu \nabla \boldsymbol{u} \nabla \boldsymbol{v} d\Omega = \int_\Omega \boldsymbol{f} \cdot \boldsymbol{v} d\Omega, \tag{3}$$

for all set of functions $(\boldsymbol{v}, q)$ of the same class as $(\boldsymbol{u}, p)$, i.e. continuous, time dependent functions in $\mathbf{R}^3$ with a suitable set of boundary values. We denote these spaces by $\mathcal{V}_{\boldsymbol{u}}$ and $\mathcal{V}_p$. Since we demand that (3) should hold for all functions $(\boldsymbol{v}, q) \in \mathcal{V}_{\boldsymbol{u}} \times \mathcal{V}_p$ the solution to the variational form is the same as the one to the strong form. The "standard" integral form can be retrieved by

choosing $\boldsymbol{v}$ and q to be piecewise constant functions, i.e. equal to one in one cell and zero in all others.

Using suitable basis for $\mathcal{V}_{\boldsymbol{u}}$ and $\mathcal{V}_p$ we can split these spaces into coarse (resolved) and fine (subgrid) scale spaces. Thus, we choose two spaces $\mathcal{V}_c \subset \mathcal{V}$ and $\mathcal{V}_f \subset \mathcal{V}$ such that $\mathcal{V} = \mathcal{V}_c \oplus \mathcal{V}_f$, where $\mathcal{V}_c$ is associated with the coarse scale and $\mathcal{V}_f$ is associated with the fine scale. That is. $\mathcal{V}_c$ represents the space where we look for a numerical solution to our flow, and $\mathcal{V}_f$ spans the subgrid scales which are subject to modeling. Introducing these spaces in (3) gives us the following weak formulation: find $(\boldsymbol{u}_c, p_c) \in \mathcal{V}_c$ and $(\boldsymbol{u}_f, p_f) \in \mathcal{V}_f$ such that

$$\int_\Omega (\frac{\partial \boldsymbol{u}_c}{\partial t} + \frac{\partial \boldsymbol{u}_f}{\partial t}) \cdot \boldsymbol{v} d\Omega + \int_\Omega (\boldsymbol{u}_c + \boldsymbol{u}_f) \cdot \nabla (\boldsymbol{u}_c + \boldsymbol{u}_f) \cdot \boldsymbol{v} d\Omega + \tag{4}$$
$$- \int_\Omega (p_c + p_f) \nabla \cdot \boldsymbol{v} d\Omega + \int_\Omega \nabla \cdot (\boldsymbol{u}_c + \boldsymbol{u}_f) q d\Omega + \int_\Omega \nu \nabla \boldsymbol{u} \nabla \boldsymbol{v} d\Omega = \int_\Omega \boldsymbol{f} \cdot \boldsymbol{v} d\Omega,$$

for all $\boldsymbol{v} = \boldsymbol{v}_c, q = q_c$ and $\boldsymbol{v} = \boldsymbol{v}_f, q = q_f$. This separates the scales in the equations into two parts: choosing coarse scale test functions we get the coarse scale equation where the fine scale contributions account for the effects of the fine scales on the coarse scales, and vice versa. This formulation forms the basis for the VMS framework where the coarse scale equation acts as the LES equations and the fine scale problem, approximated or modeled, gives the subgrid information.

In this paper we rewrite the incompressible NSE by using the identity

$$\boldsymbol{u} \cdot \nabla \boldsymbol{u} = S\boldsymbol{u} + \boldsymbol{\omega} \times \boldsymbol{u}, \tag{5}$$

where $S = (\nabla \boldsymbol{u} + (\nabla \boldsymbol{u})^T)/2$ is the strain tensor and $\boldsymbol{\omega} = \nabla \times \boldsymbol{u}$ is the vorticity. Equation (4) then becomes: find $(\boldsymbol{u}_c, p_c) \in \mathcal{V}_c$ and $(\boldsymbol{u}_f, p_f) \in \mathcal{V}_f$ such that

$$\int_\Omega (\frac{\partial \boldsymbol{u}_c}{\partial t} + \frac{\partial \boldsymbol{u}_f}{\partial t}) \cdot \boldsymbol{v} d\Omega + \int_\Omega (S_c + S_f)(\boldsymbol{u}_c + \boldsymbol{u}_f) \cdot \boldsymbol{v} d\Omega + \int_\Omega (\boldsymbol{\omega}_c + \boldsymbol{\omega}_f) \times (\boldsymbol{u}_c + \boldsymbol{u}_f) \cdot \boldsymbol{v} d\Omega + \tag{6}$$
$$- \int_\Omega (p_c + p_f) \nabla \cdot \boldsymbol{v} d\Omega + \int_\Omega \nabla \cdot (\boldsymbol{u}_c + \boldsymbol{u}_f) q d\Omega + \int_\Omega \nu \nabla \boldsymbol{u} \nabla \boldsymbol{v} d\Omega = \int_\Omega \boldsymbol{f} \cdot \boldsymbol{v} d\Omega,$$

for all $\boldsymbol{v} = \boldsymbol{v}_c, q = q_c$ and $\boldsymbol{v} = \boldsymbol{v}_f, q = q_f$

In this paper, we now focus on the fine scale information contained in the two nonlinear terms involving the fine scale strain S_f and the fine scale vorticity $\boldsymbol{\omega}_f$ and thus neglect the fine scales in the other terms. Since the fine scale velocities are small compared with their derivatives and the coarse scale velocities, we also neglect the couplings between the coarse scale strain and vorticity and the fine scale velocities thereby isolating what we believe to be the most important terms. We thus get the following approximations,

$$\int_\Omega (S_c + S_f)(\boldsymbol{u}_c + \boldsymbol{u}_f) \cdot \boldsymbol{v}_c d\Omega \approx \int_\Omega (S_c \boldsymbol{u}_c + S_f \boldsymbol{u}_c) \cdot \boldsymbol{v}_c d\Omega, \tag{7}$$

and

$$\int_\Omega (\boldsymbol{\omega}_c + \boldsymbol{\omega}_f) \times (\boldsymbol{u}_c + \boldsymbol{u}_f) \cdot \boldsymbol{v}_c d\Omega \approx \int_\Omega (\boldsymbol{\omega}_c \times \boldsymbol{u}_c + \boldsymbol{\omega}_f \times \boldsymbol{u}_c) \cdot \boldsymbol{v}_c d\Omega. \tag{8}$$

The influence of the fine scales on the coarse problem is thus reduced to two extra terms in the momentum equation, $\int_\Omega S_f \boldsymbol{u}_c \boldsymbol{v}_c d\Omega$ and $\int_\Omega \boldsymbol{\omega}_f \times \boldsymbol{u}_c \boldsymbol{v}_c d\Omega$. This can be compared with the standard LES formulation where the subgrid tensor, appearing in the resolved equations, takes the form $\nabla \cdot (\overline{\boldsymbol{u}} \otimes \overline{\boldsymbol{u}} - \overline{\boldsymbol{u}} \otimes \overline{\boldsymbol{u}})$.

Let us now derive the basic approximations of the fine scale vorticity and strain in free stream flow, i.e. finding easily computable approximations $S_f(\boldsymbol{u}_c)$ and $\boldsymbol{\omega}_f(\boldsymbol{u}_c)$. We allow us here to simplify the expressions as much as possible, and thus neglect viscosity and higher order terms and end up with linear ordinary differential equations driven by a known residual quantity. For simplicity we then approximate the solution to this ordinary differential equation by the residual quantity on the right hand side. Clearly, these approximations are very crude and will not be valid in the wall region nor can thay act as a stand-alone subgrid model since, e.g., no dissipation is present. They serve however as a simple and computationally inexpensive first alternative to demonstrate the ideas and the basic character of the derived subgrid terms. Work is in progress to take both viscosity and fine scale dynamics into account.

Taking the curl of the momentum equation (1) we obtain the following equation for the vorticity

$$D_t \boldsymbol{\omega} = S\boldsymbol{\omega} + \nu \Delta \boldsymbol{\omega}, \tag{9}$$

where $D_t = \partial_t + \boldsymbol{u} \cdot \nabla$ denotes the material derivative. Setting $\boldsymbol{\omega} = \boldsymbol{\omega}_c + \boldsymbol{\omega}_f$, $S = S_c + S_f$, and $\boldsymbol{u} = \boldsymbol{u}_c + \boldsymbol{u}_f$, neglecting viscosity and higher order terms we get an approximate equation for the fine scale vorticity $\boldsymbol{\omega}_f$:

$$\int_\Omega (D_t \boldsymbol{\omega}_f - S_c \boldsymbol{\omega}_f) \cdot \boldsymbol{v}_f d\Omega = -\int_\Omega (D_t \boldsymbol{\omega}_c - S_c \boldsymbol{\omega}_c) \cdot \boldsymbol{v}_f d\Omega. \tag{10}$$

Considering only very short times, which is the case for a single time step in an LES, we assume that the coarse scale terms are constant during the time step and that the coarse scale strain has a neglectable effect. We can thus compute the fine scale vorticity as

$$\boldsymbol{\omega}_f \approx \tau_{\boldsymbol{\omega}} (S_c \boldsymbol{\omega}_c - D_t \boldsymbol{\omega}_c), \tag{11}$$

with $\tau_{\boldsymbol{\omega}}$ a positive scaling parameter.

Repeating the arguments, we have that the strain tensor S satisfies the equation, see [9],

$$D_t S = -S^T S - (\boldsymbol{\omega}\boldsymbol{\omega}^T - I\boldsymbol{\omega} \cdot \boldsymbol{\omega})/4 - \mathcal{H}(p) + \nu \Delta S, \tag{12}$$

where $\boldsymbol{I}$ is the identity matrix and $\mathcal{H}(p)$ is the pressure Hessian. Setting $S = S_c + S_f$, using (11), and neglecting higher order terms and viscosity we get the following equation for the fine scale strain tensor S_f, here written in strong form:

$$D_t S_f + (S_c^T S_f + S_f^T S_c) + \mathcal{H}(p_f) = -D_t S_c - S_c^T S_c - (\boldsymbol{\omega}\boldsymbol{\omega}^T - I\boldsymbol{\omega} \cdot \boldsymbol{\omega})/4 - \mathcal{H}(p_c). \tag{13}$$

Assuming that $p_f = 0$, and approximating the solution to this problem by the right hand side, as above, we get

$$S_f \approx \tau_S (-D_t S_c - S_c^T S_c - (\boldsymbol{\omega}\boldsymbol{\omega}^T - I\boldsymbol{\omega} \cdot \boldsymbol{\omega})/4 - \mathcal{H}(p_c)), \tag{14}$$

with τ_S a positive scaling parameter.

Inserting the approximations (11) and (14) into (6) we get the following closed problem, here expressed in strong form: find $\boldsymbol{u}_c$ and p_c such that

$$\begin{aligned} \frac{\partial \boldsymbol{u}_c}{\partial t} + (S_c + \tau_S(-D_t S_c - S_c^T S_c - (\boldsymbol{\omega}\boldsymbol{\omega}^T - I\boldsymbol{\omega} \cdot \boldsymbol{\omega})/4 - \mathcal{H}(p_c)))\boldsymbol{u}_c + \\ (\boldsymbol{\omega}_c + \tau_{\boldsymbol{\omega}}(S_c \boldsymbol{\omega}_c - D_t \boldsymbol{\omega}_c) \times \boldsymbol{u}_c + \nabla p_c - \nabla \cdot (\nu \nabla \boldsymbol{u}_c) = \boldsymbol{f}, \\ \nabla \cdot \boldsymbol{u}_c = 0. \end{aligned} \tag{15}$$

In the numerical example presented below, the aim is only to demonstrate the nature of the derived VMS terms. The terms (11) and (14) are added to an LES code called LIME, developed at Chalmers and implemented using the C++ package Diffpack [3]. LIME uses finite elements for space discretization and employs a conditionally stable second order operator-splitting technique, originally proposed by Ren and Utnes [11], combined with SUPG stabilization [2]. The SUPG stabilization is normally included only to smooth the solution slighty, but now, since the VMS terms added actually are driving, destabilizing terms, some stabilization helps convergence. We emphasize that the derived VMS-terms can be implemented in an existing code based on finite volume or finite difference techniques. The subgrid model we use for the computations is the one equation eddy viscosity model by Schumann [12] combined with an explicit eddy viscosity wall model as described in, e.g., Wikström *et al.* [8]. This combination of model and wall treatment has shown good results in several applications, see e.g. Bensow *et al.*[1].

Boundary conditions at the inlet and walls are Dirichlet conditions for the velocity field, with $\boldsymbol{u} = U_\infty \hat{\boldsymbol{x}}$ for the inlet and $\boldsymbol{u} = \boldsymbol{0}$ on walls, and homogeneous Neumann conditions for the pressure. The outlet conditions consist of a homogeneous Neumann condition for the velocity and a traction free condition for the pressure, $2\nu \frac{\partial \boldsymbol{u}_n}{\partial n} - p = 0$.

The example chosen is the flow around a wing. The main feature of this flow is the formation of a vortex at the tip of the wing. Vortices are problematic to predict since diffusion, both from the numerical scheme and from the turbulence model, very quickly kills the rotation; in an experimental setup a tip vortex can be of considerable strength several tenths of cord lengths downstream while in a computation the vortex is weakened considerably already after one or two cord lengths.

The setup consists of a NACA 0015 wing with a sharp tip, mounted in a box on the side of a wall at 10° angle of attack. The span is $s = 0.6$ m and the cord is $c = 0.3$ m and the dimensions of box is $7c \times 4c \times 4c$ with a distance from inlet to wing of $2c$. Inlet velocity is $U_\infty = 8$ m/s which gives a Reynolds number $Re \approx 1.8 \cdot 10^5$ in air with $\nu_{air} = 1.52 \cdot 10^{-5}$. Experiments for this case are described in, e.g., [10].

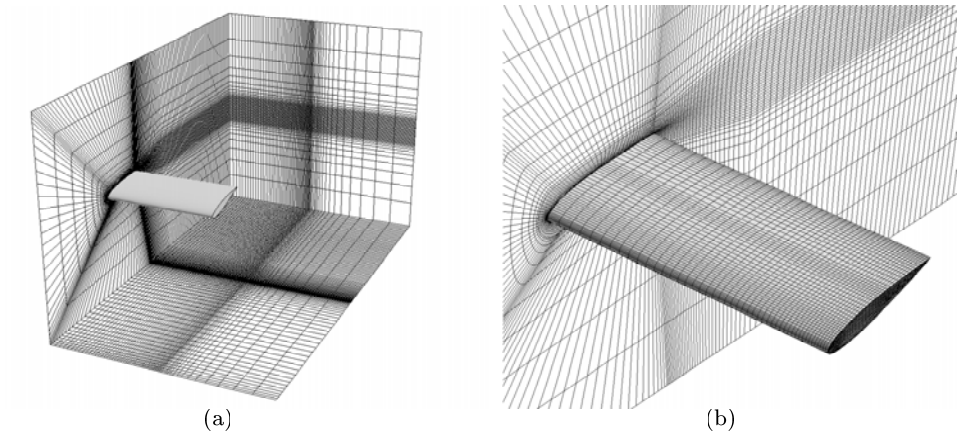

(a) (b)

Figure 1: The mesh used in the computations.

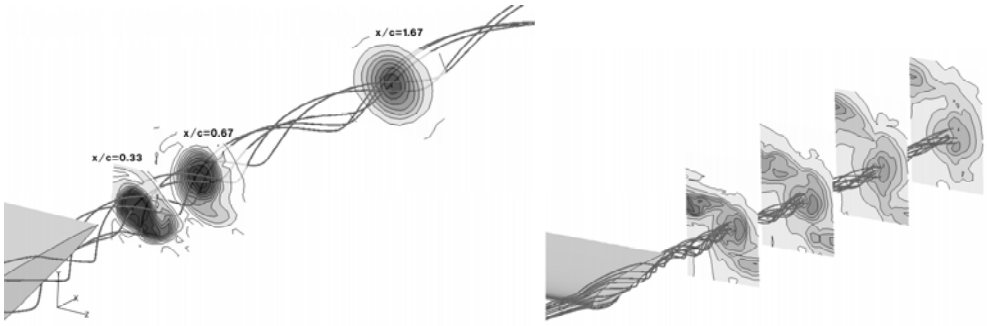

(a) (b)

Figure 2: Cuts with contours of a) u_x and b) ν_{sgs}. Figure a) shows the correct formation of the tip vortex while b) indicates the incorrect behaviour of the turbulent viscosity; physically, ν_{sgs} should be zero in the vortex.

The domain is meshed by a blockstructured approach with $0.8 \cdot 10^6$ elements, constructed so that the mesh in the wake, and especially the region occupied by the tip vortex, is as homogeneous as possible in order to avoid mesh dependent solutions. This is a relatively coarse mesh for an LES and especially the spanwise solution is insufficient, but this resolution was chosen to see the effect of the fine scale terms clearly.

The flow is dominated by a strong vortex generated by the leakage of fluid from the pressure side to the suction side over the wing tip, with the pressure difference being generated by the angle of attack. Also a sheet of secondary vortices are formed behind the wing. These smaller vortices are dragged into the larger tip vortex adding to its strength and the sheet has disappeared already after one or two cord lengths, observed both in experiments and our computations. Further downstreams the tip vortex gets more and more concentrated leading to higher maximum values of the vorticity magnitude.

The computational results are not quantitatively satisfactory due to the low mesh resolution. The absolute values of the vortex strength are too low and the velocity deficit too high. Moreover we see a zone of separation at the base of the wing that is possibly erroneous and thus might partly explain the just mentioned errors. This kind of behaviour is well known for underresolved LES. Qualitatively, however, the formation of both the tip vortex and the trailing vortex sheet is correct. In figure 2(a) contours of the longitudinal velocity deficit are shown, displaying the characteristic hook shape close to the wing while becoming more circular further back. Comparing these plots with the corresponding experimental results in [10] we note that although the shape

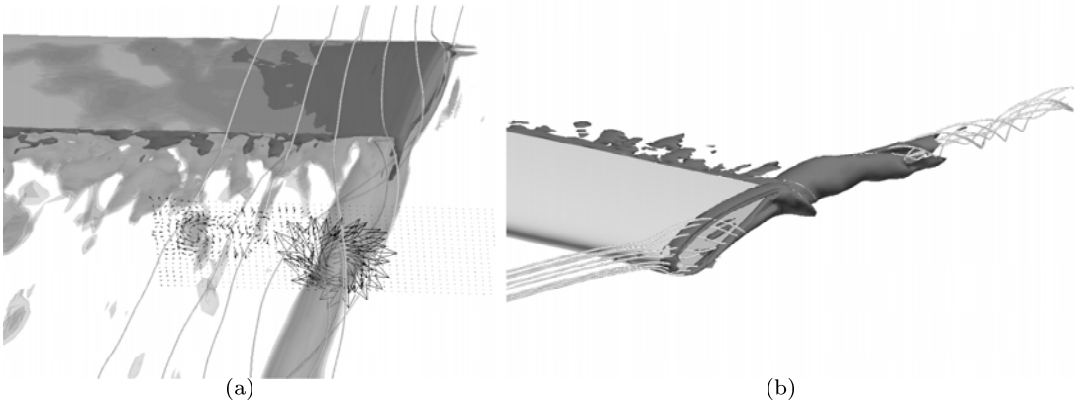

(a) (b)

Figure 3: Detail of the flow over the wing tip. Streamlines together with isosurfaces of (a) the longitudinal vorticity and (b) the fine scale vorticity $S_c\boldsymbol{\omega}_c \times \boldsymbol{u}_c$. Also the vectors included in (a) are the term $S_c\boldsymbol{\omega}_c \times \boldsymbol{u}_c$.

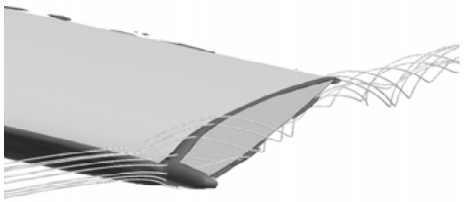

Figure 4: Detail of the flow over the wing tip. Streamlines together with an isosurface of $||S_f\boldsymbol{u}_c||$.

of the contours are correct the velocity deficit is too large.

Focusing on the influence of adding the fine scale terms, we see a clear improvement. As can be seen in figure 2(b), we have an increase in the turbulent eddy viscosity in the vortex. This is not a correct behaviour of the subgrid model since the vortex is not a turbulent phenomenon. It will never the less kill the vortex quickly. It is also reasonable to believe that the numerical diffusion is high in this region of large gradients. From figures 3(a) and 3(b) it is clear the fine scale vorticity counteracts this bad behaviour of the numerical scheme. The term (11) drives the rotation of both the primary tip vortex and the secondary structures in the trailing vortex sheet. The term is active where expected, in the formation of the vortex at the tip and along the vortices in the wake, and the direction of its driving action is correct making the vortices survive throughout the computational domain, see figure 5. The result of the fine scale strain is not as obvious, but as for the fine scale vorticity, figure , both the location and direction of the term () seem reasonably accelerating the flow over the leading edge and the tip edges.

References

[1] R. Bensow, T. Persson, , F. C., S. U., and A. N. Simulation of the viscous flow around submarine hulls. In *Proceedings for 25th Symposium on Naval Hydrodynamics*, St. John's, Canada, 2004.

[2] F. Brezzi, M.-O. Bristeau, L. Franca, M. M., and G. Rogé. A relationship between stabilized finite element methods and the galerkin method with bubble function. *Comp. Meth. in Appl.*

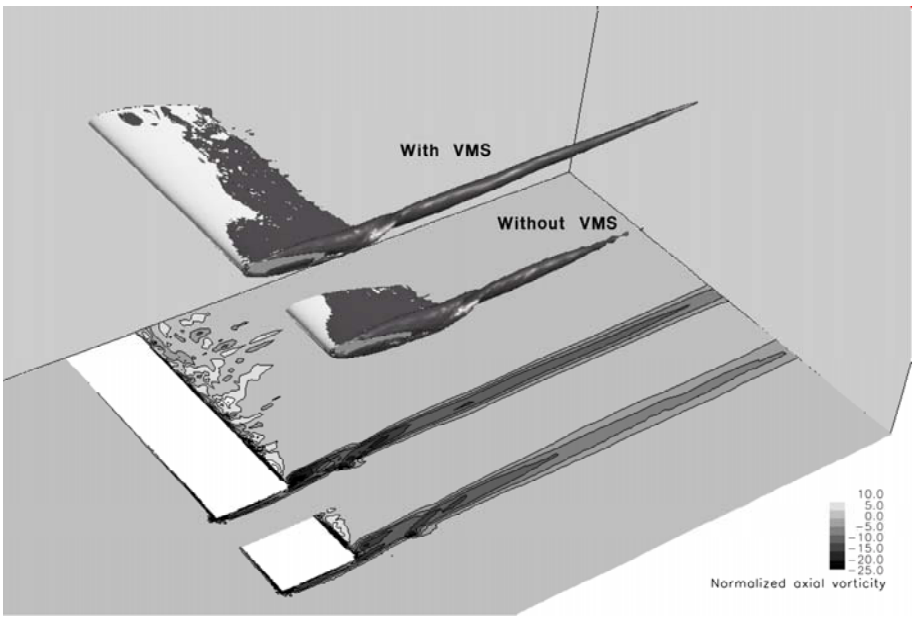

Figure 5: Comparison of the vortex strength between a computation using the VMS terms and one without them. The isosurface of the normalized longitudinal vorticity, $(\nabla \times u)_x c/U_\infty = -10$, is shown.

Mech. Engin., 96:117–129, 1992.

[3] Diffpack software package, http://www.diffpack.com.

[4] M. Fan, W. Y., D. W., X. M., and S. J. Computing blunt body flows on coarse grids using vorticity confinement. *Transactionof the ASME*, 124, 2002.

[5] T. Hughes, G. Feijóo, L. Mazzei, and J.-B. Quincy. The variational multiscale method—a paradigm for computational mechanics. *Comput. Methods Appl. Mech. Engrg.*, 166(1-2):3–24, 1998.

[6] T. Hughes and A. Oberai. The variational multiscale formulation of LES with application to turbulent channel flows. In *Geometry, mechanics, and dynamics*, pages 223–239. Springer, New York, 2002.

[7] T. J. R. Hughes, V. M. Calo, and G. Scovazzi. Variational and multiscale methods in turbulence. Preprint 2004-46, ICES, University of Texas at Austin, www.ices.utexas.edu, 2004.

[8] W. N., S. U., A. N., and F. C. Large eddy simulation of the flow past an inclined prolate spheroid. In *Proceedings for TSFP 3*, 2003. Sendai, Japan.

[9] K. Nomura and G. Post. The structure and dynamics of vorticity and rate of strain in incompressible homogeneous turbulence. *J. Fluid Mech.*, 377:65–97, 1998.

[10] B. Ramaprian and Y. Zheng. Measurements in the rollup region of the tip vortex from a rectangular wing. *AIAA Journal*, 35(12), 1997.

[11] G. Ren and T. Utnes. A finite element solution of the time-dependent incompressible navier-stokes equations using a modified velocity correction method. *Int. J. Num. Meth. in Fluids*, 17:349–364, 1993.

[12] U. Schumann. Subgrid scale model for finite difference simulation of turbulent flows in plane channels and annuli. *J. Comp. Phys.*, 18:376, 1975.

Hydrodynamic analysis of the performance of rowing boats with unsteady motions

M. Berton, B. Alessandrini, S. Barré and J.M. Kobus
Laboratoire de Mécanique des Fluides UMR-CNRS 6598
Ecole Centrale de Nantes, B.P. 92101, 1 rue de la Noë 44321 Nantes Cedex 3
mikael.berton@ec-nantes.fr, bertrand.alessandrini@ec-nantes.fr,
sophbarre@wanadoo.fr, jean-michel.kobus@ec-nantes.fr

1 Introduction

This paper discusses some of the physical processes that govern the motion of a rowing boat. The rowers and their oars transfer momentum to the boat, causing an unsteady forward speed. The process is complicated by the motion of the rowers within the boat itself, introducing coupled pitch and heave motions too. Many forms of drag are manifest in resisting the motion of the boat such as skin, form, wave and aero-dynamical. This paper focuses specifically on hydrodynamic drag, which is viscous dominated in the case of rowing boats (viscous drag is about 90% of the total resistance). What makes the problem both fascinating and challenging from an engineering and computer modeling perspective is the pulsatory form of propulsion coupled with both unsteady pitch and heave motions. However, dynamic effects are generally not taken into account in the present design process due to the complexity to simulate unsteady flows. Recent research has been devoted toward predictions that are based on the solution of the viscous flow field. The great majority of this research has been devoted to analysis of roll motions due to the obviously viscous nature of this flow. Examples of three-dimensional roll simulation are given in Chen et al. [3] for a rolling ship and Miller et al. [7] for a three-dimensional cylinder with bilge keels.

The first objective of the present work is to extend this effort in unsteady RANS simulations to the ability to accurately predict hydrodynamic drag acting on rowing boats with unsteady forward speed. Detailed comparisons with experimental results are presented in order to validate the CFD solver ICARE 3D. A particular attention has been paid to unsteady resistance for a fairly wide range of test conditions. Once the code is validated and in order to present a completely thorough analysis, response surfaces are built to determine the effects of physical parameters as frequency, amplitude or displacement on unsteady resistance. As the motion of a rowing boat is not limited to unsteady forward speed, we finally present the possibility to simulate a 3 degree of freedom rowing system, with the coupling of hydrodynamic and rowing mechanics solvers.

2 Computational Method

The ICARE 3D code provides calculation of 3D, turbulent, incompressible, unsteady free surface flow around a hull. The fluid domain is described using a set of curvilinear space variables and equations are discretised by second-order finite difference schemes in space and time. A O-O structured monobloc grid system is used in our study for better control of the density of the mesh in the boundary layer. The interface is updated with a free-surface tracking method : at each time step, the mesh is regridded following the new shape of the free surface. An original fully-coupled method is used to solve the discretised set of equations, offering a better accuracy and efficiency than weak coupled algorithms (PISO), especially for the convergence of the velocity-pression coupling. More details can be found in Alessandrini et al. [1].

3 Geometry and grid generation

The geometry selected for the validation of both steady and unsteady simulations is a rowing boat whose main characteristics are summarized in table 1.

Grid resolution and quality play a crucial role for the accuracy of viscous flow calculations. Here, the ship geometry is simple and the commercial grid generating program GRIDGEN (from Pointwise, Inc) was used to generate a single-block structured grid. Grid fairness was achieved by using a Poisson solver. The Poisson

LWL (m)	8.15
S_{WL} (m^2)	2.15
Draft(m)	0.088
Beam (m)	0.274
Longitudnal prismatic coeffcient C_P	0.621
Block coefficient C_B	0.467

Table 1: Geometric parameters for skiff. Static condition.

solver was applied also for the grids on the boundary surfaces. The tolerance for solving (by iteration) the Poisson equations was 10^{-3}. Normally 30 to 40 iterations were required. As the problem is symmetrical, the computation is realized on a half domain.

A parametric study was performed on the sensitivity of the flow solutions to changing grid parameters. Distance from the body to the outer grid boundary and number of grid points were examined as parameters. This investigation was based on a single flow solver, ICARE 3D, and may not be directly applicable to other RANS codes. If we do not want to take into account the diffracted effects in our simulation (open sea problem), the grids is generated using large expansion factors in order to concentrate most grid cells near to the ship and get larger cells further outside. In this way, the wave pattern is better captured and wave reflexion from the boundaries is minimised without artificial damping. However, the towing tank experiments have been made with a full scale slender ship whose speed was near the critical one defined by depth Froude number : $F_h = 1$. That is why we have decided to use ICARE 3D to exactly reproduce a towing tank experiment and then quantify side walls effects both at subcritical and critical speed. Then, in order to exactly make validation of the code, we have to take into account the basin geometry (width = 5 m, depth = 3 m). In this case, when wave reflexions on the side walls are part of interest, pressure terms are canceled only in two restricted zones as it is shown on figure 3 in order to stabilize the numerical simulation. The outer boundary is moving downward from an original location at 1.25 L of the ship bow/stern until the variables of interest do not vary anymore. Then, its location does not influence the numerical results.

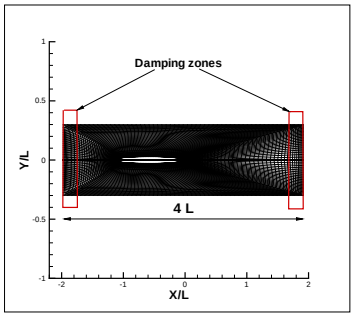

Figure 1: basin geometry and damping zones.

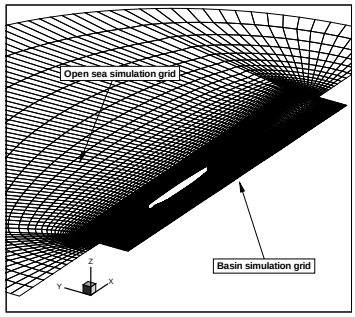

Figure 2: $O-O$ grids generated for open sea and basin simulations.

4 Verification and validation (V&V) procedure

With the increasing use of CFD in ship hydrodynamics, there is a growing interest in the quantitative accuracy of CFD predictions as stated by Roache [9], to make sure that they can be used with sufficient confidence. It is not necessarily clear or obvious what is a good grid for a particular flow field prediction and results are often experience driven for complicated predictions. To better estimate the quality of a solution there have been efforts to develop uncertainty estimates and validation procedures for computations [2], [4], [10]. Briefly, the error in a simulation, can be decomposed into its numerical and modeling components. Using generalized Richardson extrapolation using a set of six grids, the uncertainty in the solution U can be estimated. The difference between the simulation and the data is the comparison error E. This is compared to the validation uncertainty U_V which is made up of the numerical uncertainty U_{SN} and the uncertainty in the data U_D. If the error is less than the uncertainty, the model is validated. This procedure has been applied with success in this work both for steady and unsteady case. Forces and moment coefficients are examined and validated. Results obtained for unsteady resistant coefficient are briefly described below.

For unsteady simulations, unsteady resistant coefficient is compared to experiments in terms of time histories and Fourier components (FS). The decomposition into the mean and the first two harmonics amplitude and phase is realized with a moving window of one period long.

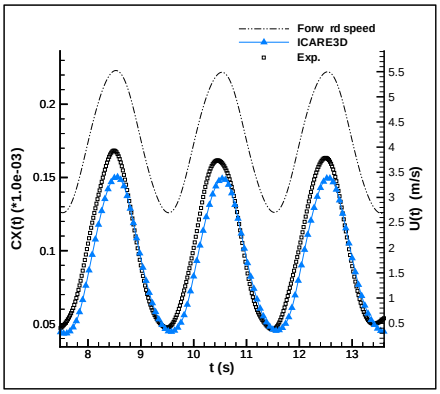

(a) Validation test case : numerical and experimental results on time histories of resistant coefficient C_X

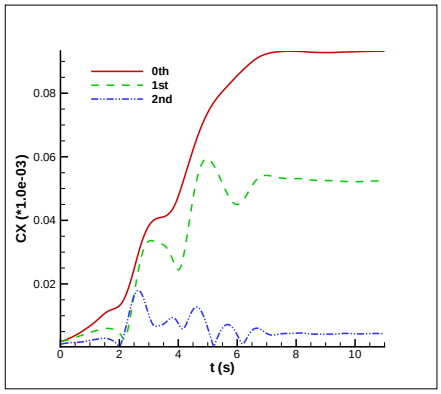

(b) Stabilisation of the Fourier components of the resistant coefficient.

Figure 3: Resistant coefficient : experimental and numerical results for the validation test case. $Fr = 0.45$, $A_m = 0.45\,m$ and $\Omega = \pi\ rad.s^{-1}$.

The V&V procedure has been applied using a set of six grids. The simulations were run at $Fr = 0.45$, with the following imposed velocity :

$$U(t) = U_0 + A_m \Omega cos(\Omega t) \tag{1}$$

U_0 is the mean velocity ($4.1\ m.s^{-1}$), A_m and Ω are the amplitude (m) and the pulsation ($rad.s^{-1}$) of the surge motion respectively. In our test case, $A_m = 0.45\,m$ and $\Omega = \pi\ rad.s^{-1}$.

Description of the unsteady validation test case is shown on figure 3(a) : time domain comparison of numerical (with the finest grid and time step) and experimental results are also presented. If numerical results show a good accuracy with a well estimated resistant coefficient amplitude, a small phase lag can be observed. Stabilisation of Fourier components of the numerical resistant coefficient is shown on figure 3(b). V&V results for the mean (C_{X0}) and the first harmonic (C_{X1}) resistant coefficient are summarized in table 2; fine grid and time step are used. As expected, the uncertainty U_V is greater than the comparison error E. The model is then validated with success for this case.

	U_{SN} (%)	U_D (%)	U_V(%)	E (%)
C_{X0}	3.35	3.5	4.87	4.40
C_{X1}	3.38	3.5	4.86	3.16

Table 2: Validation of the mean and the first harmonic of the resistant coefficient for fine grid and time step.

5 CFD and statistical experimental design

In this section, we show how statistical design of experiment (DOE) offers a particulary efficient way to conduct numerous parametric studies. Its application to unsteady hydrodynamics problems is also described.

Experiment design is a strategic approach to reveal the complex and interacting effects that often appear in engineering systems. A class of designs, known as response surface method (RSM), are able to capture system knowledge in a polynomial regression model. This model can serve as a surrogate for the complex system response, if properly constructed (see Fig.4).

The concept of a polynomial RSM based upon “computer experiments” seems to have arisen one decade ago and the literature contains several examples of RSM applied successfully to computer experiments. However, if we can see a variety of aerospace analyses that have benefited from this approach [5], little work can be found in hydrodynamics problems [8]. This work contains an example that relies upon CFD solution of unsteady Navier-Stokes equations with free surface for the response data.

Most computer experiments differ from physical experiments in one very significant manner : the computer experiment is a deterministic problem, whereas the physical experiment is a stochastic one (measurement

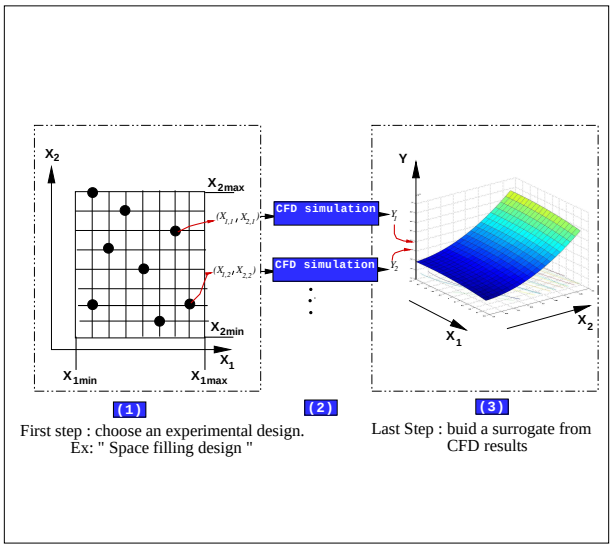

Figure 4: Experiment design : principle.

uncertainty). However, traditional lack-of-fit statistics can be used to quantify the agreement between the polynomial model itself, and the underlying response data used to build the model.
The objective of this work is to demonstrate how RSM and CFD have been incorporated to analyse and model unsteady hydrodynamic efforts acting on a rowing boat. It can be stated that our work is not restricted to this particular case and offers a general approach that could be used for other hydrodynamic problems.
In our problem we have listed five parameters (Froude number, displacement, trim, amplitude and frequency of the surge motion) that could influence the resistant coefficient. In order to fit a second order polynomial surface with 5 factors, 21 runs at least are necessary. With only 24 runs, surrogate models with high statistical properties are built and can be used with confidence for sensitivity analyses.
Thanks to RSM surrogate models, force and moment coefficient values can be predicted accurately all over the design space.
In order to validate our methodology, we compare the mean and the first harmonic of the resistant coefficient predicted with surrogate models and experimental results. We then introduce the dimensionless frequency and amplitude : $f^* = \frac{f}{f_{max}}$ with $f_{max} = 0.6\,Hz$ and $a^* = \frac{A_m}{A_{m_{max}}}$ with $A_{m_{max}} = 0.5\,m$. The comparison results are shown on figure 5 where the relative error E is also estimated (for a quantity X, $(E(\%) = \| \frac{X^{RSM} - X^{Exp.}}{X^{Exp.}} \|)$) for each case.

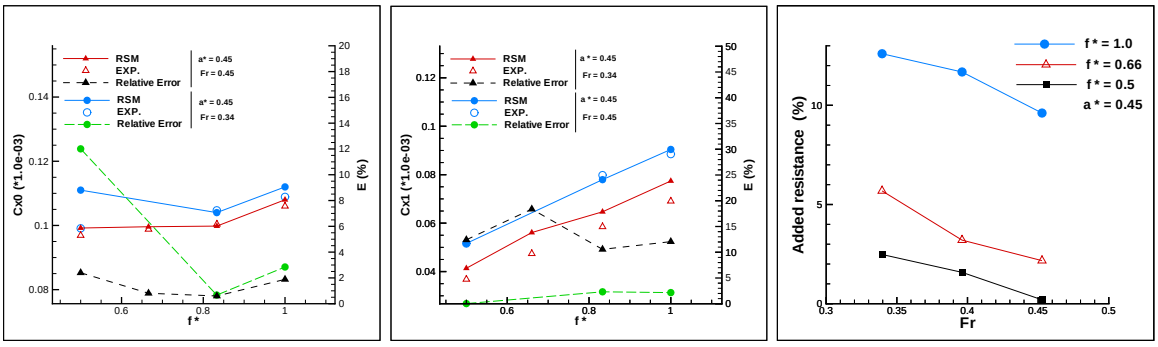

(a) C_{X0} (b) C_{X1} (c) $C_{X_{ad}}$

Figure 5: (a) and (b) : RSM estimation of the mean and first harmonic resistant coefficient; validation with experimental data. (c) : Added resistance evaluation.

The mean and first harmonic of the resistant coefficient are well described all over the design space with a small to reasonable relative error (except at low Froude number for the first harmonic where the relative error reaches 16%). From these results, it can be stated that the mean amplitude increases non-linearly with increasing frequency. The first harmonic shows the same trend but increases linearly with increasing frequency.

The added resistance, defined as : $C_{X0_{ad}}(\%) = \frac{C_{X0} - C_{X_{steady}}}{C_{X_{steady}}}$ is shown on figure 5(c). Significant difference (up to 13%) can be observed between steady and mean unsteady resistant coefficient for a fairly wide range of Froude number : $C_{X0_{ad}}$ increases nonlinearly with increasing frequency and decreases linearly with Froude number.

6 Coupling of rowing mechanics and hydrodynamic solvers

An other part of our work consists in simulating the complete rowing system by coupling mechanics and hydrodynamics solvers.
The first step is to pre-compute forces and moments due to the rowers and their oars. Hydrodynamic forces on the blade are calculated as a function of relative fluid velocity and angle of attack : a simple quasi-steady model is adopted [11]. Giving an angle of attack, rowers kinematics is deduced and used to evaluate their position, velocity and acceleration at each time step. The ship motion equations are written using Euler's law. Those equations are discretized with explicit first and second order schemes (prediction and correction). The use of explicit schemes means that at each time step, the hydrodynamic sensor is computed on the previous ship position [6].

The following tests and computations protocols have been tested and validated with success :

1. The boat starts without forward speed and is accelerated until it reaches its nominal speed, e.g. 4.5 $m.s^{-1}$.
2. The rowing tensor is imposed and the simulation is performed with one or two degrees of freedom (first ddl : surge motion, second ddl : pitch motion).

The heave motion has not been simulated with success until now : instabilities occur when all coupling motions are taken into account. Explicit resolution could explain these difficulties and more research on this subject has to be done. Two examples of successfull simulations are presented below : the first one is realized with only one degree of freedom (unsteady forward speed) and the second shows how pitching motions coupled with unsteady forward speed can affect the last results. To validate these numerical simulations, measurements made by J.M Kobus and S. Barré (realized with a rower on the real boat) are also presented. In order to help the reader's comprehension, the difference steps of the rowing cycle are included (see figure 6).

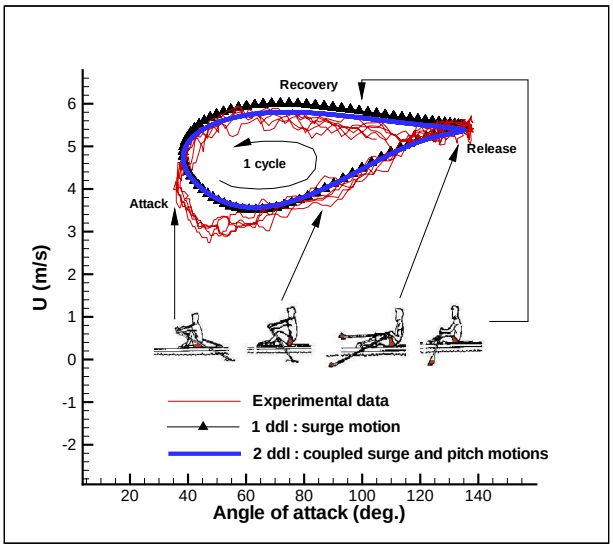

Figure 6: Numerical simulations with one or two degrees of freedom compared to experimental data measured on real boat.

A good agreement can be observed except at the end of the cycle because the real style of the rower (and thus the real dynamics) is not accurately described in our mechanical solver. The global trend of the phenomena are correctly captured and tend to confirm the capability of the method in such application.

7 Conclusions

In this work, the ICARE 3D code has been successfully validated : V&V procedure is applied to unsteady case with an imposed surge velocity. Results are analyzed and compared to experimental data in terms of time histories and Fourier components.
Once the ICARE 3D code has been validated, its results can be used to identify and fit an appropriate response surface model. This method provides results of acceptable accuracy for both steady and unsteady hydrodynamic assessment and is cheap regarding computational time required (a surrogate model with 5 factors can be fitted and analyzed with only 24 CFD runs with confidence), which is essential for parametric studies. The parametric study shows the significant influence of the frequency on the mean and first harmonic drag coefficient amplitudes. The added resistance is also studied and increases considerably when the frequency is increasing. That is not the case when amplitude is considered where a slight variation is observed.
The last part of this work concerns the fully coupled mechanics and hydrodynamics solvers. Results are very promising and tend to confirm the significant role played by pitching motions in global performance.

References

[1] B. Alessandrini and G. Delhommeau. A multigrid velocity-pressure-free surface elevation fully coupled solver for calculation of turbulent incompressible flow around a hull. In *21 Symposium on Naval Hydrodynamics*, pages 328–345. The National Academy of Sciences, 1997.

[2] I. Celik and O. Karatekin. Numerical experiments on application of richardson extrapolation with nonuniform grids. *Computer Methods in Applied Mechanics and Engineering*, 119:584–590, September 1997.

[3] H. Chen, T. Liu, and E. Huang. Time-domain simulation of large amplitude ship roll motions by a chimera rans method. In *11th International Offshore and Polar Engineering Conference*, volume 3, pages 299–306. Stavenger, June 2001.

[4] L. Eça and M. Hoekstra. On the application of verification procedures in computational fluid dynamics. In *2nd Marnet-CFD workshop*. Copenhagen, 2000.

[5] A. Giunta. *Aircraft multidisciplinary design optimization using design of experiments. Theory and response surface modeling methods.*. Ph.D. thesis, Faculty of Virginia Polytechnic Institute, Blacksburg, Virginia, May 1997.

[6] E. Jacquin, P. Guillerm, Y. Roux, and B. Alessandrini. Toward numerical vpp with the coupling of hydrodynamic and aerodynamic solvers for acc yachts. In *17th chesapeake sailing yacht symposium*. Annapolis, Maryland, March 2005.

[7] R. Miller, J. Gorski, and D. Fry. Viscous roll prediction of a cylinder with bilge keels. In *24th Symposium on Naval Hydrodynamics*. Fukuoka, Japan, July 2002.

[8] Y. Minami and M. Hinatsu. Multi objective optimization of ship hull form design by response surface methodology. In *24th Symposium on Naval Hydrodynamics*. Fukuoka, Japan, July 2002.

[9] P. Roache. Verification of codes and calculations. *AIAA journal*, 36(5):696–702, May 1998.

[10] F. Stern, R. Wilson, H. Coleman, and E. Paterson. Verification and validation of cfd simulations. Technical Report 407, Iowa Institute of Hydraulic Research, University of Alabama in Huntsville, September 1999.

[11] J. Wellicome. Report on resistance experiments carried out on three racing shells. Technical report, NPL Ship T.M., 1967.

PDSTRIP – A Strip Method for Ship and Yacht Seakeeping

Volker Bertram, ENSIETA, Brest/France, volker.bertram@ensieta.fr
Heinrich Söding, TU Hamburg-Harburg, Hamburg/Germany h.soeding@tu-harburg.de
Kai Graf, FH Kiel, Kiel/Germany, kai.graf@fh-kiel.de

ENSIETA, www.ensieta.fr, is a French university teaching naval architecture and offshore engineering. Research in one department focuses on the mechanics of marine structures, with seakeeping as one of the areas of interest. In 2005, ENSIETA faced a situation that motivated the development of a shared seakeeping analysis tool:

- Seakeeping formed part of the standard curriculum as in most universities offering degrees in naval architecture and/or offshore engineering. Exercises supplemented lectures, but students felt rightfully that examples were unrealistic in simplicity of geometry or reduction of physics, e.g. having only one degree of freedom. Three hours dedicated to exercises with a commercial seakeeping program (3-d Green function method) were appreciated by the students, but not by the financial department, as even with splitting students into groups and having three students per terminal, the necessary number of licenses for this commercial program placed a heavy burden on ENSIETA, while at most only one license was used for the remainder of the year. Hence the desire to have a no cost/low cost software for seakeeping analysis which could be used in unlimited parallel installations, perhaps even given to students who had their own private computers.

- Funds for research cooperation between the University of Applied Engineering in Kiel (FH Kiel) and ENSIETA were available and FH Kiel was interested in adding a seakeeping analysis tool to its existing design software for competitive sailing yachts. Required computational response and available computing resources made a linear strip method approach the obvious choice. As expected, there was no such method on the market for sailing boats with their own particular hydrodynamics (involving roll damping due to the sails, asymmetric hulls due to heel, large lifting surfaces such as keel swords and rudders). Neither was a 'regular' strip method program available that was suitable for modification for the particular problem at hand. Commercial programs as listed in Appendix 2, were only available in executable versions, published research approaches were only given in form of papers generally without giving sufficient details for re-programming and even then such a development would have taken man-months even for very limited functionality.

The decision appeared obvious: Use the research project to fund the development of a strip method code, incorporating the necessary functionalities to support sailing boat seakeeping analysis, but also capable for most other ships. The resulting software should then also support teaching students involving advanced applications. This requires multiple installations of a documented and user-friendly code. Fortunately, the involved partners in the project have avoided so far the commercialization of the academic field imposed in many countries of the world. From the beginning, the intention has been to make the research results, particularly the software, widely available.

The closest starting point to our intended goal was the Fortran 77 strip method program STRIP of Prof. Söding of the Institut für Schiffbau in Hamburg (The IfS was subsequently integrated into the TU Hamburg-Harburg). STRIP was freely given to whoever asked, but

- the source code was not written with the intention of being easy to understand and modify;
- the documentation was in German;
- the documentation was not consistently updated with the source code;
- the programming assumed a Linux/Unix operating system allowing easy assignment of input and output files on the operating system level;
- STRIP covered only parts of the required functionality, in particular roll damping due to sails, shallow water, and second-order forces (added resistance and drift force) were not considered.

The new strip method, released as open-source, public domain code, was called PDSTRIP, Bertram et al. (2006). It was implemented in Fortran 90/95. This allowed to incorporate most existing subroutines reducing programming effort and error sources. GUI scripts for executable versions for Windows 95 to Windows XT were added for those who just wanted to use the program (students and industry). The extension and modernization of the source code has still involved considerable effort, which is not yet finished, although a workable executable version is already available. The appendix shows examples of source code in the original version and the corresponding source code in the new version. Improvements are due to largely self-explanatory variable names, 'cosmetics' (indentation), and use of the extended standard functions in Fortran 90/95 for vector and matrix operations.

PDSTRIP computes the seakeeping of ships and sailing yachts according to the strip method which was proposed originally by *Korvin-Kroukowski and Jacobs (1957)*. Here, however, the slightly different method of *Söding (1969)* is applied for motions, and the procedure of *Hachmann (1991)* for the pressure. Responses in regular waves are given as transfer functions, i.e. as ratio between the response amplitude and amplitude of the wave causing that response. For so-called linear responses this ratio is independent of the wave amplitude. The program is mainly confined to such linear responses; however, it takes into account some nonlinear effects. Responses in natural seaways are given as significant amplitudes. These are defined as the average of the one-third largest positive maxima of the response, neglecting the 2/3 smaller positive maxima. The significant amplitude is twice the standard deviation (from the average value zero) of the response.

The following responses are computed:

- Translations in directions *x,y,z* of the ship-fixed coordinate origin
- Rotations around the three coordinate axes
- The translation of user-specified points on the body in 3 coordinate directions
- The relative translation between these points and the water assumed to be disturbed by the waves, but not by the ship
- The acceleration at these points; if required, after weighing with a function of motion frequency (encounter frequency)
- The pressure at a specified number of points on each offset section
- Sectional force (3 components) and moment (3 components) in cross sections (x = constant) of the ship

The program cannot deal with multi-hulls, air-cushioned vehicles or planing hulls. But PDSTRIP has several special features making it suitable for practical applications to most ships and sailing yachts:

- Consideration of discontinuous sections (as found at forebodies with bulbous bows)
- Consideration of transom sterns
- Consideration of unsymmetrical cross sections (as in heeled ships)
- Consideration of shallow or deep water
- Consideration of fins (such as rudders, bilge keels, etc.)
- Consideration of active fins (such as roll stabilizers)
- Consideration of roll damping due to sails in sailing yachts. With some precautions the method to take account of sails may also be applied to wind forces on superstructures of ships without sails, or on deck containers etc.
- Consideration of suspended loads (as in crane ships)

Different 'players' have different requirements for documentation:

1. Users form the largest group of 'players'. PDSTRIP Users would include students at different levels, as well as researchers and industry users. It is difficult to combine extended functionality and user-friendliness. At present, we accepted that the input is complicated if advanced features are used like incorporating rudders and sails. The ideal user (from a developers perspective) is well educated in the underlying physics and understands thus also limitations of

the code, avoiding input that may be formally correct, but will still result in results without physical meaning. The typical user in reality does not even like to read a user manual, leave alone theoretical background requiring a post-graduate education in naval architecture. As an intermediate approach, we developed a user manual, specifying the format of the input, but have so far very few checks by the program concerning the correctness of the input. We also prepared an overview of the physical model behind the PDSTRIP, which a serious user is expected to read. For simple computations of responses of naked ship hulls in regular waves, the code is easy to use.

2. Programmers need not only access to the source code, they need to understand the source code completely in order to modify or extend it. 'Programmers' for our case would understand the hydrodynamics and extend the model. They need essentially an explanation of the code structure and the algorithms behind the individual modules. We focused here on the hydrodynamics modules, namely
   - a 2-d strip module to compute added mass, damping and exciting forces
   - the global module giving 3-d values by integrating over all 2-d strips
   - a module for converting responses in regular waves to significant responses in natural seaways
   - modules for appendages like rudders, bilge keels, sails
   - a module for second-order forces
   - a module for special treatment of surf-riding (very low encounter frequency)

   Bertram et al. (2006) describe the core 2-d module.

At present, the code has been tested with different compilers under Linux and Windows. Test cases include the Series-60 hull. The test cases so far indicate that the code is properly implemented, showing typical results for a strip method (good heave and pitch prediction, poor surge prediction, 'reasonable' prediction for other degrees of freedom for slow to moderate Froude number and small wave amplitude.

The focus was on obtaining an executable version quickly to supply demand in research and teaching. Further documentation and conversion of the source code to a more structured code in more homogeneous programming style intended for faster understanding by other programmers remain to be done. At present, the input data for advanced options (like rudders) requires advanced knowledge in ship hydrodynamics. This knowledge could be documented in external text documents, but could also be incorporated in pre-processing programs. Such programs may be called (somewhat pretentiously) 'expert systems'. Interactive graphical programs for grid generation, check and modification would further facilitate analyses using PDSTRIP. Similarly, the output is at present purely text based. Post-processing programs could automatically create curves of transfer functions or even visual displays (snap-shots, videos, virtual reality models) of the ship motions. It would benefit the whole industry and academic community if such further extensions would likewise be shared and published.

The URL for PDSTRIP is http://sourceforge.net/projects/pdstrip/ or you can contact Volker Bertram.

References

BERTRAM, V. (2000), *Practical Ship Hydrodynamics*, Butterworth+Heinemann, Oxford

BERTRAM, V.; VEELO, B.; SÖDING, H.; GRAF, K. (2006), *Development of a Freely Available Strip Method for Seakeeping*, COMPIT'06,
http://www.3me.tudelft.nl/live/binaries/cf8c31ad-a975-4aa0-9f0e-e680d5aad97d/doc/Compit06_Proceedings.pdf

HACHMANN, D. (1991), *Calculation of pressures on a ship's hull in waves*, Ship Techn. Research 38, pp.111-133

KORVIN-KROUKOVSKI, B.V.; JACOBS, W.R. (1957), *Pitching and heaving motions of a ship in regular waves*, SNAME Transactions

SÖDING, H. (1969), *Eine Modifikation der Streifenmethode*, Schiffstechnik 16, pp.15-18

SÖDING, H. (1993), *A method for accurate force calculation in potential flows*, Ship Techn. Research 40, pp. 176-186

Appendix: Examples of original and new source code

Some lines of source code of original STRIP code:

```
      read(5,*,END=400)H,T,HAUPTR,EXPON,SPUH
      if(H.eq.0)stop
      WRITE(8,'(/1x,1A80)')TEXT
      WRITE(8,'(/
     & '' Seegangsdaten: Kennzeichnende Hoehe          '',F10.3/
     & '' Periode T1 entspr. Schwerpunkt des Spektrums '',F10.3/
     & '' Laufrichtung (0 von hinten, 90 Grad von Stb.)'',F10.3/
     & '' Exponent in Winkelverteilung (meist 2 bis 4) '',F10.3/
     & '' Spitzenueberhoehung (1 bei Pierson-M.-Sp.)   '',F10.3)')
     & H,T,HAUPTR,EXPON,SPUH
C Hauptrichtung des Seegangs muss zwischen 0 und 180Grad liegen. ABSCHAFFEN
C Vorbereitungsrechnungen fuer Integration
      OMPEAK=(4.65+0.182*SPUH)/T
      DOMSP=0.025*OMPEAK
      DMUE=0.05
      DO 20 IOM=1,NOM
      OM(IOM)=SQRT(2*3.14159*G/RLA(IOM))
 20   continue
      DO 30 IART=1,NART+3*nb
      DO IV=1,NV
      AMPKEN(IART,IV)=0.
      enddo
 30   continue
```

Some lines of source code of the new PDSTRIP code:

```
  read(5,*,END=400) H,T,HAUPTR,EXPON,SPUH !reads seaway datda
  if (H.eq.0.0) stop
  write(6,*) '--------------------------------------------------------------------------------'
  write(6,*)
  write(6,'('' Significant wave height                    '',F10.3)'), H
  write(6,'('' Period T1 corr. to c.o.g. of spectrum      '',F10.3)'), T
  write(6,'('' Central wave dir.(0 from stern, 90 from stb.)'',F10.3)'), HAUPTR
  write(6,'('' Exponent n in cos^n angular spreading funct. '',F10.3)'), EXPON
  write(6,'('' Peak enhancement factor (1 for P.-M.spectrum)'',F10.3)'), SPUH
! Preparations for integration
  OMPEAK=(4.65+0.182*SPUH)/T
  write(6,*)
  write(6,'('' Peak period                                '',F10.3)') 6.283/OMPEAK
  DOMSP = 0.025*OMPEAK
  do IOM = 1,NOM   ! compute wave number for all frequencies omega
     WAVEN=2.*3.14159/RLA(IOM)
     OM(iom)=sqrt(WAVEN*G*tanh(WAVEN*(ZBOT-ZWL)))
  end do
  do IART = 1,NART+3*NB
     do IV = 1,NV
        AMPKEN(IART,IV)=0.
        MAXDAMPKEN(IART,IV)=0
     end do
  end do
```

Validation of the RANSE wake computations for the training vessel Nawigator XXI and the dredger Uilenspiegel.

Tomasz Bugalski, Marek Kraskowski

Ship Design and Research Centre S.A., Poland
tomasz.bugalski@cto.gda.pl
marek.kraskowski@cto.gda.pl

Validation of the wake filed computations for two vessels, both in model scale and full scale, was one of the main tasks of the European project EFFORT. The results obtained from RANSE solvers were compared with the following experimental data:

- Pitot probe measurements – at model scale.
- Particle Image Velocimetry (PIV) measurements – at model scale.
- Laser – Doppler Velocimetry (LDV) measurements – at full scale.

Ship Design and Research Centre S.A. participated in EFFORT and was engaged primarily in the model tests; however, some comparative computations were carried out, using the experience of other partners, in order to implement an effective procedure for the computations of wake field.
The following paper presents the alternative method for the accurate wake field prediction, which gave promising results, as well as sample results of the PIV measurements for the model with working propeller, which were quite innovative. The PIV results were compared with the CFD results obtained by Ecole Centrale de Nantes (ECN).

Although different measurement methods were used and the experiment was carried out also at full scale, the correctness of the CFD results was assessed basing mainly on the most standard test results: the Pitot probe measurements at model scale. Other experimental results were used to assess the usability of alternative measurement techniques.

Fig.2 presents some examples of the comparison of measured and computed wake field for one of the database vessels: the training vessel Nawigator XXI. The shape of Nawigator is presented in Fig.1.

Fig. 1 Nawigator XXI.

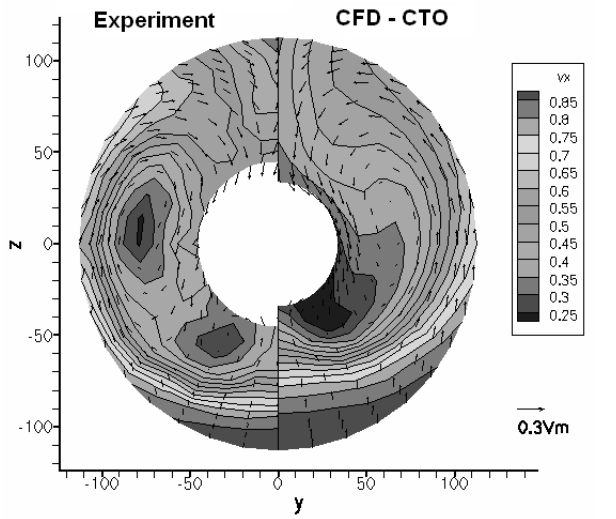

Turbulence model: standard k-ε

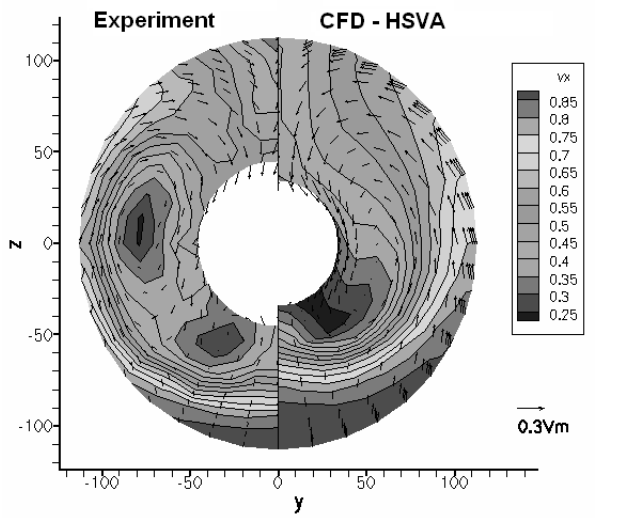

Turbulence model: SST k-ω

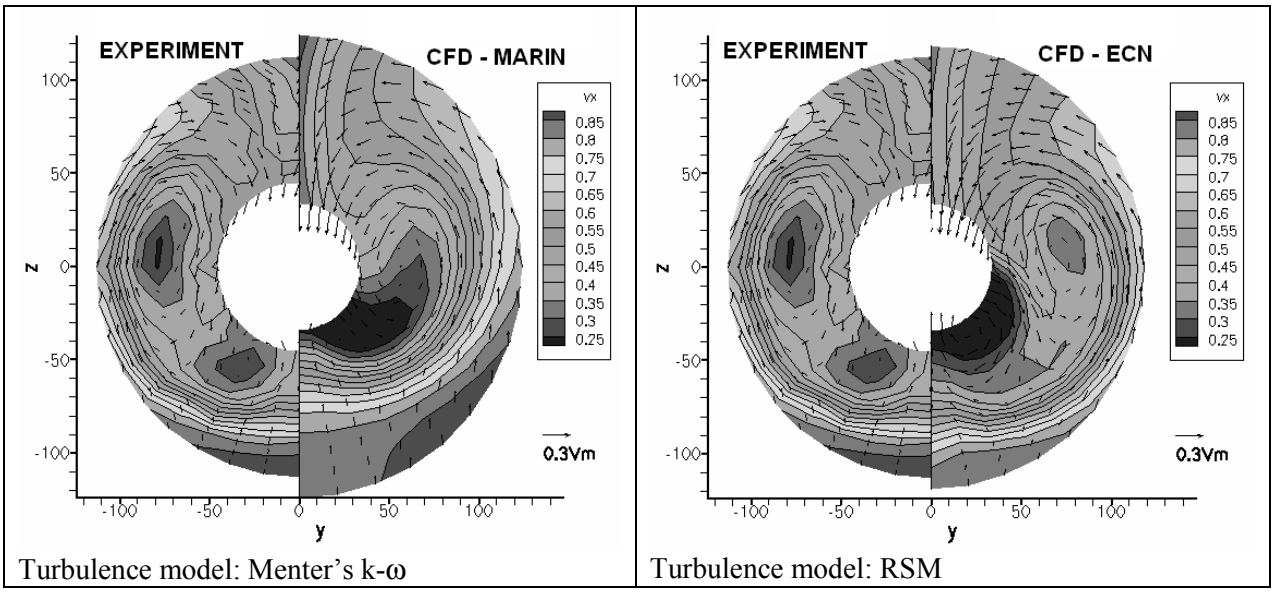

Turbulence model: Menter's k-ω | Turbulence model: RSM

Fig. 2 Comparison of measured and computed wake field for Nawigator XXI.

The following conclusion can be drawn basing on the above comparison:

- A general tendency can be observed to underestimate the axial velocity in a narrow region in the upper part of the propeller disc.
- The experiment reveals a separated region of low axial velocity, to the side from the propeller hub (y~-75, z~0). This phenomenon was predicted correctly only in ECN's computations, where RSM turbulence model and a very dense mesh were used.

The computations of CTO were carried out with the use of a relative coarse mesh (700 000 cells). The mesh consisting of less than 1 million cells is CTO's standard for the free surface ship flow computations. The free surface shape and the resistance value obtained for such mesh revealed to be accurate enough for comparative studies of different versions of the hull, and this is the most frequent computational task in CTO. However, the comparison presented above shows that such a rough model is not sufficient for correct prediction of the wake field. On the other hand, accurate results obtained by ECN show that the RANSE model is able to capture the wake flow phenomena if only the mesh resolution is sufficient and proper turbulence model is applied. This encouraged CTO to carry out some additional computations in order to work out an affordable procedure for accurate prediction of the wake field.

The following observations were taken into account:

- Modification of the standard model for free surface flows simply by increasing the mesh density and changing the turbulence model to obtain an accurate wake field would result in unacceptable computational time.
- The time required to obtain a convergence of the free surface flow is even few times longer than the convergence time for the flow without free surface. For a displacement ship, sailing at low or moderate Froude number, the influence of the free surface on the wake field can be often neglected. It is then reasonable to compute the wake field separately, without taking the free surface into account.

It was also assumed that the flow can be computed accurately for the aft part of the hull only, using the velocity field computed on the coarse mesh as the inlet boundary condition. The idea of the model for wake field computations is presented in the sketch below.

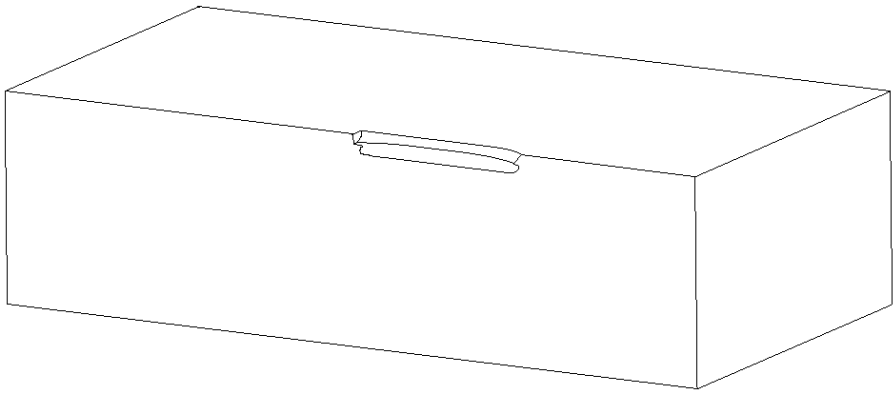

Fig. 3 Domain for free-surface computations.

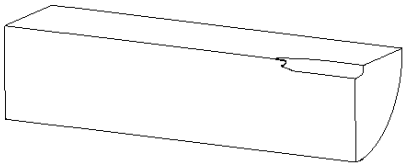

Fig. 4 Domain for wake field computations.

The domain for computing the free surface flow is rectangular and ranges 1 ship length upstream, two lengths downstream and to the side and one length downward. To compute the wake field, the domain dimensions were greatly reduced, as shown above, and the domain shape was changed to cylindrical (the cylinder radius was 0.55 of the model length). The hull was cut in the middle and the inlet boundary condition was applied there, using the velocity field computed with the coarse mesh (it was then assumed that the flow in this region is still relatively simple and the coarse mesh is sufficient to evaluate it accurately). Similarly, the velocity field computed with the coarse mesh was imposed on the cylindrical wall bounding the domain. The outlet was located closer to the hull.
The block-structured, hexahedral mesh was generated with the use of ANSYS ICEM CFD Hexa. The number of cells was about 2 000 000.

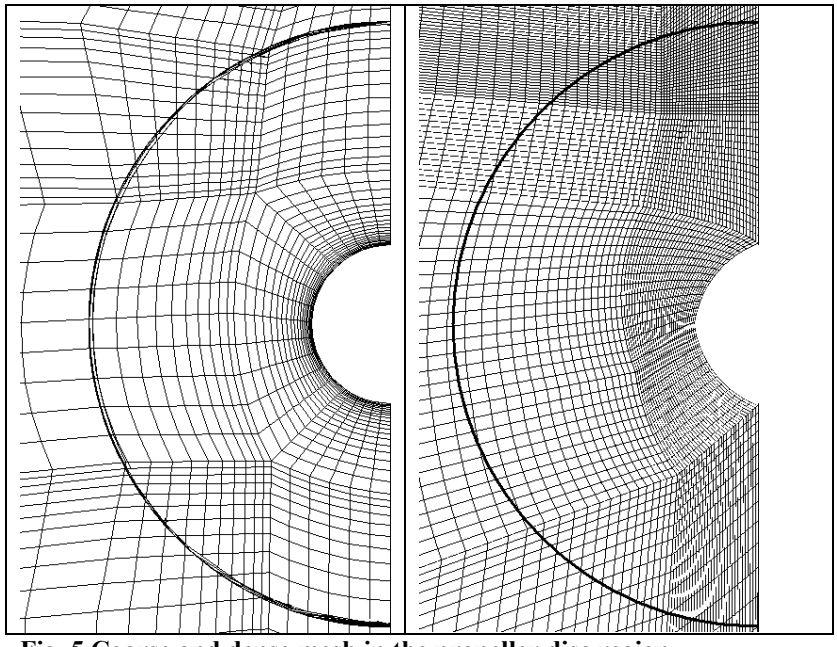

Fig. 5 Coarse and dense mesh in the propeller disc region.

The computations were carried out using the FLUENT solver with two turbulence models: SST k-ω and RSM. The results are presented below.

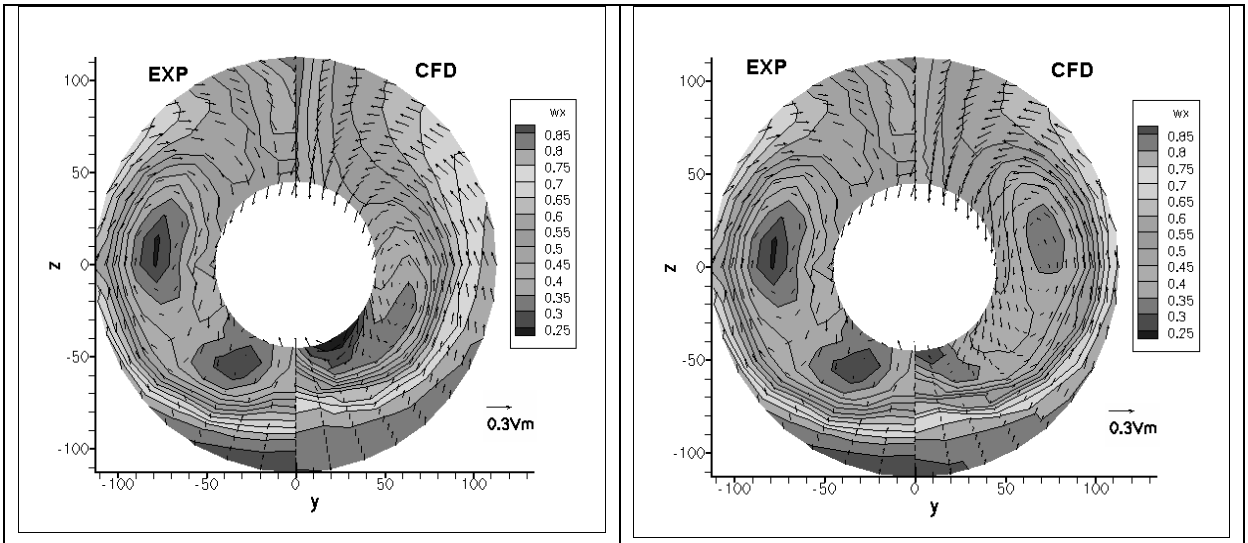

Turbulence model: SST k-ω

Turbulence model: RSM

Fig. 6 Comparison of computed and measured wake field.

The results of the wake field computations with the mesh of high density yields the following conclusions:

- The results obtained with the two-equation SST k-ω model are better than the results obtained with the coarse grid, but still poor.
- The results obtained with the RSM model are satisfactory, so this model of turbulence seems to be a good choice for the accurate wake field computations.
- The numerical prediction in both cases tends to underestimate the velocity in the upper part of the propeller disc. This effect is stronger for the SST k-ω turbulence model.

In case when the computer resources are limited and the results from the coarser mesh for entire hull are available, the proposed method for wake field computations can be considered attractive as the results are sufficiently accurate. However, the problem of overestimation of the hull shade in the upper part of the propeller disc remains unsolved.

A large task realized in the framework of the EFFORT project was the application of PIV method for the velocity field measurements near the ship model, with or without the working propeller. As the method is relatively new, the results were treated more carefully than those obtained with the Pitot probe. Despite some problems faced during taking the measurements and processing the results, the obtained results look promising and show large potential of the PIV method in research purposes. Some obvious advantages of this method, compared to the Pitot probe measurements, are:

- Smaller intrusiveness.
- Possibility of taking measurements in some regions not available for the Pitot probe measurements (e.g. a region close before the working propeller).
- A velocity field in a relatively large area can be measured in the negligible period of time, which makes the method usable for the measurements of an unsteady flow. The Pitot probe measurements are usable only for a steady flow.

The principles of the method, arrangement of the measurement stand and sample results are described here.

As the measurements were taken around the model towed in the towing tank, the PIV equipment had to be located in a device moving together with the model. This device houses two cameras and a laser light source. The scheme of the measurement system arrangement and the photograph of the measurement stand are shown below.

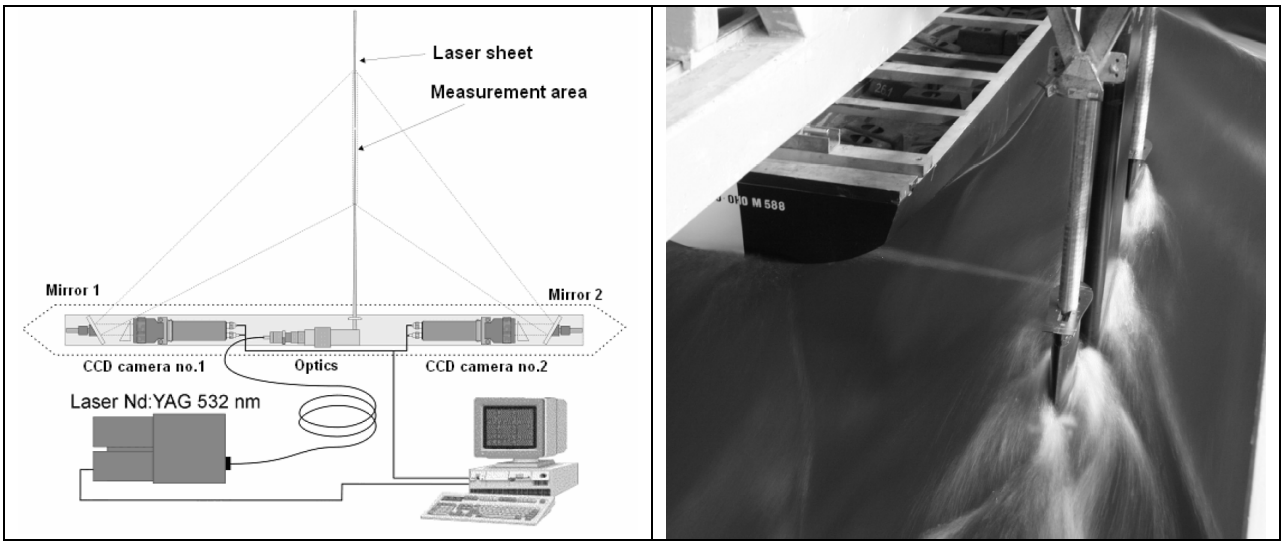

Fig. 7 PIV measurements – scheme of the equipment and the measurement stand.

The photograph below shows the model of the second example vessel – the hopper dredger. The PIV measurements were carried out for fully appended hull with working propeller. The velocity field was measured in two planes perpendicular to the symmetry plane and the base plane – one of these planes is marked in the photograph with the dashed line.

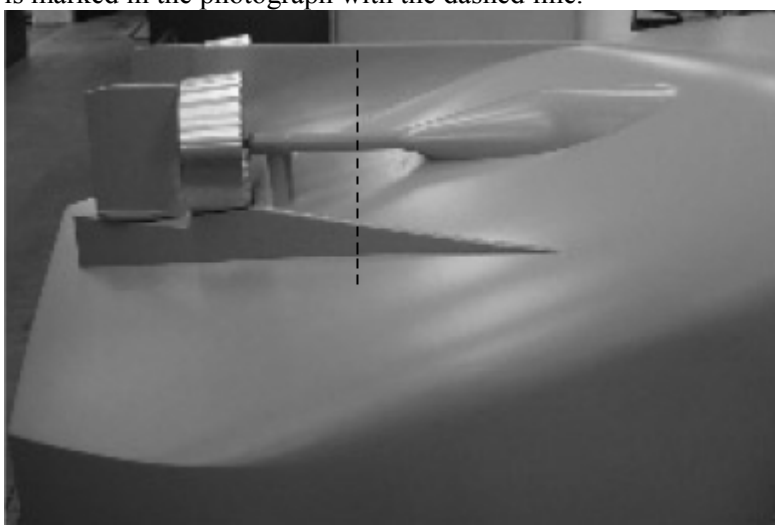

Fig. 8 Aft part of the dredger.

As can be seen in the picture showing the arrangement of the measurement stand, the laser sheet points in the direction perpendicular to the symmetry plane. This implies that a small part of the measurement plane shown in Fig.7 is hidden in the shade of the propeller shaft and it is not possible to measure the velocity field in this region at the assumed arrangement of the measurement equipment.
The velocity field measured in the remaining part of this plane showed an outstanding conformity with the CFD results obtained by ECN – the comparison is presented in Fig.8.
In figures showing the PIV results, a narrow horizontal strip of non-physical velocity can be observed at z/D ~ 0.6. This comes from the fact that the measurements were taken in two stages on different height in order to cover the entire measurement area, and then the pictures from CCD cameras, overlapping in a small part, were merged.
A conclusion can then be made for the future that if the measurements have to be taken in few stages, the boundaries between the measurement areas in single stages should not be located in regions where complex flow can be expected.

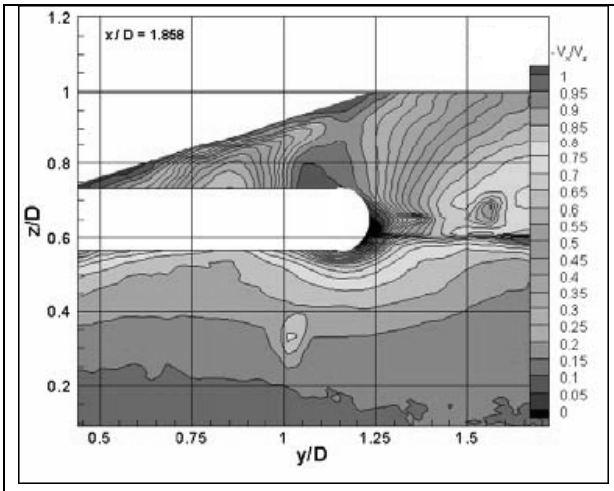

Axial velocity component – PIV (CTO)

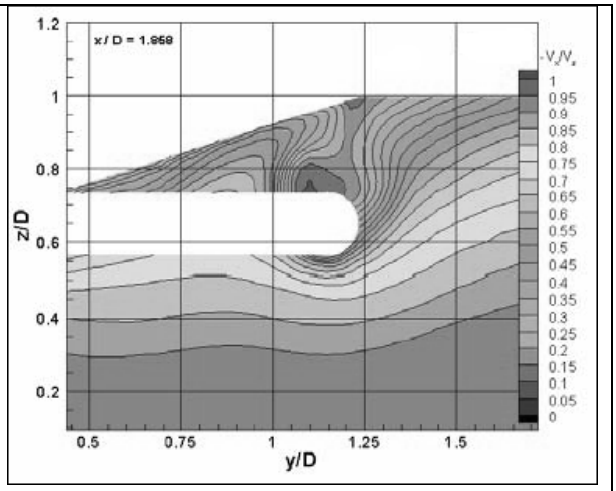

Axial velocity component – CFD (ECN)

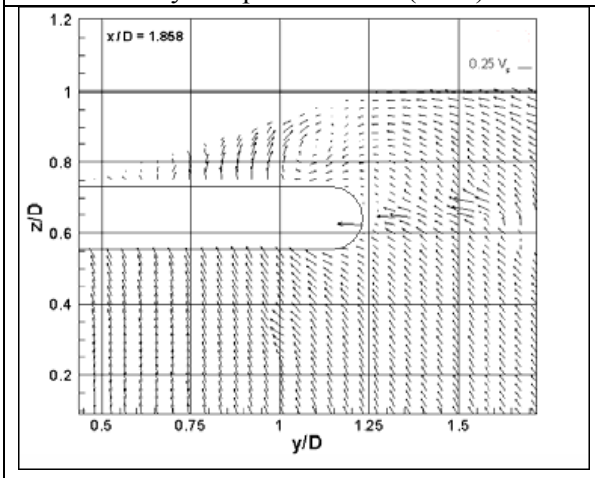

Transversal velocity component – PIV (CTO)

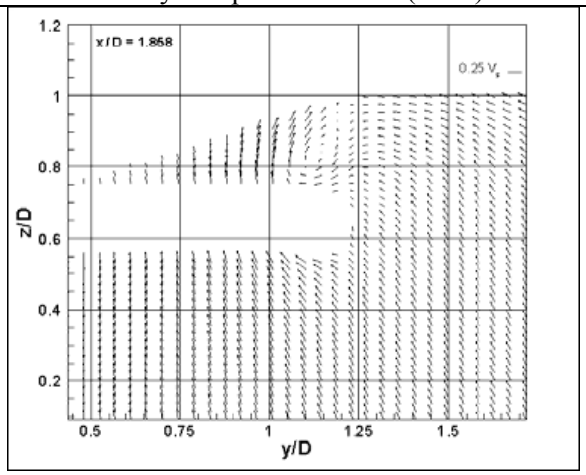

Transversal velocity component – CFD (ECN)

Fig. 9 Comparison of PIV measurements and CFD computations (sketches generated by Bram Starke from MARIN).

Free Surface Slow around Ship Hulls Using the Slightly Compressible Flow Formulation

Cosmin Ciortan[1], Juan Wanderley[2], Carlos Guedes Soares[1]

[1] Technical University of Lisbon, Instituto Superior Técnico, Lisbon, Portugal
e-mail: cciortan@mar.ist.utl.pt, guedess@mar.ist.utl.pt
[2] Federal University of Rio de Janeiro, Brasil
e-mail: juanw@peno.coppe.ufr.br

Introduction

The free surface flow around ship hulls is one of the most dynamic fields in CFD, due to its promising potential. The perspective of replacing (at least partially) the towing tank test is attractive due to the spared resources – human, time and material, the first two being the most important.
For the time being, transient simulations are little used, due to the high amount of computational and time resources required. Even using massive parallelization, time-domain runs are rarely used.
Most of the codes simulating free surface flows use the Finite Volumes formulation for discretizing the flow equations (e.g., Hino; Kleefsmann). The Finite Volumes are seducing due to their ability of working on unstructured grids and to the easiness of the boundary conditions implementation. The unstructured grids “mould” easier on complex geometries; however, their generation is more difficult than the one of structured grids.
The finite differences discretization is, in fact, equivalent to the Finite Volumes from the mathematical point of view. However, the finite differences can not be implemented on unstructured grids and the implementation of the boundary conditions is more difficult as compared to the Finite Volumes. On the other hand, structured grids are easier to generate and generally better suited for the calculation of most of the flows, while the multi-block technique added the degree of versatility needed for representing complex geometries.
The free surface representation is a difficult task, due to the fact that it is a moving boundary. The most important techniques used for displacing it are the interface capturing and interface tracking one.
The interface tracking techniques treat the free surface as a sharp boundary whose motions are followed. The kinematic and dynamic free surface boundary conditions are used for displacing the boundary. This method is a very accurate one; however, it has its weak points: it cannot represent highly distorted free surfaces and it requires a re-meshing of the computational at each time step.
Interface capturing methods use fixed grids and determine the position of the free surface by computing the fraction of volume of fluid present in each computational cell. This is achieved either by using massless particles introduced in the liquid phase near the free surface or by solving a transport equation for the liquid phase.
In the present paper, a somewhat hybrid method is used for displacing the free surface. A fixed grid is used; however, the position of the latter is determined by solving the kinematic and dynamic boundary conditions. The technique is implemented in a

transient, finite-difference code, using the Slightly Compressible Flow formulation. The code was parallelized using the MPI libraries and runs on 4-nodes cluster.
The code has two versions: one that calculates the flow around a Wigley hull, and another, general one, that calculates the flow around an arbitrary hull. In the present paper, the flow around a 280,000 t dwt FPSO is simulated.

Mathematical formulation

The Slightly Compressible flow formulation uses the continuity equation in the form modified by Wanderley (2001). The idea behind the new algorithm is to find a new form of the continuity equation, which allows maintaining the characteristics of the incompressible flow while facilitating the solving of the physical model.

The definition of the isothermal compressibility in Tannehill (1997) is given by:

$$\tau = \frac{1}{\rho}\frac{\partial \rho}{\partial p} \tag{1}$$

In the case of isothermal flows, developing the density in Taylor series with respect to the pressure around p_∞ yields:

$$\rho = \rho_\infty + \frac{\partial \rho}{\partial \overline{p}}\Bigg)_T (p - p_\infty) + \frac{1}{2}\frac{\partial^2 \rho}{\partial p^2}\Bigg)_T (p - p_\infty)^2 \tag{2}$$

Combining the definition of the isothermal compressibility given by equation (1) and the Taylor series development given by equation (2), one obtains a relation between the density and pressure in which the isothermal compressibility appears as coefficient:

$$\rho = \rho_\infty + \rho_\infty \tau (p - p_\infty) + \frac{1}{2}\rho_\infty \tau^2 (p - p_\infty)^2 + ... \tag{3}$$

As τ is very small, it is sufficient to consider only the first two terms of the development (3). After rearranging the resulting expression, equation (4) is obtained.

$$\rho = \rho_\infty (1 - \tau p_\infty) + \rho_\infty \tau p \tag{4}$$

After substituting equation (4) in the continuity equation for compressible flows, one obtains

$$\tau \rho_\infty \left[\frac{\partial p}{\partial t} + \nabla \cdot (pV)\right] + \rho_\infty (1 - \tau p_\infty)\nabla \cdot V = 0 \tag{5}$$

In the incompressible formulation, in which it is assumed that $\tau = 0$, equation (5) reduces to the well-known continuity equation for incompressible flows, i.e.,

$$\nabla \cdot V = 0$$

On the other hand, one can notice that equation (5) is also satisfied when

$$p_\infty = \frac{1}{\tau} \tag{6}$$

and

$$\frac{\partial p}{\partial t} + \nabla \cdot (pV) = 0 \tag{7}$$

Hence, the continuity equation in the compressible form reduces to equation (7), with the condition given by equation (6). It is obvious that equation (7) is much easier to solve numerically than continuity equation for incompressible flows, due to the inclusion of the term with the pressure time derivative. On the other hand, there is no need to alter the momentum equations. Moreover, the substitution of $\rho = \rho_\infty$ introduces a convenient simplification of the problem, without any degeneration of the momentum equations. Hence, the working equations will be the new form of the continuity equation (7) together with the momentum equations (8).

$$\begin{aligned}
&\frac{\partial u}{\partial t} + V \cdot \nabla u = -\frac{1}{\rho}\frac{\partial p}{\partial x} + \nu \nabla^2 u + \rho f_x, \\
&\frac{\partial v}{\partial t} + V \cdot \nabla v = -\frac{1}{\rho}\frac{\partial p}{\partial y} + \nu \nabla^2 v + \rho f_y, \\
&\frac{\partial w}{\partial t} + V \cdot \nabla w = -\frac{1}{\rho}\frac{\partial p}{\partial z} + \nu \nabla^2 w + \rho f_z.
\end{aligned} \tag{8}$$

Governing equations

The Navier-Stokes equations for slightly compressible flows are written in conservative form, in general coordinates and in nondimensional form. Boundary conditions are imposed for solving them.

On the hull, the no-slip condition is imposed; on the lateral boundaries, zero-order extrapolation is used, as well as at the outlet; at the inlet, constant velocity is imposed.

On the free surface, several boundary conditions were used for imposing the pressure and velocities in the points above the free surface. They are summarized in the table below, together with the appreciation of their accuracy in the code:

Pressure/ velocity	Extrapolated/ Extrapolated (1)	Constant/ Extrapolated (2)	Constant gradient/ Extrapolated (3)	Constant/ Normal velocity constant (4)
Behaviour	-	-	-	+

Table 1 Boundary conditions for the free surface

A previous version of the code (Ciortan *et. al.*, 2004) used moving grids for a Wigley hull. The results compared well with experiments.

The grid is generated using an algebraic grid generator (Fletcher, 1991); the grid is orthogonal to the boundaries. A second-order Runge-Kutta scheme is used for marching in time the numerical scheme. For generating the grid of the arbitrary ship, an own grid generator (Ciortan *et. al.,* 2004) is used.

Numerical results

The simulations are carried for the classical case of a Wigley hull at Fn=0.316 (Hino, 1989) and for a FPSO built on a tanker hull at full load conditions (280.000 t dwt; Fn=0.133). Both grids use geometrical stretching in order to concentrate grid points next to the hull and free surface (see Fig. 1). In both cases, the computational domain extends for 3 ship lengths upstream, 3.5 downstream and 3 sideways. The distance between the keel and the bottom is one ship length. The simulations were performed in the laminar cases.

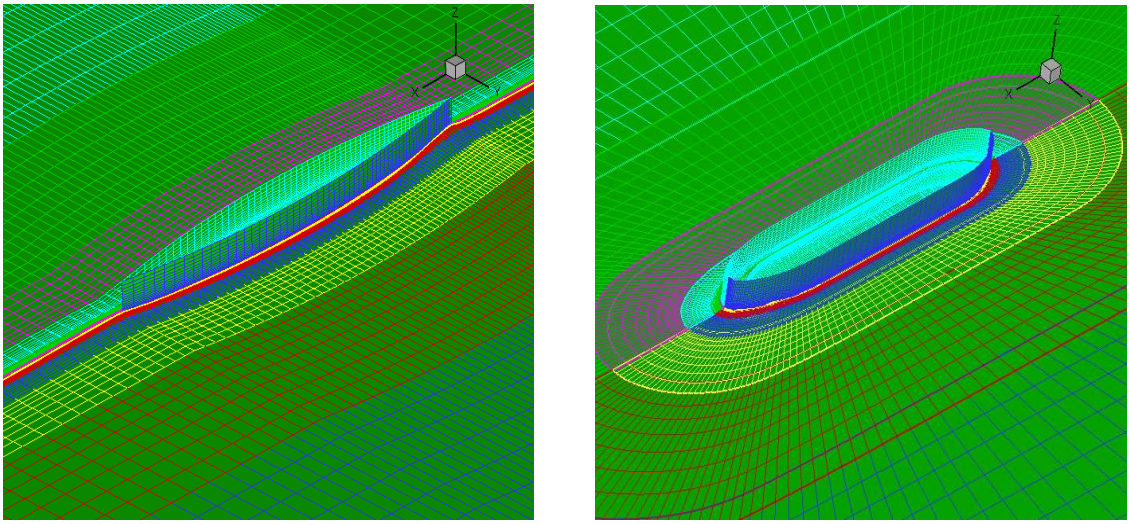

Fig. 1 Details of the grids for the Wigley and FPSO cases

The results – though far from reaching a steady-state like behavior show an encouraging trend.

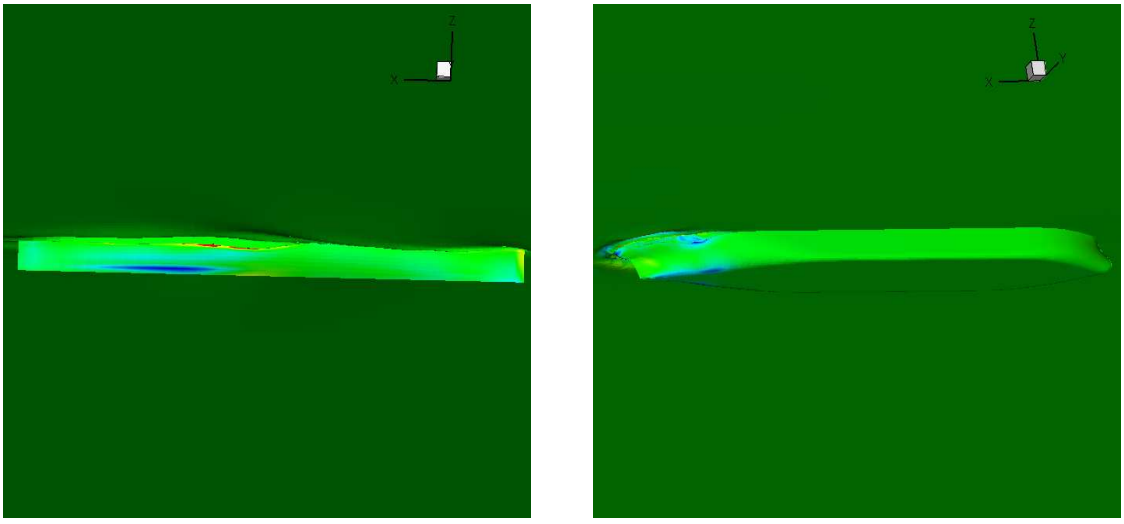

Fig. 2 Pressure contours on the hulls, seen from beneath the waterline

In Fig. 2, pressure contours on the hulls are depicted. In the case of the Wigley hull, the stagnation point at the bow is more visible, compared to the FPSO hull; in the case of the FPSO, the lack of evidence comes from the higher negative gradients that overshadow the smaller positive ones.

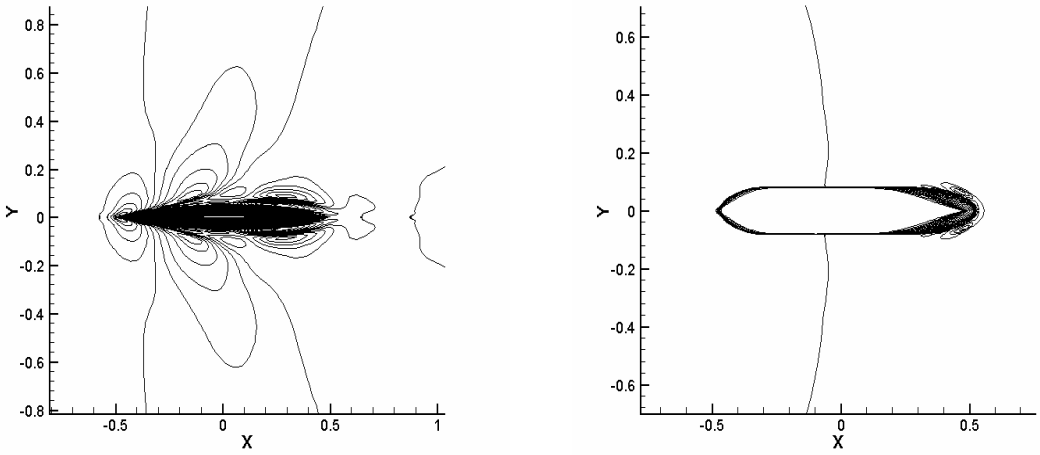

Fig. 3 Wave contours in the domains

In Fig. 3, contours of the waves in the domains are depicted. The Wigley hull case is better developed, due to the shorter acceleration time required. For comparison, the number of iterations used for accelerating the flows is of 10,000 (Wigley hull) against 1,000,000 (FPSO). The number of iterations used for the FPSO might even be quite low, considering that 1 s in real ship time scale needs about 100,000 iterations.

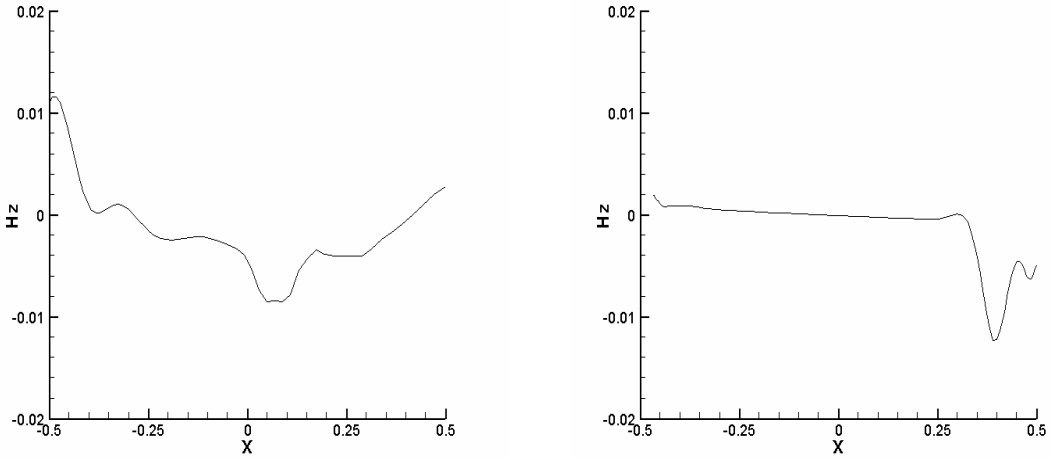

Fig. 4 Wave cuts along/close to the hull

In Fig. 4, wave cuts along the hull (in the Wigley case) and close to the hull (FPSO) are depicted. Interestingly, for the FPSO, the higher wave amplitude is not along the hull, but rather a bit farther. Bear in mind that the results are still partial and not fully developed.

It should be emphasized that especially in the more complicated case (FPSO), the wave cut has quite steep zones; however, the free surface algorithm deals well with it, which is an indication of its robustness.

A short comment on the boundary conditions for the free surface is appropriate. As shown in table 1, several boundary conditions were tested; only one performs well. The first three yield an absolutely unrealistic free surface shape, with high wave amplitudes; on the other hand, the last one considers that the process is nearing a steady-state one, hence the changes in velocity from the points immediately below the free surface to the ones immediately above are negligible; likewise, the changes in pressure are not considered, therefore constant (atmospheric) pressure is imposed. The results appear to be backing this approach.

Conclusions

A free surface code, using the Slightly Compressible Flow formulation, was tested in two cases-the classical test case of a Wigley hull and the more complicated one of a FPSO hull. The code performs well in both cases, with emphasis on the real hull, which is rather a bluff body with complicated free surface. For the time being, the codes are tested in the laminar cases, until stabilizing the solution. Turbulent simulations are at hand, as the subroutines are already built and implemented, and as soon as the laminar cases are completed, turbulent cases will be considered.

Though partial, the results show encouraging trend, especially in what concerns the free surface shape and stability. Further tests are deemed necessary for closing the case.

The physical phenomena involved in such complex a case as the free surface flow around bluff bodies are appropriately represented by the Slightly Compressible Flow formulation. The introduction of a time derivative in the continuity equation eases significantly the computational burden, especially in the transient simulations.

Bibliography

Ciortan, C, Guedes Soares, C., Wanderley, J. B. V., Levi, C. A., Calculation of the Flow around Ship Hulls Using a Parallel CFD Code, Parallel CFD 2004, Las Palmas de Gran Canaria, Spain: *Multidisciplinary Applications*, G. Winter, A. Ecer, J. Periaux, N. Satofuka, and P. Fox (Asst. Editor), Elsevier Publishing Co. 2005.

Ciortan, C., Guedes Soares, C., Wanderley, J. B. V., Levi (2004), C. A., Structured Grid Generation for Computational Fluid Dynamics (in Portuguese), Congresso de Métodos Computacionais em Engenharia (Congress for Computational Methods in Engieneering), Lisbon

Hino, T. (1987), Numerical Simulation of a Viscous Flow with a Free Surface around a Ship Model, Journal of the Society of Naval Architects of Japan, 161

Kleefsmann, K. M. T., Fekken, G., Veldman, A. E. P., Iwanowski, B., Buchner, B., A Volume-of-Fluid Based Simulation Method for Wave Impact Problems

Tannehill, J. C., Anderson, D. A., Pletcher, R. H. (1997), Computational Fluid Mechanics and Heat Transfer, Taylor & Francis, 2nd Edition, Washington

Wanderley, J. B. V. (2001), An algorithm for slightly compressible flows, Proceedings of the 20th Offshore Mechanics and Arctic Engineering (OMAE), ASME, OFT 1191, 519

A simple analytical criterion to predict if a ship in steady motion generates an unsteady bow wave

Gérard Delhommeau[1], Michel Guilbaud[2], Francis Noblesse[3]

[1] Laboratoire de Mécanique des Fluides (UMR CNRS n6598), École Centrale, Nantes, France
[2] Laboratoire d'Études Aérodynamiques (UMR CNRS n6609), Université de Poitiers, Poitiers, France
[3] David Taylor Model Basin, NSWCCD, West Bethesda, MD, USA

Abstract

Elementary analytical considerations — based on a simple analytical expression for the height of a ship bow wave and the Bernoulli equation for steady flows — show that a ship that advances at constant speed along a straight course in calm water (i.e. a ship in steady motion) necessarily generates an unsteady bow wave if the waterline entrance angle $2\,\alpha_E$ of the ship exceeds 25° and the ship speed is smaller than a critical speed, defined in terms of α_E by a remarkably simple analytical expression. In spite of its simplicity, this "unsteady-bow-wave criterion" is in fairly good agreement with experimental observations for the waves generated by an inclined flat plate. A simple one-parameter family of parabolic bow waves, which are in reasonable agreement with experimental measurements for the front-half of a ship bow wave, is also given. As one approaches the unsteady-flow limit, the parabolic bow wave defined by this family of analytical solutions becomes a vertical wall of water, evidently unstable.

Introduction

A ship that advances at constant speed along a straight path through a large body of calm water is usually assumed — notably for numerical-calculation and analytical purposes — to generate a steady bow wave; but of course this is not necessarily always true. Indeed, common observations show that a ship in steady motion can generate an unsteady bow wave. More generally, steady motion of a body through a fluid at rest does not necessarily result in a steady flow; the von Karman vortex sheet that can be observed (under some conditions) behind a bluff body advancing steadily through a fluid at rest is a well-known example of unsteady flow generated by steady motion of a body. As far as the authors are aware, no analytical or empirical criterion exists for predicting when a ship in steady motion generates an unsteady bow wave.

The criterion recently given in *Noblesse et al. (2006a)* is further considered here. This criterion — based on the Bernoulli equation for steady flows and the simple analytical expression for the height of a ship bow wave given in *Noblesse et al. (2006b)* — shows that a ship with a sufficiently fine waterline (with waterline entrance angle $2\,\alpha_E$ smaller than approximately 25°) may be expected to generate a steady bow wave at any speed. However, a ship having a fuller waterline can only generate a steady flow if the ship speed is higher than a critical speed, defined in terms of α_E by a remarkably simple analytical expression. Further insight into the occurrence of an unsteady bow wave is provided by a simple one-parameter family of analytical ship bow waves. Specifically, the wave defined by this family of analytical solutions becomes a vertical wall of water, evidently unstable, as the unsteady-flow limit is approached.

A criterion to predict when the bow-wave of a ship in steady motion cannot be steady

The height (above the plane $z = 0$ of the mean free surface) $z_b = Z_b\, g/U^2$ of the bow wave generated by a ship that advances at constant speed U in calm water is approximately determined in terms of the speed U, the draft D and the waterline entrance angle $2\,\alpha_E$ of the ship by the remarkably simple analytical expression

$$z_b = \frac{Z_b\, g}{U^2} \approx \frac{C^Z}{1+F_D}\,\frac{\tan\alpha_E}{\cos\alpha_E} \quad \text{with} \quad F_D = \frac{U}{\sqrt{g\,D}} \quad \text{and} \quad C^Z \approx 2.2 \tag{1}$$

This analytical expression — based on fundamental theoretical considerations (dimensional analysis and asymptotic behavior in limits $\alpha_E \to 0$, $D \to 0$ and $D \to \infty$) and experimental measurements that are used to determine the constant C^Z — is shown in *Noblesse et al. (2006b)* to be in excellent agreement with experimental measurements for wedge-shaped ship bows. Expression (1) is also in

good agreement with measurements for the Wigley hull and the Series 60 model, and similar ship-bow forms, especially if a simple procedure is used to define an effective draft D and an effective waterline entrance angle $2\,\alpha_E$; *Noblesse et al. (2006b)*. This agreement between experimental measurements and theoretical predictions can be observed in Fig.1 , where the normalized bow-wave height $(Z_b\,g/U^2)\cos\alpha_E\,/\tan\alpha_E$ is depicted as a function of the draft Froude number F_D defined by (1). Experimental measurements for nine ship hulls are shown in Fig.1 , where the solid line corresponds to the approximation $2.2/(1+F_D)$.

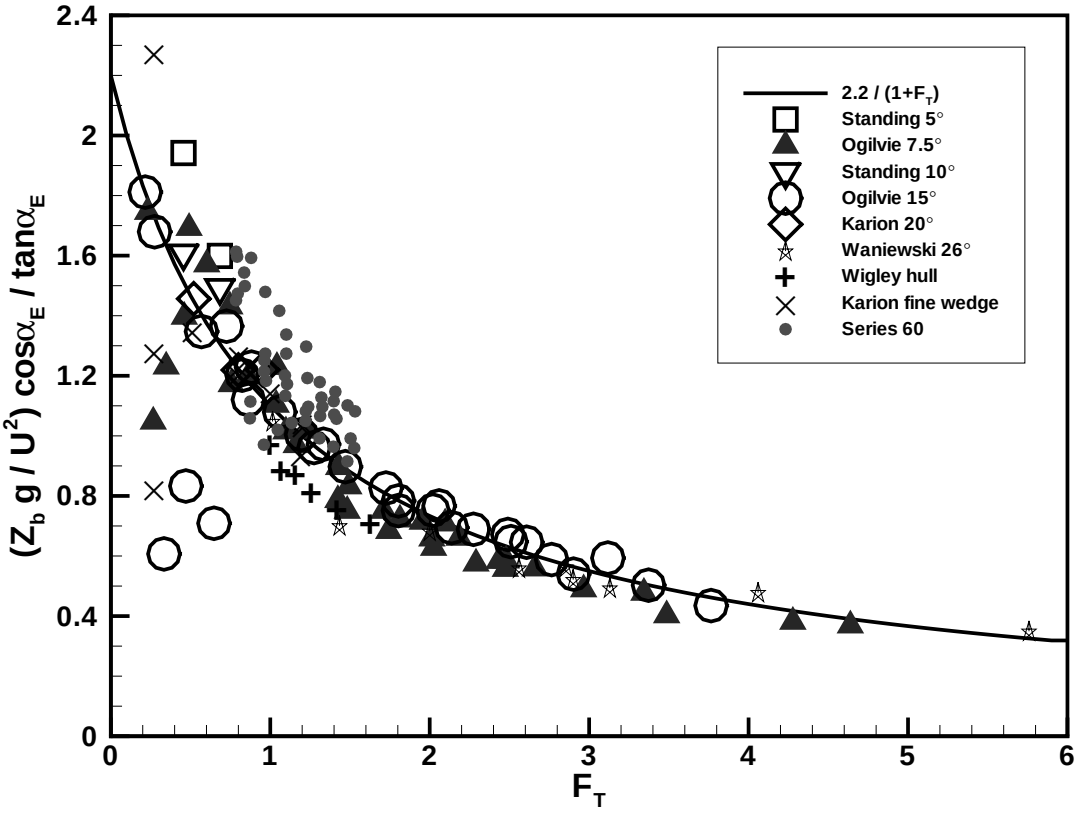

Figure 1: Bow-wave height $(Z_b\,g/U^2)\cos\alpha_E\,/\tan\alpha_E$ for nine ship hulls. The solid line corresponds to the approximation $2.2/(1+F_D)$

For a steady free-surface flow observed from a system of coordinates (X,Y,Z) attached to a ship advancing along a straight path at constant speed U in calm water, the velocity of the total flow (uniform stream opposing the forward speed of the ship + flow due to the ship) is $(V_x-U\,,V_y\,,V_z\,)$. Here, $(V_x\,,V_y\,,V_z\,)$ is the flow due to the ship. Furthermore, the X axis lies along the ship path and points toward the bow, and the Z axis is vertical and points upward with the mean free surface taken as the plane $Z=0$. The Bernoulli relation

$$P/\rho+g\,Z+[\,(V_x-U)^2+V_y^2+V_z^2\,]/2=P_{atm}/\rho+U^2/2 \tag{2}$$

applied at the free surface, where $P=P_{atm}$, shows that an upper bound for the free-surface elevation $Z=E$ is

$$E\,g/U^2\le 1/2 \tag{3}$$

This Bernoulli constraint is satisfied by expression (1) for the bow-wave height Z_b if $F_D^B(\alpha_E)\le F_D$ where the function $F_B^B(\alpha_E)$ is defined as

$$F_D^B(\alpha_E)=\left\{\begin{array}{c}0\\ 2\,C^Z\tan\alpha_E\,/\cos\alpha_E-1\end{array}\right\}\quad\text{if}\quad\left\{\begin{array}{l}\alpha_E\le\alpha_E^B\\ \alpha_E^B\le\alpha_E\end{array}\right\} \tag{4a}$$

with

$$\alpha_E^B=\sin^{-1}(\sqrt{(C^Z)^{\,2}+1}-C^Z)\approx 12.51^\circ\quad\text{for}\quad C^Z\approx 2.2 \tag{4b}$$

Thus, the Bernoulli constraint is satisfied for every value of F_D if $\alpha_E \leq \alpha_E^B$, but is only satisfied for a sufficiently high value of the Froude number F_D if $\alpha_E^B < \alpha_E$. For $F_D < F_D^B(\alpha_E)$, the Bernoulli constraint does not permit a steady-flow solution, and unsteady flow must then be expected. Expressions (4) show that a ship with waterline entrance angle smaller than approximately 25°, i.e. with a sufficiently fine waterline, may be expected to generate a steady bow wave at any speed. However, a ship having a fuller waterline can only generate a steady flow if the ship speed is higher than the critical speed (4a).

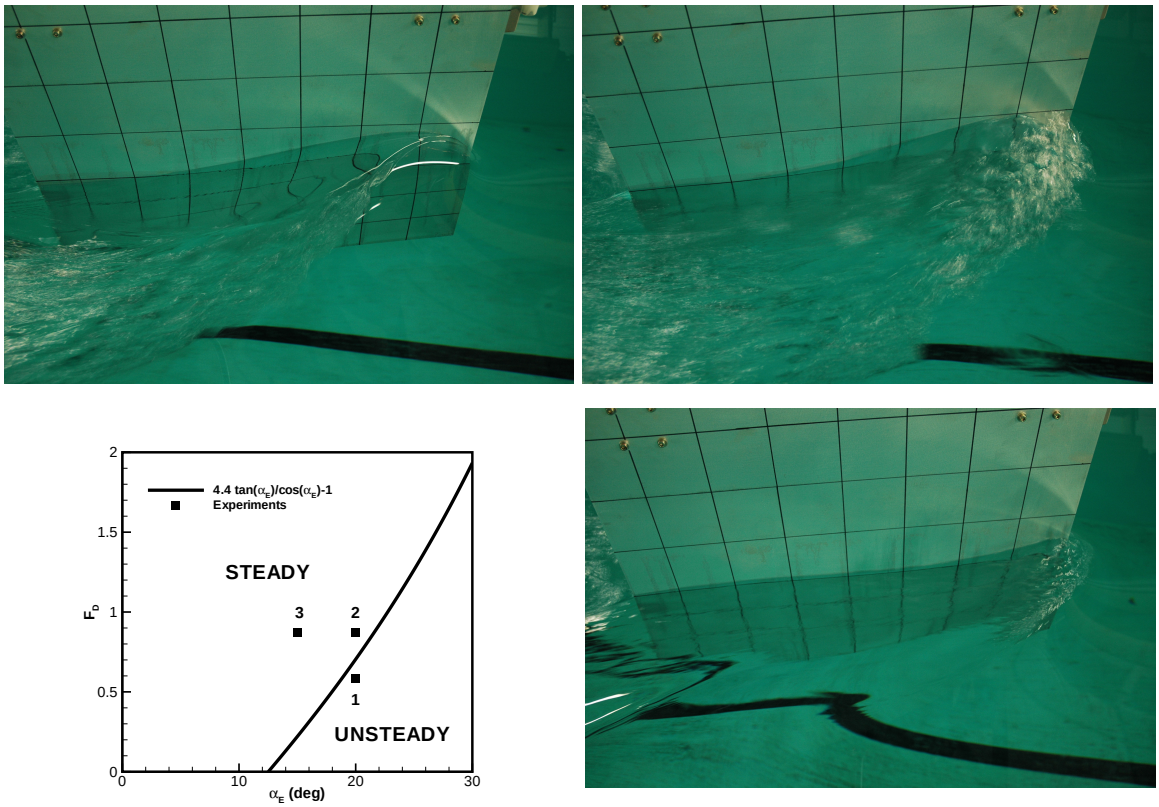

Fig.2a - Unsteady flow region and experimental observations for a vertical flat plate towed at an incidence angle α_E with speed U characterized by the draft-based Froude number F_D. The bow waves for points 1 and 2, which are near the unsteady-flow boundary, are unsteady. The bow wave for point 3 is a steady overturning thin sheet of water.

The Bernoulli-constraint Froude number $F_D^B(\alpha_E)$ defined by (4) is depicted in the lower left sides of Fig.2a and Fig.2b. These figures also show three points identified as points 1, 2 and 3. Experimental observations of the flow about a rectangular flat plate, immersed at a draft $D = 0.3\,m$, towed at an incidence angle α_E and a flare angle γ with speed U are also shown in Fig.2a and Fig.2b for the points 1, 2 and 3. The flare angle γ is null in Fig.2a and equal to 20° in Fig.2b. The incidence angle α_E is equal to 20° for the experimental data points 1 and 2, and to 15° for point 3. The speed U is equal to $1\,m/s$ ($F_D = 0.58$) for point 1, and to $1.5\,m/s$ ($F_D = 0.87$) for points 2 and 3. In Fig.2a, i.e. for $\gamma = 0°$, the bow waves are unsteady for points 1 and 2, which are closest to the unsteady-flow boundary (4). The bow wave for point 3, which is well inside the steady-flow region defined by the Bernoulli bound, is a steady overturning thin sheet of water. In Fig.2b, i.e. for $\gamma = 20°$, the bow wave is unsteady for point 1, which lies within the unsteady-flow region. The bow waves for points 2 and 3, located in the steady-flow region, are steady overturning thin sheets of water. Fig.2a and Fig.2b show that the "unsteady-bow-wave criterion" (4) appears to be in reasonably good agreement with experimental observations for the bow wave generated by an inclined flat plate.

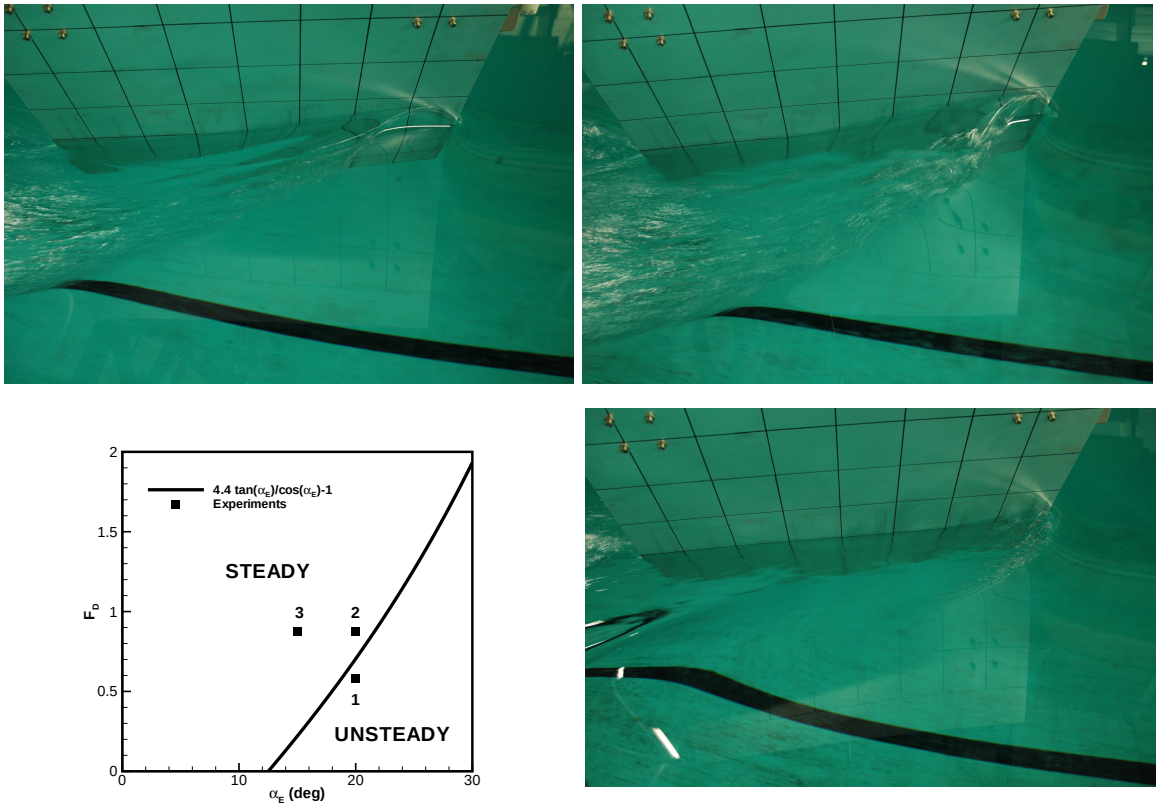

Fig.2b - Unsteady flow region and experimental observations for a flat plate towed at a flare angle $\gamma = 20^\circ$ and an incidence angle α_E with speed U characterized by the draft-based Froude number F_D. The bow wave for point 1 is unsteady, and the bow waves for points 2 and 3 are steady overturning thin sheets of water.

A simple one-parameter family of parabolic bow waves

Define nondimensional coordinates $(x\,,y\,,z)$ and flow velocities $(v_x\,,v_y\,,v_z)$ as

$$(x\,,y\,,z) = (X,Y,Z)\,g/U^2 \qquad\qquad (v_x\,,v_y\,,v_z) = (V_x\,,V_y\,,V_z) \tag{5}$$

At a point of the free surface $z = e\,(x\,,y)$, the Bernoulli relation (2) with $P = P_{atm}$ and expressions (5) yield

$$q = \sqrt{(v_x - 1)^2 + v_y^2 + v_z^2} = \sqrt{1 - 2\,e}$$

where q evidently stands for the magnitude of the total flow velocity (flow velocity due to the ship plus uniform current opposing the ship speed). Thus, the magnitude of the flow velocity a ship stem, where the free-surface elevation e is small, is given by

$$q_{stem} \approx 1 \tag{6}$$

in accordance with *Noblesse et al. (1991)*.

Define a horizontal axis that is tangent to the mean ship waterline at the ship bow, and points toward the ship stern. Let $t = Tg/U^2$ stand for the distance along the t axis, measured from the ship bow (intersection of the ship stem line with the mean free-surface plane $z = 0$). Thus, the ship bow is located at $t = 0$ and $z = 0$. Furthermore, define the nondimensional time $\theta = \Theta\,g/U$, and let β stand for the angle between the horizontal (mean free-surface) plane and the (total) flow velocity at the ship bow $(t = 0\,, z = 0)$. The components of the flow velocity at the bow along the horizontal t axis and the vertical z axis are then equal to $\cos\beta$ and $\sin\beta$, respectively.

A simple approximation to a ship bow wave may be obtained by assuming that a water particle that passes through the bow $(t = 0\,, z = 0)$ roughly follows the path dictated by Newton's equations

$d^2t/d\theta^2 = 0$ and $d^2z/d\theta^2 = -1$. This elementary Lagrangian analysis, which evidently ignores all interactions among water particles, shows that the path of a water particle is defined by

$$t = \theta \cos\beta \qquad z = \theta \sin\beta - \theta^2/2 \tag{7}$$

Here, the water particle is assumed to be located at the ship bow ($t = 0\,, z = 0$) at the time $\theta = 0$.

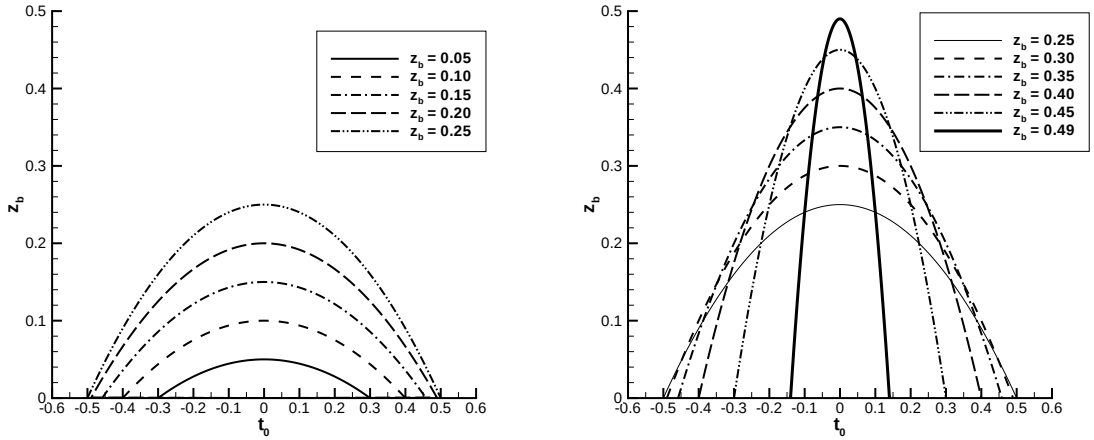

Fig.3 - One-parameter family of parabolic bow waves (9) for $z_b = 0.05\,,\ 0.1\,,\ 0.15\,,\ 0.2\,,\ 0.25$ (left side) and $z_b = 0.25\,,\ 0.3\,,\ 0.35\,,\ 0.4\,,\ 0.45\,,\ 0.49$ (right side).

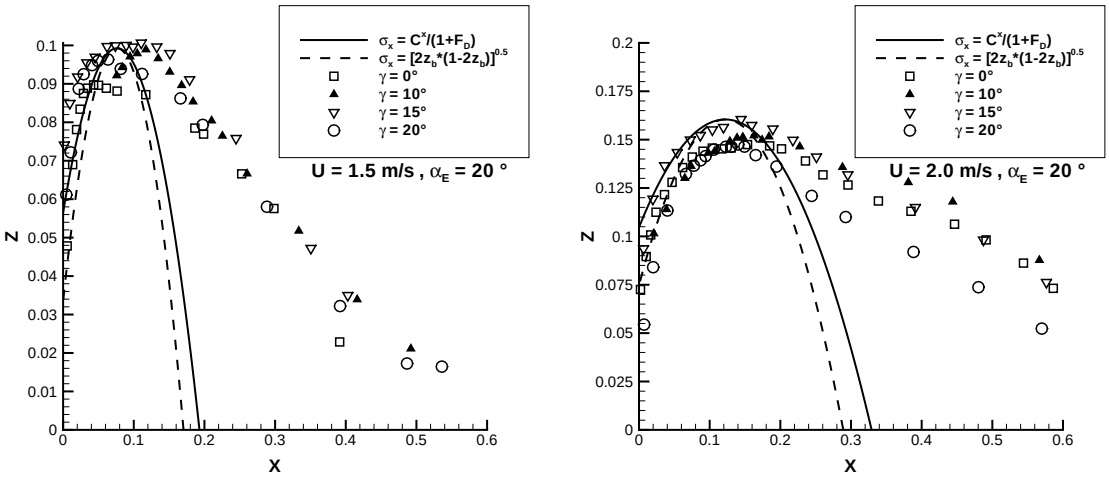

Fig.4 - Parabolic bow wave (9) and experimental measurements of the bow waves due to a rectangular flat plate towed at an incidence angle $\alpha_E = 20°$ and at flare angles $\gamma = 0\,,\ 10°,\ 15°,\ 20°$ at speeds $U = 1.5\,m/s$ ($F_D = 0.87$; left side) or $2\,m/s$ ($F_D = 1.17$; right side).

The parametric equations (7) yield the parabolic bow wave

$$z = \frac{t}{\cos^2\beta}\left(\sin\beta\cos\beta - \frac{t}{2}\right) \tag{8}$$

Thus, one has $z = 0$ for $t = 0$ and $t = 2\,\sin\beta\cos\beta$. Equation (8) also shows that the highest value of z is reached for $t = t_b = \sin\beta\cos\beta$, and is given by $2\,z_b = \sin^2\beta$. It follows that one has

$$\sin\beta = \sqrt{2\,z_b} \qquad t_b = \sqrt{2\,z_b\,(1-2\,z_b)}$$

These relations and the change of variable $t = t_0 + t_b$, which places the origin $t_0 = 0$ at the bow-wave crest and orients the t_0 axis toward the ship bow (instead of the ship stern, as for the t axis), show that (8) can be expressed as

$$z = z_b - (t_0^2/2)/(1-2\,z_b) \quad \text{with} \quad -\sqrt{2\,z_b\,(1-2\,z_b)} \le t_0 \le \sqrt{2\,z_b\,(1-2\,z_b)} \tag{9}$$

Expression (9) defines a family of parabolic ship bow waves that depend on the single parameter z_b. This one-parameter analytical family of bow waves is depicted in Fig.3. In the limit $z_b = 0.5$, the width of the bow-wave vanishes, and the bow wave becomes a vertical wall of water; see right side of Fig.3. Thus, the bow wave (9) becomes a vertical wall, evidently unstable, as the wave height z_b approaches the upper bound $z_b = 0.5$ allowed by the Bernoulli relation for steady flows; a property that provides further insight into the Bernoulli unsteady-flow boundary defined earlier.

The bow wave defined by (9) is shown in Fig.4 (dashed line) with experimental measurements of the bow waves due to a rectangular flat plate towed at an incidence angle $\alpha_E = 20°$ and at flare angles $\gamma = 0$, $10°$, $15°$, $20°$ at speeds $U = 1.5\,m/s$ or $2\,m/s$, which correspond to $F_D = 0.87$ or $F_D = 1.17$. Fig.4 also depicts an alternative bow wave (shown as a solid line) given in *Noblesse et al. (2006b)*. Fig.4 shows that the simple parabolic bow wave (9) agrees reasonably well with the experimental measurements for the "front-halves" of the bow waves, but does not agree past the bow-wave crests.

Conclusion

In summary, a remarkably simple analytical criterion that predicts when a ship that advances at constant speed along a straight course in calm water (i.e. a ship in steady motion) cannot generate a steady bow wave has been given. This criterion, based on elementary analytical considerations (the Bernoulli equation for steady flows and a simple analytical expression for the height of a ship bow wave), shows that a ship with a "full waterline" (with entrance angle $2\,\alpha_E$ greater than approximately $25°$) necessarily generates an unsteady bow wave if the ship speed is smaller than a critical speed, defined in terms of α_E by the simple analytical expression (4). In spite of its simplicity, this "unsteady-bow-wave criterion" is in fairly good agreement with experimental observations for the waves generated by an inclined flat plate.

Further insight into the Bernoulli-based unsteady-bow-wave criterion given here is provided by the simple one-parameter family of parabolic bow waves (9). This family of analytical solutions predicts that a ship bow wave becomes a vertical wall of water, evidently unstable, as one approaches the Bernoulli bound that determines the occurrence of unsteady-flow. The simple family of parabolic bow waves (9) is in reasonable agreement with experimental measurements for the front-halves of the bow waves generated by an inclined flat plate.

The unsteady-bow-wave criterion (4) defines an unsteady-flow region where use of a steady-flow calculation method (e.g. a method based on RANSE or Euler equations) may be problematic and "converged" steady-flow solutions may not be expected.

References

Noblesse F., Hendrix D., Karafiath G. (2006a) "When is the bow wave of a ship in steady motion unsteady?", *21st Il Workshop on Water Waves and Floating Bodies", Loughborough, UK*
Noblesse F., Hendrix D., Faul L., Slutsky J. (2006b) "Simple analytical expressions for the height, location, and steepness of a ship bow wave", J. Ship Research*, in press*
Noblesse F., Hendrix D.M., Khan L. (1991) "Nonlinear local analysis of steady flow about a ship", J. Ship Research *35:288–294*

Numerical Computation of Propeller Characteristics with the Use of Periodic Non-Matching Boundary Condition

Pawel Dymarski (padym@cto.gda.pl), Marek Kraskowski (marek.kraskowski@cto.gda.pl)

31st August 2006

Ship Design and Research Centre S.A. (CTO S.A.), Poland

1 Introduction

The main target of the paper is to show state of development of computer program SOLAGA, especially its ability to solve problems connected with flow around ship propeller. Program SOLAGA has been developed in the framework of research project supported by Polish Committee of Science. It is also the main subject of the first author's PhD thesis.

2 Governing Equations

The closed system of motion equations, derived for incompressible fluid, is based on the momentum and mass conservation laws. An integral form of mass conservation equation formulated for control volume Ω with a surface S reads

$$\int_S \rho \mathbf{v} \cdot \mathbf{n} \mathrm{d}S = 0,$$

and the conservation equation of ith momentum component has the following form:

$$\frac{\partial}{\partial t} \int_\Omega \rho u_i \mathrm{d}\Omega + \int_S \rho u_i \mathbf{v} \cdot \mathbf{n} \mathrm{d}S = \int_S (\tau_{ij} \mathbf{i}_j - p \mathbf{i}_i) \cdot \mathbf{n} \mathrm{d}S,$$

where $\mathbf{v}$ is velocity vector, u_i - ith velocity component, p - pressure, ρ - density, $\mathbf{n}$ - normal unit vector to S surface, $\mathbf{i}_i$ - Cartesian unit vector and τ_{ij} is a viscous stress tensor.

When the flow is turbulent, $\mathbf{v}$ and u_i refers to mean velocity vector and mean ith velocity component, p is a mean value of pressure. The word "mean" denotes average in a time period T, which is long compared to the period of turbulent oscillations [2].

The viscous stress tensor τ_{ij} is specified by following formula:

$$\tau_{ij} = 2 (\mu + \mu_t) S_{ij},$$

where μ is a molecular viscosity, μ_t is the turbulent viscosity and S_{ij} is the mean strain-rate tensor. The turbulent viscosity is calculated with the use of Spallart-Almaras turbulence model [2],[3].

3 Numerical Methods

The solution algorithm is based on Finite Volume Method. The Finite Volume Method is based on integral form of conservation equations. The solution domain is subdivided into a finite number of control volumes, and the conservation equations are applied to each of them. At the centroid of each control volume (CV) lies the computational node at which field values are to be calculated.

To express value of each field quantity on CV surface S, suitable interpolation methods are used. In the present program two methods are applied: upwind UDS (first order) and linear interpolation CDS (second order). Surface and volume integrals are approximated using midpoint quadrature [1]. As a result of FV discretization approach, one obtains an algebraic equation for each CV. The system of equations

(after linearisation) is solved using iterative method. In present program two algorithms are used: ICCG for symmetric systems and Bi-CGSTAB for non-symmetric systems [1] .

The problem is treated as unsteady. The time integral in the Navier-Stokes equation is approximated with the use of implicit Euler method.

3.1 Rotating grid

Computation of flow around ship propeller require the use of rotating grid or rotating coordinate system. In the first method, the mass conservation equation has to be modified in order to take into account a relative velocity between grid (control volumes) and coordinate system. The mass conservation of equation for single rotating control volume in integral form reads

$$\int_S \rho \left(\mathbf{v} - \mathbf{v}_b \right) \cdot \mathbf{n} \mathrm{d}S = 0,$$

$\mathbf{v}_b = \omega \times \mathbf{r}_b$ is a velocity of CV boundary, ω - rotational velocity of the grid, $\mathbf{r}_b$ - position vector of a point at S.

The momentum conservation equation for ith momentum component takes the following form:

$$\frac{\mathrm{d}}{\mathrm{d}t} \int_\Omega \rho u_i \mathrm{d}\Omega + \int_S \rho u_i \left(\mathbf{v} - \mathbf{v}_b \right) \cdot \mathbf{n} \mathrm{d}S = \int_S \left(\tau_{ij} \mathbf{i}_j - p \mathbf{i}_i \right) \cdot \mathbf{n} \mathrm{d}S.$$

3.2 Periodic boundary conditions

In case of computation of open water characteristic of a propeller, it is possible to use periodic boundary conditions. We can reduce the size of domain z - times (where z is a number of blades).

At the periodic boundaries we have the following conditions:

$$p_L = p_R, \quad \phi_L = \phi_R, \quad \mathbf{v}_L = \mathbf{Q}_{RL} \mathbf{v}_R$$

where ϕ is a scalar quantity (i.e.: turbulent viscosity), $\mathbf{Q}$ is a transformation matrix from "Right" to "Left" periodic boundary:

$$\mathbf{Q}_{RL} = \begin{bmatrix} 1 & 0 & 0 \\ 0 & \cos\alpha & -\sin\alpha \\ 0 & \sin\alpha & \cos\alpha \end{bmatrix},$$

$\alpha = 2\pi/z$ is an angle between left and right periodic boundary.

3.3 Non-matching interfaces

From the numerical point of view periodic boundary condition is an interface between two sub-domains (Fig. 1 a,b). In SOLAGA solver, the grid at periodic interface can be non-matching, it allows to build almost orthogonal grids with better structure than "matching" grids (Fig. 1 c,d).

4 Computations

Computations were carried out for two propeller models: model A - conventional propeller and model B - skewed propeller. Computations were carried out with rotating grid.

Computational settings:

Time step	0.0001 s
Number of iterations per time step	3
Interpolation scheme	CDS (blending factor 0.8)
Time integral approximation	Implicit Euler

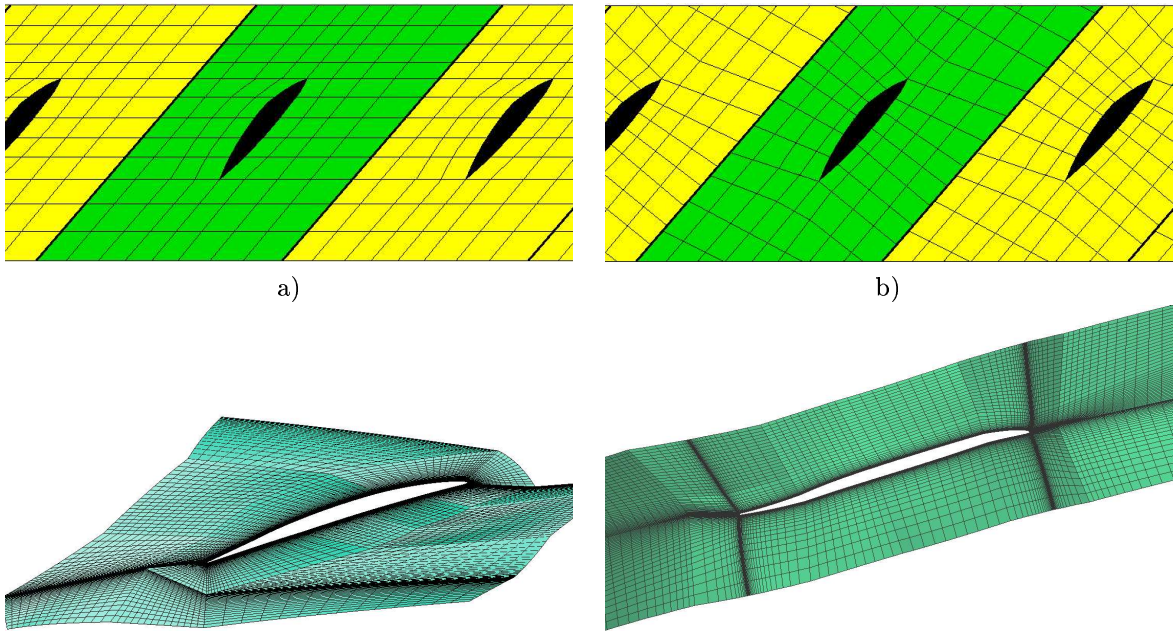

Figure 1: Scheme of matching (a) and non-matching (b) connections at periodic boundary. Difference between structure of periodic matching (c) and non-matching grid (d) for calculation of flow around propeller blade.

4.1 Test case 1 - model A. Flow around conventional propeller

Geometry of propeller model A:

Type	Fixed pitch
No of blades	4
Diameter	183.90 mm
Pitch ratio at 0.7 radius	0.7413
Expansion area ratio	0.574
Hub ratio	0.175
Blade width at 0.7 radius	55.79

Open water test conditions:

Propeller revolutions n	28.0 1/s
Propeller velocity v_p	0.0 - 4.2 m/s

Computational conditions:

Propeller revolutions n	28.0 1/s
Propeller velocity v_p	1.0; 2.0; 3.0; 4.0 m/s
Advance coefficient J	0.194; 0.388; 0.583; 0.777

The domain size and grid structure

Size of the domain: the inlet is located 2.3 D upstream from the propeller, the outlet is 2.2 D downstream, the diameter of the domain is 2.9 D. The boundary faces of the domain are presented in Fig 2 a;

The grid was generated with the use of program ICEM CFD Hexa. The grid is hexahedral and block-structured, number of CV's (per one blade) is 974 424. The grid structure on blade, hub and periodic surface is shown in Fig. 2 b.

Results of computations

Pressure distribution over the suction and pressure side of the propeller blade is presented in Fig 3.

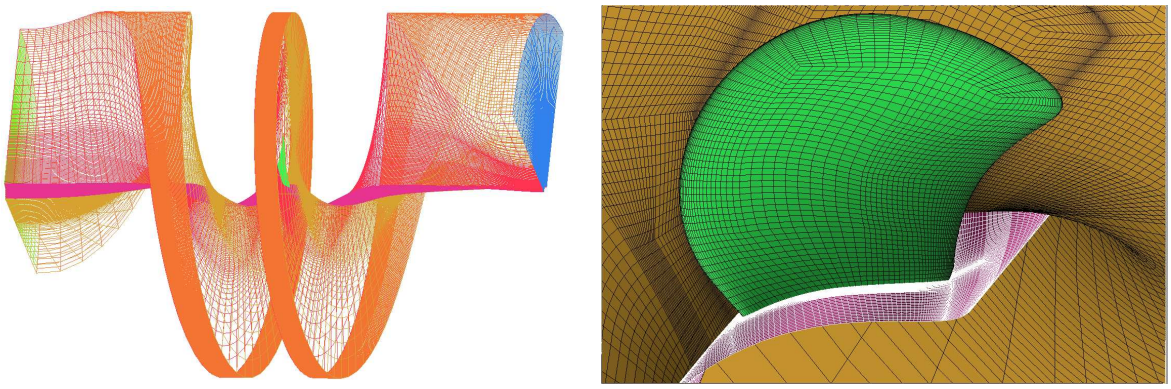

a) b)

Figure 2: a) Model A: domain of computations, b) Grid structure on the propeller blade, hub and periodic surface

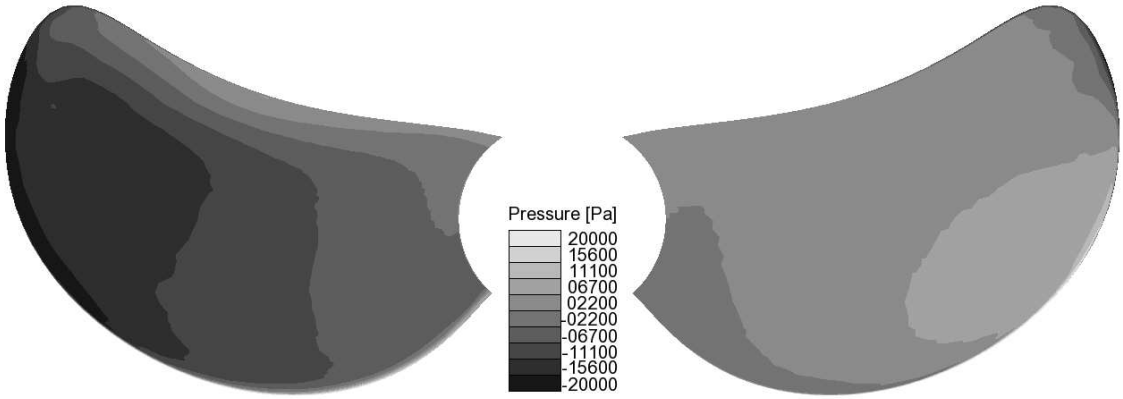

Figure 3: Pressure distribution over the suction (left) and pressure (right) side of the conventional propeller, $J = 0.388$.

The comparison of the calculated and experimental values of K_T and K_Q for several values of J is presented in Fig. 4 a.

4.2 Test case 2 - model B. Flow around skewed propeller

Geometry of Propeller model B:

Type	Controllable pitch
No of blades	5
Diameter	265.73 mm
Pitch ratio at 0.7 radius	1.4281
Expansion area ratio	0.820
Hub ratio	0.3026

Open water test conditions:

Propeller revolutions n	11.0 1/s
Propeller velocity v_p	0.5 - 4.1 m/s

Computational conditions:

Propeller revolutions n	11.0 1/s
Propeller velocity v_p	1.0; 2.0; 3.0; 4.0 m/s
Advance coefficient J	0.342; 0.684; 1.026; 1.368

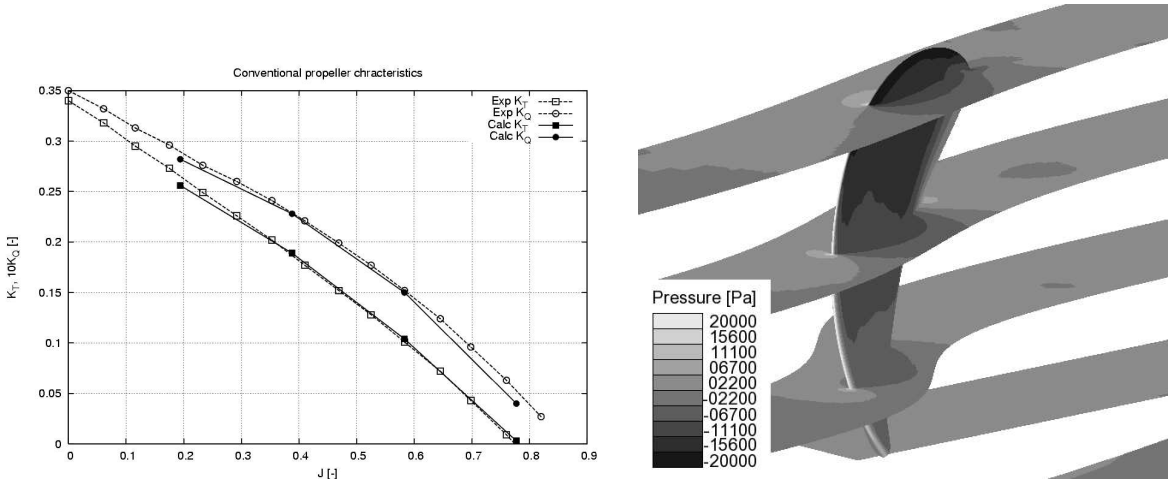

a) b)

Figure 4: a) K_T, K_Q characteristics of model A - conventional propeller, b) pressure distribution at the domain intersections, $J = 0.388$.

The domain size and grid structure

Size of the domain: the inlet is located 1.9 D upstream from the propeller, the outlet is 1.9 D downstream, the diameter of the domain is 2.4 D. The boundary faces of the domain are presented in Fig 5 a.

The grid was generated with the use of program ICEM CFD Hexa. The grid is hexahedral and block-structured, number of CV's (per one blade) is 1 086 176. The grid structure on blade, hub and periodic surface is shown in Fig. 5 b.

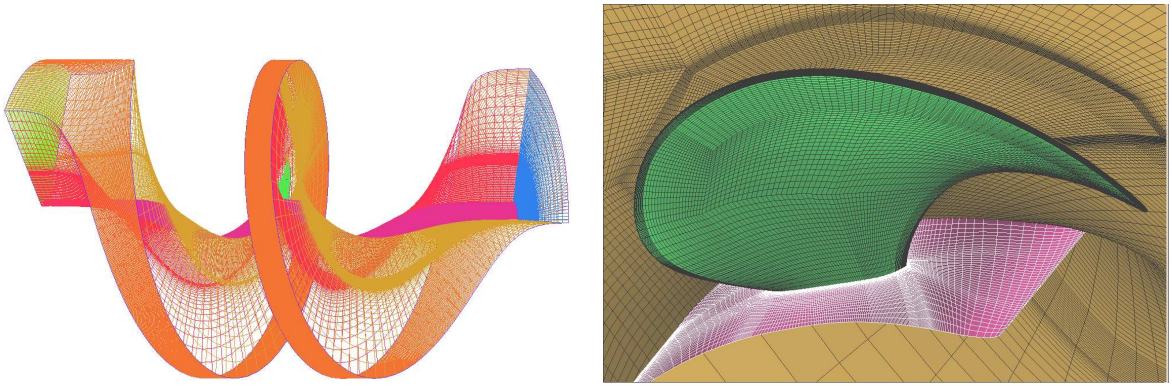

a) b)

Figure 5: a) Madel B: domain of computations, b) grid structure on the propeller blade, hub and periodic surface

Results of computations

Pressure distribution over the suction and pressure side of the propeller blade is shown in Fig 6.

The comparison of the calculated and experimental values of K_T and K_Q for several J is presented in Fig. 7 a, however picture 7 b shows pressure distribution inside the domain. The low pressure area which is stretched behind a blade tip is caused by a strong vorticity of tip vortex. The tip vortex is visible even far than 180 degree behind the blade.

5 Conclusions

- Pressure distribution over the blades of the propellers is smooth, without any numerical oscillations, also there are no pressure oscillations near periodic, non-matching boundaries.

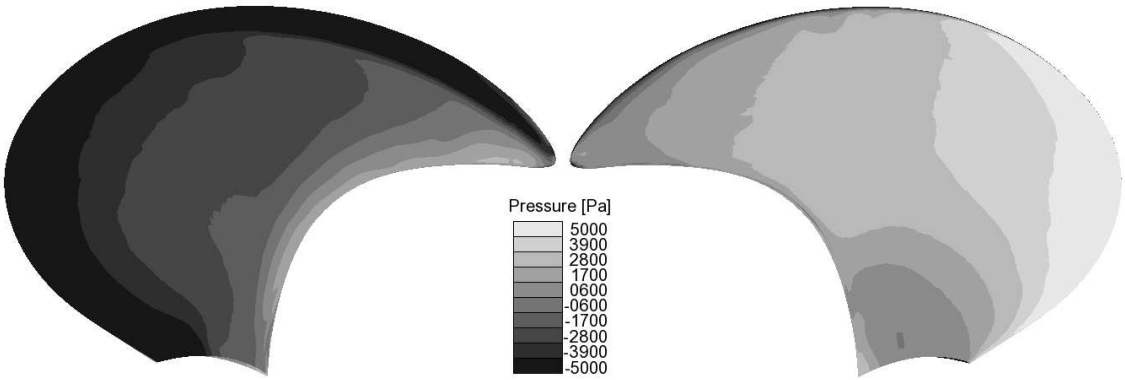

Figure 6: Pressure distribution over a suction (left) and pressure (right) side of the skewed propeller, $J = 0.684$.

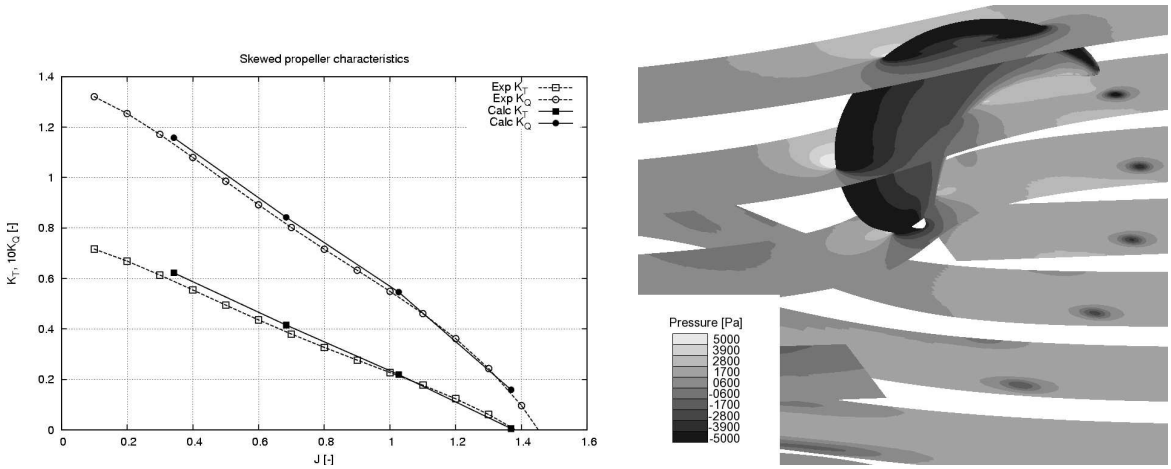

a) b)

Figure 7: a) K_T, K_Q characteristics of the skewed propeller (model B), b) pressure distribution at intersections of the domain, $J = 0.684$.

- Propeller characteristics: trust K_T and torque K_Q coefficient, have a good agreement with the experimental results for both conventional and skewed propeller.
- Program SOLAGA can be also a good tool for the tip vortex modelling. The low pressure area caused by vorticity is clearly visible far behind the propeller blade (Fig. 7 b). The perceptive reader can observe the core of the vortex created by the next blade in this figure.

References

[1] Ferziger J.H, Peric M.(1999): Computational Methods for Fluid Dynamics, 2nd ed., Berlin, Springer

[2] Wilcox D.C. (2002): Turbulence Modeling for CFD, DCW Industries

[3] Blazek J. (2001): Computational Fluid Dynamics: Principles and Applications, ELSEVIER

Effects of Gas Bubbles and Their Compressibility on Slamming Loads

Bettar El Moctar*, Samir Muzaferija** and Milovan Perić**
*Germanischer Lloyd AG, Hamburg, **CD-adapco, Nürnberg
ould.el-moctar@gl-group.com, samir@de.cd-adapco.com, milovan@de.cd-adapco.com

Slamming loads can induce high stresses and cause deformations of local structural components. The accurate assessment of slamming loads is essential for the design of the ship's structure. Classification society rules contain formulas for slamming loads (e.g., Germanischer Lloyd, 2005). Generally, these formulas are adequate for conventional ships, as they are based on operational experience.

A satisfactory theoretical treatment of slamming has been prevented so far by the complexity of the problem. Most theories and their numerical procedures were applied on two-dimensional bodies; however, slamming is a strongly three-dimensional non-linear phenomenon that is sensitive to the relative motion between the ship and the water surface. Slamming is characterized by highly peaked local pressures of short duration. Hence, slamming peak pressures can not be applied on larger areas to estimate structural response to slamming impacts. Moreover, the influence of hydro-elasticity, compressibility of water, and air pockets may have to be accounted for as well. Mainly because of these phenomena, potential flow methods are not well suited to accurately predict slamming loads. Recent progress has been made to develop numerical methods that predict slamming pressures. El Moctar predicted ship motions and loads with an extended version of the Navier-Stokes solver COMET to also solve the non-linear equations of motions. The influence of structure deformation on slamming-induced sectional loads was investigated by el Moctar et al. (2006). Extreme load cases were presented.

In this study, water entry of a wedge at a constant speed of 5 m/s was studied under two conditions:

- Entry into pure water (incompressible)
- Entry into water with air bubbles (air treated as a compressible ideal gas).

The aim of the analysis – which, for the sake of simplicity and without loss of generality, was performed two-dimensionally – was to study the difference in pressure history over the wedge surface for these two conditions and to evaluate the effects of bubble compressibility on the loads the structure was subjected to. At this stage, the structure was still considered rigid in order to be able to investigate the effect of compressibility alone.

The analysis was then repeated by replacing the wedge by a typical ship section exposed to slamming in order to demonstrate that the results obtained for a wedge can be applied to other body shapes.

Simulations were performed using the code Comet of CD-adapco. The compressibility feature of all components in free-surface flow simulations was recently added to this code. The flow solver is based on the Finite-Volume method and can use control volumes of any polyhedral shape. Details of the method were documented by Muzaferija and Perić (1999) and details of its application to predict slamming by Sames at al (1999).

The wedge was 0.6 m wide, the half nose angle was 80° (almost flat), and the water was 1.4 m deep. Simulations were first done using a moving grid, treating the bottom boundary as a wall. Another set of simulations was performed by assuming infinite water depth. In this case it was possible to carry out the computations with reference to a coordinate system attached to the wedge and prescribing a constant inlet velocity of 5.0 m/s at the bottom boundary. The grid was locally refined around the wedge, as shown in Fig. 1. Figure 1 also shows the initial position and the initial shape of the air bubbles. The thickness of cells parallel to the wedge wall (the first four layers) was between 0.3125 and 0.3500 mm. A two-dimensional simulation for a half-wedge was performed, applying the symmetry condition at the wedge symmetry plane. The other lateral boundary was a rigid wall at 1.25 m away from the symmetry plane.

Simulations with a moving grid were performed using time steps of 50 μs; for the fixed grid, the time

step was 10 μs. Because of the fine mesh near the wall, using smaller time steps with a moving grid resulted in strong pressure oscillations due to the single-precision computations of mesh coordinates, so that round-off errors became significant when computing volumes swept by cell faces over one time step.

Figure 2 shows the free-surface deformation in the vicinity of the wedge for the two conditions (pure water and water with compressible bubbles). They show that the advance of water along the wedge wall was significantly faster for the incompressible case. This was because bubbles under the wetted wedge surface were distorted; they were first reduced in size by compression (some bubbles split to become two bubbles), while at later stages some bubbles expanded in size and were compressed again (bubble size oscillation took place).

Figure 3 shows the distribution of pressure in the vicinity of the wedge at several time instants for the two conditions investigated. Again, significant differences were observed: for the incompressible case, higher pressures were obtained and the pressure propagated deeply into the water, while for the case with compressible bubbles, pressures were lower and the pressure increase was limited to a smaller area near the free surface in contact with the wedge (peak pressure occurred where the deformation of the free surface was largest). For the incompressible case, only one local maximum was present (at the intersection of the free surface and the wedge wall), while for the case with air bubbles, local maxima and minima also existed away from the wall (high pressure inside compressed bubbles and low pressure in expanding bubbles; see also the corresponding volume fraction distribution in Fig. 2).

The computations indicate that compressibility of air bubbles significantly affected the pressure history along the wall slamming onto the water. For the incompressible case, just one short-duration pressure peak occurred, while for the compressible case, air bubbles led to multiple occurrences of pressure peaks. Although peak pressures were somewhat higher for the incompressible case, the structure was exposed to high pressures over a longer time for the compressible case, and these pressures oscillated.

Literature

Sames, P.C., Schellin, T.E., Muzaferija, S., Peri'c, M.: Application of a two-fluid finite volume method to ship slamming, *ASME J. Offshore Mech. Arctic Engrg.*, **121**, pp. 47-52 (1999).

Muzaferija, S., Peric, M.: Computation of free surface flows using interface-tracking and interface-capturing methods, chap. 2 in O. Mahrenholtz and M. Markiewicz (eds.), *Nonlinear Water Wave Interaction*, pp. 59-100, WIT Press, Southampton, 1999.

El Moctar, O., Schellin, T., Priebe, T. "CFD and FE Methods to Predict Wave Loads and Ship Structural Response" *26th Symposium on Naval Hydrodynamics,* Rome, 2006.

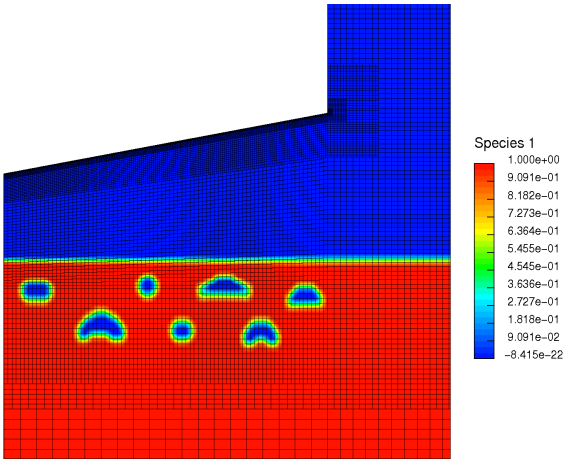

Fig. 1 Geometry of half-wedge, locally refined grid, and initial position and shape of air bubbles. The actual width of the solution domain was about three times larger than shown.

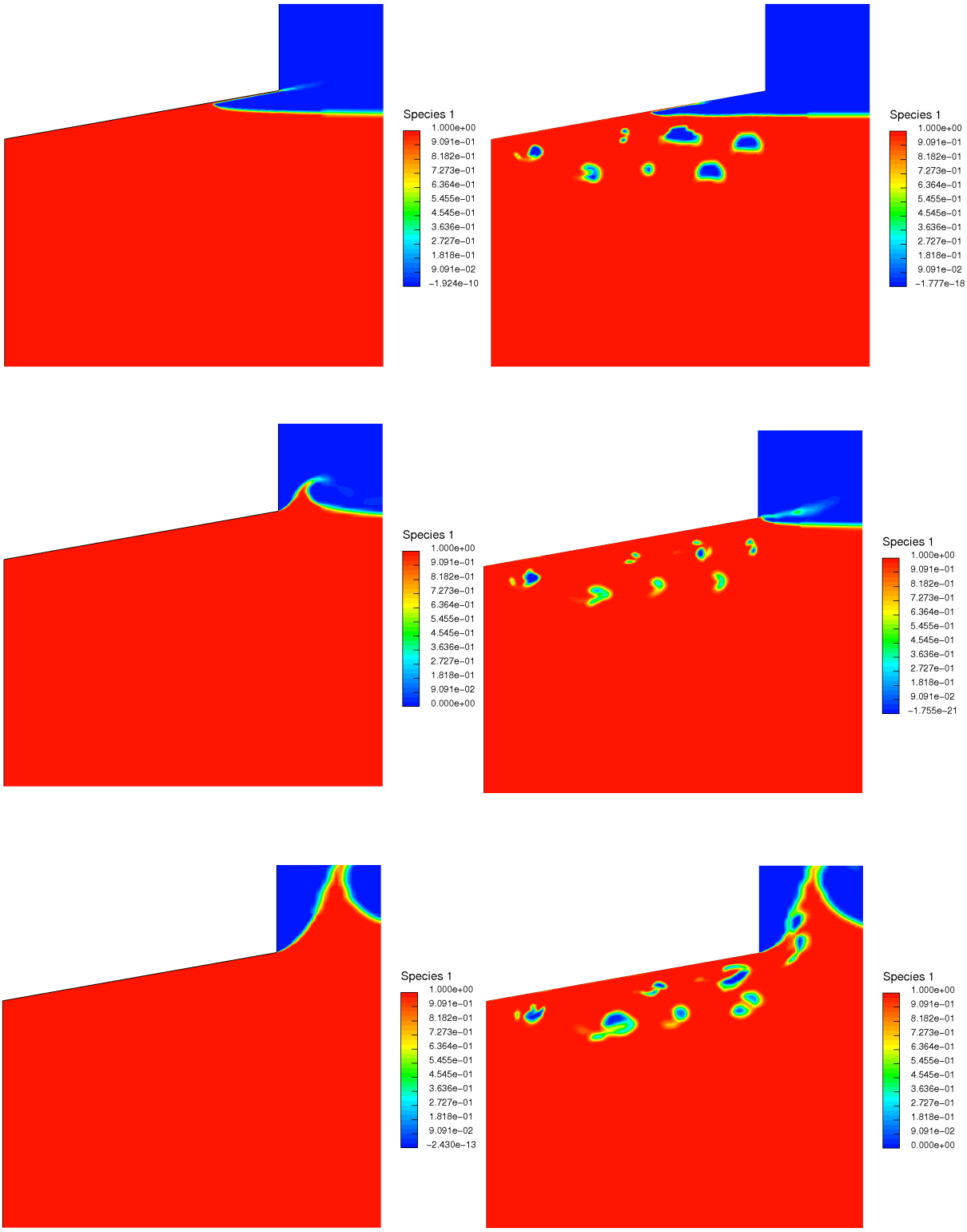

Fig. 2 Distribution of volume fraction of water at three time instants, predicted under incompressible conditions without air bubbles (left) and under compressible conditions with air bubbles (right). Compared to the initial bubble size and position shown in Fig. 1, the motion of bubbles, their compression and splitting, and subsequent expansion can be observed.

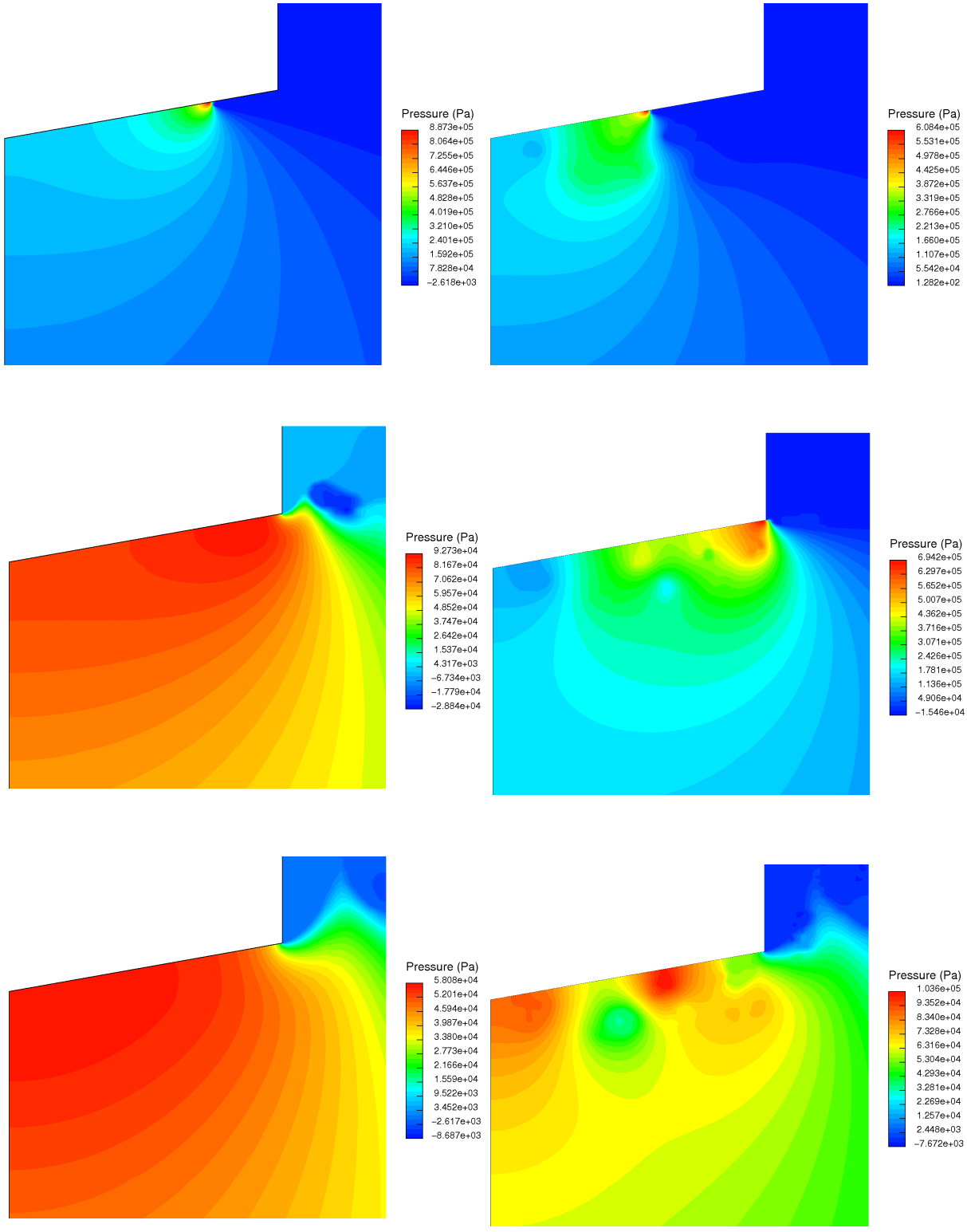

Fig. 3 Distribution of pressure in water at three time instants, corresponding to those of Fig. 2 (left: incompressible water; right: water with compressible air bubbles). Note that, in the early stages (before wedge corner passes free surface), the maximum pressure coincides with the location where extended free surface would cut the wedge. After that, the peak pressure is situated at wedge nose (stagnation point) when incompressible water without air bubbles is considered; with compressible air bubbles, local maxima and minima are present at several locations in the wedge vicinity, leading to a larger force on wedge wall.

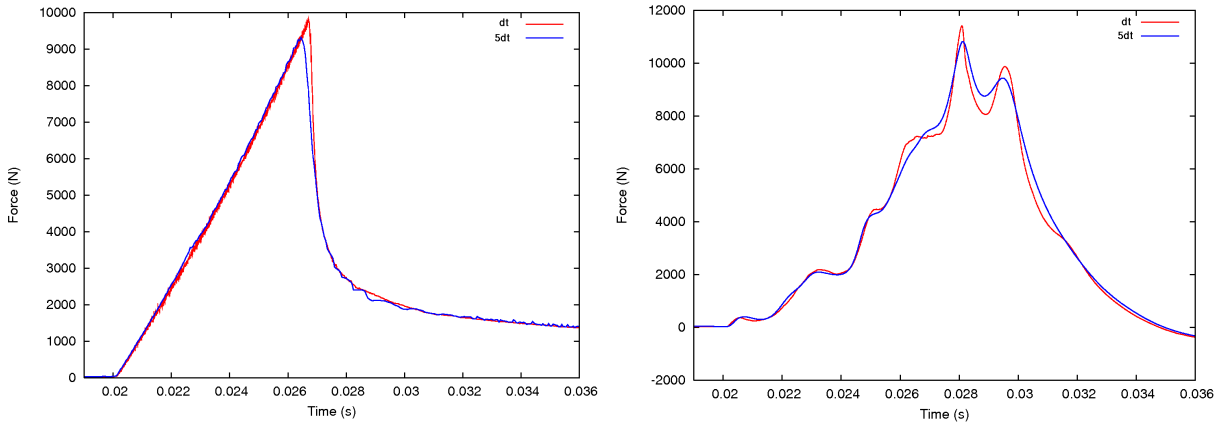

Fig. 4 Time variation of force on wedge (left: pure water, incompressible; right: water with compressible air bubbles). Shown are results obtained in a wedge-fixed reference frame (infinite water depth) with a time step of 10 μs (labeled dt) and a five times larger time step using a moving grid for a finite water depth of 1.4 m (labeled 5dt). Results for these two time steps differ relatively little. For the case with air bubbles, the maximum force was about 18 percent larger, and it occurred 1.3 ms later than in the incompressible case. For the latter, the force grew almost linearly and then dropped suddenly, approaching thereafter a nearly constant value, while for the case with air bubbles, the force oscillated during the growing phase, reaching a second peak after the first peak, and then it dropped gradually and eventually changed sign.

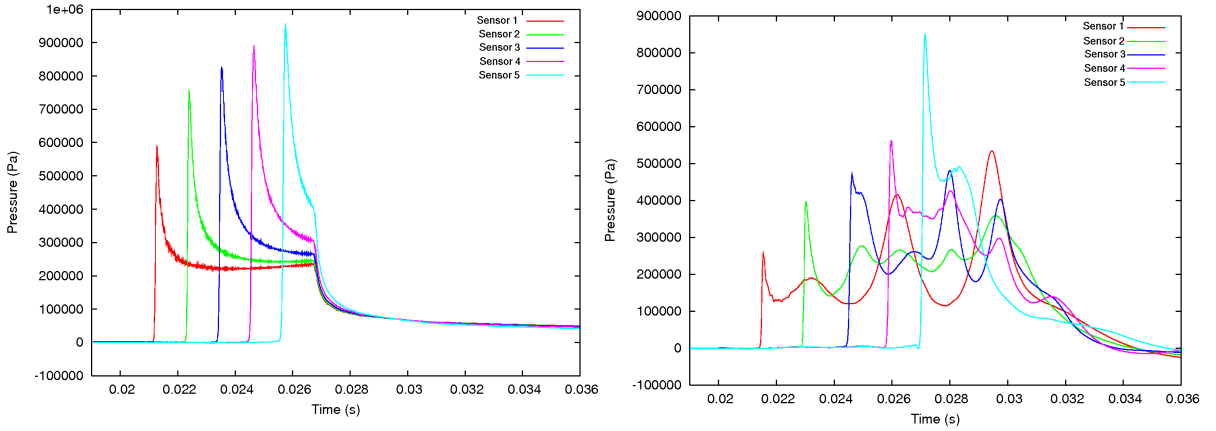

Fig. 5 Time variation of pressure at five sensors, distributed uniformly spaced 5.0 cm apart along the wedge; sensor 1 was 5 cm away from wedge nose (left: pure water, incompressible; right: water with compressible air bubbles). For the incompressible case, pressure peaks were much higher and closer to each other. When air bubbles were present, peak pressures were substantially lower: At sensor 1, the first peak was less than half as high as for the incompressible case. However, for the compressible case, pressures oscillated at sensor 1. The fourth peak of about 5.5 bar was twice as high as the first peak. For the incompressible case, at the time of the last peak, pressures were already down to about 0.5 bar. However, for the compressible case, pressures eventually fell below atmospheric, due to bubble dynamics. The pressure peak at sensor 5 was nearly as large as the pressure peak for the incompressible case.

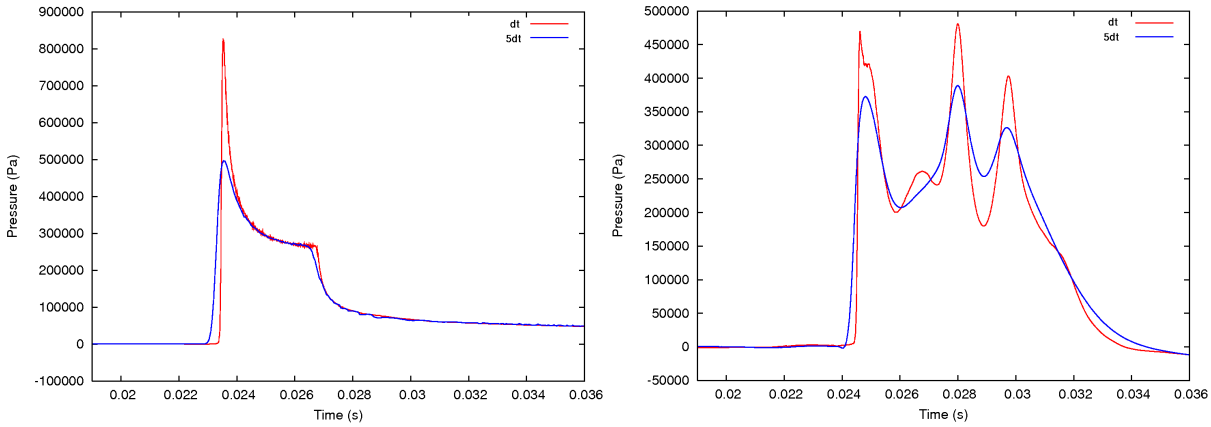

Fig. 6 Time variation of pressure at sensors 3, computed using two different approaches and time steps for the incompressible case (left) and for the compressible case (right). The pressure rise was steeper and the maximum higher when the time step was five times lower, but the force was nearly the same. In the compressible case, amplitudes of oscillations increased with time step reduction, but there was no shift in phase.

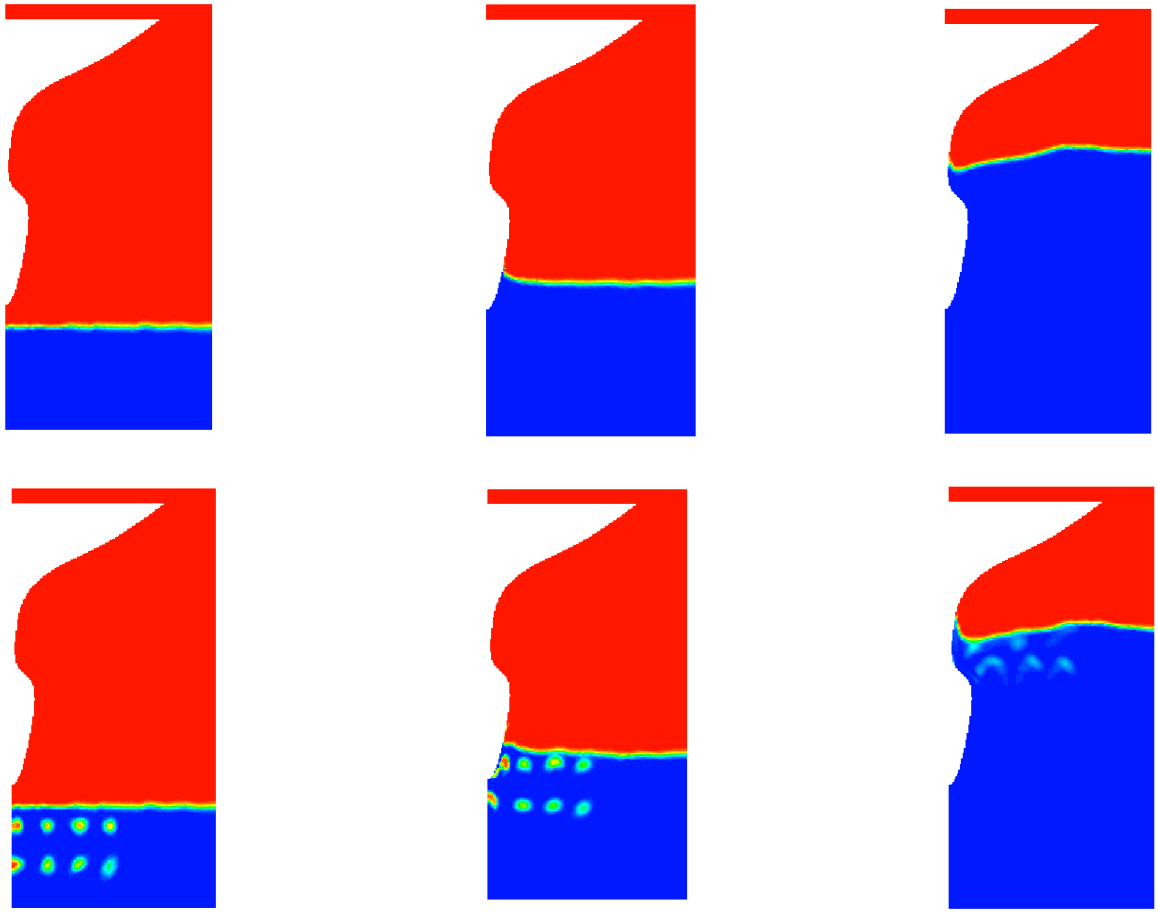

Fig. 7 Preliminary simulation (coarse grid) for water entry of a ship section: without air bubbles (incompressible; upper row) and with air bubbles (compressible; lower row). Results from simulation on a finer mesh and a comparison of pressures and forces will be presented at the workshop.

AN EXPERIMENTAL STUDY OF THE MANEUVERABILITY OF A BLUNT SHIP: THE EFFECT OF THE WATER DEPTH

L. FABBRI, L. BENEDETTI, B. BOUSCASSE, F. LA GALA, C. LUGNI
INSEAN, The Italian Ship Model Basin - Rome, Italy

1. INTRODUCTION

In infinite depth and calm water conditions the wave resistance is important for the cost necessary to maintain the design speed. In shallow water the safety aspects become more important [1]. First, wave generation in shallow water can lead to an increase of the trim and sinkage with high risk of ship grounding. Second, due to the strong variation of the added mass, i.e. of the linear derivatives, even small changes in trim and sinkage cause a local variation of the depth-to-draft ratio, h/T, altering the features of the directional stability [2]. Finally in very shallow water conditions, three-dimensional effects can matter, causing a strong flow around the ends of the ship and influencing the wave pattern around the hull. Therefore the possibility to predict the characteristics of maneuverability in shallow water is a fundamental task for blunt and large draft vessels during the operations near the coast or in the harbors.
Here we discuss an experimental study of the maneuverability features of a VLCC ship versus the ratio h/T.
Because our study is of fundamental nature, particular care has been given in performing a dedicated uncertainty analysis of the PMM experiments, following the procedure described in Simonsen (2004).

2. EXPERIMENTAL SET-UP

A dedicated and comprehensive experimental campaign has been performed to study the maneuverability performance of a blunt ship model in shallow water conditions. A KVLCC2 model (INSEAN model C2487) in bare hull condition has been considered for the tests in forced motions; a picture of the wooden model is shown in Figure 1.
The experiments have been carried out at the INSEAN model basin nr.2 (LxWxH=220m x 9m x 3.6m) using the INSEAN PMM mechanism, a false bottom with adjustable depth and a total length of approximately 60 m reproduces the shallow water conditions. Its length has been chosen larger than five times the longitudinal distance covered by the model. A preliminary FEM analysis of the steel false bottom structure has been carried out to account for the squat effect. The calculation predicted negligible deformation of the steel structure. However it could not take into account the small oscillations related to problems of fixation of the steel structure to the real bottom of the basin. These oscillations actually developed at the passage of the model and they were negligible for the considered h/T ratio.

Figure 1: Wooden model (C2487) of the KVLCC2 containership.

	L_{pp} (m)	**B** (m)	T_m(m)	∇(ton)	**Scale**	C_b	Z_g (m)	KM_T (m)	GM_T (m)
KVLCC2	320	58	20.8	312622	1	0.81	18.60	24.318	5.718
C2487	7	1.27	0.45	3.27	45.71	0.81	0.407	0.532	0.125

Table 1: Geometrical and dynamical characteristics of the model.

During the tests the model was free to sink and trim, while the roll motion was completely restrained. Resistance and lateral forces have been measured in two points along the model, so that the yaw moment is calculated straightforward by the knowledge of the distance between the lateral force transducers. Moreover, a dedicated measurement of the local wave pattern around the hull in shallow water regime has been performed. The measurement of the steady wave pattern for several drift angles has been carried out using a capacitance wave-probe system for longitudinal cut. A suitable stretching of the position of the wave probes in the transverse direction was used to follow the steep gradients of the near wave field system.
In order to study the behavior of the hydrodynamic coefficients moving from deep to shallow water conditions, both static and dynamic tests have been performed for several water depths, corresponding to h/T_m=1.2, 1.5, 3 and deep water. Two different carriage speeds, corresponding to ship-length Froude number, Fn = 0.0643 and 0.1423, have been considered. This assured a smooth variation of the depth-based Froude number, Fn_h, within the subcritical region as indicated in Table 2.
Preliminary tests in calm water with a null drift angle have been carried out, both to investigate the influence on the loads of the transient phase due to the passage over the step and to evaluate the steady forces reached in shallow water. In each case, the last four cycles appeared unaffected by the transient regime of the step; so they are the ones considered during the analysis.

h/T_m	Fn =0.0643	Fn =0.1423
1.2	0.23	0.51
1.5	0.21	0.46
3.0	0.15	0.32

Table 2 Froude number referred to water depth, $Fn=U/\sqrt{gh}$, being U the velocity of the model

Our studies are of fundamental nature and particular care has been devoted in performing a dedicated error analysis. Aiming to ensure the repeatability, each test for the measurement of the wave pattern has been repeated between 5 to 12 times. Concerning the measurement of the global forces, a limited number of cases were chosen for a suitable repeatability analysis at the lower speed. In the case of the static tests, the repeatability has been carried out for drift angle equal to 4°, for the dynamic ones a pure yaw with $r'=0.4$ has been considered, io both cases for h/T was 1.2.

3. DISCUSSION OF THE RESULTS

Hereafter the results for the static and dynamic tests in shallow, medium and deep water regimes will be discussed. The cases refer to the lowest velocity of the ship model. Test results at the highest velocity will be shown at the symposium.

3.1 Static Tests

Figure 2 shows the maximum hydrodynamic force (left panel) and moment (right panel) as a function of the drift angle β in static conditions.
The parametric dependence from the ratio h/T_m, i.e. from the Fn_h, is also reported. At each Fn_h, the typical behaviour of the hydrodynamic loads can be identified as follows: they increase with the drift angle, showing a non linear trend near the highest β as a consequence of the flow separation from the ends of the model. More interesting is the dependence of the forces from the Fn_h: a large increase of the hydrodynamic loads appears by reducing the water depth, i.e. by increasing the Fn_h. This behaviour can be partly explained by the sudden variation of the trim and sinkage of the model induced by the peculiar wave generation mechanisms in shallow water condition. The wave elevation measured during the experiments can help us to better understand the involved physical phenomena. In particular Figure 3 shows the steady wave pattern of the model for two different Fn_h (from top to bottom) and two different drift angles (from left to right). The increase of the Fn_h causes a quite significant growth of the wave amplitude for both the drift conditions. Three dimensional effects are emphasized at the sides of the hull for smaller H/T, larger waves are produced and larger variations of trim and sinkage happen.

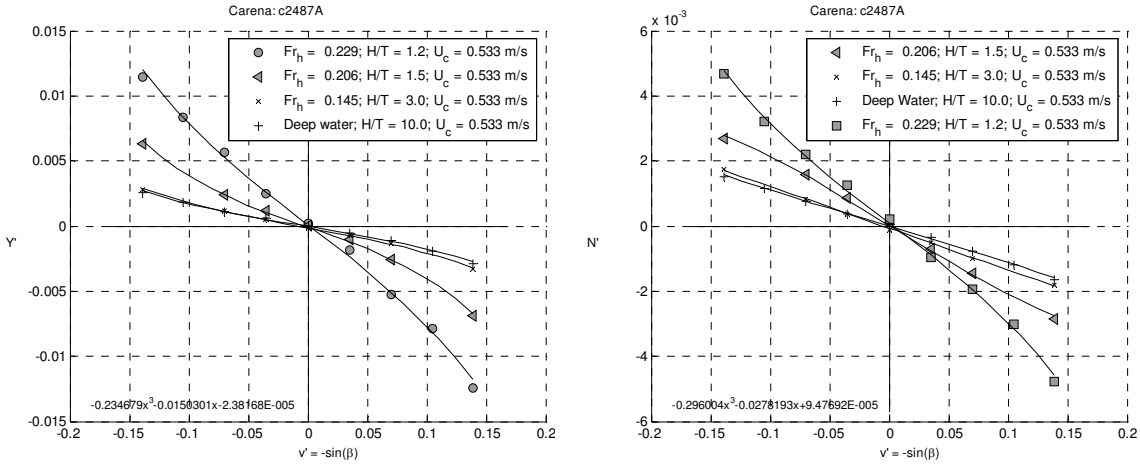

Figure 2 Nondimensional hydrodynamic force (Y', left panel) and moment (N', right panel) vs drift angle

The large depression region around the model induced by the vertical pressure under the hull can cause a suction force towards the bed; this phenomenon is called *squat effect*. The subsequent reduced clearance between the keel line and seabed leads to a higher risk of ship grounding. As expected, see Figure 4, increasing the Fn_h the squat effect is strongly amplified.

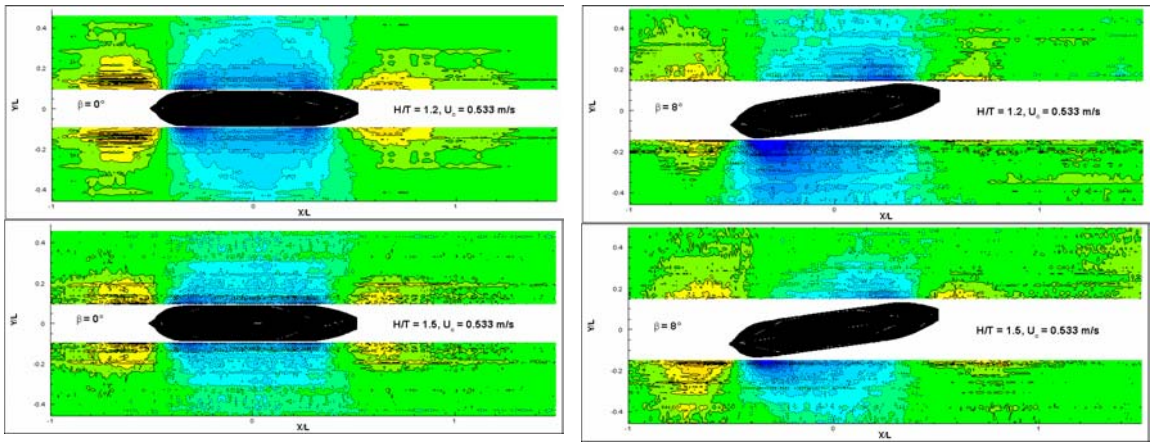

Figure 3 Steady Wave pattern generated by the model at U_c=0.533 for two different drift angles: β=0 (left panel) and 8° (right panel) and two different water depths, h/T_m=1.2 (Fn_h=0.229, top panel) and h/T_m=1.5 (Fn_h=0.206, bottom panel)

An accurate and systematic uncertainty analysis has been performed for measure of forces. Table 3 gives the results for the non dimensional lateral force and yaw moment, in terms of bias error (B), precision index (P) and global uncertainty $U_\Gamma^2 = B_\Gamma^2 + P_\Gamma^2$ being Γ the physical quantity measured. More detail of the procedure used can be found in [4]. A total uncertainty less than 5% has been estimated in shallow water, while higher value arises in deep water condition. This is due to the high values of the measured loads leading to a smaller relative uncertainty though the absolute total uncertainty is higher in shallow water.

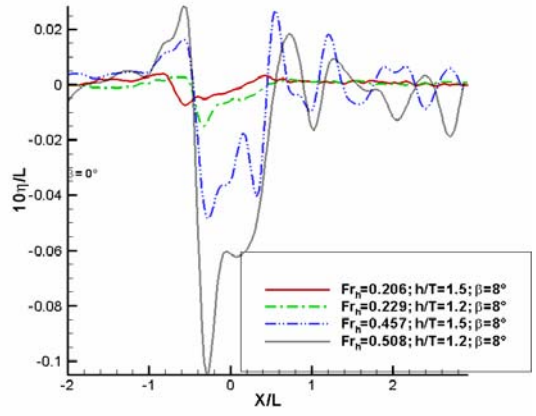

Figure 4 Longitudinal Wave cut (Y/L=-0.164) for several Fn_h (β=8°).

h/T_m	**Y'**	B_Y'	P_Y'	U_Y'	**U_Y' %**	**N'**	B_N'	P_N'	U_N'	**U_N' %**
1.2	**0.0818**	0.0004	0.0033	0.0033	**4.01**	**0.0348**	1.7E-3	6.8E-4	7.0E-4	**2.02**
10	**0.0169**	0.0022	0.0005	0.0021	**12.41**	**0.0118**	7.0E-4	3.7E-4	7.9E-4	**6.74**

Table 3: Mean value and uncertainty analysis of the lateral force and yaw moment (U_c=0.533m/s, β=4°).

3.2 Dynamic Tests

Figure 5 shows the hydrodynamic force (left panels) and moment (right panels) as a function of the nondimensional yaw rate *r'* (out-phase component: top panels) and yaw acceleration (in-phase component: bottom panels). Dependence from the water depth to draft ratio is also reported. Due to the increased added mass contributes two main features can be highlighted varying the water depth: 1) a quite significant increase of the nonlinear effects in restricted water depth, with higher order derivatives strongly affected; 2) a growth of the steepness of the curves around the zero value of the reference parameter, highlighting the strong dependence of the linear derivatives from the water depth.

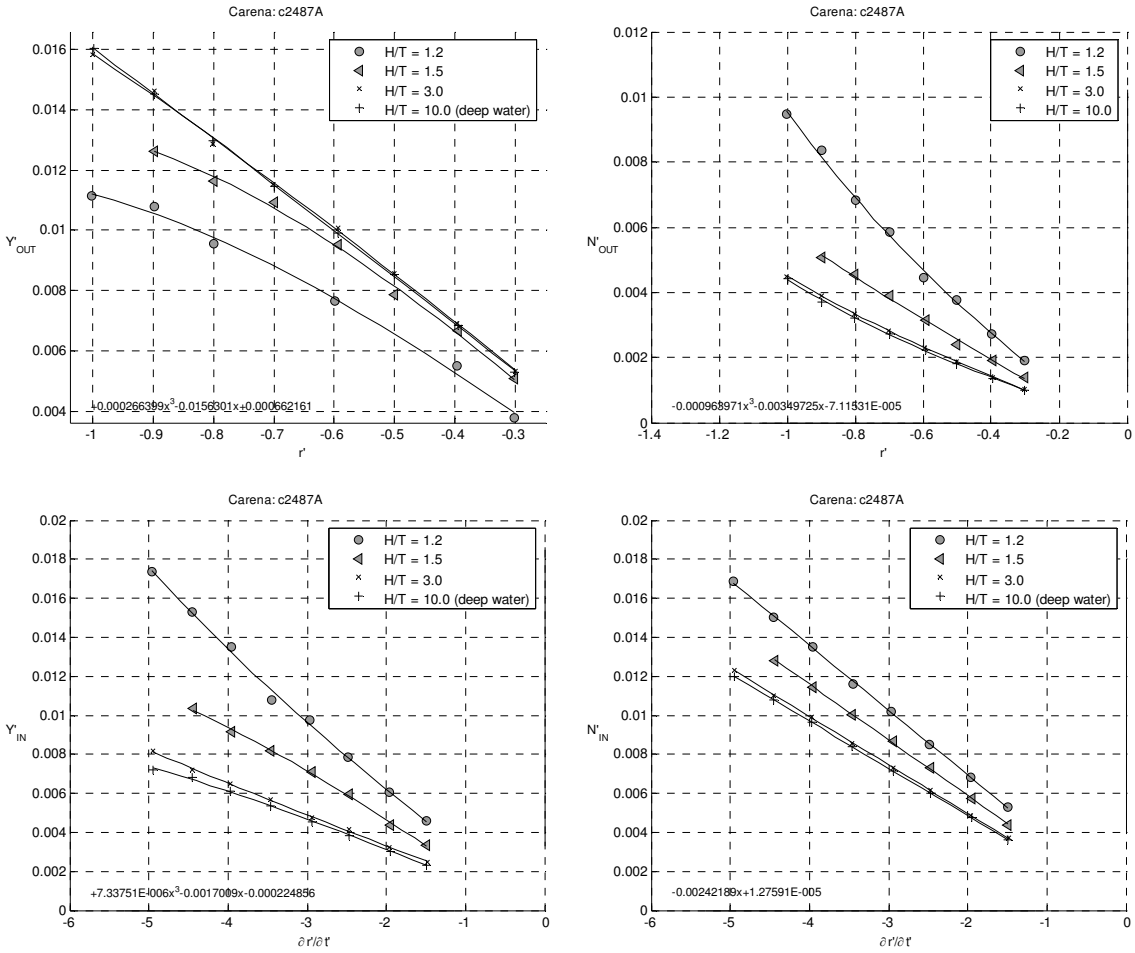

Figure 5 Nondimensional hydrodynamic lateral forces (left panels) and yaw moment (right panels): out-phase (top panels) and in-phase (bottom) components.

Figure 6 highlights the shallow water effects, the experimental ratio between the linear derivatives in finite depth and the relative quantities in deep water (square symbol) versus T/h are shown in figure. According to the suggestion reported in [6], three regimes can be distinguished by decreasing the water depth: deep water (h/T>3), medium depth (1.5<h/T<3), shallow water (1.2<h/T<1.5) and finally, very shallow water (h/T<1.2). In particular in infinite depth regime the linear derivatives are quite constant with the T/h ratio. Decreasing the water depth, i.e. in medium depth, they slightly increase and they get

steep gradients in the shallow water regime. Besides the experimental data, the figure reports data obtained with two mathematical models. Both of them ([7] and [8]) are based on an analytical approach of the added mass calculation. According to the slender-body-strip methods, the linear derivatives in deep water are obtained by the distribution of two-dimensional horizontal added mass coefficients along the length of the hull. In shallow water, analytical approach based on the use of conformal mapping has been used [7] to determine the variation of the added mass due to the presence of the bottom. It is worth notice as the Clarke model [7] is applicable for $1.25<h/T<\infty$, while Ankudinov [8] extended his model in very shallow water regime. A satisfactory agreement between experiments and mathematical models is found in infinite depth regime, i.e. for $h/T>3$. Small discrepancies appear in finite depth conditions to become quite relevant in the shallow water regime. As expected, Ankudinov model is closer to the experimental data. Nevertheless the discrepancies in the comparisons highlight the need to improve the proposed theoretical models. In particular vortex shedding, neglected by the analytical models, as well as its interaction with the bottom, plays a relevant role. More, 3D effects at the ends of the hull, not included in the slender-theory approximation, dominate in shallow water regime and, moreover, increase by reducing the underkeel clearance. Finally in very shallow water regime, the interaction of the boundary layer of the ship with the one developing on the bottom can influence the hydrodynamic forces.
The dependence of the linear derivatives from the h/T ratio also influences the directional stability of the ship. Figure 7 shows the stability index as function of the water depth to model draft ratio. According to the results of Crane [5], summarised by the 16th ITTC Manoeuvring Committee [9], stability index first decreases when moving from deep to finite depth, and then rapidly increases in shallow water regime.

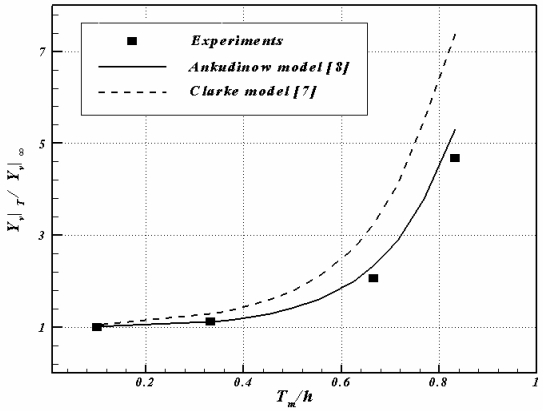

Figure 6: Ratio between linear derivatives in finite depth and deep water, as function of the model draft-to-water depth ratio. Experiments (square) and mathematical models (continuous and dashed lines).

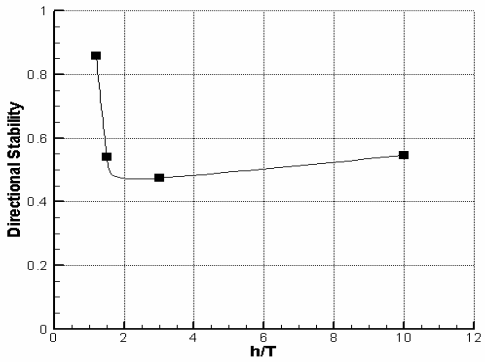

Figure 7: Stability index: $(N'_r/(Y'_r - \Delta') - N'_v/Y'_v)$ as a function of h/T.

Uncertainty assessment has been performed for estimating the total error of the measurements. Major details of the procedure used can be found in Fabbri et al. [4]. Figure 8 shows a typical result of the uncertainty assessment in shallow water. Nondimensional total uncertainty ±U' has been superimposed to the nondimensional mean value of the signals recorded, hydrodynamic lateral force (left) and yaw moment (right), respectively. Due to the unsteadiness of the phenomenon investigated, the total uncertainty must be evaluated at each time instant. A deeper discussion will be proposed at the symposium.

4. CONCLUSIONS

Manoeuvrability features of a blunt ship in shallow water regime have been investigated through a validated experimental campaign using PMM mechanism. The analysis of the results highlights the strong dependence of the hydrodynamic loads from the water depth. As consequence the directional stability can be affected: stability index first decreases from deep to finite depth, and then rapidly increases in shallow water regime. Comparison with some theoretical models existing in literature confirms the strict correlation between the growth of the hydrodynamic loads and the increased added

mass contributes in finite depth regime. Nevertheless, in shallow water condition, these models need to be improved to better reproduce the involved physical phenomena.
Measurements of the steady wave pattern around the model help to understand the physical mechanisms involved in the squat effect. In particular the large low pressure area under the model is strongly influenced by the variation of the water depth and, in general by the Fn_h. Future activity will be devoted to study the influence of the shallow water regime on the efficiency of the rudder and of the propeller.

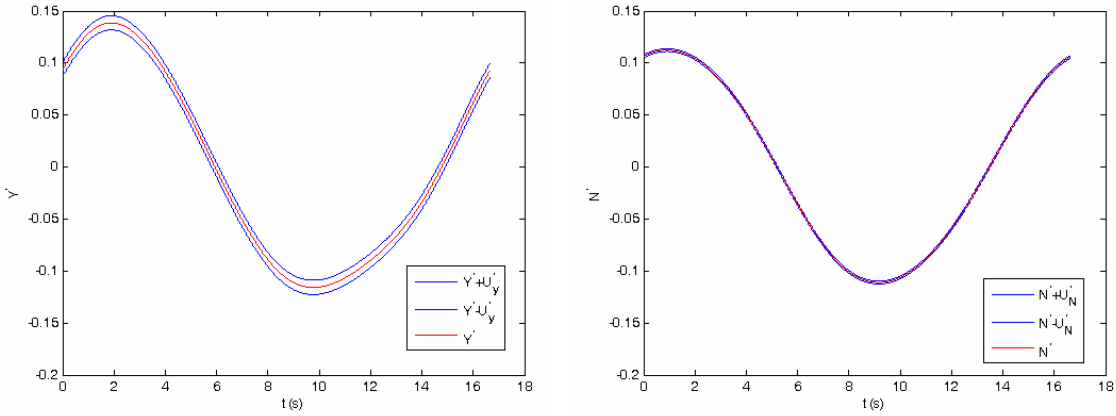

Figure 8: Pure Yaw test (U_c=0.533 m/s, r'=0.4, h/T=1.2): Uncertainty analysis for the lateral force (left) and yaw moment (right).

5. REFERENCES

[1] Tao Jiang, (2001), "Ship Waves in shallow water", PhD Thesis, Nr. 466,VDI Verlag
[2] Faltinsen, O.M. (2005), "Hydrodynamics of high speed marine vehicles", Cambridge Univ. Press.
[3] Simonsen (2004), "PMM model test with DDG51 including uncertainty analysis", Force Tech. Report.
[4] Fabbri L., Benedetti L., Bouscasse B., La Gala F., Lugni C. "Uncertainty assessment for PMM tests on DDG51 frigate model", INSEAN Report 2005-069
[5] Crane, C.L. (1979), "Maneuvering trials of a 278000 DWT Tanker in shallow and deep waters", SNAME Trans., Vol. 87, pp. 151-283.
[6] PIANC, (1992), "Capability of ship manoeuvring simulation models for approach channels and fairways in harbours", Report of Working Group no. 20 of Permanent Technical Committee II, Supplement to PIANC Bulletin No. 77, 49 pp.
[7] Clarke, D., (1997), "The shallow water effect on linear derivatives", Proceedings MCMC'97, Brijuni, Croatia, pp. 87-92.
[8] Ankudinov, V.K., Miller, E.R., Jakobsen, B.K., and Daggett, L.L., (1990), "Manoeuvring performance of tug/barge assemblies in restricted waterways", Proceedings MARSIM 90, Tokyo, Japan, pp. 515-525.
[9] Maneuvering Committee: "Final report. Proceedings of the 16th ITTC, Vol.I.
[10] Hirano, M., Takashina, J., Moriya, S., and Nakamura,Y., 1985, "An experimental study on manoeuvring hydrodynamic forces in shallow water", TWSNA, Vol. 69, pp. 101-110.

Multiphase CFD Modelling of a Lateral Sloshing Tank

Bernhard Godderidge*, Mingyi Tan*, Chris Earl & Stephen Turnock***

*Fluid-Structure Interaction Research Group, School of Engineering Sciences, University of Southampton, Highfield, Southampton SO17 1BJ, UK

**BMT SeaTech, Grove House, 7 Ocean Way, Southampton SO14 3TJ, UK

Corresponding author's email: bg401@soton.ac.uk

Introduction

Sloshing presents a design problem often encountered in naval architecture. Ships with large ballast tanks and liquid bulk cargo carriers (e.g. oil tankers) are subjected to often significant sloshing loads during their operational life. The inclusion of structural members in the tanks dampens the sloshing liquid sufficiently in all but the most severe cases. Liquefied Natural Gas (LNG) carriers cannot use this approach and sloshing has thus evolved into a central design problem for this type of vessel.

Natural gas, consisting of typically 90% methane, is transported in liquefied form for economic reasons, as it is considerably cheaper than building pipelines, especially over long distances [15]. The liquefication temperature of $-163°$C introduces design challenges for the structural material as well as tank insulation. It is not possible to dampen the sloshing liquid through additional structure. Rather, the loads must be quantified to design a sufficiently strong tank and supporting structure.

Various methods are used to determine sloshing loads. Abramson [1] is considered a cornerstone of modern sloshing anlysis, while Ibrahim ([13] & [14]) gives an up to date survey of sloshing modelling techniques. In general, sloshing is quantified using one or a combination of the following three methods.

1. Experimentation is widely used by classification societies, among them Det Norske Veritas [3], Lloyd's Register [19] and the American Bureau of Shipping [21]. However, there are limitations, especially when scaling the sloshing loads [1].

2. Theoretical fluid dynamics models have been developed as well, a linear model intended for the aerospace industry is given by Graham & Rodriguez [10]. However, in the marine field the nonlinear model developed by Faltinsen [5] is prevalent. The restriction imposed by shape complexity has been overcome using boundary element methods [5].

3. The most general modelling technique is the solution of the Navier-Stokes equations using Computational Fluid Dynamics (CFD). Some recent examples of sloshing simulation include el Moctar [4], Fallon et al [11], Rhee [18] and Standing et al [22].

More recently the sloshing problem has been considered by Gallarde et al [8] and Kim [16] in a seakeeping context, underlining the importance of sloshing. The objective of this paper is the investigation of the suitability of a multiphase flow model, implemented in the commercial CFD code ANSYS^{TM} CFX-10^{TM}, for sloshing flows.

Method

The computational results obtained from the above model are compared to experimental steady state sloshing pressures given by Hinatsu [1] [12]. The procedure outlined by Godderidge et al [9] is used to transform the pressure data to give a physically consistent result. Figure 1 shows the experimental setup. The tank motion is given as

$$x = A \sin\left(\frac{2\pi}{T}\ t\right), \tag{1}$$

where $A = 0.015$ m is the displacement amplitude, $T = 1.404$ sec the sloshing period and t the elapsed time. In the current case, the tank motion is solely in the x-direction indicated in figure 1. Olsen [17] observed that the most important kind of sloshing is the lateral sloshing, hence this motion was adopted as a test case.

Typical sloshing pressure histories are divided into two transient phases, lasting ten sloshing cycles each, followed by a steady state phase. However, Faltinsen et al [6] observed up to five different transient stages when considering sloshing near the natural frequency

[1]The authors wish to thank Dr Munehiko Hinatsu at the National Maritime Research Institute of Japan for making available the experimental sloshing data.

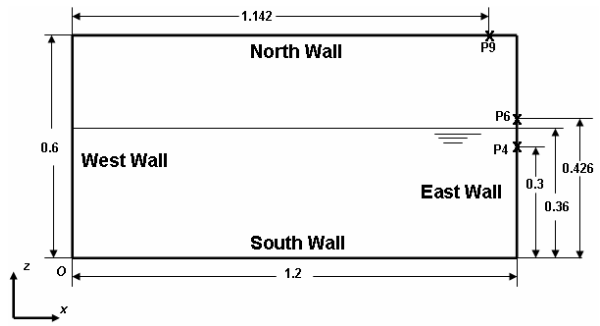

Figure 1: The sloshing problem (all dimensions in m)

with gradual convergence to the steady state. Therefore, a valid assessment of the results identifies the steady state and compares steady state phase of the computational results to the experimental data.

This sloshing problem is modelled using multiphase theory, that is both fluids have a distinct velocity field matched at the fluid interface. The pressure field is shared by both fluids. For two phases denoted by subscripts α and β, mass conservation for compressible phase α is given by

$$\frac{\partial}{\partial t}\left(r_\alpha \rho_\alpha\right) + \nabla\cdot\left(r_\alpha \rho_\alpha U_\alpha\right) = m_\alpha + \Gamma_{\alpha\beta}, \qquad (2)$$

where $\Gamma_{\alpha\beta}$ is mass transfer between the phases and m_α mass sources, ρ_α density, r_α volume fraction and U_α velocity of phase α. Conservation of momentum for phase α is given as

$$\begin{aligned}\frac{\partial}{\partial t}\left(r_\alpha \rho_\alpha U_\alpha\right) + \nabla\cdot\left[r_\alpha\left(\rho_\alpha U_\alpha \otimes U_\alpha\right)\right] = \\ = -r_\alpha \nabla p + \nabla\cdot\left[r_\alpha \mu_\alpha\left(\nabla U_\alpha + \left(\nabla U_\alpha\right)^T\right)\right] + \\ + \left(\Gamma^+_{\alpha\beta} U_\beta - \Gamma^+_{\beta\alpha} U_\alpha\right) + B_\alpha + M_\alpha, \qquad (3)\end{aligned}$$

where B_α are body forces, M_α forces on the interphase caused by the presence of phase β, μ_α the dynamic viscosity and the term $\left(\Gamma^+_{\alpha\beta} U_\beta - \Gamma^+_{\alpha\beta} U_\alpha\right)$ interphase momentum transfer caused by mass transfer - not an issue in the current problem but potentially significant when dealing with LNG. Note that $(\cdots)^T$ indicates the transpose and $\otimes$ the tensor product, so that $U \otimes V$ would be $U_i V_j$ in tensor notation. Equations (2) and (3) are closed using an energy equation if a compressible fluid is included [2].

As the sloshing flow is assumed to be turbulent, the governing equation (3) employs a turbulence model to account for the effects of turbulence. The $k-\epsilon$ model is the prevalent turbulence model, used in the sloshing studies by Hadzic [11] and Rhee [18]. The current study employs the $k-\epsilon$ model as well as the more advanced SSG model by Speziale et al [20]. The transient nature of the sloshing flow results in a constantly changing y^+, which puts a premium on turbulence model robustness.

The recommended best practice in marine CFD [23] is to ascertain independence of a CFD solution from the computational parameters. The grid independence of the current solution has been demonstrated by Godderidge et al [9]. The grid used is shown figure 2, the grid contains 9605 elements, with the first node located 0.3 mm perpendicular to the wall. Time is discretised using a second order backward scheme. The time step is adapted using a maximum root mean square Courant number, calculated over the entire domain, of 0.2. This was selected following a time discretisation independence study [9].

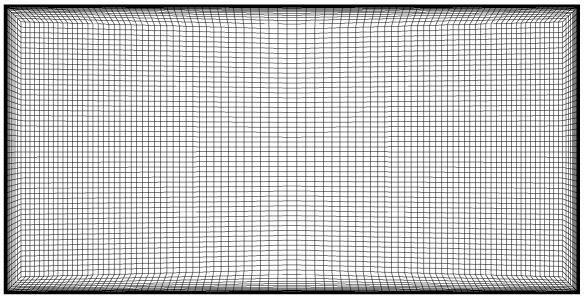

Figure 2: Computational Grid

As the computational domain is fully enclosed, a reference pressure was set by defining one node at the middle of the North wall (see figure 2) as a one cell wide outlet with $p_{static} = 1$ atm. This was found to be more stable than explicit specification of the pressure at the corresponding node. Water is modelled as a dispersed fluid to further aid computational stability, as fluid fragmentation at a macroscopic scale is difficult to achieve using the present numerical scheme. The sloshing motion is simulated using an oscillating body force in the x-direction as outlined by Hadzic [11]. Finally, the flow is initialised using a single velocity field as the multiphase model experienced problems when commencing using stationary initial conditions.

Results

Figure 3(a) gives the pressure history at sensor point P4. The initial transient phase is well defined, lasting about 10 oscillations, with a secondary, less obvious transient phase between oscillations 11 and 20. This trend is confirmed in figures 3(b) and 3(c), giving the pressure histories at P6 and P9 respectively. It is apparent that the computational results underestimate the experimental data. This is most significant at P6, figure 3(b), where the shortfall is in excess of 50% of the observed pressure.

The ratio of current to initial water mass and corresponding additional static pressure ($p_{static} = \rho g h$) is shown in figure 3(d). As the simulation progresses past oscillation 30, 10% of the water has been lost due to numerical diffusion. The corresponding static pressure of 350 N/m^2 is nearly 25% of the computed

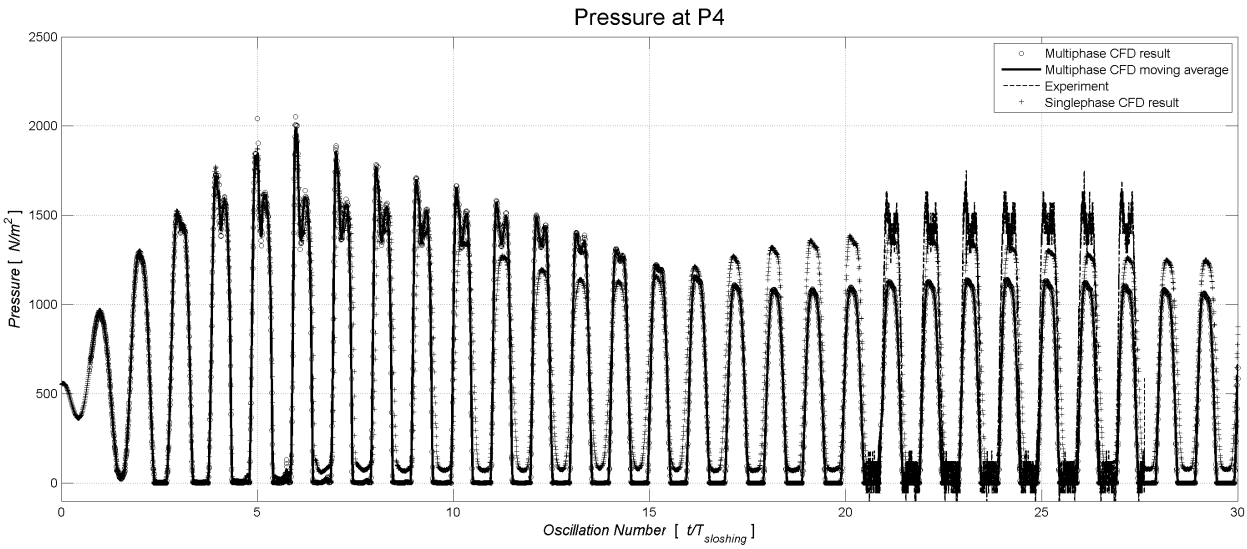

3(a): Pressure at P4

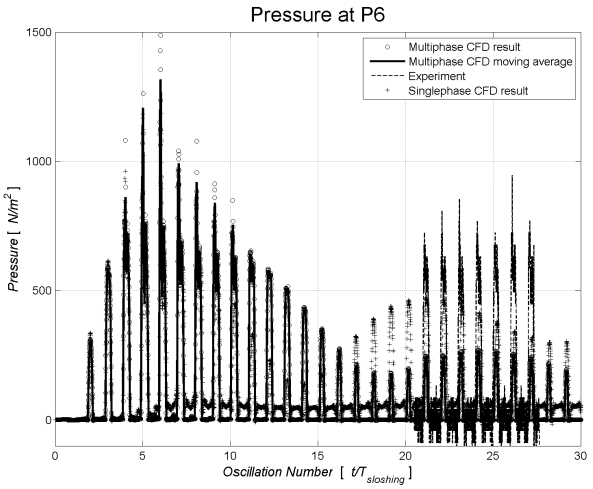

3(b): Pressure at P6

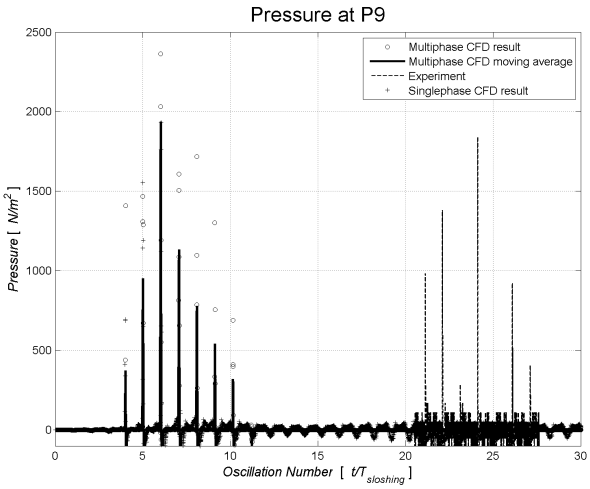

3(c): Pressure at P9

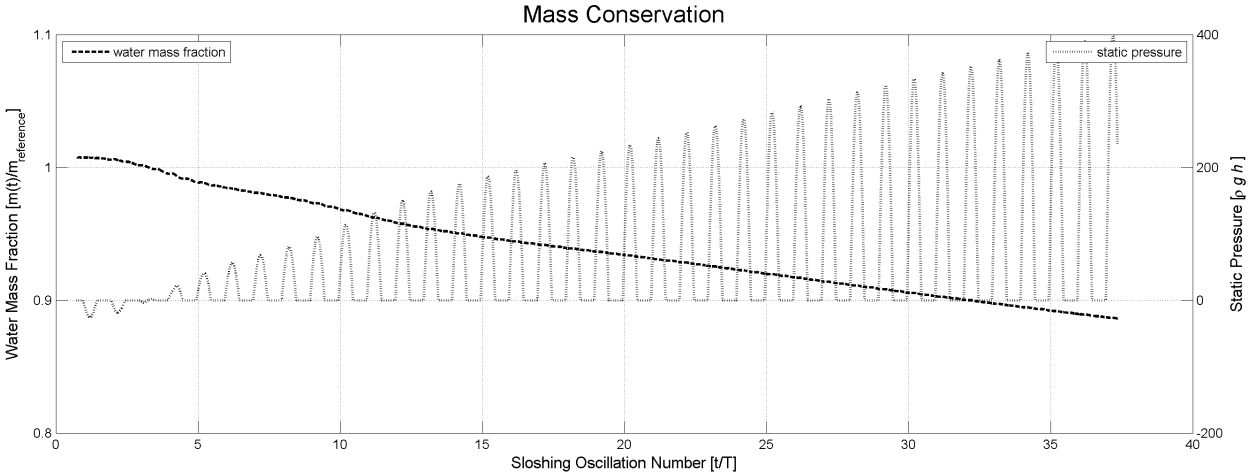

3(d): Mass Fraction and Static Pressure

Figure 3: Pressure history and mass conservation from multiphase fluid model

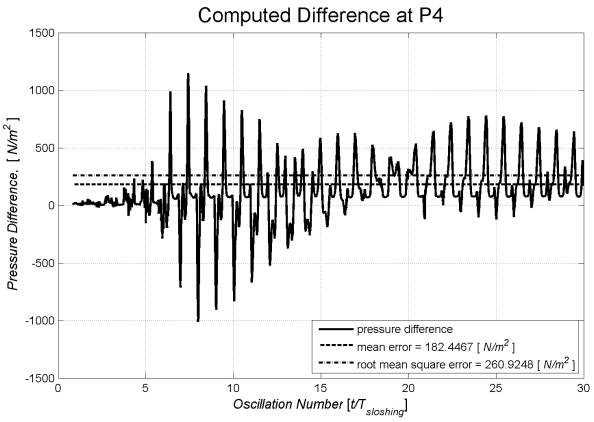

4(a): Difference at P4

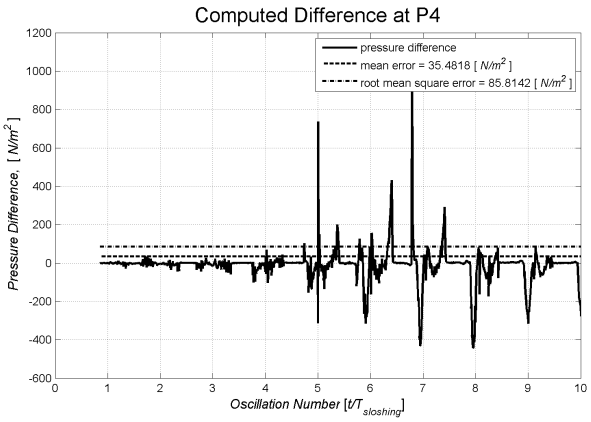

4(b): Difference at P4

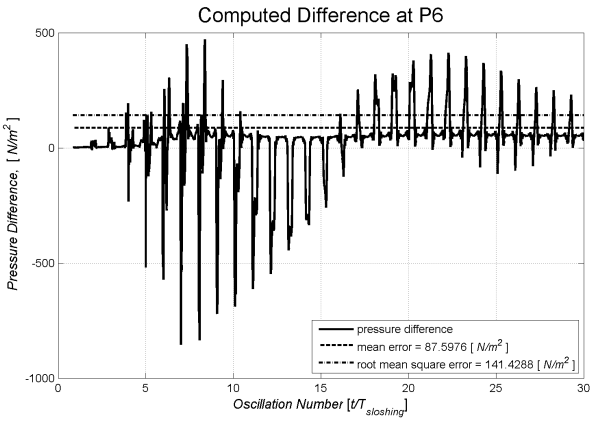

4(c): Difference at P6

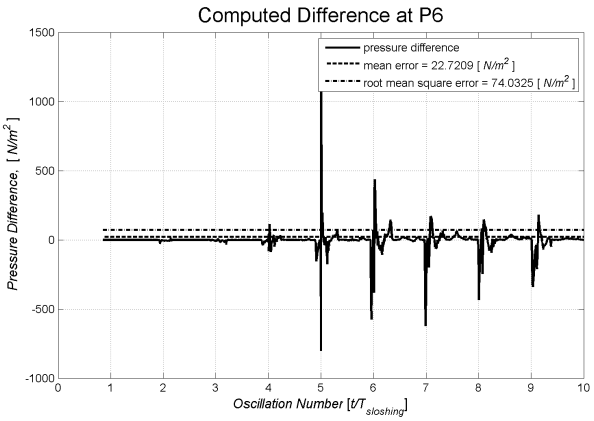

4(d): Difference at P6

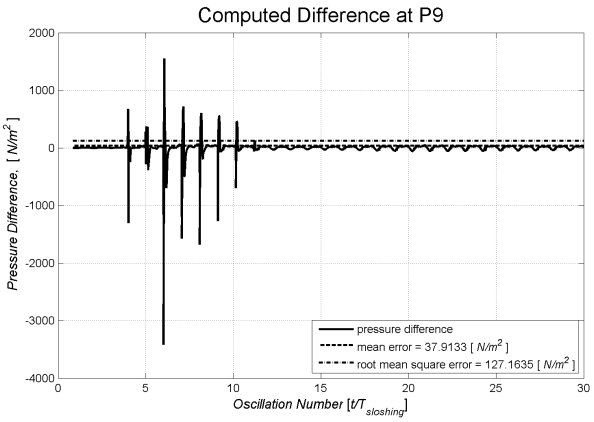

4(e): Difference at P9

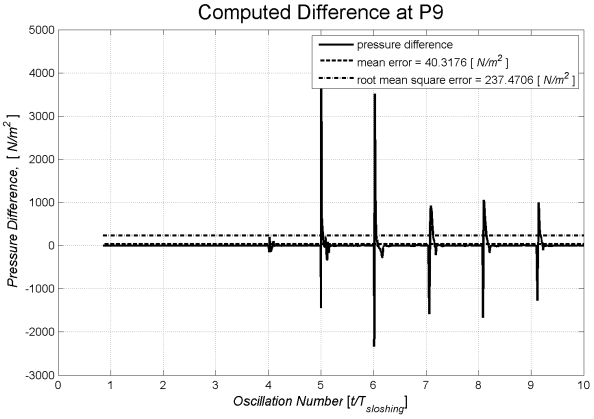

4(f): Difference at P9

Figure 4: Pressure differences between single v multiphase solution (left column) and $k-\epsilon$ v SSG turbulence models (right column)

total at P4, a significant amount even when ignoring any dynamic pressure contributions. Figure 4 shows the impact of selecting a multiphase fluid model and explores the effect of using the advanced SSG [20] turbulence model. The multiphase, $k-\epsilon$ solution was used as the reference case, the mean error is defined as

$$\frac{1}{n}\sum_{n}|\Delta P_i| \tag{4}$$

for n pressure differences ΔP_i. The substitution of the SSG turbulence model has made little difference to the pressure history. Comparing the differences at the pressure sensor points, the impact of using a multiphase model is considerably more significant, both in the transient and steady state.

Finally, the pressure results obtained from the multiphase model given in the previous figure 3 are corrected for the static pressure lost due to water mass diffusion. Provided that the pressure can be split into a static and dynamic component and assuming that the pressure at flow reversal is dominated by the static contribution, incorporating the diffused static pres-

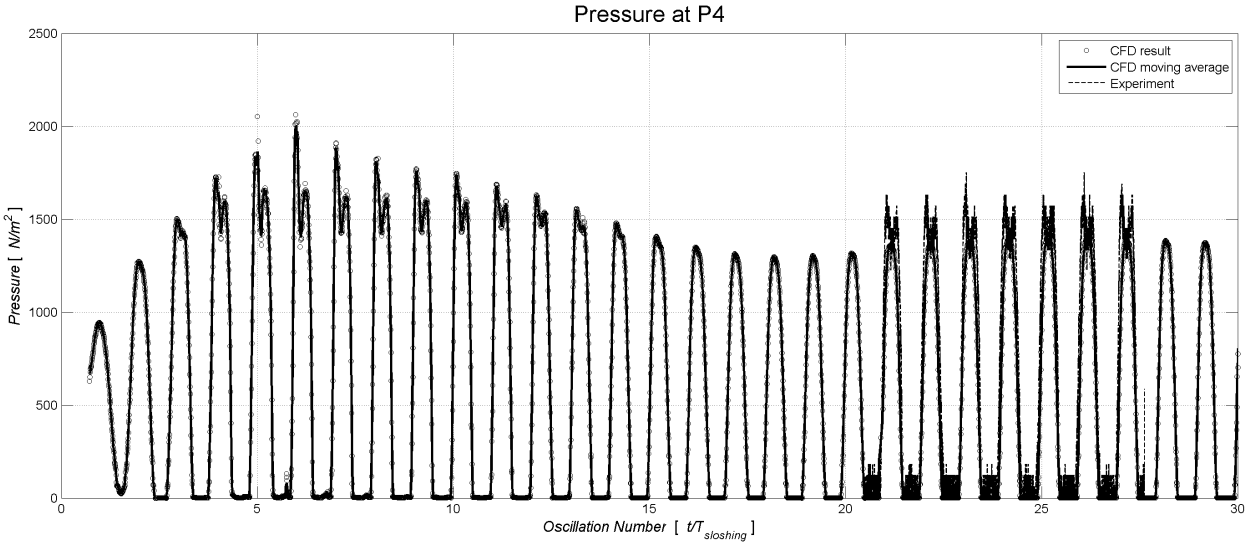

5(a): Pressure at P4

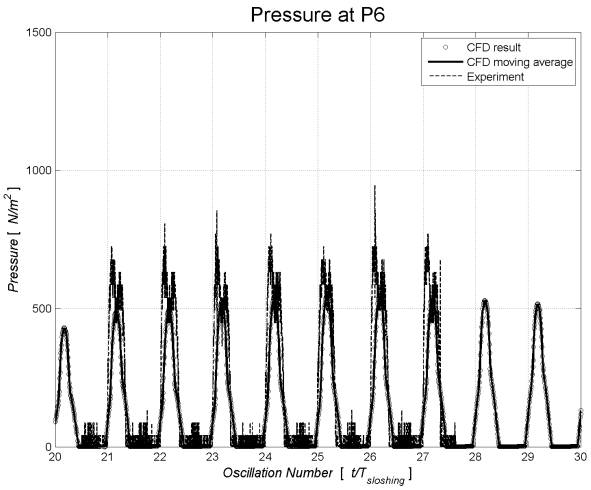

5(b): Pressure at P6

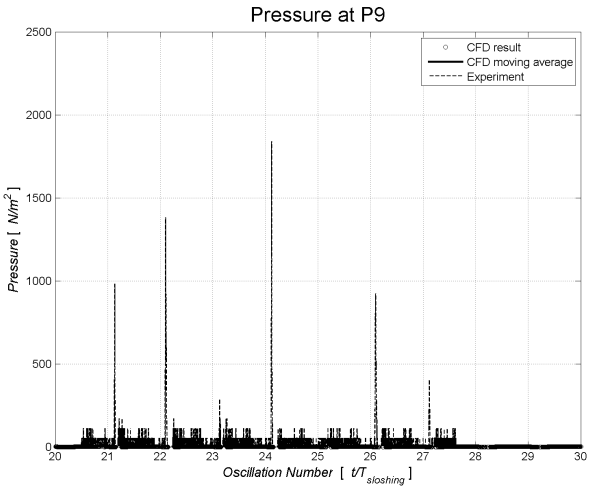

5(c): Pressure at P9

Figure 5: Pressures at P4, P6 and P9 obtained by correcting the computational result for static pressure

sure component is expected to give a more realistic result. There is a significant improvement in correlation between experimental and computational data. At P4, shown in figure 5(a), the static pressure correction gives acceptable correlation between experimental and computational data. The pressures at P6 and P9 are still underestimated, indicating the importance of the dynamic pressure contribution.

Discussion

The impact of using a multiphase fluid model has been quite significant. The biggest drawback of solving a multiphase problem is the increased computational time. The multiphase simulation required $1.3 \cdot 10^6$ sec to simulate 45 sec, compared to $2.9 \cdot 10^5$ sec for a single phase simulation [2]. Considering figure 3(a) one may be tempted to conclude from the pressure history at P4 that the single velocity field produces a better result. However, the pressure histories at P6 and P9 are not acceptable for either result. If corrected for the loss of fluid mass, the multiphase result in figure 5 matches the experimental data by Hinatsu [12] in the steady state far better.

While most authors (e.g. [11] & [18]) generally model this sloshing problem as a turbulent flow, the choice of turbulence model does not influence the quality of the computational results in a significant way. The SSG model proved to be rather unstable and sensitive to the choice of computational grid, unlike the $k-\epsilon$ model which did not adversely influence the computational stability of the run. As the SSG model introduces five additional transport equations, the computational effort required makes this choice of turbulence model unsuitable for most practical sloshing applications.

[2]The simulations were run on a 64 bit, 2.2 GHz processor with 2 GB of RAM at the University of Southampton Iridis 2 computational facility

A big drawback of the multiphase solution is the numerical diffusion of water. As shown in figure 3(d), the multiphase simulation diffuses approximately 10% of the total water mass after 30 oscillations. While the static pressure lost can be easily corrected for, the dynamic effects associated with this problem are far more complicated and cannot be corrected for in a similar fashion. The direct dependence of the sloshing natural frequency [1] on the tank filling level and hence the sensitivity of the time history on small perturbations, illustrated by Faltinsen [7], emphasises the importance of ensuring the correct amount of fluid mass within the sloshing container.

Nonetheless, when comparing the corrected multiphase and single phase results to the experimental results, it is found that the multiphase results produce a better match to the experimental data than the single phase result. Moreover, the pressures obtained using the multiphase simulation tend to be higher than when using only a single velocity field. This has clear implications to the use of CFD when modelling sloshing in a design environment, especially for safety critical components such as LNG tanks.

Conclusions

Provided that mass conservation can be ascertained in the multiphase model, it is evident that the results obtained from the multiphase model are superior to those from a single velocity field. The multiphase pressure history shows reasonable agreement in the steady state with the experimental data. Despite the additional computational cost, it is recommended that a multiphase fluid model, solving separate velocity fields for each fluid, is used for sloshing flows where violent fluid motion is to be expected.The most crucial problem of the present multiphase flow simulation is the numerical diffusion of water mass. This problem appears to occur in multiphase simulations only. Several ways to overcome this problem have been identified.

1. The water is subjected to numerical diffusion during multiphase flow only. Therefore, one could ovcome the problem within the code by adding a third sacrificial fluid, which increases the computational requirements significantly.

2. A more refined grid may alleviate the numerical diffusion. However the additional computational work restricts this approach for industry-oriented applications.

3. A third method is to introduce additional mass into the domain to counteract the numerical diffusion. While CFD best practice generally frowns on this approach, the properties of the sloshing problem may permit it. Several implementations are being evaluated by the authors at present.

References

[1] H Norman Abramson. The dynamic behavior of liquids in moving containers, with applications to space vehicle technology. Technical report, National Aeronautics and Space Administration, 1966.

[2] Ansys Inc. *CFX-10 User's Guide*, 2005.

[3] Stuart Brewer. Research and development new research into LNG tank sloshing. *Classification News*, 1:6–7, 2004. Det Norske Veritas Corporate Publication.

[4] Ould El Moctar. Assessment for tankers. *Shipping World and Shipbuilder*, 204:28–31, 2006.

[5] Odd M Faltinsen. A nonlinear theory of sloshing in rectangular tanks. *Journal of Ship Research*, 18:224–241, 1974.

[6] Odd M Faltinsen, Olav F Rognebakke, and Alexander N Timokha. Resonant three-dimensional nonlinear sloshing in a square-base basin. *Journal of Fluid Mechanics*, 487:1–42, 2003.

[7] Odd M. Faltinsen and Alexander N. Timokha. Asymptotic modal approximation of nonlinear resonant sloshing in a rectangular tank with small fluid depth. *Journal of Fluid Mechanics*, 470:319–357, 2002.

[8] G Gaillarde, A Ledoux, and M Lynch. Coupling between LNG and vessels motion for partially filled tanks: Effect on seakeeping. In *Royal Institution of Naval Architects: Design and Operation of Gas Carriers*, 2004.

[9] Bernhard Godderidge, Mingyi Tan, and Stephen Turnock. CFD simulation of sloshing. Ship Science Report (To be published), University of Southampton, 2006.

[10] E W Graham and A M Rodriguez. The characteristics of fuel motion which affect airplane dynamics. *Journal of Applied Mechanics*, September:381–388, 1952.

[11] I Hadzic, Frank Mallon, and M Peric. Numerical simulation of sloshing. Technical report, Technische Universitt Hamburg-Harburg, 2002.

[12] Munehiko Hinatsu. Experiments of two-phase flows for the joint research. In *Proceedings of SRI-TUHH mini-Workshop on Numerical Simulation of Two-Phase Flows*. National Maritime Research Institute & Technische Universität Hamburg-Harburg, NMRI, 2001.

[13] Raouf A Ibrahim. *Liquid Sloshing Dynamics*. Cambridge University Press, 2005.

[14] Raouf A Ibrahim and V N Pilipchuk. Recent advances in liquid sloshing dynamics. *Applied Mechanics Review*, 54:133–199, 2001.

[15] James T Jensen. LNG and pipeline economics. In *The Geopolitics of Gas Meeting*, 2002.

[16] Yonghwan Kim. Coupled analysis of ship motions and sloshing flows. Technical report, American Bureau of Shipping, 2001.

[17] Harald Olsen. What is sloshing? In *Seminar on Liquid Sloshing*. Det Norske Veritas, 1976.

[18] Shin Hyung Rhee. Unstructured grid based reynolds-averaged navier-stokes method for liquid tank sloshing. *Transactions of the American Society of Mechanical Engineers*, 127:572–582, 2005.

[19] Dolly Robinson. Horizons. Lloyds Register, December 2004. LR Newsletter.

[20] Charles G Speziale, Sutanu Sarkar, and Thomas B Gatsi. Modelling the pressure-strain correlation of turbulence: An invariant dynamical systems approach. *Journal of Fluid Mechanics*, 227:245–272, 1991.

[21] ABS Technical Staff. Dynamic strength analysis of membrane type LNG containment system due to sloshing impact load. Technical report, American Bureau of Shipping, 2004.

[22] R G Standing, S Amaratunga, F Lopez-Calleja, S Orme, and R Eichaker. Marine hydrodynamics modelling using CFD. In *CFD 2003: Computational Fluid Dymamics Technology in Ship Hydrodynamics*, 2003.

[23] WS Atkins Consultants. MARNET best practice guidelines for marine applications of computational fluid dynamics. Technical report, MARNET, 2003.

Wave-Body Interaction Experiments for Validation of CFD method on Strongly Nonlinear Problems

Changhong HU and Masashi KASHIWAGI
RIAM, Kyushu University, Kasuga Fukuoka 816-8580, Japan
Email: hu@riam.kyushu-u.ac.jp

1. INTRODUCTION

The goal of the current research is to develop an efficient and robust CFD method for Strongly nonlinear seakeeping problems such as ship motions in large-amplitude waves, resultant slamming on ship's bottom and flare, the green-water impact on deck, and so on. We considered a Cartesian grid approach for our method and let the CIP (Constraint Interpolation Profile, Yabe et al. 2001) be the base numerical scheme. Main features of the method can be summarized as (1) the use of a Cartesian grid covering the whole computation domain, (2) applying the CIP method in the flow solver for water and air, (3) a CIP-based interface capturing method for the free surface, and (4) a Cartesian grid method for calculation of body motions. Recently, the method has been given a code name of RIAM-CMEN (Research Institute for Applied Mechanics, Computation Method for Extremely Nonlinear hydrodynamics).

The wave-body interaction problem is treated by RIAM-CMEN as a multiphase problem, which includes a liquid phase (water), a gas phase (air) and a solid phase (floating body). The free surface and the body boundary are viewed as immersed interfaces in a stationary Cartesian grid. To recognize different phases we define a density function ϕ_m, in which m=1, 2, 3 denotes liquid, gas, and solid phase, respectively. The density function for each computational cell has the relation of $\sum \phi_m = 1.0$ and follows the equation:

$$\frac{\partial \phi_m}{\partial t} + u_i \frac{\partial \phi_m}{\partial x_i} = 0 \tag{1}$$

The flow solver deals with an unsteady, viscous and incompressible flow for water and air. The governing equations are the incompressible continuity equation and Navier-Stokes equations. Numerical calculation of the Navier-Stokes equations is performed by a fractional step method in which the equations are divided into one advection step and two non-advection steps. In the advection calculation step, time evaluation is done by the CIP scheme. The pressure is treated in a following non-advection calculation step, in which a Poisson equation for the pressure is solved by an iterative method. The pressure equation is assumed valid for liquid, gas and solid phase. Solution of it gives the pressure distribution over the whole computation domain. The pressure distribution obtained inside the solid body is a fictitious one, which satisfies the divergence free condition of the velocity field. The boundary condition for pressure at the interface between different phases is not necessary, and a fast solver or parallel computing technique can be easily applied.

The free surface is determined in our method by solving Eq. (1) with a CIP based method for the density function of liquid ϕ_1. Numerical treatment is done to enhance the sharpness of the density function variation across the free surface. For the calculation of the solid-liquid or solid-gas interface, such as the floating body boundary, we only consider the rigid body case. A Lagrangian method is developed to directly calculate the density function for the solid phase ϕ_3 and the local velocity of the body $\hat{U}_i^{n+1}$. In order to treat complicated

3-D bodies in an easy way, we use virtual particles to define the body surface. Fig. 1 shows a 2-D example. The pressure at these particles is calculated by interpolation among the surrounding grid points. The hydrodynamic forces on the body can be obtained by integrating the elementary forces on those particles. The translational and rotational velocities at the gravity center of the rigid body are calculated and the position of the particles and the velocity at these particles for new time step are therefore obtained. Then the velocity at the body boundary cell $\hat{U}_i^{n+1}$, which is used to modify the flow field, can be calculated by using the velocities at these particles.

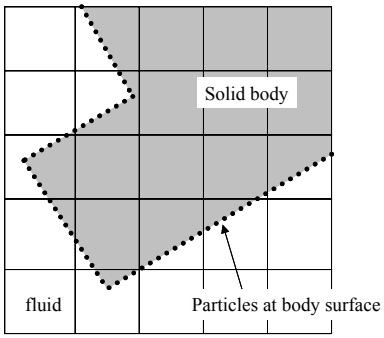

Fig.1 Body surface represented by distributing virtual particles

Numerical simulations on many strongly nonlinear wave-body interaction problems by RIAM-CMEN have been carried out (Hu and Kashiwagi, 2004, Hu et al., 2006). Quantitative assessment of the code by comparing to the experiment was done at the same time. However, as very few experimental data are available in public resources on such strongly nonlinear problem, we have also done a series of experiments on both 2-D and 3-D problems in RIAM for the purpose of CFD code validation.

In the experiments, we focused on the strongly nonlinear wave-body interaction problems. By strongly nonlinear we mean the floating body performs large amplitude motion in large incident waves, in which slamming and water on deck phenomena may occur. We consider that such strongly nonlinear phenomena may have an important effect to the global hydrodynamic behaviors of the floating body.

The 2-D experiment was performed in a small wave channel. A rectangular floating body model with a box type upstructure installed on the deck was used for the experiment. Heave, roll and sway of the floating body and the wave elevation were measured in the experiment. The variation of the free surface was recorded by a high-speed digital video camera. In the 3-D experiment, a modified Wigley type ship model with an upstructure installed on the deck was used. The ship model was towed at a constant speed in head waves and both motion-fixed and motion-free conditions were tested. The measurement includes the motion of the ship model, the green water impact pressures on the deck and the upstructure. The free surface variations around the bow area were also recorded by a high-speed digital camera.

In this extended abstract, details about experiments are described. One 3-D example of comparison between the computation and the experiment is then presented.

2. EXPERIMENT

2.1. 2-D Experiment

The experiment was performed in a two dimensional wave channel (10*m* long, 0.3*m* wide and 0.4 *m* deep) at RIAM, Kyushu University. As shown in Fig. 2 and Fig. 3, the floating body model used for the experiment is of 0.5*m* in length, 0.10*m* in depth, and 0.023*m* in freeboard. The model width is 0.29*m*, slightly smaller than the width of the wave channel. A box type upstructure is installed on the deck. More details of the floating body are shown in Table 1. The incident waves are generated by a plunger-type wave maker. A wave-absorbing apparatus installed at the other end of the wave channel was actuated. This implies that the wave reflection may occur

between the wave maker and the floating body, but transmitted waves past the body may be absorbed.

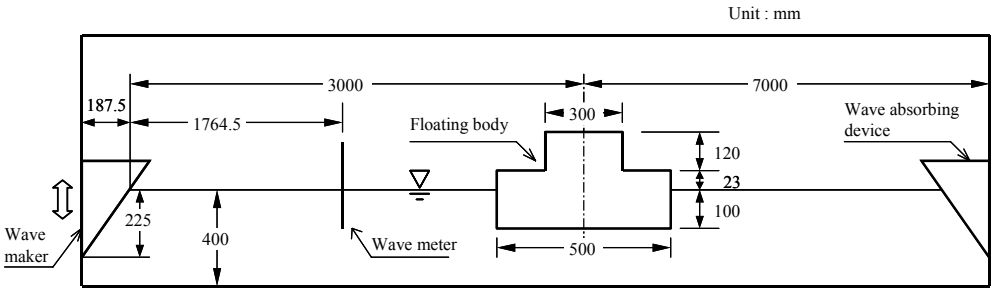

Fig. 2 Experimental setup for 2-D problem

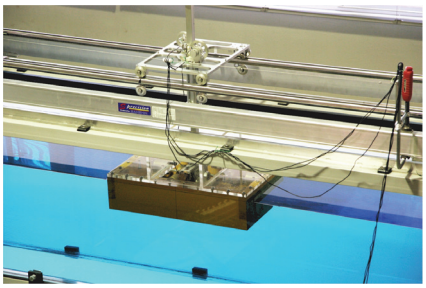

Fig. 3 Photo of 2-D floating body model

In the experiment for wave-body interactions, we measured the forced motion of wave maker, the free motions in heave, roll, and sway of the floating body, and the wave elevation at a point between the wave maker and the floating body. The heave and roll motions of floating body were free, while the sway motion was either fixed or weakly restrained by a spring with a spring constant of 7.6 N/m^2.

In addition to the above experiment, a forced oscillation test in heave was also carried out using the same floating body. The hydrodynamic force (added mass and damping) coefficients are obtained to check the accuracy of the present calculation method.

The contents of the 2-D experiments are shown in Table 2. In the table, $Kb = 0.5\omega^2 B/g$, A is the amplitude of the forced oscillation, T_W and y_{WA} are the period and the amplitude of the wave maker motion, respectively. Here B stands for the length of floating body, g the acceleration of gravity.

Table 1 Data of the 2-D floating body

Parameter	Value
Displacement	14.5 *kg*
Mass center from the bottom	0.079 *m*
Radius of moment of inertia	0.1457 *m*

Table 2 Contents of 2-D experiment

Forced oscillation in heave	
Kb	0.5 ~ 2.5
A (mm)	5, 10
Wave-body interaction	
T_w (s)	0.70, 0.85, 1.00, 1.15, 1.50
y_{WA} (mm)	15, 25

2.2. 3-D Experiment

The 3-D experiments were conducted in the towing tank (65m long, 5m wide, and 7m deep) at RIAM, Kyushu University. The ship model used in the experiments is a modified Wigley model which is of mathematical form represented by

$$\eta = \left(1-\zeta^2\right)\left(1-\xi^2\right)\left(1+a_2\xi^2+a_4\xi^4\right)+\zeta^2\left(1-\zeta^8\right)\left(1-\xi^2\right)^4 \tag{2}$$

where $\xi = 2x/L$, $\eta = 2y/B$ and $\zeta = z/d$. L, B and d stand for the length, breadth and draft, respectively. The

bluntness parameters, a_2 and a_4, are chosen as $a_2 = 0.6$ and $a_4 = 1.0$.

Figure 4 is a photo of this modified Wigley model set in the towing tank. As shown in this photo, a vertical wall is installed on the deck of the ship model to block the inflow of green water. The principle dimensions of the ship model are shown in Table 3. Three drafts are used: standard (0.175m), deep (0.205m) and light (0.175m).

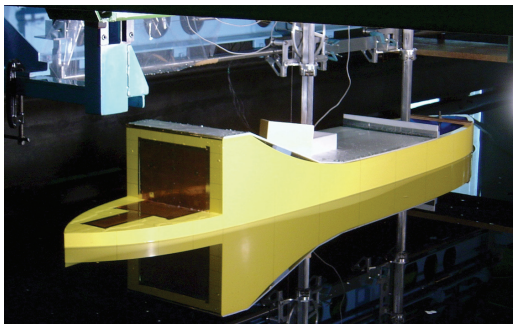

Fig. 4 Photo of the ship model in the towing tank

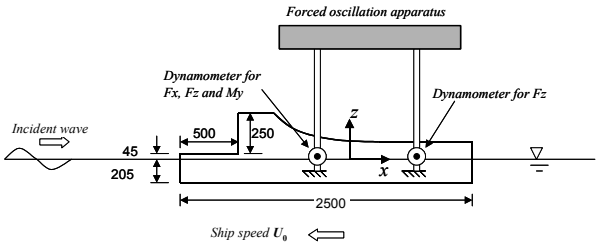

Fig. 5 Setup for motion-fixed experiment

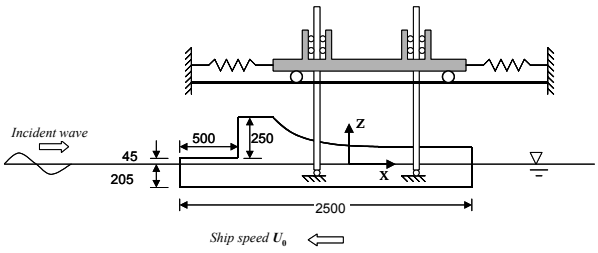

Fig. 6 Setup for motion free experiment

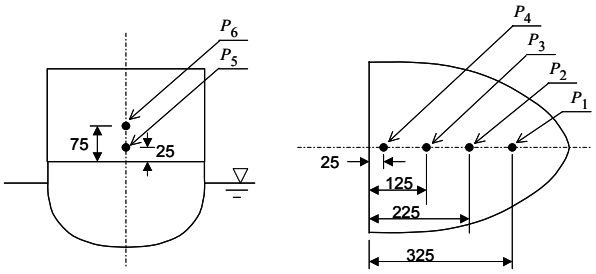

Fig. 7 Pressure measurement points

Experiments are conducted for both motion-fixed and motion-free conditions. Three drafts are considered. The experimental setup is shown in Fig. 5 for the motion-fixed case and in Fig. 6 for the motion-free case, respectively. For motion-free case, the surge motion is restrained by a strong spring with the spring constant of 2800N/m. There are six pressure gauges installed on the horizontal deck and the vertical wall, which are shown in Fig. 7.

In the experiment, the pressures induced by the green water at the six points are measured and the free-surface profile is recorded by a high-speed digital video camera. For the motion-fixed case, the force and moment acting on the ship model, while for the motion-free case, the motions of the ship (surge, heave and pitch) are measured, respectively. Regular plane progressive waves of three different wavelengths were generated as incoming head waves, the period and steepness of which are shown in Table 4. In each incident wave, the ship model was towed at three different forward speeds shown in Table 4. For each case experiment has been repeated twice. To check repeatability of the measurement, some motion-fixed cases are carried out for 5 times.

Table 3 Principal dimensions of the ship model

Length $L(m)$		2.5	
Breadth B (m)		0.5	
Draft d (m)	0.205	0.175	0.125
Free board f (m)	0.045	0.075	0.125
Displacement W (kg)	168.77	138.77	89.21
Moment of inertia in pitch I_{y} (kgm)	62.85	57.55	42.97

Table 4 Experiment conditions

Incident waves			
T (s)	1.096	1.266	1.415
λ/L	0.75	1.0	1.25
H/λ	0.064	0.052	0.045
Forward speeds			
U_0 (m/s)	0	0.7425	0.9899
Fn	0	0.15	0.2

3 Comparison of RIAM-CMEN Computation and 3-D Experiment

Numerical computations by RIAM-CMEN corresponding to the 3-D experiments were performed in a numerical wave tank schematically shown in Fig. 8. The example shown here is a motion-free case at light draft. The incident wave is of $\lambda/L = 1.0,\ H/\lambda = 1/20$ and the Froude number based on the ship forward speed is $Fn = 0.15$.

A non-uniform grid of $165 \times 80 \times 100$ in the x-, y-, and z-axes, respectively is employed for this numerical wave tank, where the minimum grid spacing was $\Delta x = 0.006L$ near the ship bow and $\Delta y = \Delta z = 0.005L$ near the ship hull and free surface. The time step size was taken equal to $\Delta t/T_w = 2000$, where T_{w} is the period of the incident wave. In Fig. 9, the pitch and heave of the ship model, and in Fig. 10, the pressures measured at $P_1 \sim P_5$ are compared, respectively. The computed pitch and heave agree well to the experiment. For the pressures, the computed values are generally lower than the measurements. In Fig. 11, we compare the experimental photos and the computed images, in which T_{e} stands for the encounter period. In computed results, the overall characteristics seem to be simulated well, but details of the flow are different between the experiment and computation; which can be attributed to lack of resolution in the numerical computation.

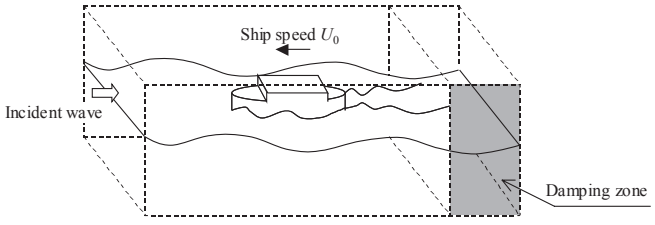

Fig. 8 Numerical wave tank for RIAM-CMEN

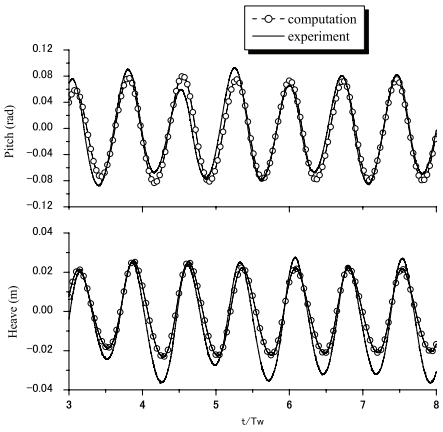

Fig. 9 Comparison of ship motions

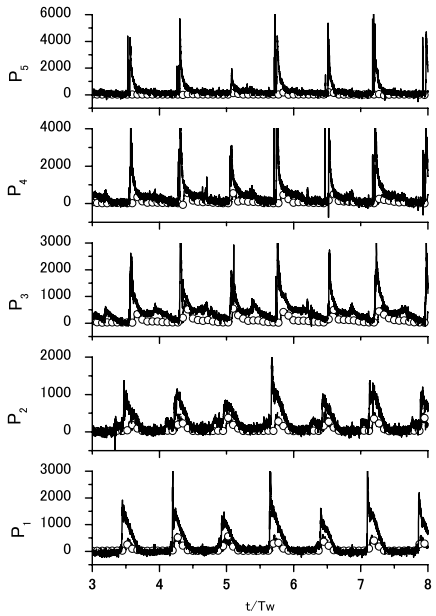

Fig. 10 Comparison of pressures at five measuring points

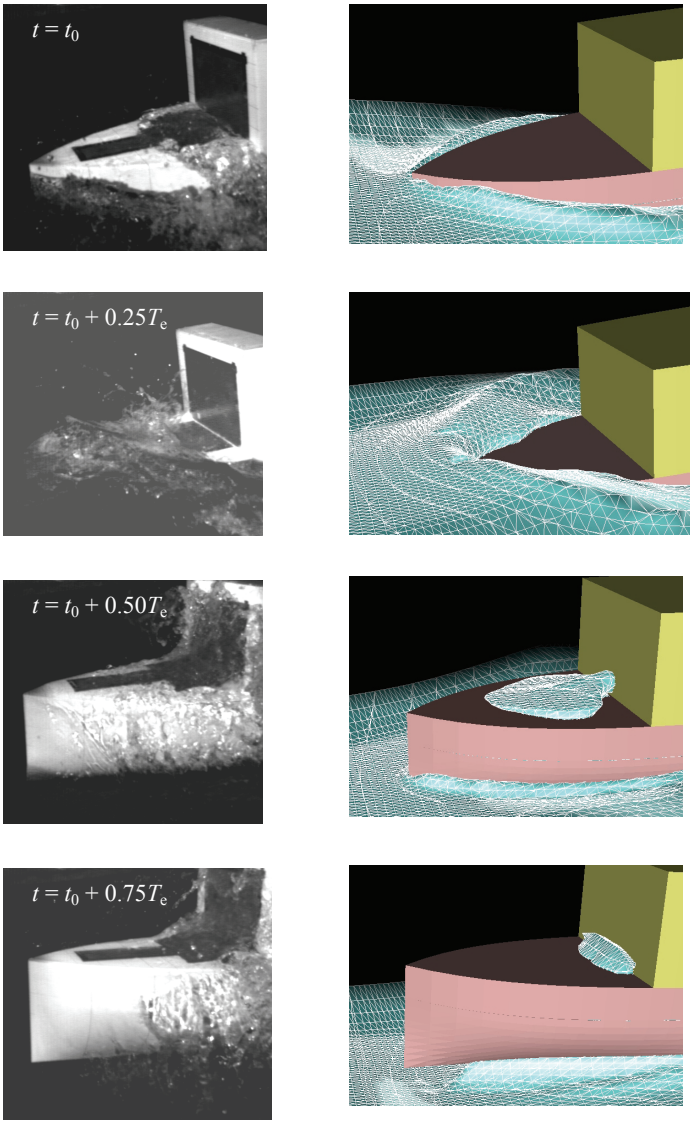

Fig. 11 Comparison of free surface profiles

REFERENCES

Yabe, T, Xiao, F and Utsumi, T (2001). The Constrained Interpolation Profile Method for Multiphase Analysis, J. Comput. Phys., 169, 556-593

Hu, CH, and Kashiwagi, M, (2004). A CIP-Based Method for Numerical Simulations of Violent Free Surface Flows, Journal of Marine Science and Technology, 9, 143-157

Hu, CH, Kashiwagi, M, Kishev, Z, Sueyoshi, M and Faltinsen, O (2006). Application of CIP Method for Strongly Nonlinear Marine Hydrodynamics, Ship Technology Research, 53 (2), pp 74-87.

Ship Dynamic Simulation, Based on a Three-Dimensional Viscous Free Surface Flow Solver

E. Jahanbakhsh, R. Panahi and M.S. Seif
Marine Lab., Dept. of Mechanics, Sharif University of Technology, Tehran, Iran
seif@sharif.edu

1- Introduction

Optimization procedures increasingly demand the performance of a ship to be assessed in its early design stage. This leads to a prediction tool independent of experimental results, although model tests will still be indispensable. CFD modeling based on numerical solution of the governing equations is a good choice. It must be remembered that, such a problem combines the complexity of free surface flow problem with the problem of rigid body motions.

In solving such a problem, one encounters to three subproblems which are: a) velocity and pressure distribution, b) free surface deformation and c) rigid body motion.

Solving the first two subproblems results in interfacial flow simulation. By computation of velocity and pressure distribution, tangential and normal stresses are calculated. Integration of such stresses over the body yeilds to forces and moments acting on it. Solving the last subproblem, in conjunction with such values, gives a time-history of body motions in one or two phases e.g. submarine maneuvering or ship dynamic. The important point is that, although potential theory methods [1] are capable of predicting motions with lower run time but they are not suitable where viscous effects, breaking waves or large amplitude motions play an important role. For many practically important cases, large errors are introduced by the potential theory assumptions.

The motion of a floating body is a direct consequence of the flow-induced forces acting on it while at the same time these forces are functions of the body movement itself. Therefore, the prediction of flow-induced body motion in viscous fluid is a challenging task and requires coupled solution of fluid flow and body motions. In recent two decades, with the changes in computer hardware, ship motion simulation is the subject of many numerical hydrodynamic researches. These researches were started from the restricted motions such as trim or sinkage by Miyata [2], Hochbaum [3] Alessandrini [4] and Kinoshita [5] and continiued to the evaluation of 6-DoF motions by Miyake [6], Azcueta [7], Vogt [8] and Xing [9].

In this paper, an appropriate numerical algorithm is described briefly and some applications of the developed software are presented. Comparisons of all test cases show the ability of the proposed procedure to be extended as a numerical hydrodynamic tank for full nonlinear ship motions simulation.

2- Formulations and Solution Algorithm

Here a finite volume time dependent three-dimensional viscous free surface flow solver is used [10]. Velocity and pressure fields are coupled using fractional step of Kim and Choi [11]. One must take into account the presence of high density ratio phases e.g. water and air in discretisation of pressure integral which is treated in a new way [10]. Also, a surface capturing method is used which solves a transport equation for calculation of fluids volume fraction. CICSAM interpolation has great advantages in comparison to other interpolations and used in this study [12]. There are a variety of motion simulation strategies in numerical hydrodynamic applications. Here, a body-attached mesh following the time history of body motions is used [7]. In other words, linear and angular momentum equations are solved in each time step which results in 6-DoF motions. Such motions are applied on body and computational domain simultaneously to make it ready for the next time step. It must be noted that, all of the fluid governing equations are written for a moving control volume in Newtonian Reference system [13] which results in using relative face velocity for flux calculation while keeps the simplicity of equations.

As mentioned earlier, one encounters three subproblems in CFD simulation of ship motions. These parts which are marked with dashed lines are solved in a loop as shown in Fig.1.

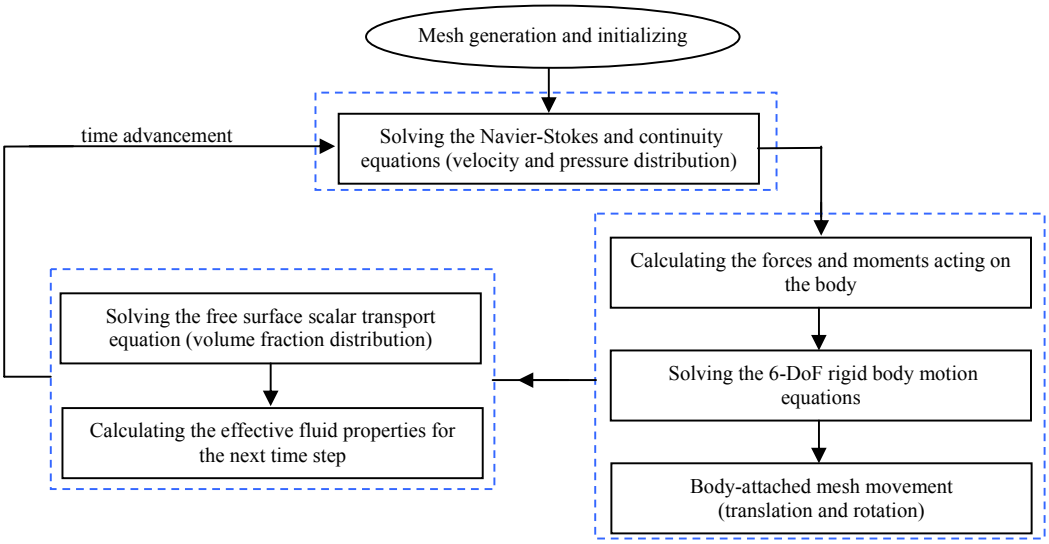

Fig.1: Solution algorithm

3- Numerical Results

3-1- Circular Cylinder Slamming

To evaluate the rigid body motion coupling with fluid flow, water entry of a circular cylinder is studied. The neutrally-buoyant circular cylinder and the computational grid of 18900 rectangular CVs are considered as shown in Fig.2. As Xing reported, use of such a rectangular grid plays a vital role in capturing the water spray [9]. The cylinder is released from a position just above the still water level and intersects the water surface with downward velocity of 4 m/s. Here, no-slip boundary condition at cylinder wall, zero value at down boundary and zero-gradient at other boundaries are applied on velocity. Also, zero-gradient condition is used for pressure at whole boundaries.

After the cylinder impacts on water surface, the velocity of cylinder is decreased significantly due to the effects of hydrodynamic forces and buoyancy. As shown in Fig.3 for three time instants, water spray is thrown up at each side of the cylinder and travel straight upward until they become unstable. Time history of vertical displacement and acceleration of the cylinder are also shown in Fig.4. The instantaneous vertical positions of the cylinder in Fig.4 are compared with experimental data of Greenhow [14] and numerical simulation of Xing [9]. The figure shows a reasonably good agreement between present study and experimental data in comparison to similar numerical results.

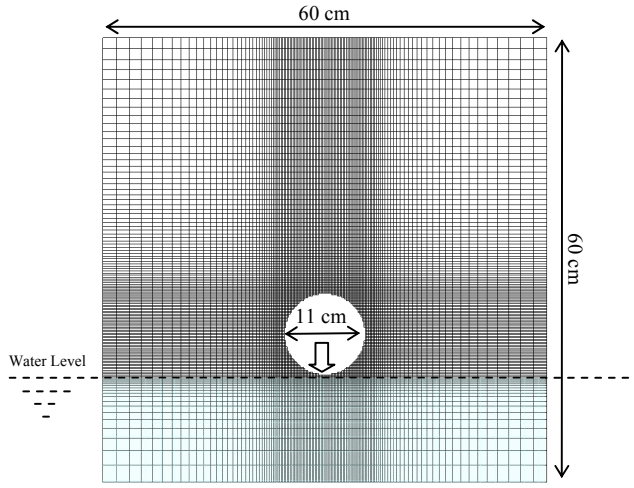

Fig.2: Geometry and computational grid of cylinder slamming

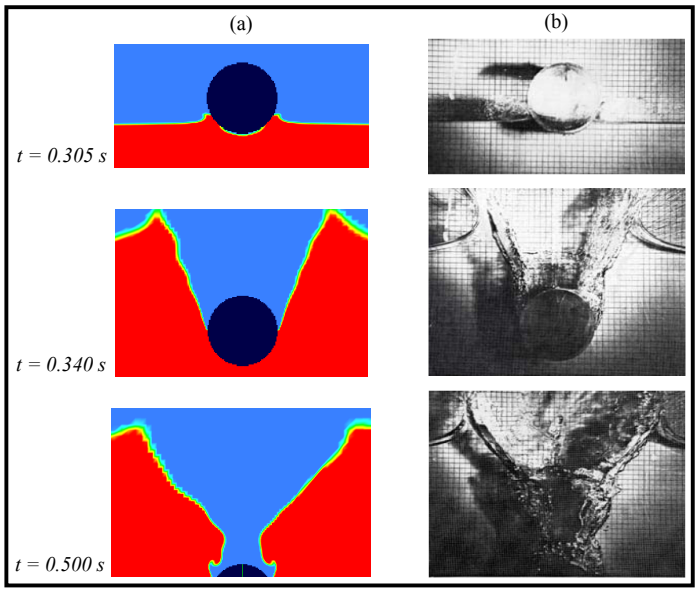

Fig.3: Free surface deformation in cylinder slamming; (a): simulation, (b): experiment [14]

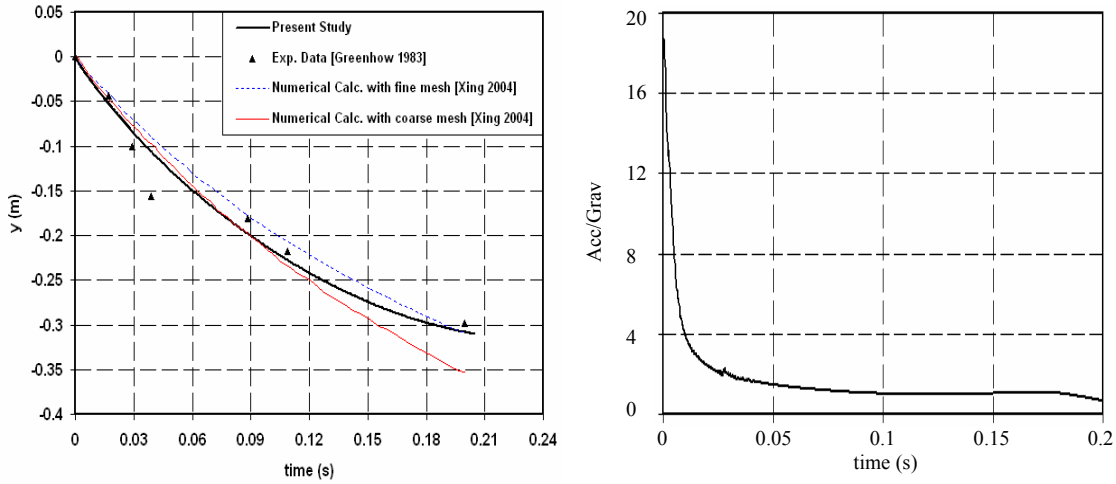

Fig.4: Time history of the vertical motion (left) and the normalized acceleration (right) during the cylinder water entry

3.2 Barge resistance

In numerical calculation, the model is usually considered with fixed trim and draft. But, draft and trim may change in moving conditions due to hydrodynamic effects. In order to show the importance of motion simulation -especially in ship resistance calculation- a barge ship is simulated in two cases of fixed and 2-DoF steady forward motion and the numerical results are compared with the experimental data. The barge model characteristics are shown in Fig.5 and Table 1. No-slip and zero-gradient boundary conditions are applied for velocity at wall and other boundaries, respectively. Also, zero-gradient boundary condition is used for pressure at all boundaries. In order to minimize the reflection of flow a damping zone is considered in outlet boundaries [15].

Experimental test is done at V=0.807 m/s in marine laboratory of Shrif University of Technology. Fig.6 shows the free surface deformation in front of barge which is of good agreement with experiment. This results in appropriate prediction of total resistance although it could be captured better with finer mesh.

In the case of 2-DoF motion, barge is free to heave and pitch and the resistance is calculated when two aforementioned motions reach constant positions. It must be noted that, many factors include in the accuracy of resistance calculation. But, for similarity the turbulence flow and grid resolution are considered similar in both fixed and 2-DoF cases. Taking these into account, the error relative to experimental result is decreased from 23.2 % in fixed condition into 5.9% in 2-DoF condition (Table 2).

In other words, since the model test is performed with free model (heave and pitch motions were not restricted), the numerical results in 2-DoF condition simulation is much better than fixed condition. This means that in usual numerical resistance we always have errors if we can not predict the moving condition (draft and trim) with good accuracy. But the present numerical method can find out moving conditions automatically which results in better estimation of resistance.

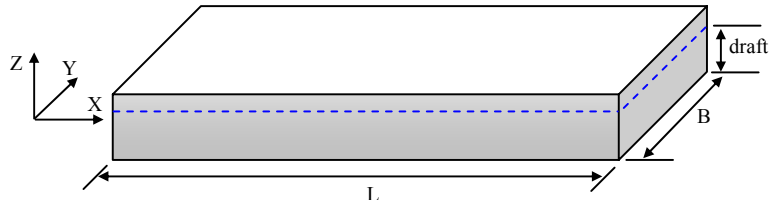

Fig.5: Barge ship geometry definitions

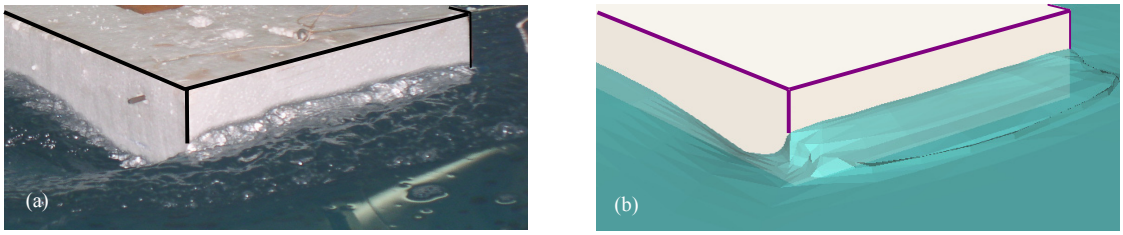

Fig.6: Free surface deformation in front of barge ship: (a): experiment, (b): simulation

Table 1: Barge ship characteristics

Characteristic	Value
L	1.05 m
B	0.29 m
draft	0.025 m
C_B	1.0
Mass	7.26 Kg
I_{YY}	0.7 Kg.m^2
KG	0.025 m

Table 2: Barge ship resistance

Resistance	Value (N)	Error (%)
Experiment Calculation	3.53 (N)	-
Numerical calculation in fixed motion	2.71 (N)	23.2%
Numerical calculation in 2-DoF motion	3.32 (N)	5.9%

3-3- Ship Turning

Turning maneuver is one of the important tests which introduces some essential factors of maneuverability and controllability for a ship. These parameters should be evaluated in early design stages. Here, turning of a barge-shape ship of Fig.5 and Table 3 is simulated with 3-DoF (Surge, Sway and Yaw). The computational domain has 35000 cells and boundary conditions are similar to previous test case. External forces and moments of Table 4 are exerted for 3 different rudder angle of dr = 5, 10 and 15 degrees. It should be noted that rudder assumed to come into action just after 10 second from the beginning of simulation. This permits the ship to reach a nearly steady forward motion due to propeller force.

Fig.8 shows the time history of ship speed in three rudder angles. The velocity magnitude increases gradually due to propeller force till tenth second and decreases when rudder activates. This continues until reaching a constant speed. It is obvious that, the difference between maximum and steady speed increases as rudder angles become larger. Path of ship center of gravity is shown in Fig.9. The turning circle and its diameter are decreased as rudder angle increased. Such behaviors are reasonable and qualitatively similar with experiment.

The turning velocity relative to approach velocity is plotted versus the non-dimensional turning diameter and compared with experimental data [16] in Fig.10. These diagrams indicate that speed reduction is a function of turning diameter and block coefficient. Fig.10 shows that computed results follow the tendency of existed experimental data appropriately. It must be mentioned that, in present study the propulsion force is assumed to be constant, which is in contrast with what is happened in real world. In fact, during the turning the angle between rudder's foil and flow direction changes resulting in propulsion force variation. In other hands, in lower turning diameters, the angle between the rudder and flow direction is bigger than the case of higher turning diameters. It seems that the deviation in the region of low turning diameter from which could be expected arises from such assumption.

Fig.11 shows five snapshots of ship turning. Free surface elevation contours are plotted only for first and last position. Flow velocity magnitude is also shown on ship body by different colors.

Table 3: Barge ship characteristics

L	3.0 m
B	0.75 m
T	0.25 m
C_B	1.0
Mass	562.5 Kg
I_{zz}	424.8 Kgm^2
KG	0.15 m

Table 4: External forces and moments

Propeller Force	278 (N)
Rudder Force Lateral	445 * dr (N)
Rudder Moment	445 * dr (N.m)

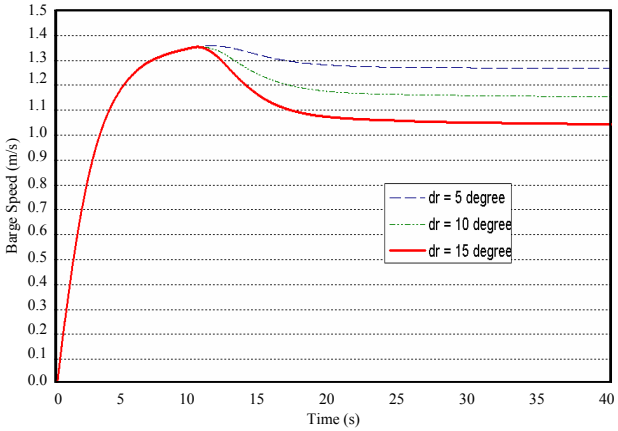

Fig.8. Time history of barge speed in three different rudder angles

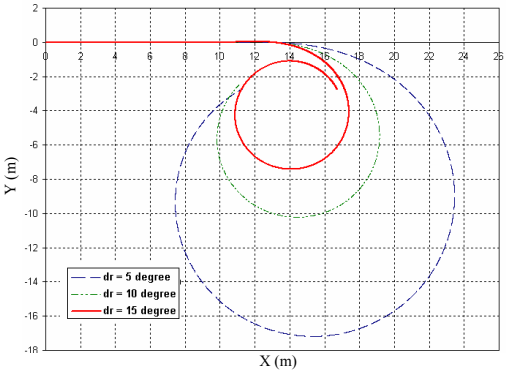

Fig.9. Ship mass center pass

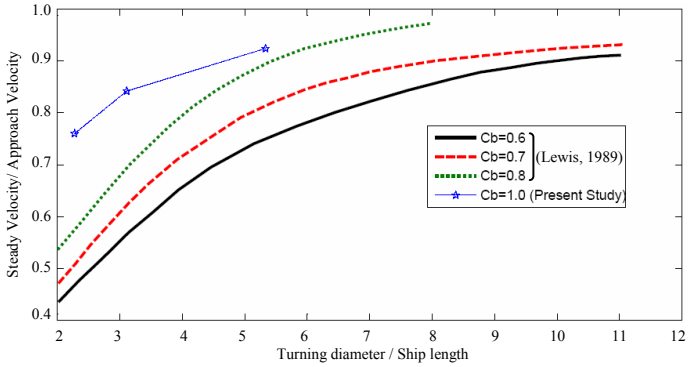

Fig.10. Speed reduction as a function of turning diameter and block coefficient

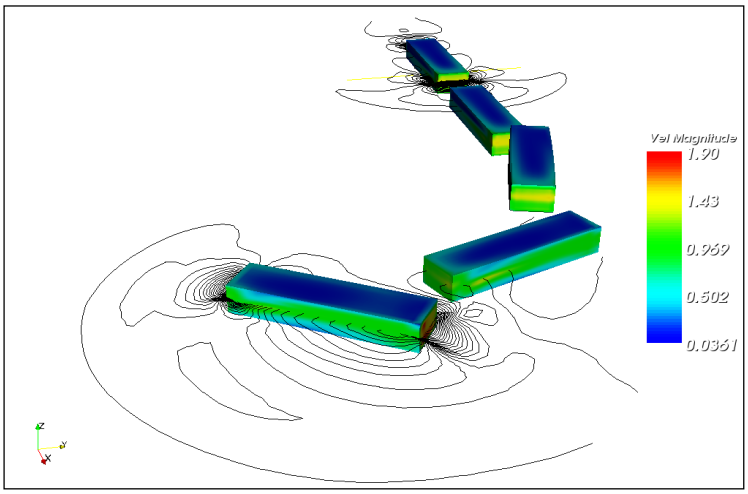

Fig.11. Barge ship turning simulation

4- Conclusion

The proposed numerical algorithm is capable of simulating different ship dynamic problems. Typical case studies are presented for slamming, resistance and maneuvering. Numerical results show good agreement with available data. As it is described in this and other recent papers by the authors, the developed computer software can be used for nonlinear fluid structure interactions. The method has no geometrical restriction and is applicable for usual ship body forms as well.

5- References

1- Bertram, V., *Practical ship hydrodynamics*, Butterworth-Heinemann, Oxford, (2000).

2- Miyata, H., Sato, T. and N. Babo, *Difference solution of a viscous flow with free-surface wave about an advancing ship*, J. Comput. Phys., Vol.72, p.393-421, (1987).

3- Hochbaum, C., A finite volume method for turbulent ship flows, Ship Technology Research Schiffstechnik, Hamburg, Germany, (1994).

4- Alessandrini, B. and Delhommeau, G., *Simulation of three-dimensional unsteady viscous free surface flow around a ship model*, Int. J. of Numerical Math. Fluids, Vol.19, p.321-342, (1994).

5- Kinoshita, T., Kagemoto, H. and Fujino, M., *A CFD application to wave-induced floating-body dynamics*, 7th Int. Conference on Numerical Ship Hydrodynamics, Nantes, France, (1999).

6- Miyake, R., Kinoshita, T. and Kagemoto, H., *Ship Motions and loads in large waves*, 23rd ONR Symp. On Naval Hydrodynamics, Val de Reuil, France, (2000).

7- Azcueta, R., *Computation of turbulent free surface flow around ships and floating bodies*, PhD Thesis, Teschnichen Universitat Hamburg-Harburg, (2001).

8- Vogt, M. and Hochbaum, C., *Numerical simulation of ship motions in head waves with a RANSE method*, HSVA Report 1649, Hamburg, Germany, (2002).

9- Xing-Kaeding, Y., *Unified approach to ship seakeeping and maneuvering by a RANSE method*, PhD Thesis, Teschnichen Universitat Hamburg-Harburg, (2004).

10- Jahanbakhsh, E., Panahi, R. and M.S. Seif, *Numerical Simulation of Three-Dimensional Interfacial Flows*, International Journal of Numerical Methods for Heat & Fluid Flow, accepted for publication, (2006).

11- D. Kim, and H. Choi, *A second-order time-accurate finite volume method for unsteady incompressible flow on hybrid unstructured grids*, J. of Comput. Phys., Vol.162, p.411-428, (2000).

12- Panahi, R., Jahanbakhsh, E. and Seif, M.S., *Effect of interpolation in interface capturing methods*, 8th Numerical Towing Tank Symposium (NuTTs), Varna, 2-4 October, (2005).

13- White, F.M., Fluid mechanics, Mc Graw-Hill, 4th Ed, (2001).

14- Greenhow, M. and Lin, W., *Nonlinear free surface effects: experiments and theory*, Report No. 83-19, Massachusette Institute of Technology, (1983).

15- Park, J.C. and Miyata, H., *Numerical Simulation of Fully-Nonlinear Wave Motions around Arctic and Offshore Structures*, J. Society of Naval Architects Japan, Vol.189, p.13-19, (2001).

16- Lewis, E. V., *Principle of Naval Architecture*, Second Revision, Vol. III, The Society of Naval Architectures and Marine Engineering, (1989).

Simplified RANSE simulation of the side launching

Marek Kraskowski

Ship Design and Research Centre S.A., Poland
marek.kraskowski@cto.gda.pl

In some of Polish shipyards, building small vessels like AHTS, fishing vessels and container feeders, side launching is the basic method of launching. Due to safety reasons, in some cases Ship Design and Research Centre S.A. is asked to perform the model tests of side launching to estimate the following parameters of the hull motion during the launching:

- Heel angles – too large heel angle causes the risk of capsize or hit the quay.
- Minimum distance between the cribbing of the hull and the bottom of the basin.

A series of such tests for 115m container ship were performed lately. On the other hand, a numerical method for solving the flow around moving bodies was successfully implemented by Ship Design and Research Centre S.A. – till now it was used for evaluating the flow around the ship hull free to trim and sink. Satisfactory results of these computations encouraged to try the numerical method for the prediction of hull motion during side launching, and the first attempt on such computations is presented here.

The flow solver COMET, extended with the user-programmed rigid body motion module, was used for the computations. The basic features of the simulation were as follows:

- The RANSE model of the flow and the finite volume method were applied.
- The VOF method was used to solve the free-surface flow.
- The dynamic mesh, moving rigidly together with the hull, was used to enable the motion of the hull.
- The forces obtained from the flow solver were used to solve the equations of motion.

Figure 1 presents the sketch of the modelled situation as well as the location of the global coordinate system XYZ (the X axis points from stern to bow).

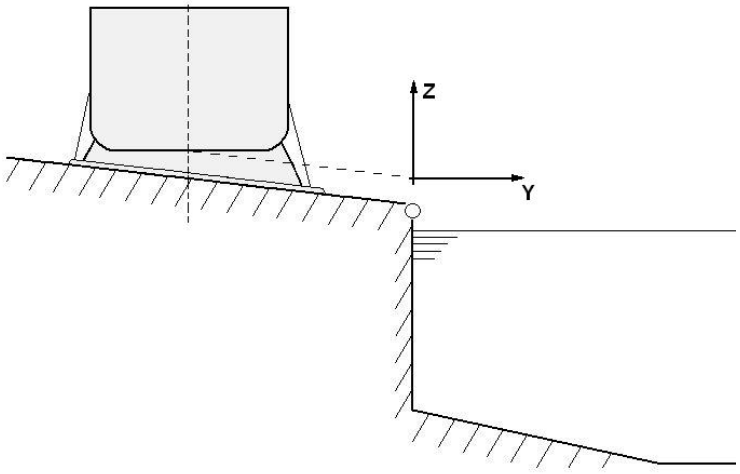

Fig. 1 Modelled situation.

Due to complexity of the problem, it was radically simplified in the first approach. The following assumptions were done:

- The presence of the quay was taken into account only as the constraint of the motion in the initial phase of the launching. Its influence of the flow was neglected.
- The geometry of the cribbing was greatly simplified – only the elements causing the largest damping of the rolling were considered.
- Only 3 degrees of freedom were considered in the model of motion. This dramatically simplifies the computer code for solving the motion.

Figure 2 presents the mechanical model of the motion.

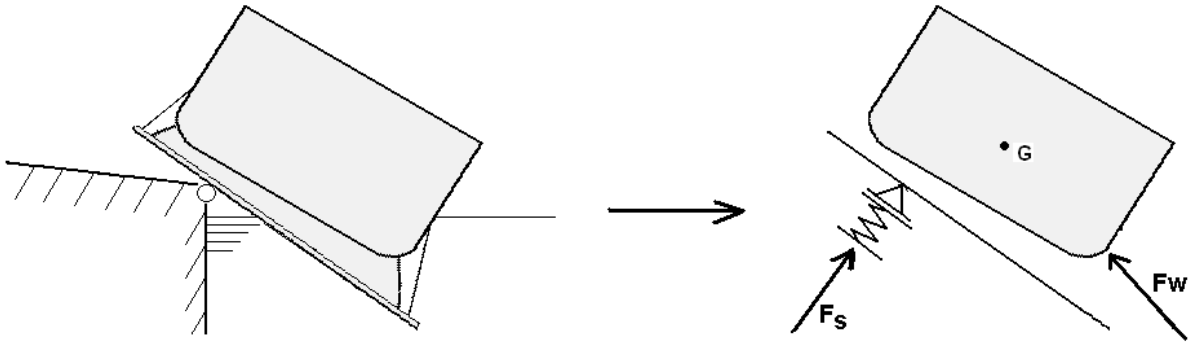

Fig. 2 Mechanical model of the motion.

As shown above, the slipway is modelled with the pivot bearing of finite stiffness.

The following denotations were used in figure 2:

- F_S : force exerted on the hull by the slipway.
- F_W : force exerted on the hull by the water.

Force F_W is obtained from the flow solver, and the force F_S is calculated by the rigid body motion module basing on the current location of the hull. Its location in the coordinate system connected with the slipway is fixed, and its direction is perpendicular to the skids. The value of this force is proportional to the deflection of the bearing.
The forces exerted by the slipway and the water are reduced to the gravity centre of the hull with cribbing, and thus they produce some moment M_X. The equations of the motion are solved for the gravity centre, so they can be written in the simplest form:

$$\frac{d^2Y}{dt^2} = \frac{F_Y}{m} \qquad \frac{d^2Z}{dt^2} = \frac{F_Z}{m} \qquad \frac{d^2\varphi}{dt^2} = \frac{M_X}{I_X}$$

where φ is the angle of heel.

The following initial conditions were applied:

- Location of the hull: the gravity centre of the hull is located directly above the end of the slipway.
- Initial velocity was taken from the model test.

(it was assumed that it is possible to estimate the hull velocity in this location correctly and thus it is not necessary to solve the motion from the moment of release).

Numerical integration of these equations is realized with the use of the explicit scheme. The algorithm of the motion computations can thus be described in the following way:

1. Compute the displacements in Y and Z direction using the initial velocity components:

   $$\Delta Y = V_{0Y} \cdot \Delta t \qquad \Delta Z = V_{0Z} \cdot \Delta t$$

   Compute the flow for the new location of the hull.
   Compute the force exerted by the water and the reaction of the slipway (basing on the deflection of the bearing).

2. Compute the translational and angular acceleration basing on the old values of forces:

$$a_Y = \frac{F_{Yold}}{m} \qquad a_Z = \frac{F_{Zold}}{m} \qquad \varepsilon_X = \frac{M_{Xold}}{I_X}$$

Compute new values of velocity:

$$V_Y = V_{Yold} + a_Y \cdot \Delta t \qquad V_Z = V_{Zold} + a_Z \cdot \Delta t \qquad \omega_X = \omega_{Xold} + \varepsilon_{Xold} \cdot \Delta t$$

Compute the displacements:

$$\Delta Y = V_Y \cdot \Delta t \qquad \Delta Z = V_Z \cdot \Delta t \qquad \Delta \varphi = \omega_X \cdot \Delta t$$

Compute the deflection of the bearing and its reaction.

Compute the force exerted by the water. Average the water forces using the values from the current and old time step:

$$F_{Yw} = 0.5\left(F_{Yw} + F_{Yw\_old}\right) \qquad F_{Zw} = 0.5\left(F_{Zw} + F_{Zw\_old}\right)$$
$$M_{Xw} = 0.5\left(M_{Xw} + M_{Xw\_old}\right)$$

Note: averaging the water forces in two time steps turned out to be necessary to assure the stability of the computations. On the other hand, this procedure must not be applied to the slipway forces – this would produce increasing oscillations of the hull sliding on the bearing. Each component of the force is thus computed as follows:

$$F = F_s + 0.5\left(F_w + F_{w\_old}\right)$$

3. Repeat step 2 until desired time of simulation is reached.

As mentioned above, the numerical mesh is moving as a rigid body together with the hull – there is no relative motion between the nodes of the mesh. The idea of the computations with the dynamic mesh is presented in figure 3.

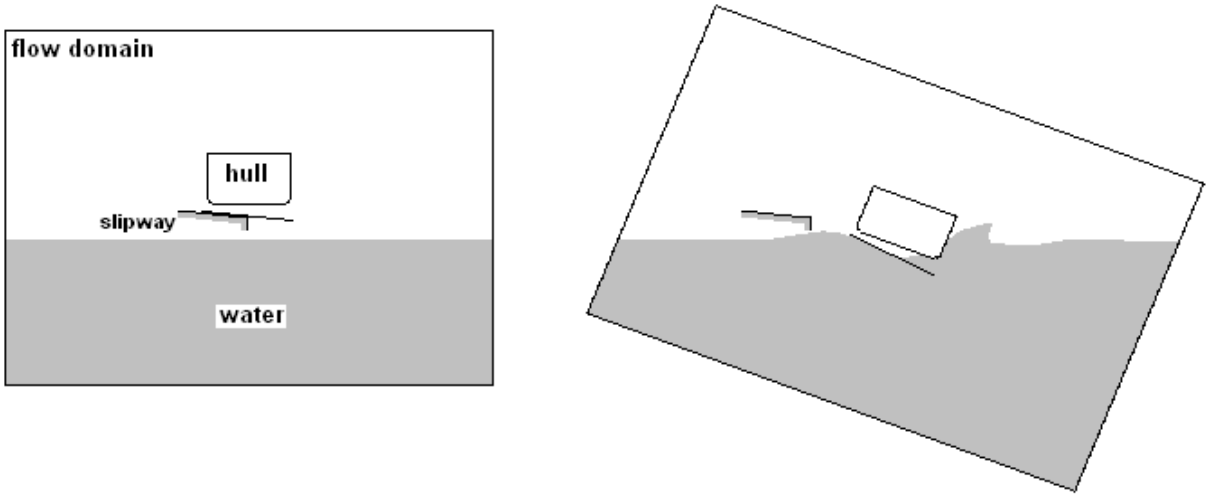

Fig. 3 Idea of the computations with the dynamic mesh.

The slipway geometry is not taken into account in the mesh, its presence is only considered in the motion model by adding its reaction to the motion equations. In figure 3, the slipway is drawn to make the sketch clearer.

The flow in the moving domain was solved with the following settings:
- Time step was set to 0.001s.
- Five iterations per time step were executed.
- The discretization scheme for the convective terms in momentum equations was Second Order Central, blended with First Order Upwind with the blending factor 0.8.
- Low under-relaxation of the velocity was applied, as the time-accurate results are required.

Before performing the simulation of the hull launching, a 2D test case was computed in order to check the correctness of the user-coding.
The boundary conditions were:
- Hydrostatic pressure on the boundaries of the domain.
- No-slip wall condition on the hull and the parts of the cribbing.

The proposed method turned out to be robust and the obtained motion of the hull section in water was looking physically.

The figures below show the example results in two chosen time points of simulation.

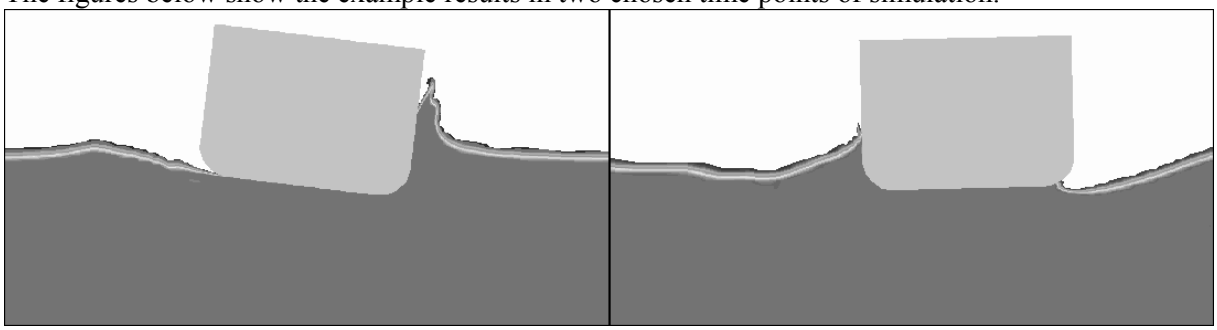

Fig. 4 Results for 2D test case.

After obtaining qualitatively correct results of the 2D analysis, the mesh for 3D hull with simplified cribbing was generated. It was a block-structured, hexahedral mesh containing about 1 million cells, and it was generated with ICEM CFD HEXA.
The range of the domain dimensions, in the ship coordinate system, was:
- X: $\boldsymbol{-L \div 2L}$ ($\boldsymbol{L}$ is the hull length)
- Y: $\boldsymbol{-L \div L}$
- Z: $\boldsymbol{-L \div 0.6L}$

Figure shows the surface mesh on the hull with parts of the cribbing and chosen sections of the mesh interior.

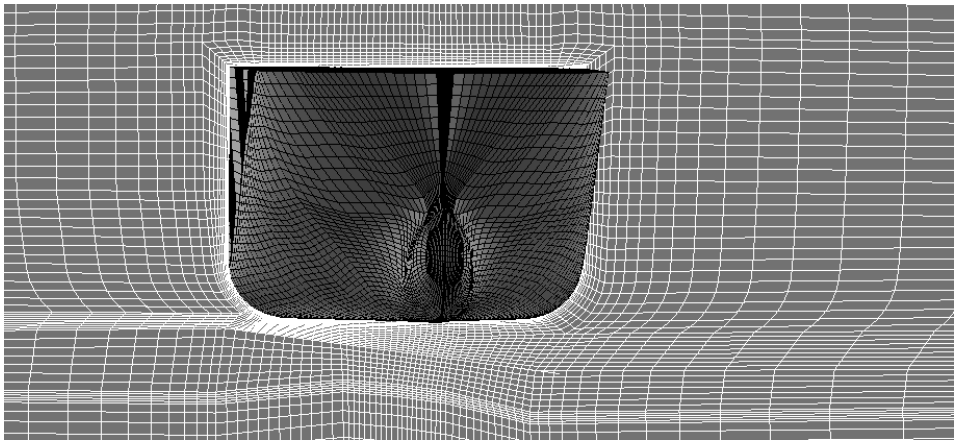

Fig. 5 Mesh for the ship.

As can be seen above, the mesh of 1 million cells, covering both sides of the hull and large space above the hull, is quite coarse. It is not refined in any particular horizontal plane, as the location of the free surface changes rapidly during the simulation.

The simulation was carried out for model scale 1:40 in order to enable the direct comparison of the results.

The figures below show the example results in two chosen time points of the 3D simulation.

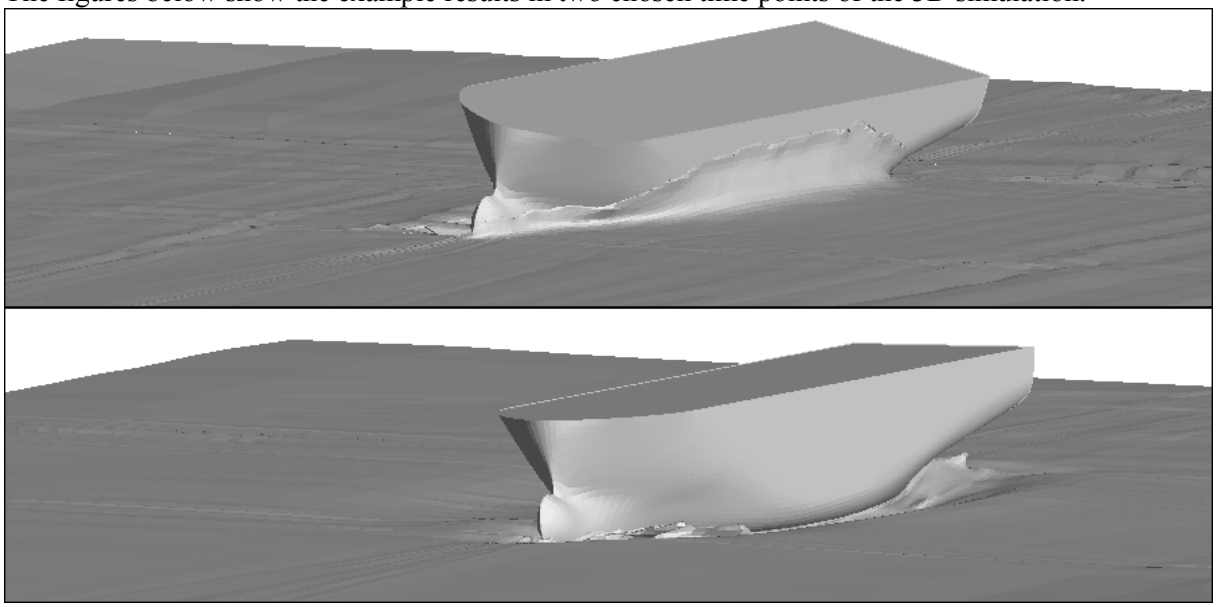

Fig. 6 Example results

Figure 8 shows the comparison of the computed and measured trajectory of two characteristic points, shown in figure.

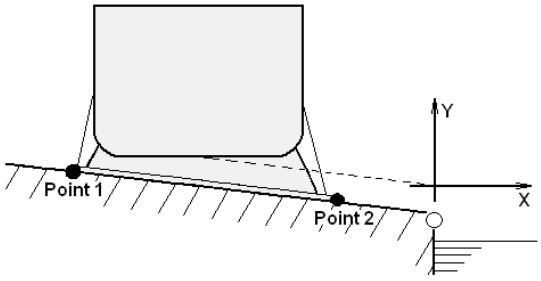

Fig. 7 Definition of the coordinate system.

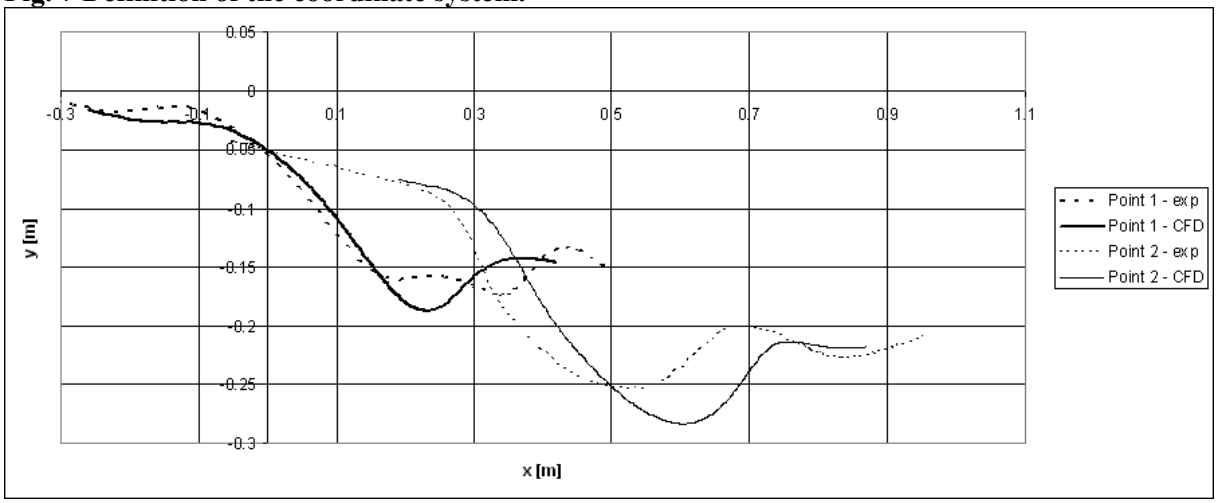

Fig. 8 Comparison of the computed and measured trajectory.

The following figure presents the heel angle as a function of time. The first and second maximum of the heel angle are most important for the safety of launching.

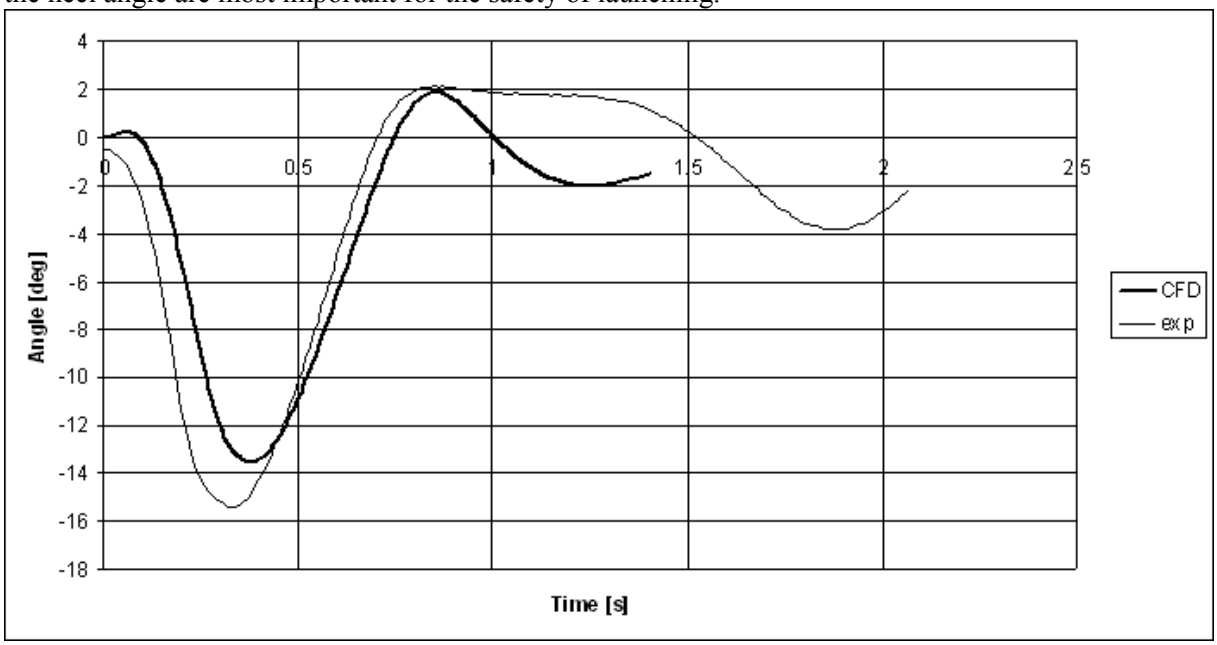

Fig. 9 Comparison of the computed and measured heel angle.

Comparison of the CFD results with the experiment yields the following conclusions:

- The rotation of the hull around the edge of the slipway in the simulation, compared to the experiment, is delayed, which means that the applied model of motion introduces some unphysical inertia and has to be improved.
- Qualitative comparison of the trajectories and heel angles shows that the restoring forces and damping forces are modelled quite correctly despite the coarseness of the mesh, which shows in the comparison of the computed and measured heel angles (up to ~ 0.8 s).
- For the simulation time larger than 0.8 s, large divergence is observed between the computation and the experiment, and this is probably due to the neglect of the quay in the simulation – after that time the wave reflecting from the quay starts to influence the hull motion.
- Although the first results are not accurate enough at the moment, it seems that improving the mechanical model and increasing the mesh resolution can produce an usable method for the prediction of the very initial stage of side launching, and this stage is the most important for the safety.

A Procedure for Hydrodynamic Shape Optimization Using RANSE Solver

Stefan Kyulevcheliev, Bulgarian Ship Hydrodynamics Centre, stefan.q@bshc.bg

1. Introduction

The most popular modern methods for hydrodynamic shape optimization using RANSE require or are more readily applicable with having an access to the CFD source code. This access is needed for easier integration of the solver in the relevant optimization chain as a called external function, or for calculating the flow sensitivities – either directly or in an adjoint way. The latter is not so easy even having the source code, which has led to development and application of automatic differentiation (AD) software.

The situation of interest to the author is the use of a commercial CFD code for hydrodynamic shape optimization. In that case we neither have the source code nor is the solver easily callable from an outside optimization procedure.

Hence, the objective of the work presented here has been a feasibility study on an economic procedure for hydrodynamic shape optimization based on and integrated in the commercial CFD solver FLUENT.

2. Outlines of the optimization procedure based on Fluent

Most generally speaking, the basic elements or steps of every hydrodynamic optimization cycle are:

- a flow solver;
- evaluation of the objective function and (optionally) its gradients;
- shape deformation and mesh movement.

FLUENT, as all state-of-the-art commercial CFD products, provides these functions. The task then remains to organize them in an optimization procedure filling in the missing elements by means of user-defined functions (UDF) – Fig. 1.

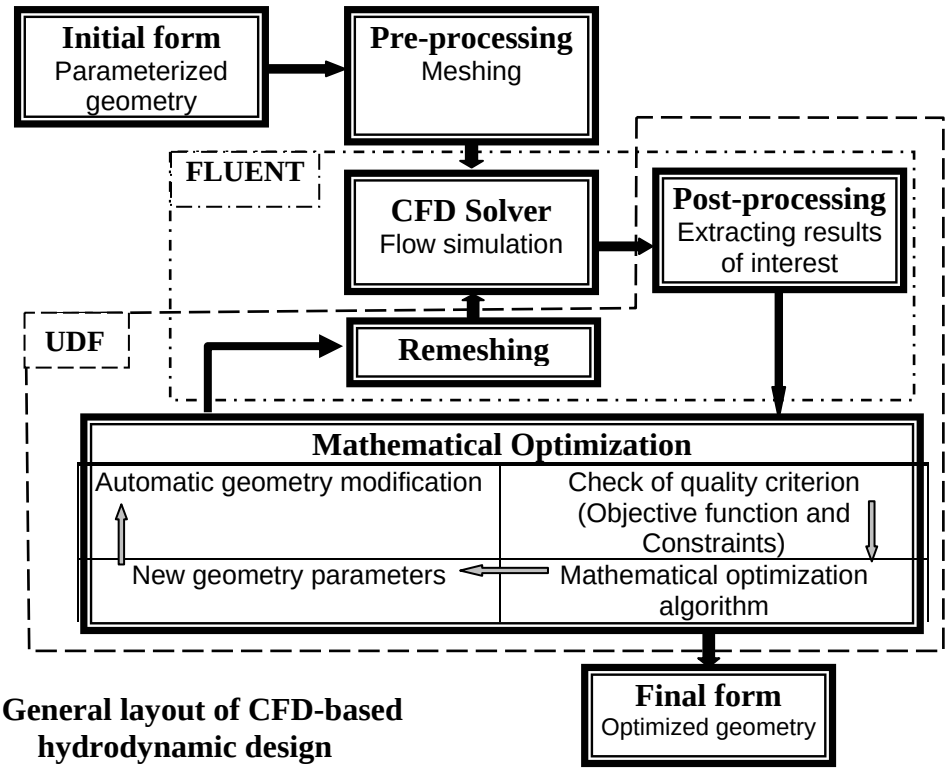

Fig. 1. General layout of CFD-based hydrodynamic design

The most specific task in the cycle – the dynamic mesh feature –works in Fluent only with the unsteady solver. Since we are aimed at shape optimization in a steady flow, at first sight this circumstance looks like an obstruction. It can be utilized, however, by replacing the time steps with optimization iterations, i.e. decide on and perform shape and mesh deformation at each time step.

The problem with this is that we apply a deformation acceleration, which will give rise to an inertial hydrodynamic force (that we normally account for with the added mass concept). Since we are not interested in the dynamics of the process it is necessary to eliminate that effect. One way to do so is, after each time step involving a deformation, to do several time steps without any deformation waiting for the flow to steady up. Another idea would be to make very large time steps. With the normally very small deformations at each step this will result in negligible accelerations and inertial forces.

These two options have been tested by calculations with a foil section subjected to symmetrical bending at every fifth time step with the interim four steps of no deformation. The chord length of the foil has been 1 m and the maximum bending deflection 0.5 mm. Four different values for the time step have been tried: 0.1 s, 1 s, 10 s. Fig. 2 shows the results for the lift coefficient variation during two series of deformation. It can be seen that with the two shortest time steps the values jump at first but do tend to converge with the next “steady” time steps. With the longest time step already at the first step the value is close to the convergence value. So the option of making only one long time step per deformation has been adopted in the procedure as being more economical.

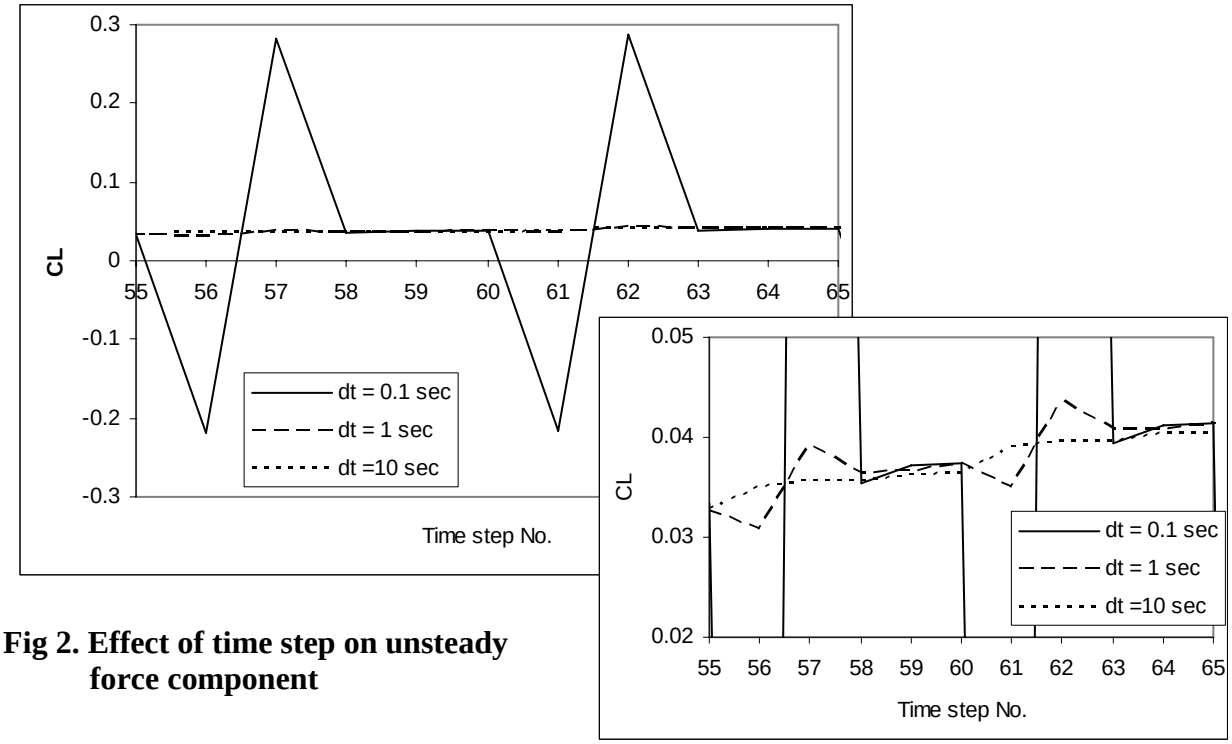

Fig 2. Effect of time step on unsteady force component

In terms of programming organization the procedure is as if turned inside-out. Normally an optimization process is controlled by the optimization algorithm calling whenever necessary the objective function and constraints calculation procedures. In this case the process progresses in the environment of the unsteady solver getting instructions for shape and mesh deformations from the optimization algorithm at each time step.

In the specific case with Fluent this can be done with the help of the DEFINE_GRID_MOTION macro. It allows the user to control the motion of each node on a dynamic zone independently. The way this has to be done is programmed by the user within this macro. With the proposed procedure it is here that we have to incorporate the optimization algorithm.

This user-supplied function has to:

- access the necessary solver data, e.g. forces, pressure, etc.
- calculate the current value of the objective function;
- initiate a single step of the optimization algorithm based on comparison with objective function value(s) from previous time step(s);
- check the suggested variations of the independent variables against the constraints and change them if necessary;
- change the body nodes positions as a function of the values of the independent variables.

In addition the fluid domain around the body has to be defined as a deforming-mesh zone subject to spring-based smoothing and/or local remeshing driven by the body nodes movement.

The optimization starts from the steady solution for the initial body shape.

3. Verification of the procedure by foil section optimization

The suggested procedure has been verified on the most popular test case for shape optimization – foil section optimization.

3.1. Optimization algorithm

The direct search method of Hook and Jeeves [B&Sh] has been used in the tests because it is easy to program while considered quite effective for problems without objective function derivatives.

The algorithm has been slightly modified to accommodate simple bounds type constraints.

3.2. Parametric model of shape deformation

For efficiency of the optimization it is important to use shape parametrization scheme capable of generating sufficiently smooth geometries during the whole optimization process with as little as possible number of parameters.

The following model for shape deformation has been defined for the case in consideration (Fig. 3):

A Bezier curve b(x) defined by four control points is used as a sort of chamber line, i.e.

$$y(x)^{NEW} = y(x)^{INI} + b(x)$$

The leading and trailing edge points remain fixed. The two points P_1 and P_2 are free to move, i.e. there are four independent variables – the coordinates of these two points.

Though very simple this model can produce a variety of shapes.

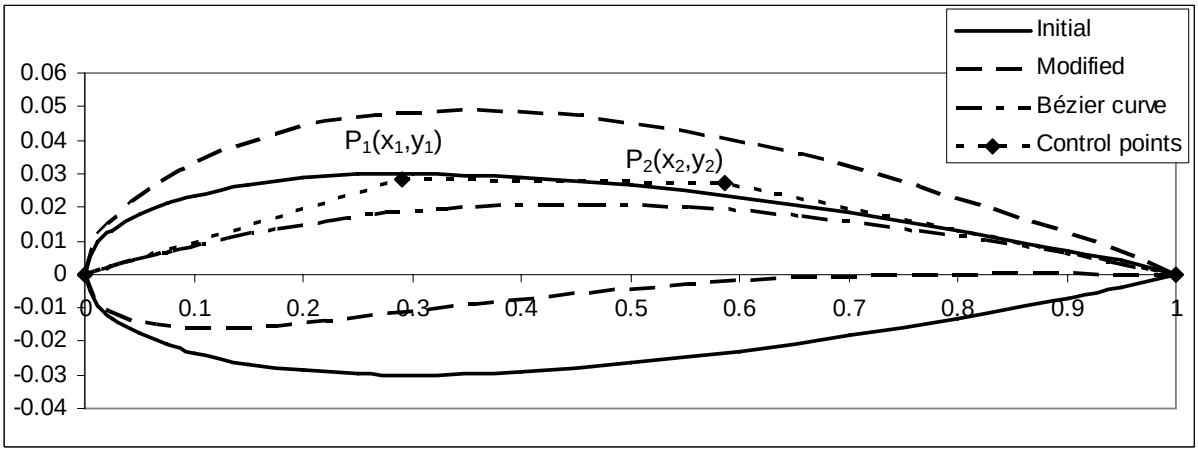

Fig. 3. Parametric model of shape deformation

3.3. Lift/drag ratio maximization

The first typical foil optimization problem tried has been lift/drag ratio maximization. The subject of optimization has been the NACA 0009 at Rn = $5x10^5$. Optimization has been carried out for two angles of attack – 0^0 and 10^0.

The two optimum shapes obtained are shown in Fig. 4.

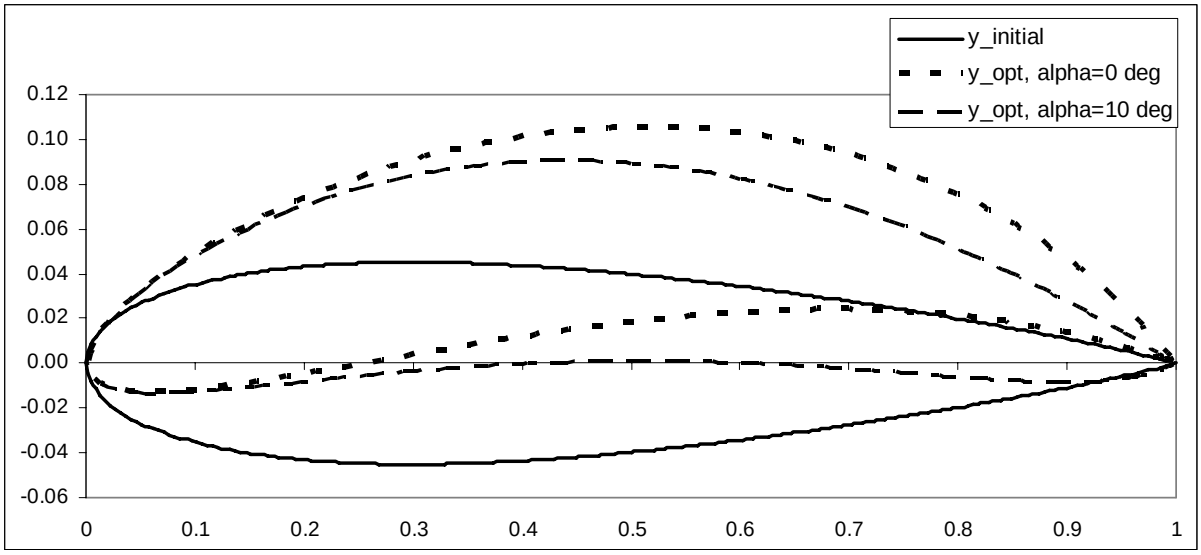

Fig. 4. Optimum shapes for lift/drag ratio maximization

Figure 5 shows the variation of the objective function and of the two individual hydrodynamic characteristics, as well as the "trajectories" of the two control points in the process of optimization for the two angles of attack.

In both cases the point P_1 reaches the bounds in a search of maximum lift, after which the point P_2 takes care of reducing the drag.

Angle of attack 0^0 **Angle of attack 10^0**

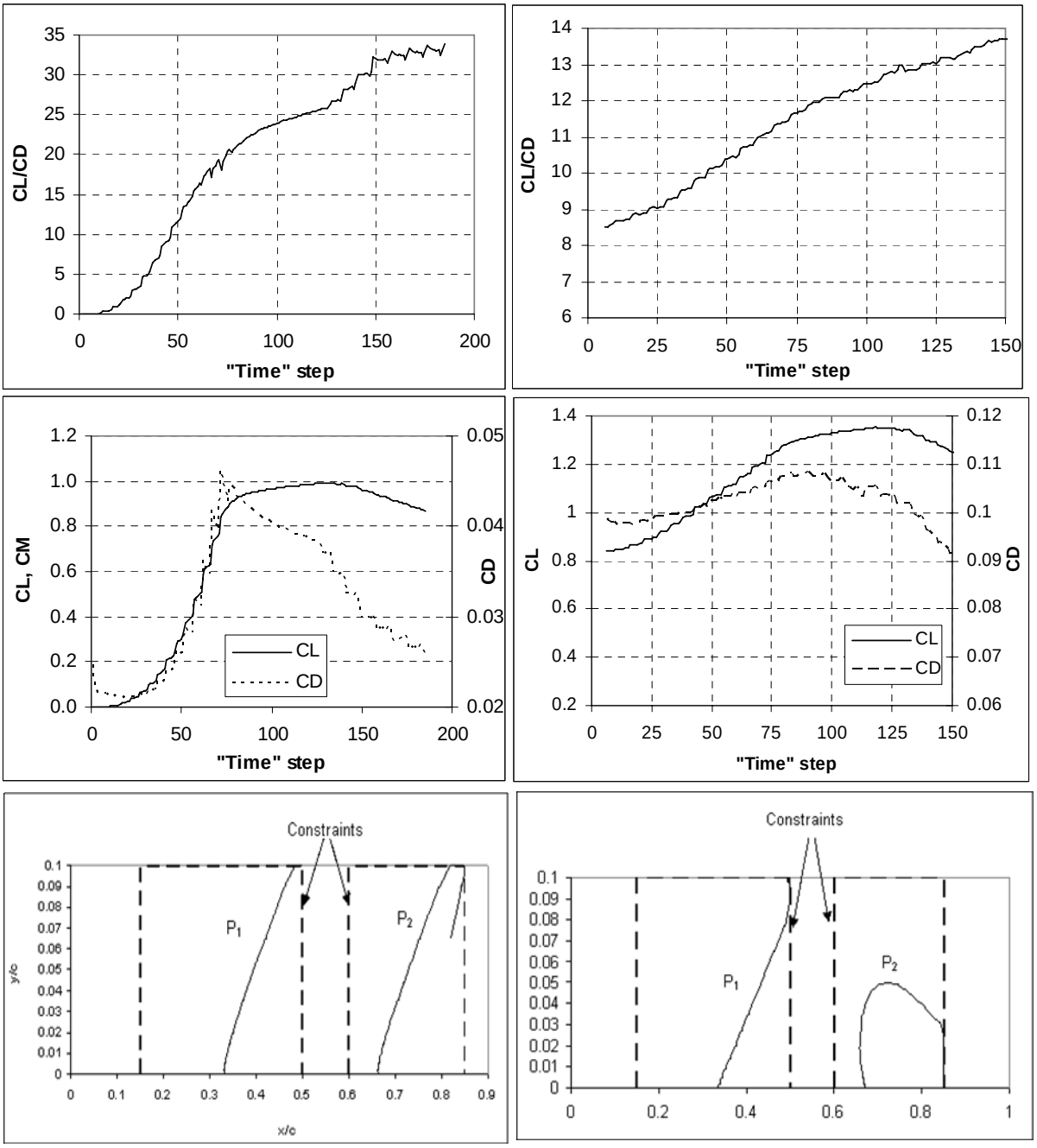

Fig. 5. Objective function and independent variables evolution

3.4. Inverse design

The other optimization problem tested has been the so called inverse design, i.e. design of a foil with prescribed pressure distribution. The flow around the profile NACA 65209 has been computed beforehand and the obtained pressure distribution set as a target, starting from a symmetrical profile of the same thickness – NACA 0009. The objective function has been defined as:

$$F_{OBJ} = \sum_i \left| CP_i - CP_i^{TARG} \right| \Rightarrow \min$$

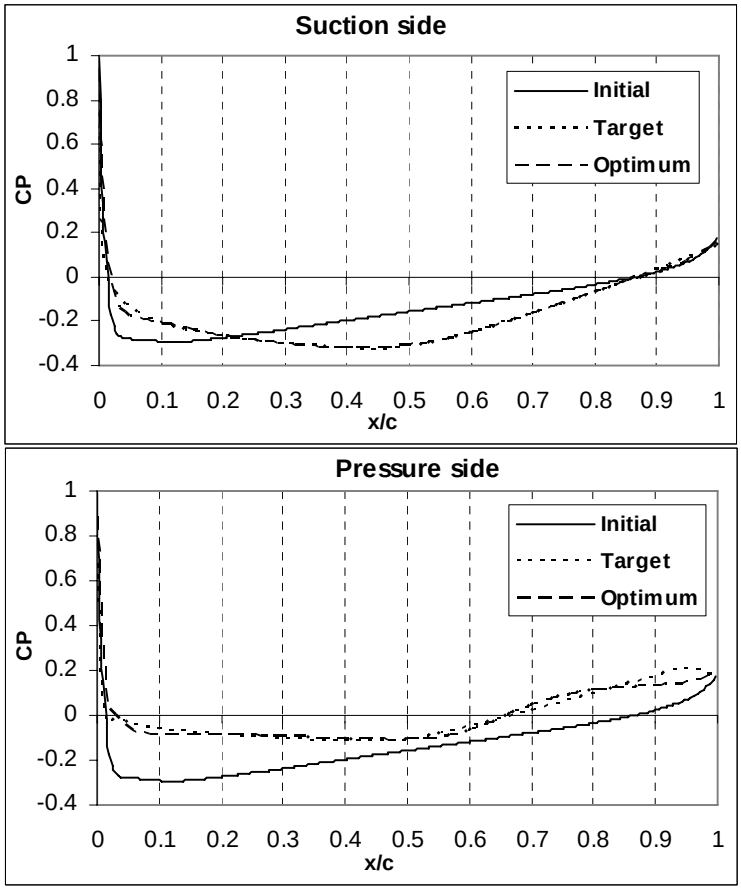

Fig. 6. Optimization for prescribed pressure distribution

Figure 6 shows the optimization results for pressure.

An interesting check in this case would be to see how close is the obtained foil shape to that whose pressure is used as an objective.

Figure 7 compares the shapes.

It can be seen that both pressure and shape are almost perfectly reproduced on the suction side.

On the pressure side the deviations are bigger. The reason for this must be the more complicated shape of that foil side, which can not be well approximated with the very simple parametric model that is used.

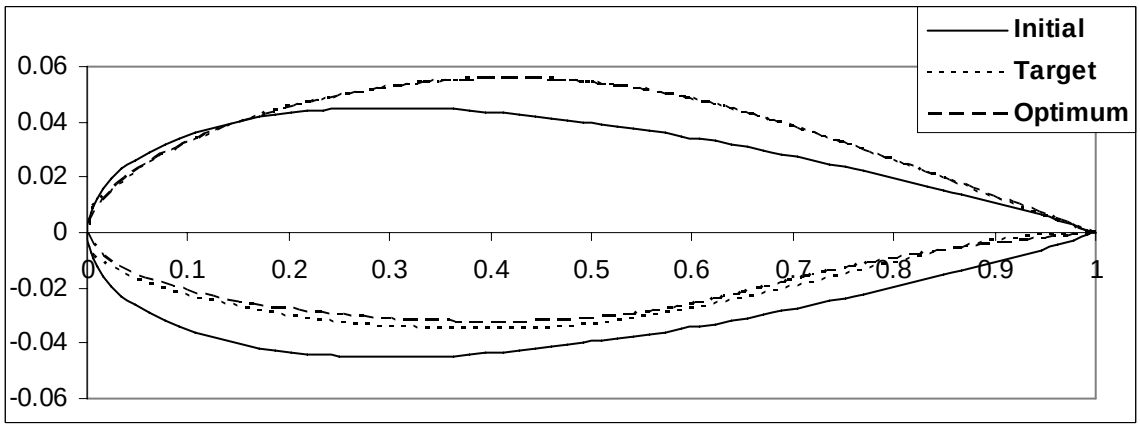

Fig. 7. Reconstruction of the target pressure shape

Conclusions

A procedure has been devised for hydrodynamic shape optimization integrated with the commercial RANSE solver Fluent. It is economical and offers flexibility in terms of formulated optimization problems and employed optimization algorithms.

2D tests with foil section optimization confirm the feasibility of the suggested approach.

It is believed that the proposed technique will be applicable also to 3D shape optimization. A possible route to explore would be to parametrize the geometry perturbations over a (limited) area of the body rather than the geometry itself, which will reduce the number of design variables.

Visualisation Techniques for Interpreting Performance of High Speed Craft

Lewis, S.G. *, Hudson, D.A.†, Turnock, S.R.‡
Fluid Structure Interactions Research Group, School of Engineering Sciences
University of Southampton, Southampton, SO17 1BJ, UK

1 Introduction

Validation of numerical predictions for the performance of high speed planing craft in waves presents a considerable challenge. The work undertaken here shows how the use of a 3D virtual reality simulation can help identify specific events such as slam impact when comparing towing tank or full scale experimental data with numerical predictions. Boat motion data obtained during towing tank testing is compared with video footage of the same experiment. Numerical predictions of the motion can also be visualised, and compared with the experimental data.

The visualisation code is developed from a simulation of the battle of Trafalgar, produced using a graphics rendering engine. The program, called Virtual Trafalgar (VT) [6], provides a realistic 3D environment using C++. VT will be used in conjunction with a computational fluid dynamics (CFD) package to model the motions of high speed craft.

2 Background on the program

VT was designed in 2005 as part of a group design project within the University of Southampton. The visualisation part of this simulation provides a useful base for simulating the motions of three dimensional objects and is used to produce a an environment capable of replicating the predicted or measured motions of high speed craft. VT is written in Visual C++ .NET 2003, and makes use of various open source packages as described in Section 2.1.

Virtual Trafalgar was developed not only as a visualisation device, but also to calculate the hydrodynamic and aerodynamic forces on ships such as the HMS Victory. These results are then used to predict the motion for a 3 degree of freedom model. This part of VT is not used in this project, but highlights the modular design of the software, and also provides an area that could be developed to predict marine craft motions using a 6 degree of freedom model. VT is now on display as an interactive sailing simulator at the Royal Navy Portsmouth Historic Dockyard.

2.1 Open source programs used

OGRE is an acronym for Object-orientated Graphics Rendering Engine. It is compiled using a C++ class library, with support for OpenGL and DirectX. OGRE has good support for scene management, shaders, and the documentation is comprehensive. OGRE v1.2 represents the culmination of five years of development, resulting in what is now one of the leading free real time 3D rendering engines [9].

Blender is used as a 3D modelling and shading program [3]. Blender is able to import DXF or VRML files, making it easier to create 3D craft from ship modelling software. DXF is probably one of the most widely supported

*sgl101@soton.ac.uk
†dominic@ship.soton.ac.uk
‡steve@ship.soton.ac.uk

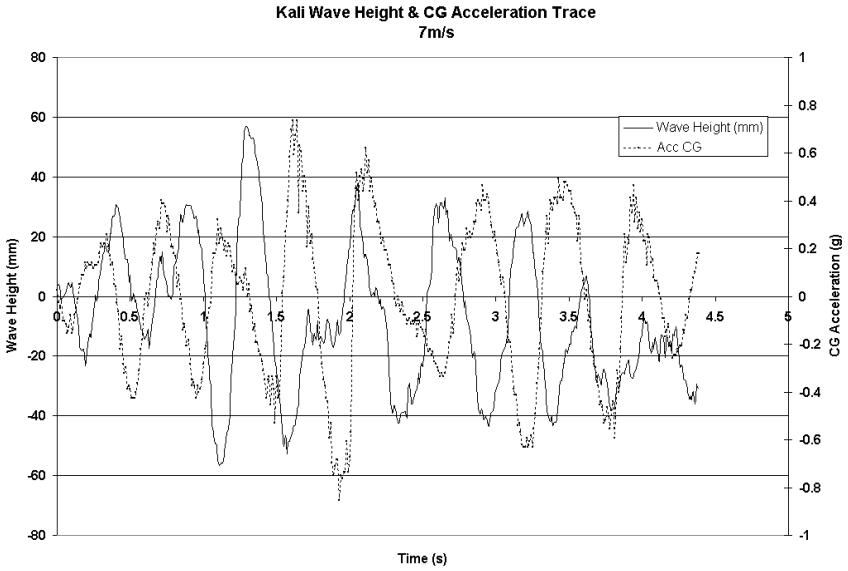

Figure 1: Example of the results obtained in the towing tank experiments

vector formats in the world today. The files are relatively easy to use, and are text based and therefore human readable [4]. VRML 1.0 files describe geometry, the material properties associated with that geometry. It can also handle multiple geometries and their location relative to each other within a single virtual world. This file format includes other properties such lights and camera points, which are very useful for visualisation [5]. VRML files are used to create the geometries shown in Figures 3, 4 and 5. It is just as important for blender to be able to export the files for use in OGRE (.mesh file). This is achieved using Python, an interpreted object orientated programming language [7].

3 Model Testing

Two models were tested in a towing tank:

- A wave piercing rigid inflatable boat (RIB), called Kali, designed to be the fastest boat to travel around the British Isles.
- An Atlantic 21 RIB.

Experiments were conducted at speeds of up to 12m/s in a 200m towing tank. The models used are scaled from full size by a factor of five. The experiments were conducted using a range of regular wave frequencies for three wave heights, and realistic JONSWAP sea spectra.

Five channels of data were recorded during each run: drag, heave, pitch, bow acceleration, CG acceleration and wave height, although drag data is not required by the visualisation software. The pitch was measured directly from the force block on the tow post fitting. The heave was measured by a linear potentiometer on the tow post and accelerations by uni-axial accelerometers mounted at the CG and the bow. A two fin wave probe mounted to the carriage was used to measure the wave height. This was located as close to the model as possible to allow identical wave spectra to be encountered. A graph of the wave height, and model accelerations at the center of gravity is presented in Figure 1. It is not possible to ascertain any uncertainties that may be present in the data. For example, the peaks values may not be accurate unless a sufficiently high sampling frequency is used. Visualising the boat motions using both the data and the video of the experiment would reveal any inconsistencies.

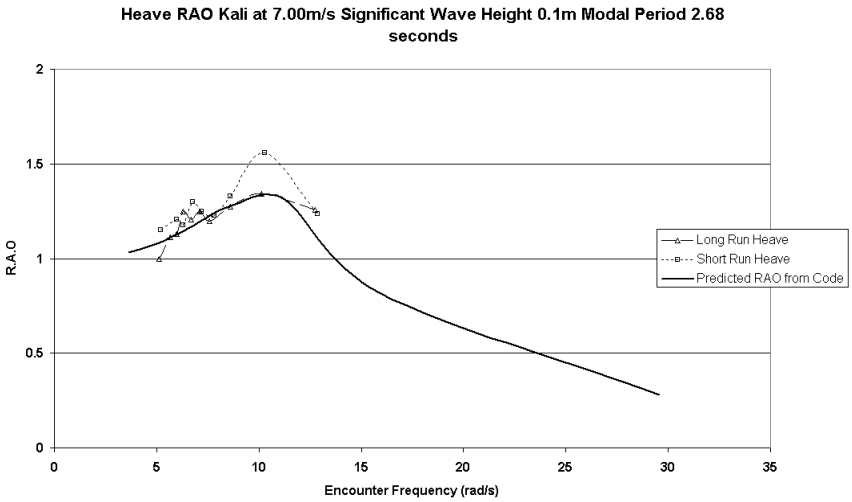

Figure 2: Example of a comparison between numerical and experimental results

4 Numerical modelling

4.1 Limitation in current methods of validation

Although discrete data is measured during experiments, a Fourier Transform is usually applied to convert the signal from a time base to a frequency base. This is used to analyse the generated spectrum of the wave pattern. Although this simplifies the analysis of irregular waves and boat motions, some of the data is lost particularly the peak values. Results can be presented as a percentage probability that the crest value exceeds a certain value [1]. When comparing predicted motions with those measured from experiments, the uncertainty in both the experiment and the numerical code must be taken into account. A required validation level is set, and the results are only validated when this criterion is reached [8].

4.2 Numerical model background

The numerical code used in this project was developed as part of a PhD at Southampton University [2]. The model is based on non-linear strip theory through calculation of the forces occurring on wedge impact. Figure 2 shows both numerical and experimental responses of Kali to regular waves. This response of the boat to waves of a given frequency is given in terms of response amplitude operators (RAOs), which are the ratio of the size of vertical response of the boat to the size of the wave.

5 Results

Figure 3 shows a visual comparison between the towing tank video and simulation for the Atlantic 21 RIB in calm water. The visualisation program can be used to produce a model that is comparable to the towing tank pictures. Much of the information is lost in still pictures, and a video would better illustrate the two motions. Figure 4 shows the same RIB travelling at 12 m/s in irregular waves. Figure 5 shows Kali in regular waves, and compares the experimetal data with the video. The models used in the visualisation are fairly basic, although Blender does have the capabilities to produce models with significantly greater detail.

6 Recommendations and Conclusions

There is a significant amount of work required to improve the software, and expand its capabilities:

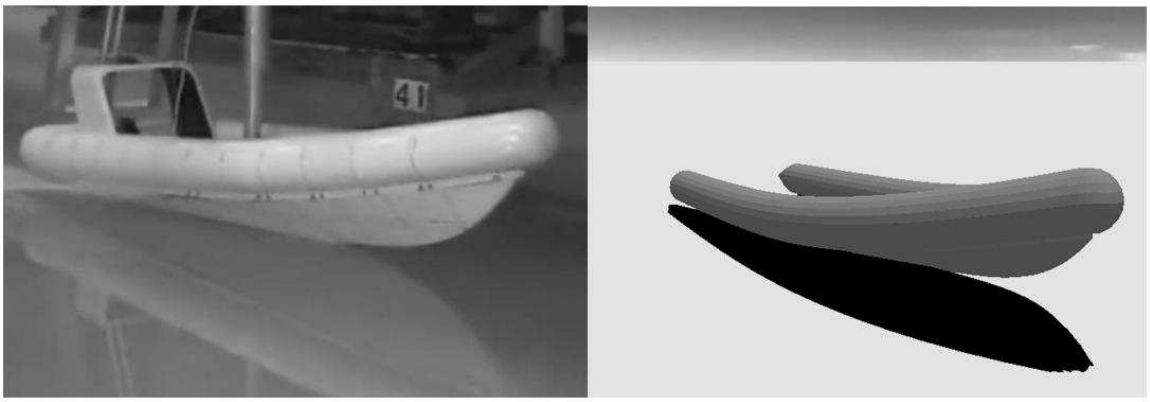

Figure 3: Comparison between the towing tank experiment [left] and the visualisation [right] of the Atlantic 21 RIB in flat water

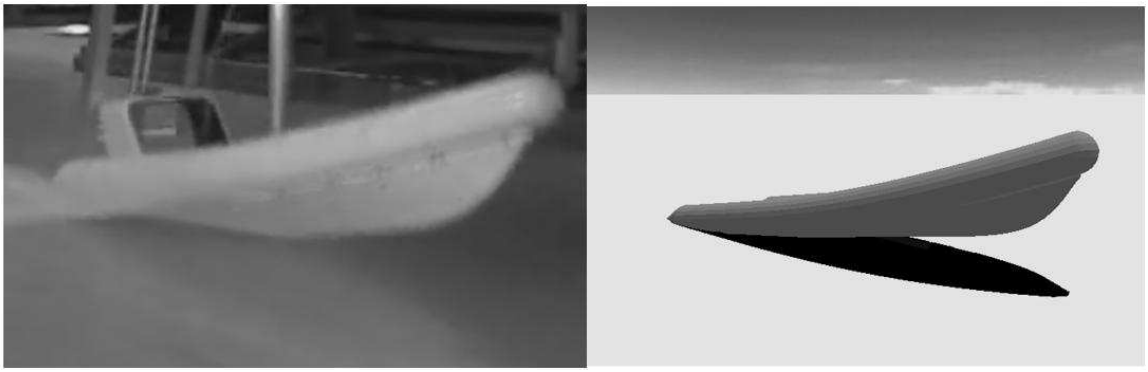

Figure 4: A similar comparison of the Atlantic 21 RIB in irregular waves

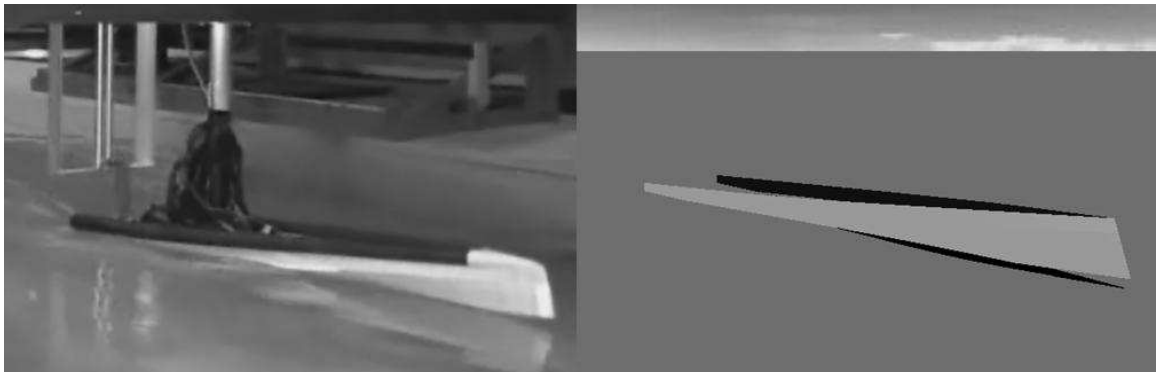

Figure 5: Another comparison of a different hull, Kali, experiencing a regular sea state

- Waves need to be included in the visualisation of the motions. This would help to ensure that the two videos are properly synchronised. The lack of a moving interface between the water and air makes the simulation seem unrealistic. Viewing the waves would also give an idea of the accuracy of the wave data obtained during the experiments, as this can be a source of uncertainty.

- The surface texture of the water should be more realistic. The water is represented by a solid shade of blue, and OGRE has the capabilities to change the texture to water. This has to be linked to the modelling of waves.

- The input procedure for data obtained in experiments needs to be improved. A simple text file for each parameter is currently used, and this greatly increases the time taken to prepare each simulation.

The results are encouraging, and show that the visualisation technique can be used to interpret both numerical predictions and experimental data. A good visualisation of the motions gives a greater understanding of any limitations in a numerical model or experimental data.

7 Acknowledgements

This work is supported by the EngD program at the University of Southampton, with sponsorship from the Wolfson Unit for Marine Technology and Industrial Aerodynamics. Thanks are due to all the members of the Virtual Trafalgar group design project for software support. Model testing data and video footage is provided by the group design project focusing on Design Procedure for a Record Breaking Craft from a Human Factors Perspective.

References

[1] Akers, R., ”Dynamic Analysis of Planing Hulls in the Vertical Plane”, Presented at the New England Section of *The Society of Naval Architects and Marine Engineers*, April 1999.

[2] Blake, J.I.R., ”Investigation into the Vertical Motions of High Speed Planing Craft in Calm Water and in Waves”, *University of Southampton Doctor of Philosophy*, May, 2000.

[3] Blender [online] http://blender.org [accessed april 2006]

[4] Graphic Region, ”Professional Graphic Tools - DXF Format Specifications”, [Online] http://www.graphicregion.com/convert

[5] JavaTM 3D API Specification, ”VRML Support” [Online] http://www.graphcomp.com/info/specs/java3d/j3dguide/AppendixVRML.doc.html, [Accessed May 2006].

[6] Leszczynski, R., Parker, R., Rock-Evans, M., van Someren, M, Squibb, A.,“Virtual Trafalgar, development of a Napoleonic Naval Simulator,” *University of Southampton Group Design Project*, April 2005. Further information available at www.virtualtrafalgar.com.

[7] Python [Online] http://www.python.org. [Accessed May 2006].

[8] Stern, F., Wilson, R.V., Coleman, H.W., Paterson, E.G. “Verification and Validation of CFD Simulations”, *Office of Naval Research*, IIHR Report No. 407, Iowa Institute of Hydraulic Research , September 1999.

[9] Streeting, S., Muldowney, T., O’Sullivan, J., van der Laan, W., “OGRE (Object-orientated Graphics Rendering Engine,” [Online] http://www.Ogre3d.org. [Accessed April 2006].

Investigation of sloshing phenomena near the critical filling depth through the Hilbert-Huang Transformation

Claudio LUGNI, Giuseppina COLICCHIO, Andrea COLAGROSSI
INSEAN, Rome/Italy, c.lugni@insean.it

Sloshing is a resonant phenomenon characterizing the motion of a fluid in a partially filled tank forced to move by external forces. In naval context, it is an important issue for LNG tanks and in general for the partially filled tanks on board of ships. When the motion of the ship in seaway couples with fluid motion inside the tank, the stability of the ship as well the tank structure can be undermined.

In the previous works (*Lugni et al. (2006)*, *Colagrossi et al. 2006*), experimental investigation relative to 2D sloshing flow was carried out for a square tank, $L = H = 1$ m long and $b = 0.1$ m wide (see sketch on left panel of fig. 1), in shallow water ($h/L = 0.125$) and critical filling depth ($h/L = 0.337$) conditions. The present study follows into the footsteps of *Colagrossi et al. (2006)* and it aims to investigate the possible scenarios associated with sloshing flows. Increasing the amplitude A of the horizontal sinusoidal motion $A\sin(\omega t)$ of the tank and varying its circular frequency ω around the value corresponding to the largest natural period $T_1 = 1.266$ s (see right panel of fig. 1), asymmetry of the wave elevation in space and time as well alternance of the breaking phenomenon on the lateral wall of the tank, were observed in *Colagrossi et al. (2006)*. Numerical investigation through an SPH algorithm helped the comprehension of the physical mechanism involved; vortex generation, consequence of breaking phenomena, as well damping mechanisms have been identified as the main mechanisms responsible for the peculiar evolution of the sloshing flows inside the tank. Within the frequency and amplitude region investigated, four main scenarios have been highlighted and identified as events (I) without free-surface breaking, (II) with alternate breaking, (III) long-time randomic asymmetric behavior, (IV) with local splashing jets (see right panel of fig. 1). Here, sloshing features relative to

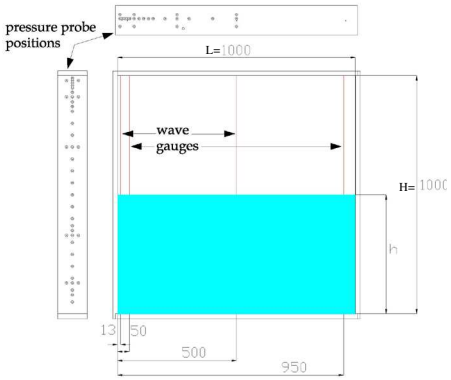

	(L=1 m)	A/L	0,03	0,05	0,07	0,10
T(sec)	T/T1					
1,00	0,79		183 (I)	174 (I)	206 (II)	414 (III)
1,10	0,87		484 (II)	175 (II)	207 (IV)	415 (IV)
1,20	0,95		186 (IV)	176 (II)	208 (II)	416 (IV)
1,30	1,03		189 (II)	178 (II)	210 (IV)	418 (IV)

Figure 1: Left: experimental set-up. Right: cases studied and main sloshing scenarios identified as a function of the excitation period T and excitation amplitude A. T_1 is the linear sloshing natural period and L is the tank length.

the scenario (II) and in particular to the cases 175 and 484 have been deeply investigated. A peculiar analysis of the experimental free surface configuration both through the classical FFT algorithm and the recent Huang-Hilbert Transform (*Huang et al. (1998)*) has been performed to highlight the mechanism responsible for the generation of sub- and super-harmonic components. During the experiment, four capacitance wave gauges in the positions shown in the left panel of the figure 1 were used to measure the evolution of the free surface. A low-speed camera with sample rate 25 Hz was used to capture the global evolution of the free surface inside the

tank. In figure 2, the free surface evolution in stationary condition for the case 484 is shown

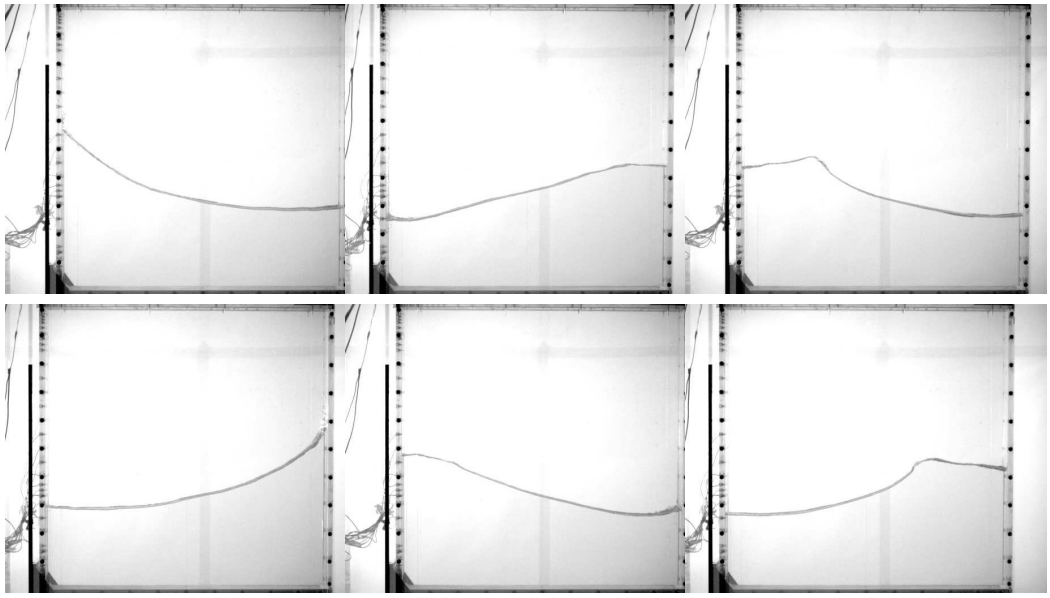

Figure 2: Case 484 ($T = 1.1$ s, $A = 3$ cm): free surface evolution for several time instants. From left to right and from top to bottom: $\#1\, t = T$, $\#2\, t = 1.5T$, $\#3\, t = 2T$, $\#4\, t = 2.5T$, $\#5\, t = 3T$, $\#6\, t = 3.5T$

for several time instants, $t = T$, $t = 1.5T$, $t = 2T$, $t = 2.5T$, $t = 3T$, $t = 3.5T$, from left to right and from top to bottom, respectively. The configuration corresponding to $t = 4T$ (not shown in figure) is identical to the first one. This behaviour is confirmed by the time history of the wave elevation recorded by the wave probe closest to the left wall of the tank and reported in figure 3. After the initial transient phase, a period tripling, consisting in three recurrent modes,

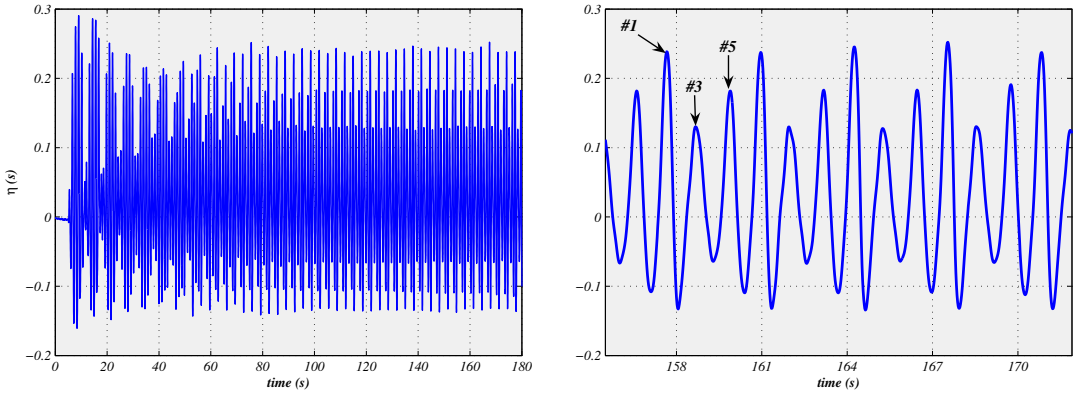

Figure 3: Case 484 ($T = 1.1$ s, $A = 3$ cm). Time history of the wave elevation recorded by the wave probe closest to the right vertical wall of the tank (left panel). On the right panel an enlarged view for steady condition is also shown. The black arrows indicate the time instant of the picture reported on the left column of figure 2.

is highlighted in the evolution of the wave at the lateral wall of the tank: $a-$ sharp crest with formation of a thin jet along the wall (see panel #1 and #4 in fig.2), $b-$ dimpled or flat crest with lateral almost spilling breaking (see panel #3 and #6 in fig.2) and $c-$ round crest without breaking (see panel #5 and #2 in fig.2). The phenomenon appears quite similar to the period tripling studied by Jiang et al. (1998), but for a completely different physical problem. Using a sloshing tank forced to move vertically for generating steep Faraday wave, they found three

distinct waveforms reproducing the period tripling phenomenon in the centre of the tank. In the following the analysis will be carried out for the stationary conditions. To further illustrate the existence of the triple mode, left panel of figure 4 shows the evolution in the phase-plane of the elevation signal reported in figure 3 (right panel). Three different orbits corresponding to several involved modes have been highlighted as well as their sequence: $a \rightarrow b \rightarrow c \rightarrow a....$ This confirms what already observed in figures 2 and 3. The widening of the orbit corresponding to the first mode can be related to the complex flow due to the drop of the steep runup along the wall.

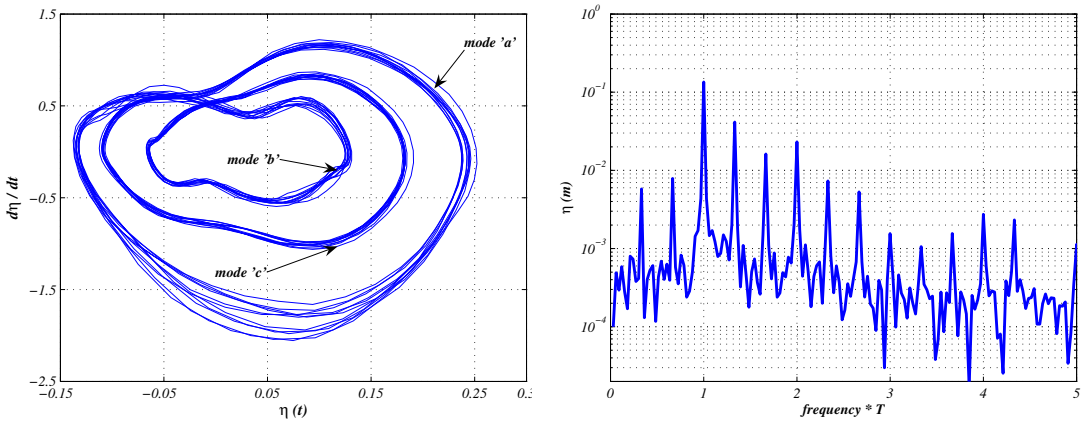

Figure 4: Case 484 ($T = 1.1$ s, $A = 3$ cm). Evolution in the phase-plane of the wave recording reported in figure 3 (right panel) and the relative FFT.

The amplitude spectrum shown in the right panel of figure 4 reflects the global and averaged characteristics of the phenomenon, disregarding any local information, as well as any interaction of the harmonics (*Perlin et al. (2000)*). The frequency modulation appears as two spectral peaks $1/3T$ apart to the lower side of the forcing frequency. The upper modulation frequency components ($1/T + 1/3T$ and $1/T + 2/3T$) are globally larger than the lower ones, highlighting a strong modulation of the first two fundamental harmonics ($1/T$ and $2/T$). Because the forcing motion is practically unaffected by the $n/3T$ frequencies, this behavior suggests a strong nonlinear interaction of the excited three modes as cause of the modulation frequency (*Jiang et al (1998)*).

The use of the Hilbert-Huang transform can reveal interesting feature of the period tripling. This technique, recently introduced by *Huang et al. (1998)*, extracts several contribute of energy from a time dependent data series, disintegrating the signal into its individual characteristic oscillations. It consists on the use of two successive steps for the analysis of the data. In the first step it decomposes the data according to their intrinsic scales properties into a finite number of Intrinsic Mode Functions (IMF), each of them representing an embedded characteristic oscillation in a separated time scale. This process, i.e. the Empirical Mode Decomposition (EMD), allows to expand the input data in a basis associated with the data itself. In the second step the Hilbert transform is applied on each IMF component, defining a time-frequency-energy spectrum, i.e. the Hilbert spectrum. By definition, an IMF is described by two properties: 1) the number of zero crossings and of extrema must be the same or differ at most by one, and 2) at any time instant, the mean value of the curve defined by the envelope of the local maxima and the envelope of the local minima, must be null. The former property is almost equivalent to the narrow band requirement of a Gaussian process, while the latter is a necessary condition to avoid unwanted oscillation in the calculation of the instantaneous frequency. Note as the EMD decomposition does not strictly satisfy the orthogonality from a theoretical point of view,

although this property is satisfied practically, as checked a posteriori. On the other hand, the total sum of the several IMF, well reproduces the original signal, ensuring the completeness of the system.

Essentially the Hilbert transform emphasizes the local properties of the signal involved, through its convolution with $1/t$. Differently from the Fourier approach, where a nonlinear dynamical system is approximated by a sum of several linear problems related to the several frequency components of the system, the Hilbert representation gives a sharper resolution in frequency and a more precise location in time. This technique has been recently applied to study several water waves problems (*Huang et al. (1999)*, *Schlurmann et al. (2002)*), and to interpret the downshifting phenomenon of the Stokes waves (*Huang et al. (2002)*), but to our knowledge no documentation of its application on the sloshing phenomena, or on the period tripling is available in literature.

In the following the HHT algorithm has been applied on a signal previously filtered with a digital filter, applied back and forth to avoid any phase shift with respect to the original signal. Figure 5 reproduces the results of the HHT. To limit the length of this work, we omitted the results relative to the IMF decomposition, forwarding its description to the symposium. Three consistent IMF's were selected from the EMD process and, for each of them, the relative Hilbert transform is reported in figure 5 . In particular the left panel shows the amplitude (in log scale) of the Hilbert transform as function of the nondimensional (with respect to the period of the forcing motion) instantaneous frequency and of the time instants. The recurrence of the period tripling is evident. For a clearer discussion of the phenomenon, the right panel shows the behaviour of the instantaneous frequency in time for each IMF (red line: IMF#1, green line: IMF#2, cyan line: IMF#3) together with wave elevation in arbitrary scale (dashed blue line), for a short time interval almost equal to $3T$. IMF#1, the most important one, recalls the time behaviour of the wave elevation and it will be discussed in the following. Three different peaks of the instantaneous frequency in the first IMF highlights the existence of three different modes. On the other hand, this modulation of the instantaneous frequency is a hallmark of the strong nonlinear effects characterizing the period tripling and then a consequence of the amplitude modulation of the wave elevation. This latter also causes a variation in time of the mean frequency, and then it is responsible for the widening of the mean frequency band. The fluctuation of the frequency is symmetric with respect to the wave profile both during the rounded runup (mode 'c') and the dimpled crest phase (mode 'b'), while presents a quite large phase shift toward the rundown time instants in correspondence of the mode 'a', i.e. in correspondence to the strong runup with jet formation at the wall and successive drop in the water below. Usually, in the Hilbert spectrum of a 'linear' sloshing flow, the highest-frequency part of a wave is almost aligned with the runp along the wall and the lowest-frequency part with the rundown phase. This phase shift of the frequency can be associated to the complex flow characterizing the mode 'a'. The propagation of the breaking on the opposite side causes a strong runup with the formation of the jet. The last one falls in the water below with the formation of a quite large hullow and generation of intense vorticity. This complex flow is confirmed also by the SPH simulation in *Colagrossi et al. (2006)*. This phase shift of the instantaneous frequency could be responsible for the formation of the successive two modes, and then of the period tripling. We are addressing our research towards the understanding of the causes of the period tripling with the help of numerical computations based on the use of SPH algorithm.

The present research activity is supported by the *Ministero Infrastrutture e Trasporti* within the *Programma Ricerche Idrodinamica Navale 2005-2007*. **References**

COLAGROSSI, A.; PALLADINO, F.; GRECO, M.; LUGNI, C.; FALTINSEN, O.M. (2006),

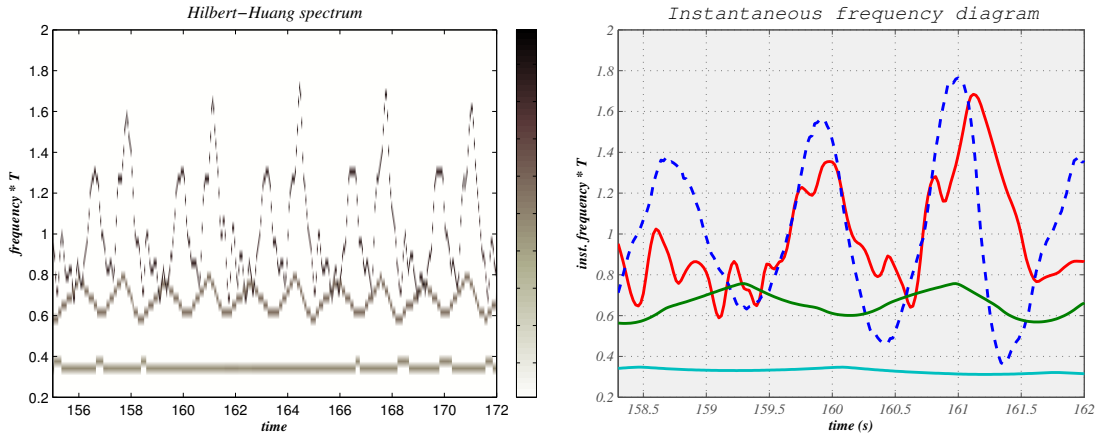

Figure 5: Case 484 ($T = 1.1$ s, $A = 3$ cm).

Experimental and numerical investigation of 2D sloshing: scenarios near the critical filling depth, 21th Int. Workshop on Water Waves and Floating Bodies, UK.

LUGNI, C.; BROCCHINI, M.; FALTINSEN, O.M. (2006), *Wave impact loads: the role of the flip-through* Under review on Physics of Fluids

COLAGROSSI, A.; LANDRINI, M.; (2003), *Numerical simulation of interfacial flows by SPH* J. Comp. Physics, **191**, pp.448-475.

PERLIN, M.; SCHULTZ, W (2000), *Capillary effects on surface waves* Annual Rev. Fluid Mech, **32**, pp.241-274.

HUANG, N.E.; SHEN, Z.; LONG, S.; WU, M.; SHIH, H; ZHENG, Q.; YEN, N.; TUNG, C.; LIU, H. (1998), *The empirical mode decomposition and the Hilbert Spectrum for nonlinear and non-stationary time series analysis* Proc. Royal Soc. London A, **454**, pp.903-995.

HUANG, N.E.; LONG, S.; SHEN, Z. (2002), *The mechanism for frequency downshift in nonlinear wave evolution* Adv. Appl. Mech, **32**, pp.59-117.

HUANG, N.E.; SHEN, Z.; LONG, S. (1999), *A new view of nonlinear water waves: the Hilbert Spectrum* Annual Rev. Fluid Mech, **31**, pp.417-457.

SCHLURMANN, T.; BLECK, M.; OUMERACI, H. (2002), *Wave transformation at artificial reefs described by the HHT* Coastal Engineering **31**, pp.1791-1804.

Comparing a Propeller Model with a Rotating Propeller in a CFD-Simulation of the Viscous Flow around a Ship

Mueller, S.-B. (sven-brian.mueller@uni-due.de)
Steden, M. (max.steden@uni-due.de)
Neugebauer, J. (jens.neugebauer@uni-due.de)
El-Haddad, M. F. (mohamed.el-haddad@uni-due.de)
Abdel Maksoud, M. (moustafa.abdel-maksoud@uni-due.de)

University of Duisburg-Essen
Institute of Ship Technology and Transport Systems (IST)
Bismarckstr. 69, Gebäude BK, 47057 Duisburg
Phone +49-203-379-1173, Fax +49-203-379-2779, Email: IST@uni-due.de
www.schiffstechnik-duisburg.de

1 Introduction

In CFD-calculations the use of several millions of control volumes is common practice in order to simulate the flow around a ship. Yet we are tending to save computation effort and time in every simulation to spend it in specific regions where it is interesting to get more detailed information. In the paper we are comparing the results of two simulations of the viscous flow around a ship in full scale. The first simulation is including a rotating propeller while the second is including a mathematical propeller model. By using the propeller model we saved many elements, moreover, a considerable amount of computation effort was reduced. Our aim is to include the free surface around the ship. By doing this we expect more realistic results than by neglecting the deformation of the free surface. Furthermore, it will enable us to compute the wave system and determine the ship resistance in conjunction with a free water surface.

2 Computation Case

The presented computations simulate the flow around the geometry of a RoRo-twin-screw-ship of the German Shipyard Flensburger Schiffbau-Gesellschaft mbH & Co. KG (FSG), Figure 2. The calculations were carried out for a Froude Number of 0.270, as the ship length between perpendiculars was 182.39 meters and the ship speed was 11.40 m/s with a draught of 7.00 meters. The commercial program CFX 10.0 has been used for the numerical calculation.
The investigated domain was 12.25 times as long, 1.5 times as wide and 0.95 times as deep as the ship length.
In this study, only half of the ship was considered in the simulation, because it is possible to make use of the symmetry at the longitudinal axis of the RoRo-twin-screw-ship. Accordingly, the size of the computed grid was reduced and simulation time was saved.
The numerical grid for the fluid around the ship was created with a cylinder cut-out for the numerical grid of the propeller or propeller model. The grids were connected using interfaces between the propeller domain and the surrounding domain.
For the boundary conditions of the investigated area the ship speed was selected as inlet term and a pressure boundary as outlet. The ship and the remaining sides of the investigated area got a wall boundary condition, whereas only the hull is afflicted with friction - the sides are frictionless.
The simulation including the rotating propeller was performed in two steps. The first step was a steady state calculation, while the second was a transient calculation. Whereas the simulation with the propeller model was performed in one calculation. For all simulations the Shear Stress Transportation Model (SST) was used as turbulence model.
In the simulation with the rotating propeller, the mesh consists of 6.97 million hexahedron elements and a rate of revolution of $2.104 s^{-1}$ was selected. The thrust calculated by the rotating propeller, which equals 411 kN, was used as input thrust for the propeller model. The flow simulation for the same ship with the propeller model at the same speed was conducted with a mesh of 4.44 million elements. The rate of revolution determined by the propeller model was $2.190 s^{-1}$.
The steady state simulation with the rotating propeller ran about 1174 CPU hours for 1534 iterations on 28 processors, and the transient computation with the rotating propeller lasted about 1010 CPU hours for 288 iterations on 28 processors. Whereas, the simulation with propeller model took only 527 CPU

hours for 1310 iterations on 29 processors. By dividing the total CPU time by the number of iterations and the number of processors, it was noticed that the simulation with propeller model required about half of the computation capacity vs. the steady state simulation with rotating propeller. Only 1/11 of the computation capacity was used considering the transient calculation. Another advantage of the propeller model is that a lot of manpower can be saved for the discretisation of the propeller domain.

2.1 Rotating Propeller

The given geometry of the rotating propeller has 4 blades and a diameter of 5.00 meters. The area ratio is about 0.51 and the pitch ratio is 1.20 at r/R=0.7.
The numerical grid was created only around one blade, afterwards it was rotated and copied around the rotation axis. Finally, the cylinder within the fluid domain mesh, which describes the propeller and the hub, contained 2.67 million hexahedron control volumes.

2.1.1 Steady state calculation

By performing the steady state simulation, the coupling of the rotating domain of the propeller and the stationary grid of the ship is realised by an interface method which is called "frozen rotor". Within the "frozen rotor" interface method the frame of reference is changed, however, the relative orientation of the domains across the interface remains fixed. The two frames of reference are connected in such a way that they each have a fixed relative position throughout the calculation, but with the appropriate frame transformation occurring across the interface. The conservation equations for the propeller domain were solved in the rotating frame of reference under consideration of the coriolis and centrifugal forces, while the conservation equations for the ship domain are computed in a stationary frame of reference. Across the interface the observance of mass flow and the consistency of the pressure is required. This model has the advantage of being robust and requiring less computational effort to couple a rotating and a stationary domain than other methods. But on the other hand this model neglects the transient effects at the frame change interface. So the real situation where the flow is mixed between the domains is not supported. A relative short computation time was required to solve the boundary layer of the ship when the steady state calculation was applied, because the size of the time step can be increased. Thus, this result was used as an initial value for the transient simulation.

2.1.2 Transient calculation

In the transient simulation the interfaces of the two domains were connected by using the "rotor stator" method, which considers the real (transient) correlation of the flow in the ship domain and the propeller domain. Within this method, the relative motion between the two areas of investigation was simulated. The connection of the domains is not in a fixed position. Non-matching grids at the interface are used, because the position of the interface is updated at each time step and the correct time dependent relative position of the rotating and the non-rotating domain is taken into consideration. These sliding interfaces ensure the observance of mass flow between the ship and propeller domain. The conservation equations are solved nearly in the same manner as the program does for the "frozen rotor" method. The drawback of this method is that the computational effort (simulation time, disk space and the post processing of the data) takes up to 30 times more than the "frozen rotor" method needs, however, the results are closer to reality.

2.2 Consideration of the Propeller Influence by means of the Integration of a Propeller Model

A propeller model is used for the realisation of the propeller influence on the flow. The propeller model is applied in a cylinder domain, which is placed at the location of the rotating propeller. This cylinder has got a hole at the place of the hub. The local coordinates of all elements within the propeller model domain are determined in relation to a local coordinate system. In the propeller model domain, there are two regions defined, a thrust region and a read-in plane. Every element in the read-in plane, in which the local velocity vector is determined, is linked to the corresponding element in the thrust region. The operating point of the replaced propeller is determined by the average local inflow velocity vector according to the open water diagram. Both, the axial and the tangential inflow velocities are considered. The axial inflow velocity is reduced by the induced axial velocity component, while the average tangential velocity is considered by the determination of the rate of propeller revolution n. By determining the operating

point, the rate of revolution, the thrust and the torque are specified considering the velocity vector at the inflow of the propeller model. The local velocity vector and the geometry of the blade at the local radius are included into the determination of the thrust and the torque contribution dT and dQ for each element within the thrust region as illustrated in Figure 1.

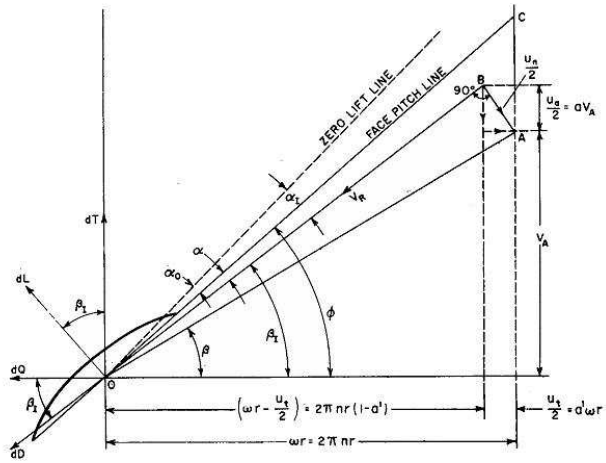

v_A	=	local axial velocity component
u_a, u_t	=	induced local velocity components
ϕ	=	pitch
α	=	effective angle of incidence
α_0	=	zero lift angle
β	=	advance angle
β_I	=	induced angle of incidence
dL	=	change of lift
dD	=	change of drag
dT	=	change of thrust
dQ	=	change of torque

Figure 1: Blade Velocity Diagram [2]

The geometry of the propeller, which is being replaced by the propeller model, including its profile length c, pitch ϕ, skew, maximum thickness t_{max} and camber f_{max}, is considered within the calculation of the lift and drag coefficient C_L and C_D for each propeller blade section. The local thrust T_{loc} and torque Q_{loc} are computed with C_L and C_D for each element, see equations (1-4).

$$C_L = 2 \cdot \pi \cdot (\alpha - \alpha_0) \tag{1}$$

$$\begin{aligned} C_D = {} & 0.0675 + 1255.0 \cdot {t_{max}}^2 \cdot {f_{max}}^2 - 3.839 \cdot f_{max} \cdot \alpha + 9.658 \cdot \alpha^2 \\ & -17.101 \cdot t_{max} \cdot \alpha^2 - 1616.0 \cdot {t_{max}}^2 \cdot \alpha^2 \cdot \alpha^2 - 5802.0 \cdot {t_{max}}^3 \end{aligned} \tag{2}$$

$$T_{loc} = \rho \cdot \frac{c \cdot {V_A}^2}{D} \cdot (C_L \cdot cos\beta_i - C_D \cdot sin\beta_i) \tag{3}$$

$$Q_{loc} = \rho \cdot \frac{r \cdot c \cdot {V_A}^2}{D} \cdot (C_L \cdot sin\beta_i - C_D \cdot cos\beta_i) \tag{4}$$

The drag coefficient equation (2) is a modified formula based on [1]. By integrating the thrust and torque distributions over the entire domain of the propeller model, a factor is computed iteratively in order to reach the actual thrust and torque, which were determined for the operating point.
The propeller model permits the variation of the thrust and torque in circumferential and radial direction. With the described method a simulation close to reality of the propeller influence became possible during the simulation of the viscous flow around a ship. Substantial differences in the pressure distribution, compared to a simulation without propeller model, can be recognised in the stern region.
In addition, the propeller model can either be used to determine the rate of revolution for a given thrust or to adapt the thrust automatically to the resistance [3].

3 Results

The analysis of the results and the comparison of the simulation with propeller model and the rotating propeller show the global quality and the effectivness of the propeller model.

Figures 3-5 show a longitudinal plane at the propeller rotation axis. The velocity is normalised by the ship speed. If the results from the transient solution, which are close to reality, are accepted as standard, it is possible to compare these results with others. Figure 3 indicates a lot of interesting regions, for example, the tip vortex and the pronounced hub dead water. The acceleration of the water due to the activity of the propeller can be noticed. Furthermore, the interaction between the flow domain and the propeller domain is obviously recognized. Behind the rudder the estimated velocity distribution is appearing and can be located in the other calculations with local deviations. The computation with the propeller model generally presents a smooth velocity distribution, which is based on the determination of the thrust distribution by the propeller model. In the steady state calculation, the smooth velocity distribution near the propeller domain depends on the "frozen rotor" coupling efficiency.
Figures 6-10 describe the wake of the ship influenced by the rotating propeller and propeller model. The presented view is a yz-plane located between the propeller and the two-leg propeller strut (distance of 1.0 meter from the propeller in x-direction). In every simulation it can be seen that there is a reduction in velocity between the struts. The velocity distributions of the propeller model and the transient calculation point out the highest reduction in this region, but it is balanced by a higher level of velocity over the rest of the plane. The velocity distribution of the steady state computation in general shows higher velocities over nearly the whole plane and therefore clearly differs from the other two calculations. The transient wake field indicates local regions around the hub, where the velocity is increased in comparison to the surrounding area. The distribution of the velocity changes with the rotation of the propeller, starting at the twelve o'clock position and turning clockwise (Figures 8-10).
Finally, the results show that the propeller model is suited to replace the rotating propeller globally. But in order to investigate details of the propeller effect close to the propeller domain the rotating propeller has to be included into the simulation.

4 Outlook

The comparison of the simulations with a propeller and a propeller model shows in general that the propeller model works fine with a constant draught of a ship. The next step is to include the free water surface around the ship. But this needs a lot of manpower on grid generation and adaptation of the numerical calculation onto the new problem. The simulation of the free water surface needs a finer numerical grid to dissolve the water surface. The computation effort increases because it takes a lot of time to form the wave pattern, as there are air and water phases. In order to investigate the influence of the free water surface onto the propeller region, two calculations were realised without consideration of any propulsion system, one with a constant draught and the other with a free water surface. These calculations showed that there is only a minor variation of the velocity distribution between the calculations in the observed yz-plane. The current calculation includes the free water surface in combination with the propeller model. First results of this calculation are shown in Figures 11-12. Figure 11 demonstrates the wave pattern and Figure 12 shows the velocity distribution of the current calculation on a longitudinal plane at the propeller rotation axis. The calculation is not finished yet, but at this moment there are only small differences between the calculation with and without free water surface. The next step is to combine the rotating propeller with the free water surface. By including the free surface we look forward to get results almost like reality.

5 Acknowledgment

The authors thank the German Shipyard Flensburger Schiffbau-Gesellschaft mbH & Co. KG (FSG) for providing the geometry data and the Center for Communication and Informationprocessing of the University of Dortmund for computation capacity on the LiDo-Cluster. Furthermore the authors thank Mrs. cand. arch. nav. S. Suplie and Mr. cand. arch. nav. M. Gutsch for their supporting work.

References

[1] Kruppa, C., Methodical cavitation test on blade sections. Three component forces and cavitation patterns. Vosper, Report no. 115, 1963

[2] Lewis, E. V., Principles of Naval Architecture, Vol.II, Resistance, Propulsion and Vibration, SNAME, 1988

[3] Steden, M., Skrzypczak, T., Abdel-Maksoud, M., Wolf, E., Simulation of Submarine Manoeuvres using CFD, UDT Europe, 2006

Figures

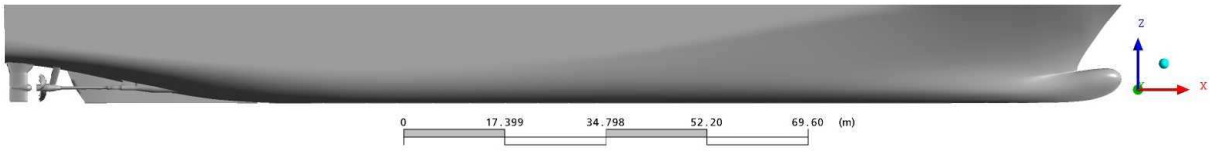

Figure 2: Investigated ship

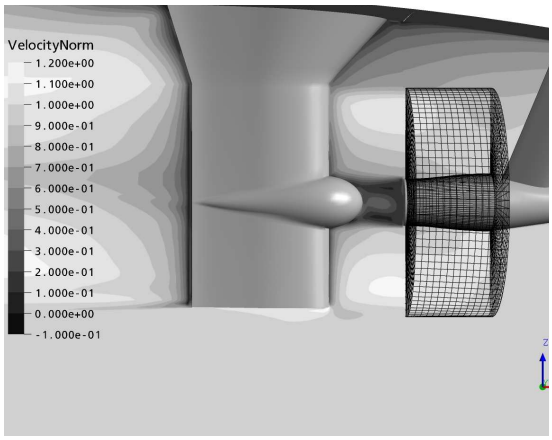

Figure 3: XZ-Plane, VelocityNorm, Propeller model

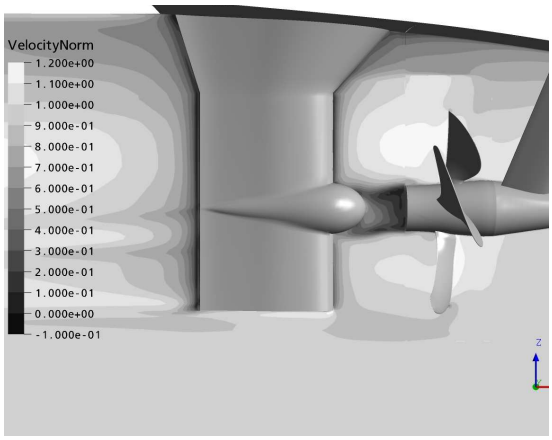

Figure 4: XZ-Plane, VelocityNorm, steady state simulation

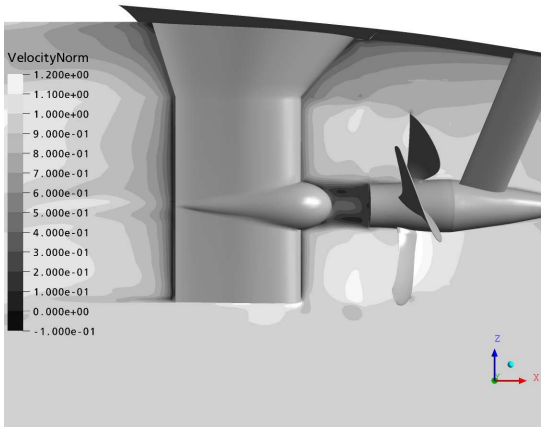

Figure 5: XZ-Plane, VelocityNorm, transient simulation, 0 and 90 degree

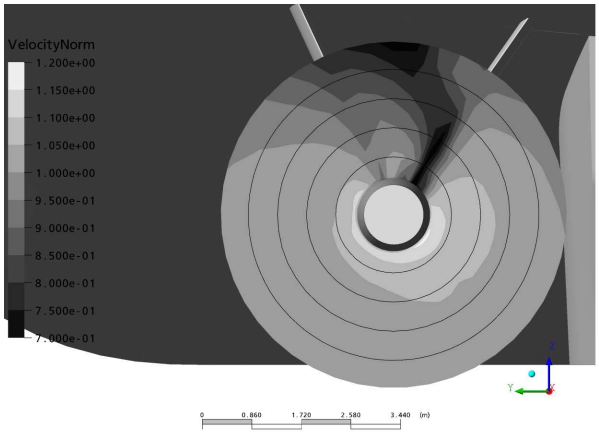

Figure 6: YZ-Plane, VelocityNorm, Propeller model

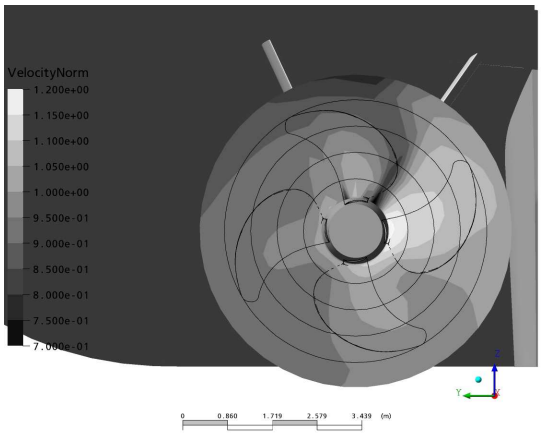

Figure 7: YZ-Plane, VelocityNorm, steady state simulation

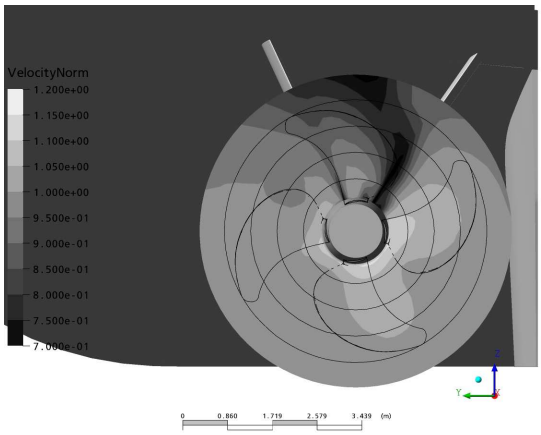

Figure 8: YZ-Plane, VelocityNorm, transient simulation, 0 and 90 degree

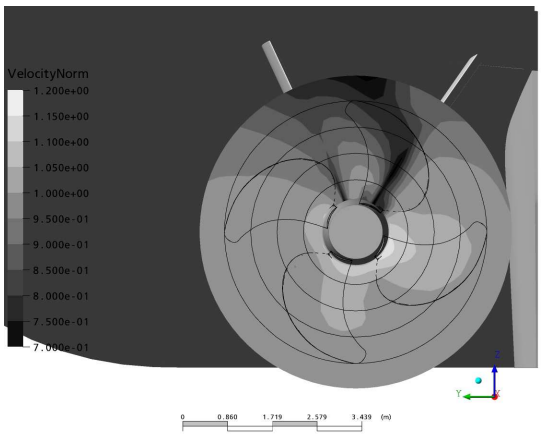

Figure 9: YZ-Plane, VelocityNorm, transient simulation, 30 degree

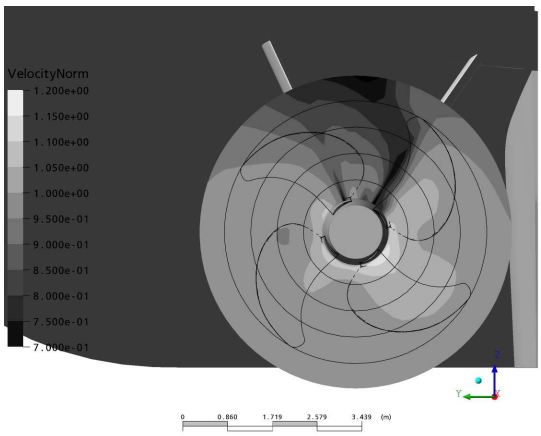

Figure 10: YZ-Plane, VelocityNorm, transient simulation, 60 degree

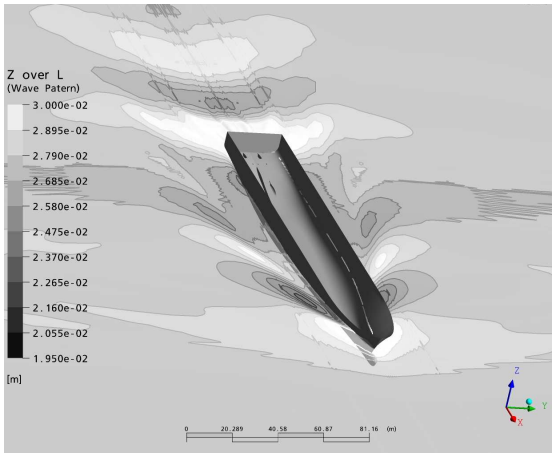

Figure 11: Wave pattern of a free water surface calculation including the propeller model

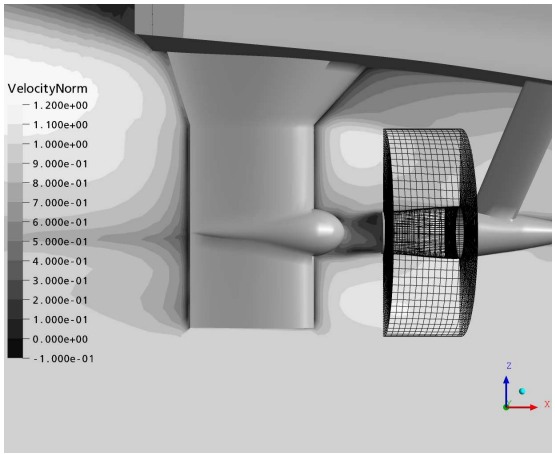

Figure 12: XZ-Plane, Free water surface, VelocityNorm, Propeller model

Validation of Ship Motion Functions of PDSTRIP for Some Standard Test Cases

Fulvio PALLADINO, Benjamin BOUSCASSE, Claudio LUGNI
f.palladino@insean.it, b.bouscasse@insean.it, c.lugni@insean.it
INSEAN, Rome/Italy
Volker BERTRAM
volker.bertram@ensieta.fr
ENSIETA, Brest/France

PDSTRIP, *Bertram et al. (2006a,b)*, computes the seakeeping of displacement ships according to the 'strip method'. The theory behind the code is extensively documented in an internal documentation available from Volker Bertram. We will focus here on a recent validation study, and just recall the essential information necessary to understand the results.

Responses in regular waves are given as response amplitude operators (RAOs). We compared so far only motion RAOs and added resistance. The test cases were standard test cases recommended by ITTC, namely the Series 60 ($C_B = 0.6$ and $C_B = 0.8$), the S-175 containership, the DDG51 destroyer hull (designated C2340 by INSEAN). We focus here on the Series-60 and DDG51, for reasons of limited space, and will publish the results for the S-175 ship in the future. The features of the analized hulls are described in Table I.

Motions are defined with respect to a right-handed coordinate system with x pointing forward, z pointing down. The coordinate system's origin is not at the center of gravity, but usually chosen at the level of the keel.

Table I: Data for investigated ships; mixed moments of inertia assumed to be zero

	Series 60, $C_B = 0.8$	DDG51	Series 60, $C_B = 0.6$
length L_{pp}	260.00 m	142.00 m	4.50 m
width B_{wl}	40.10 m	19.10 m	0.60 m
draft T	16.00 m	6.16 m	0.240 m
block coeff. C_B	0.8	0.507	0.6
LCG aft amidship	6.726 m	0.473 m	0.06 m
KG	16.00 m	7.57 m	0.230 m
mass m	133420 t	8475 t	0.388 t
r_x^2	257.282 m^2	58.369 m^2	0.0576 m^2
r_y^2	4225.00 m^2	1260.25 m^2	1.235 m^2
r_z^2	4225.00 m^2	1260.25 m^2	1.235 m^2

Computational results are compared to experiments performed at INSEAN. The model scale was $\lambda = 1 : 24.8$ for the DDG51. The experiments used the transient test approach of Clauss, described e.g. in *Landrini and Bertram (2002)*, *Lugni et al. (2000)*. In this approach, the model is accelerated to target speed, then subjected to a wave package consisting of several different wave length. The recorded time history of motions is decomposed in a Fourier analysis to obtain the RAOs for each wave length. This approach allows to measure the RAO curve for an angle of incidence for the whole interval of interesting frequencies in one measuring run, albeit at the expense of some accuracy. The RAO curves then exhibit typically some wiggles around the 'correct' RAO curve as obtained by a series of experiments with one frequency each for each measuring run.

Due to the different origin chosen in PDSTRIP and in the experiments, the results needed post-processing before they could be compared. Let x_0, z_0 denote the PDSTRIP origin (typically

keel, amidship) in the coordinate system of the experiments. (The origin is generally placed in the centerplane and thus we have always $y_0 = 0$). Then the complex amplitudes of motions are transformed to the system of the measurements for comparison by:

$$\hat{u}'_1 = \hat{u}_1 - \hat{u}_5 \cdot z_0 \quad (1)$$

$$\hat{u}'_2 = \hat{u}_2 + \hat{u}_4 \cdot z_0 - \hat{u}_6 \cdot x_0 \quad (2)$$

$$\hat{u}'_3 = \hat{u}_3 + \hat{u}_5 \cdot x_0 \quad (3)$$

Here the prime indicates the motions transformed to the coordinate system of the measurements. After transformation, the absolute values of the complex amplitudes are taken. The notation here follows *Bertram (2000)*, using the hat symbol to indicate a complex amplitude. Alternatively, PDSTRIP allows to specify points at which the motions are computed. Then the origin of the coordinate systems used in the measurements can be used.

We suspect that frequently no attention is paid to different origins in seakeeping comparisons. This is partly due to the fact that often the origin of the measurements is not well documented. Similarly, mass moments of inertia must often be estimated or guessed, as these are often not documented in reports of measurements.

The first studied test case is the Series-60, $C_B = 0.8$. Four Froude numbers were investigated: 0.15, 0.2, 0.25, 0.3. For this case, we were able to compare with model tests performed at TU Delft, *Gerritsma (1960)*. Fig.1 compares PDSTRIP results with these masurements for head seas. The computations overpredict motions near the resonance, due to neglect of non-linear damping effects. The differences become more pronounced for higher speeds, probably due to neglect of the change in trim and sinkage because of forward speed. Though the overall results appear plausible. The pitch results show again the expected behaviour for very short and very long waves, but underestimate the measured peak. This may be due to errors in specifications of the mass moment of inertia in pitch; again, care must be taken in specifying the value with respect to the origin of PDSTRIP.

The Series-60, $C_B = 0.6$ was investigated at three Froude numbers: 0.15, 0.2, 0.25, and the results compared with both model tests, TU Delft and *Nakamura (1966)*. PDSTRIP predicts larger values at heave resonance due to the larger non-linear damping in reality, Fig.2. For pitch, PDSTRIP underestimates again the maxima. Further studies on the assumed mass moment of inertia in pitch may be necessary to understand this difference. For this model, we also compare added resistance values, Fig.3. The added resistance captures the position of the maximum well, but overpredicts the total value in comparison with the experiments by *Strom-Tejsen et al. (1973)*. This is to be expected, as (a) the heave amplitude was overpredicted due to nonlinear damping effects and (b) the resistance is sensitive to errors in motions.

The DDG51 was investigated at four different Froude numbers F_n, namely 0.19, 0.28, 0.34, and 0.41. Fig.4 gives the RAOs for heave and pitch in head waves. The heave RAO of PDSTRIP show the typical behavior converging towards 1 for long waves. The maximum at resonance becomes more pronounced with increasing speed. PDSTRIP predicts larger heave amplitudes at resonance than measured. This can be attributed to the neglect of non-linear (geometric) damping. In pitch, both measurements and computations tend towards the same expected results for very short and very long waves. The measured pitch shows a more pronounced maximum.

For the DDG51, we investigated also the influence of grid fineness on the results, generating grids with different numbers of points per strip and numbers of strips as listed in Table II. The standard grid used 28 strips and 37 points over the circumference of each strip. The results showed that the standard grid was fine enough to obtain virually grid-independent solutions.

Table II: Investigated grids for DDG51; points per strip for complete section port+starboard

Grid	1	2	3	4	5	6	7	8	9
points per strip	7	13	25	37	77	97	37	77	97
strips	28	28	28	28	28	28	57	57	57

In conclusion, the validation of PDSTRIP is very much 'work in progress' and we need more information on experiments, particularly mass distribution data, as well as more information coming from other linear strip method, linear potential flow codes, nonlinear potential flow codes and CFD simulations to understand better which errors are due to the inherent flow model (potential flow, linear), which due to input errors (wrong interpretation of required input by user due to difficult user interface or e.g. wrong estimation of mass moment of inertia), which due to errors (or uncertainties) in measured data.

Acknowledgement

We acknowledge gratefully the aid and advice of Prof. H. Söding in this study.

References

BERTRAM, V. (2000), *Practical Ship Hydrodynamics*, Butterworth & Heinemann, Oxford

BERTRAM, V.; SÖDING, H.; GRAF, K. (2006a), *PDSTRIP - A strip method for ship and yacht seakeeping of a public domain strip method*, 9^{th} Numerical Towing Tank Symposium, Le Croisic

BERTRAM, V.; VEELO, B.; SÖDING, H.; GRAF, K. (2006b), *Development of a freely available strip method for seakeeping*, 5^{th} Int. Conf. Computer and IT Applications in the Maritime Industries, Ould Poelgeest
www.3me.tudelft.nl/live/binaries/cf8c31ad-a975-4aa0-9f0e-e680d5aad97d/doc/Compit06_Proceedings.pdf

LANDRINI, M.; BERTRAM, V. (2002), *Three-dimensional simulation of ship seakeeping in time domain*, Jahrbuch der Schiffbautechnischen Gesellschaft, Springer

LUGNI, C.; MASIA, M.; GRAZIANI, G. (2000), *Experimental investigation of the seakeeping of a frigate model*, Ship Tech. Res. 47/4, pp.155-160

GERRITSMA J. (1960), *Ship motion in longitudinal waves*, International Shipbuilding Progress, Vol. 7, No. 66

NAKAMURA S. (1966), *Experiments on the Series 60 $C_B = 0.6$ and 0.7 ship models in regular head waves*, Contribution to 11^{th} I.T.T.C.

STROM-TEJSEN J., YEH H.Y.H. and MORAN D.D. (1973), *Added resistance in waves*, Trans. SNAME

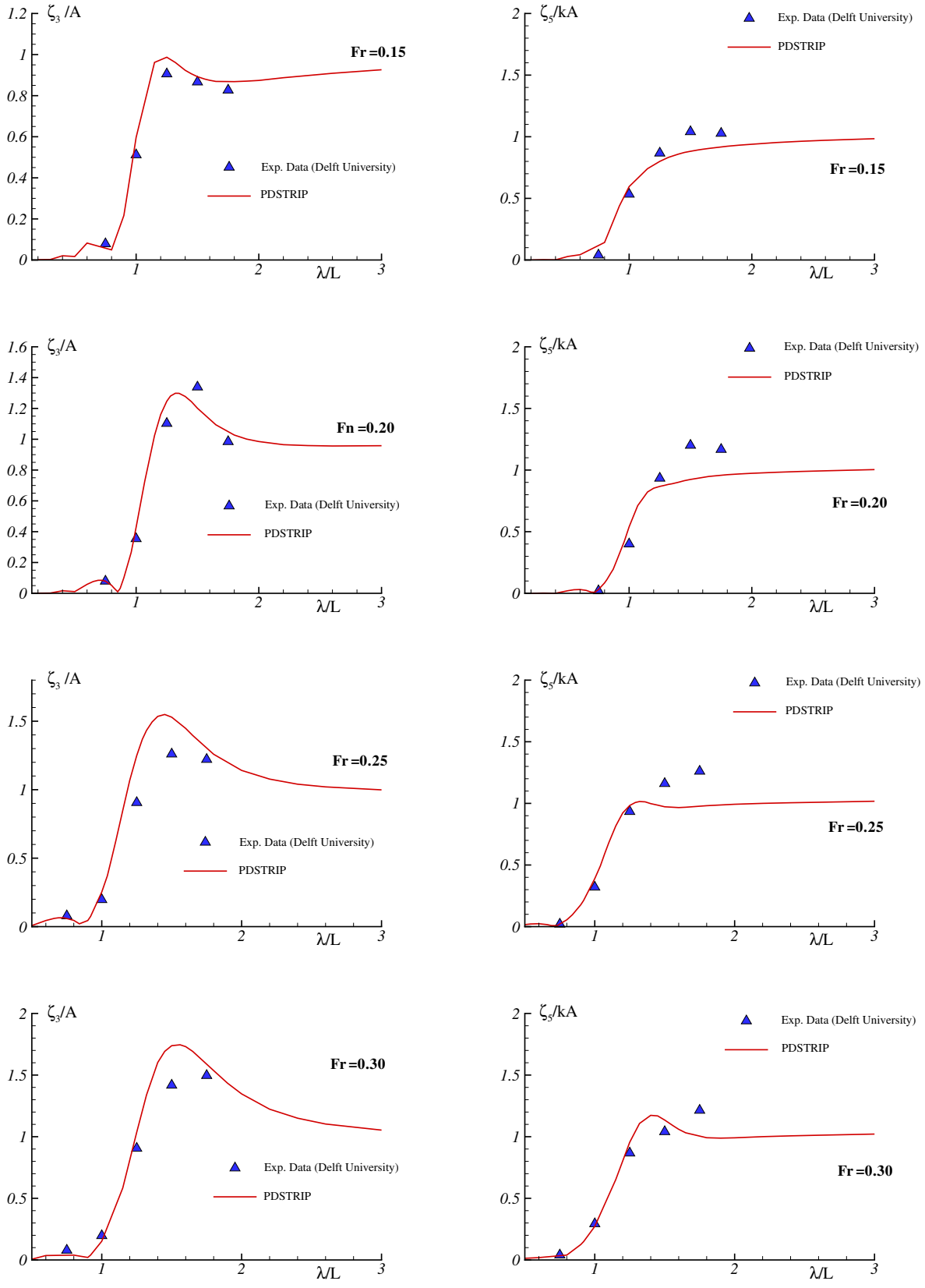

Fig.1: Heave (left) and pitch (right) RAOs for Series-60 ($C_B = 0.8$), $\mu = 180°$

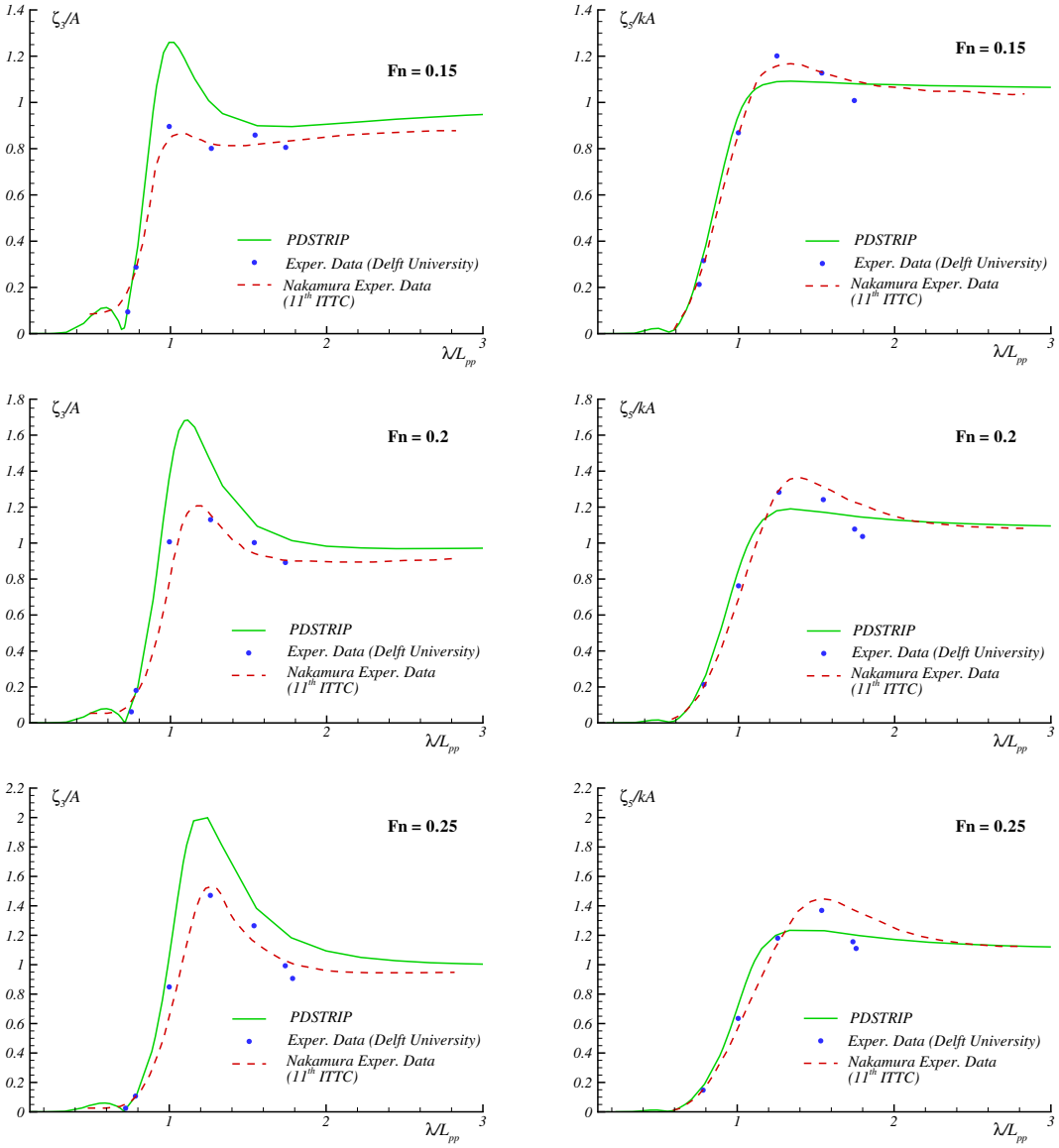

Fig.2: Heave (left) and pitch (right) RAOs for Series-60 ($C_B = 0.6$), $\mu = 180°$

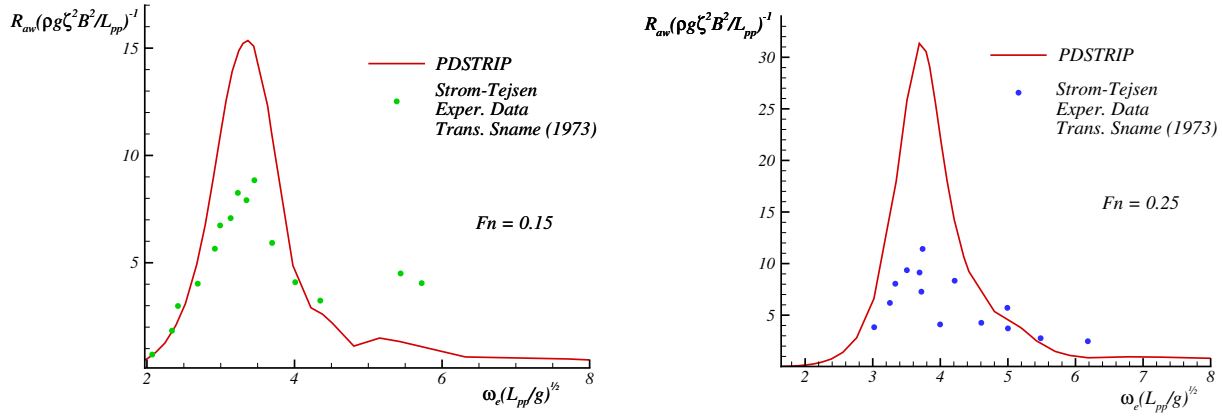

Fig.3: R_{aw} RAO for Series-60 ($C_B = 0.8$) (left) and for Series-60 ($C_B = 0.6$) (right), $\mu = 180°$

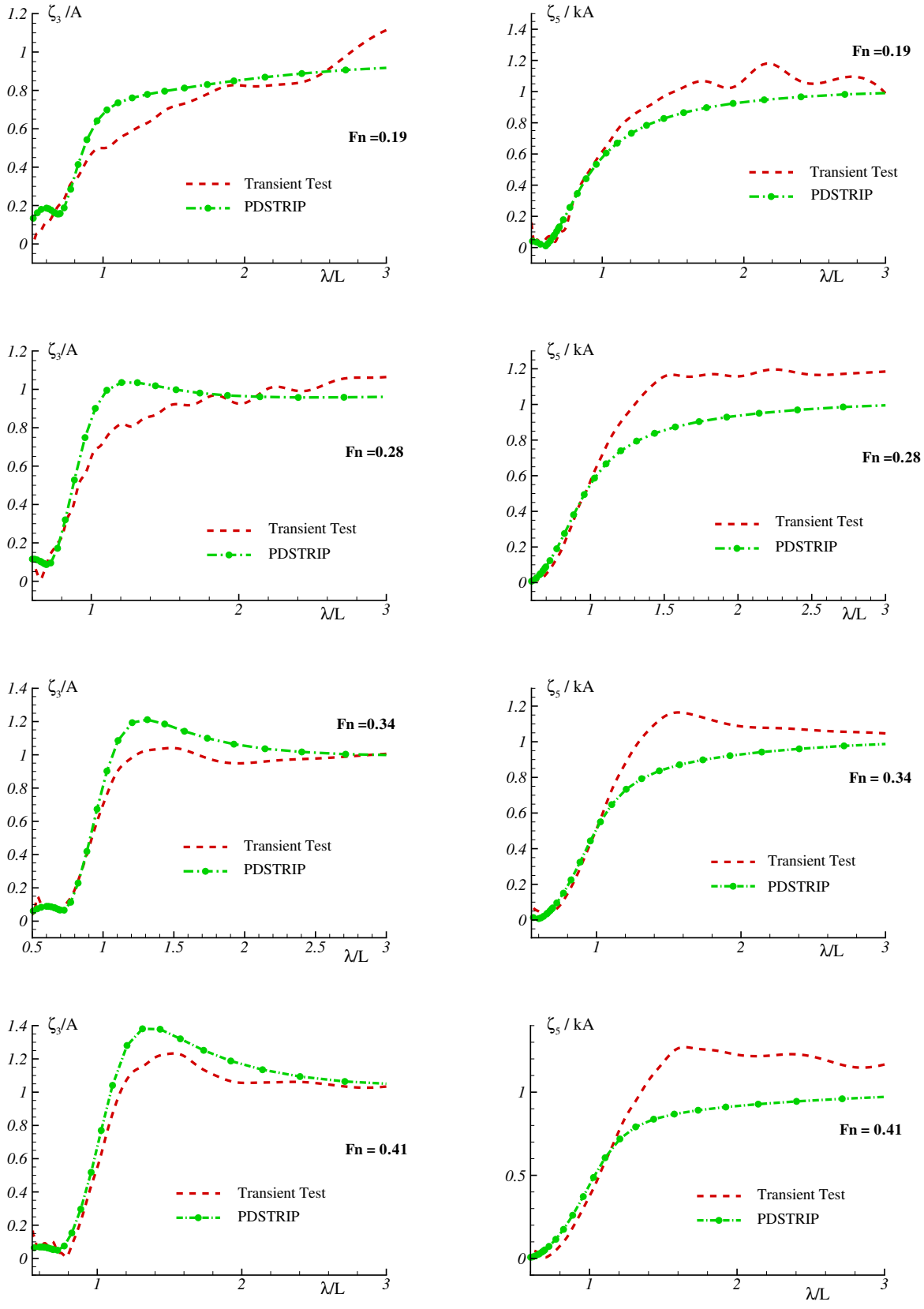

Fig.4: Heave (left) and pitch (right) RAOs for DDG51, $\mu = 180°$

Numerical Investigation on the Effect of Baffle Arrangement in Tanker Sloshing

R. Panahi, E. Jahanbakhsh, M.S. Seif
Marine Lab., Dept. of Mechanics, Sharif University of Technology, Tehran, Iran
seif@dharif.edu

Introduction

Sloshing can be described as the motion of a fluid as it attempts to attain a state of equilibrium for the instantaneous acceleration caused by the tank motion. This results in the acoustical effects in high velocity motions, impulsive loads and the effect on the dynamic motions of the tank. Sloshing is associated with various engineering problems such as liquid oscillation in large storage tanks caused by earthquake, motion of fuel in aircrafts, green water on ship decks, liquid transporting vessels e.g. LNG carriers and moored floating production storage and offloading units (FPSO).

The sloshing flow usually includes complicated phenomena such as formation of jets and sprays, wave overturning and breaking which make it a well-known complex numerical problem. It has evoked the attention of scientific researchers since as early as the 1950s [1]. In the early days of such studies, when the computer simulation was in its infancy, several analytic methods were proposed in the area of mild sloshing problems [2, 3, 4]. However, the clear limitations of analytic methods and development in computer capabilities resulted in wide variety of numerical methods. There have been four major approaches in numerical simulation of liquid sloshing which are [5]: (1) boundary element methods [6, 7], (2) finite element method for potential flow [8, 9, 10], (3) finite difference/volume methods for solving the Euler/Navier-Stokes equations [5, 11, 12] and smoothed particle hydrodynamics (SPH) method [13].

This paper is organized as follows. The numerical method including governing equations, discretisation and solution algorithm is described briefly. Then, sloshing in a fixed rectangular tank with initialized free surface is simulated and the fluid elevation is obtained to show the ability of presented method in two phase flow simulation. Water sloshing in a rotating container is also simulated and the pressure is measured in a specified point to verify the accuracy of pressure-velocity coupling. Finally, different arrangements of baffles are investigated for the first natural frequency of fluid in a rectangular tank which shows the importance of such walls in tanks. When the frequency of the tank motion approaches one of the natural frequencies of the tank fluid, large sloshing amplitudes are created. It must be mentioned that, only the first natural frequency is significant for marine applications [14]. In conclusion, such an approach can be used in any condition to optimize the design aspects related to problem.

2. Numerical Method

2.1 Governing Equations

Complex deformation of interface in hydrodynamic problems e.g. liquid sloshing leads to use of volume methods in free surface modeling. Here a scalar transport equation which is extracted from the continuity equation [15] (Eq.1) is solved to determine the volume fraction of each phase (e.g. water and air) in all computational cells:

$$\frac{\partial \alpha}{\partial t} + \vec{\nabla}.(\alpha \vec{u}) = 0 \tag{1}$$

This results in α distribution which will be zero for fluid 1, one for fluid 2 and values between zero and one at the interface. In this case, the effective fluid with variable physical properties is introduced:

$$\rho_{eff} = \alpha \rho_1 + (1-\alpha)\rho_2 \;;\; \nu_{eff} = \alpha \nu_1 + (1-\alpha)\nu_2 \tag{2}$$

where subscripts 1 and 2 represent two phases. Such an effective fluid is used in solving the fluid main governing equations. These are momentum and continuity equations which are as follows:

$$\frac{\partial u_i}{\partial t} + u_j \frac{\partial u_i}{\partial x_j} = -\frac{1}{\rho}\frac{\partial P}{\partial x_i} + \nu \frac{\partial^2 u_i}{\partial x_j \partial x_j} + g_i \tag{3}$$

$$\frac{\partial u_i}{\partial x_i} = 0 \tag{4}$$

Finally, it must be mentioned that, a body-attached mesh which follows the time history of body motions is used. This strategy enables the solver to simulate rigid body motions by solving the linear and angular momentum equations in each time step. Although, here the liquid container mesh is moved according to forced motions. In addition, all of the fluid governing equations are written for a moving Control Volume (CV) in Newtonian reference system (Fig.1).

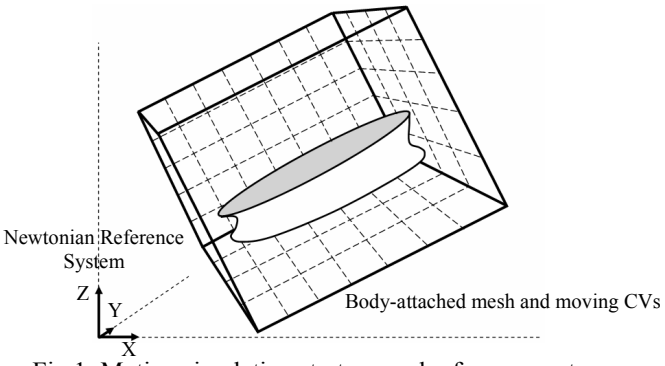

Fig.1: Motion simulation strategy and reference system

2.2. Discretisation

By applying the Gauss theorm for spatial discretisation and Crank-Nicholson scheme for time discretisation of the finite volume form of Eq.1, it becomes as follows:

$$(\alpha^{t+\delta t}-\alpha^{t})\frac{V}{\Delta t}+\frac{1}{2}(\sum_{f=1}^{n}\alpha_f^{t+\delta t}F_{f-rel}^{t+\delta t}+\sum_{f=1}^{n}\alpha_f^{t}F_{f-rel}^{t})=0 \tag{5}$$

where α_f is the face volume fraction which must be approximated based on CVs' center value. CICSAM (Compressive Interface Capturing Scheme for Arbitrary Meshes) [17] is used for this purpose which uses CBC [18] (Convection Boundedness Criteria) and UQ [19] (ULTIMATE QUICKEST) interpolations by introducing a weighting factor. More details are described by Panahi et al.[16]. $F_{f-rel}=(\vec{U}_f-\vec{U}_m).\vec{A}_f$ is the relative volumetric flux at the CV face. Here the colocated arrangement is used and therefore fluid velocity at CV face $\vec{U}_f$ must be calculated in an approperiate manner. In addition, $\vec{U}_m$ is the only effect of moving CV in governing equations.

About the Navier-Stokes equations, the diffusion and convection terms are discretised by using over-relaxed and Gamma interpolations [20], respectively. It must be mentioned that, the Crank-Nicholson scheme is used for time discretisation of diffusion and convection terms. However, the major concern in discretisation of Navier-Stokes equations is the pressure integral, especially when there are two fluids with high density ratio e.g. water and air. Using the common linear interpolations for calculation of face pressure P_f based on CVs' center value, results in severe oscillations in velocity field. Here, Piecewise Linear Interpolation (PLI), a new discretisation scheme, is introduced as shown in Fig.2. It is based on a constraint for lines L_{Af} and L_{Bf} which connect pressure values at CVs' center P_A and P_B to P_f. In this manner, P_f is estimated as Eq.6, where ρ_A and ρ_B are CVs' A and B densities:

$$P_f=P_A\frac{\rho_B\delta_B}{\rho_A\delta_A+\rho_B\delta_B}+P_B\left(1-\frac{\rho_B\delta_B}{\rho_A\delta_A+\rho_B\delta_B}\right) \tag{6}$$

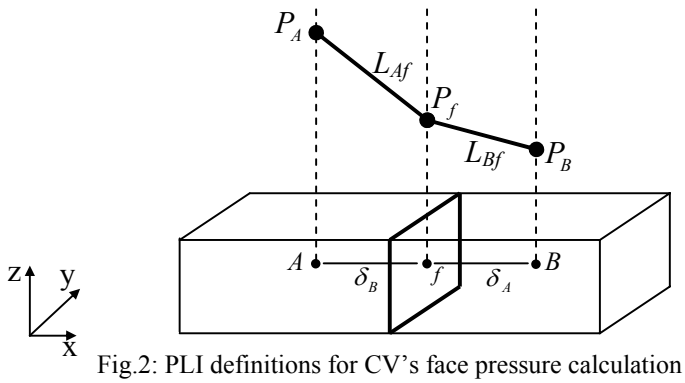

Fig.2: PLI definitions for CV's face pressure calculation

2.3 Solution Algorithm

Usual approach in calculation of velocity and pressure distribution in presence of two phase flow is to solve the Navier-Stokes and continuity equations for an effective fluid [21]. Here, Eq.1 is solved based on CICSAM interpolation which results in effective fluid properties by using Eq.2. For calculation of velocity and pressure fields, the fractional step method of Brown [21, 22] is applied.

As aforementioned, in the colocated arrangement used in the current algorithm, face velocities must be calculated separately, including the effect of pressure gradient to overcome to checkerboard pressure. Here, the method of Zang [23] is used for such a purpose.

3. Numerical Results

3.1. Wave Sloshing

The wave sloshing under the influence of gravity has been investigated. The situation is shown in Fig.3, which is the same as used by Raad et al. [24]. Initially, the quiescent fluid free surface elevation is defined by $y(x)=0.05+0.005\cos(\pi x)$. The domain is discretised with 160 cells in the horizontal direction and 104 cells in the vertical direction. Slip and zero-gradient boundary conditions are used for velocity and pressure at all boundaries, respectively. In this case, the fluid begins to slosh solely under the influence of constant gravitational field. The theoretical period of sloshing of the first mode is $T=2\pi\sqrt{g\,k\tanh(kh)}=0.3739\,s$, where k is the wave number and h the average fluid depth [24].

After a quarter of a period the potential energy of the system is transferred to kinetic energy and the velocities reach their maximum. After a half period, all the kinetic energy is transferred back into potential energy with the velocity almost back to zero. Fig.4 shows plots of the position of interface at the left boundary against time. The frequency corresponds with the theoretical one, so do the amplitudes of even periods.

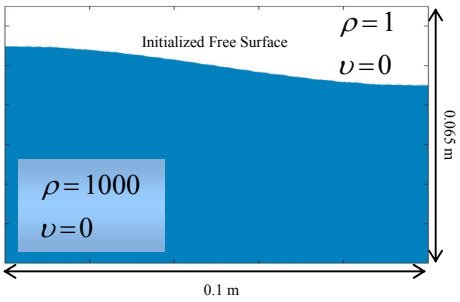

Fig.3: Initial geometry of the sloshing problem

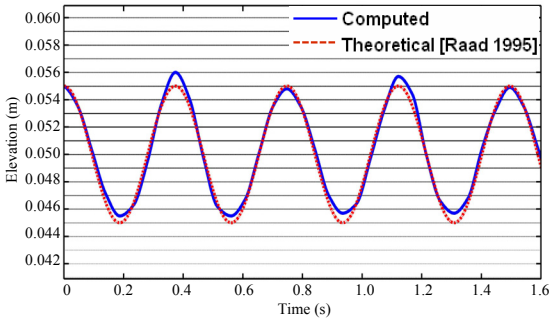

Fig.4: Position of the interface at the left wall

3.2. Oscillating Tank Sloshing

The next series of investigation is the forced oscillating tank sloshing. Rectangular tank of Fig.5 is subjected to a forced harmonic excitation. The geometry is as well as Akyildiz and Unal [25]. In their experiments they recorded pressure histories at several locations along the tank wall for up to 85 s. For the numerical computation a uniform grid of 10000 CVs is used. No-slip and zero-gradient boundary conditions are used at all boundaries for velocity and pressure, respectively. In this simulation the top boundary is located 30 cm above the bottom and water does not touch it.

Pressure history on the left wall of the tank 6 cm above the bottom for $\omega=2.0\,rad/s$, initial roll angle of zero degree, water depth of 0.154 cm and roll amplitude of 4 deg is obtained from Akyildiz. The computed and experimental pressure histories are presented in Fig.6. The figure indicates that both motion frequency and pressure values are captured very well.

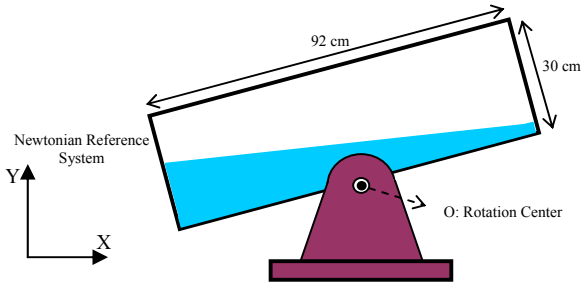

Fig.5: Oscillating tank geometry

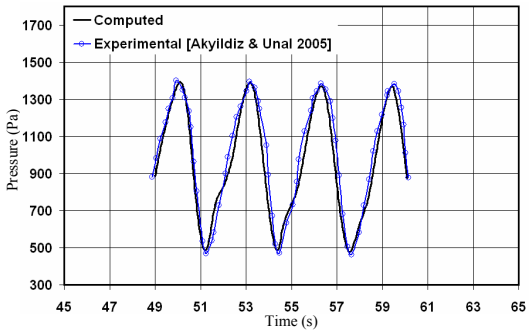

Fig.6: Pressure time history on the left tank wall, 6 cm above the bottom

3.3. Baffled Tank Sloshing

In practice, baffles are used to reduce dynamic pressures on tanks. In these cases analytical solutions can not be derived and the only solution is numerical modeling. In this section the effect of baffle arrangement is investigated for the tank shown in Fig.7 with the initial water depth of *D=0.3m*. The baffle dimension is *0.01*0.2m*. Tank is excited with sinusoidal rotation of $\omega = \omega_n$ and roll amplitude of 4 deg. It must be noted that, for a given tank geometry, the natural frequency of the fluid depend on the depth of fluid *D* and tank width L. This can be calculated from linear theories [14]. For rectangular prismatic tanks, the natural frequencies are given by $\omega_n^2 = g\frac{n\pi}{L}\tanh\left(\frac{n\pi}{L}D\right)$ where *n* is the mode number. By taking n=1, the first natural frequency is $\omega_n = 2.46\, rad/s$. At this frequency, a hydraulic jump forms that travels periodically between the walls of the tank. Here, the baffles are considered in different arrangements. For this purpose, δ which is measured from the bottom of the tank, varies up to 40 cm (Fig.7). A non-uniform grid of 9000 CVs is used for all cases, approximately. No-slip and zero-gradient boundary conditions are used at all boundaries for velocity and pressure, respectively.

A primary quantity of interest in sloshing problem is the roll moment on tank due to the motion of liquid. This can be coupled to a dynamic analysis to compute the interaction between the liquid motion and the ship. Since the motion is 2D planner in *(x ,y)*, the roll moment is in the z direction. The moment about the point O, the rotation center (Fig.5), is computed by $\vec{M}_A = \int_S P(\vec{r}\times\vec{n})dS$, where *S* is the inner wall of the tank, *P* is the wall pressure distribution, $\vec{r}$ is the position vector from O to point *dS* on the tank inner wall and $\vec{n}$ is the unit outward normal from the inner wall of the tank.

The effect of baffle level on free surface deformation is shown in Fig.7 after one period at the instant time of *t=2.55s*. Also, Fig.8 shows the maximum momentum exerted on tank wall in different baffle arrangements. The first series of investigation carried out for $\delta =$ *0.1*, *0.2*, *0.3* and *0.4 m*. Results implied that, baffles in *0.3m*, which is equal to the initial free surface elevation, apparently reduces the maximum momentum. Therefore, *0.25m* and *0.35m* arrangements were studied. In the case of *0.25 m*, the maximum momentum reduced about 67.7 percent form the case of non-baffled tank. In Fig.8 a line is fitted according to investigated arrangements. It seems that a position between *0.25* and *0.3m* is the most effective level. It most be remembered that all cases are investigated in the natural frequency which has the maximum sloshing moment because of hydraulic jump.

4. Conclusion

Numerical modeling is the only efficient way for simulation of sloshing in tanks equipped with baffles. The numerical algorithm presented in this paper shows good agreement with available data and it is possible to apply it for arbitrary tank geometry and baffles. As an example, the effect of horizontal baffle level form tank bottom has been studied. The results show considerable reduction on moment due to change in this parameter. The moment can be reduced to less than 30 percent relative to non-baffled tank. Therefore, it is possible to find out the best solution and reduce the moment exerted on tank as much as possible in an optimization process.

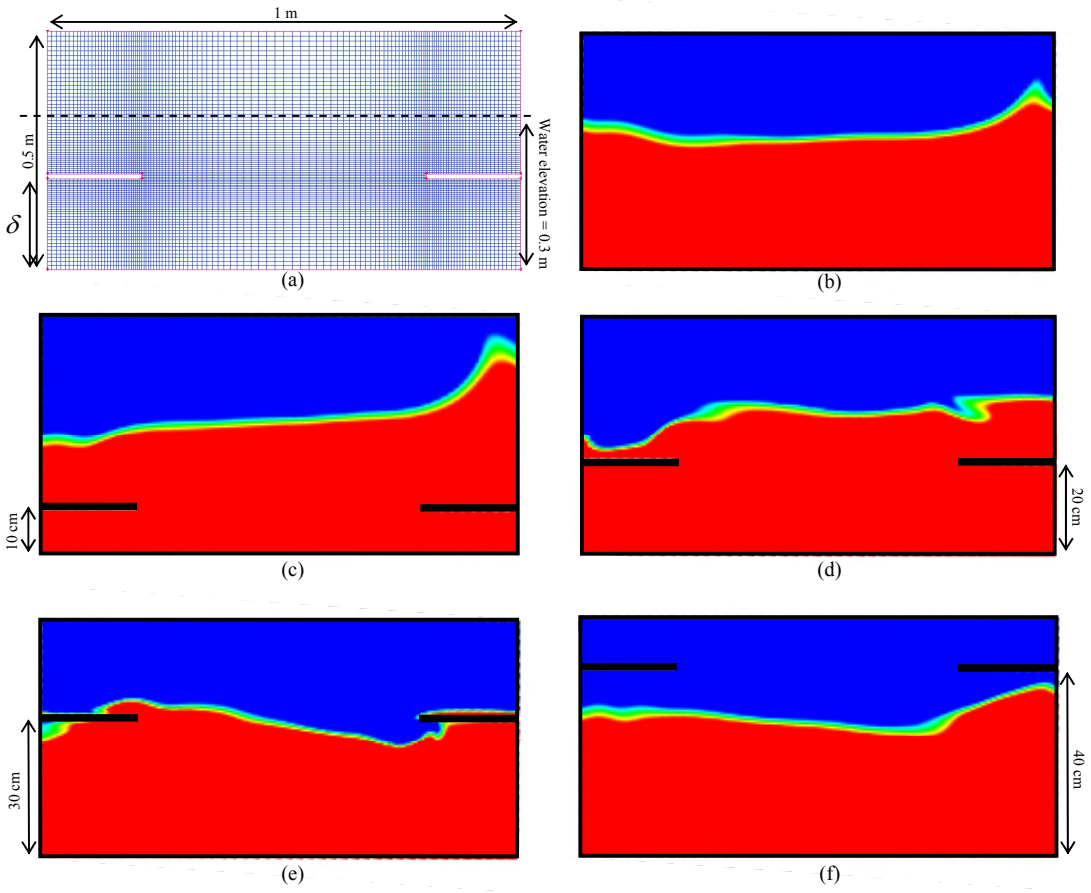

Fig.7. Free surface deformation in different baffle arrangement at t=2.55s:
(a) mesh and definition, (b) Non-baffled tank, (c) δ = 10cm, (d) δ = 20 cm, (e) δ = 30 cm, (f) δ = 40 cm

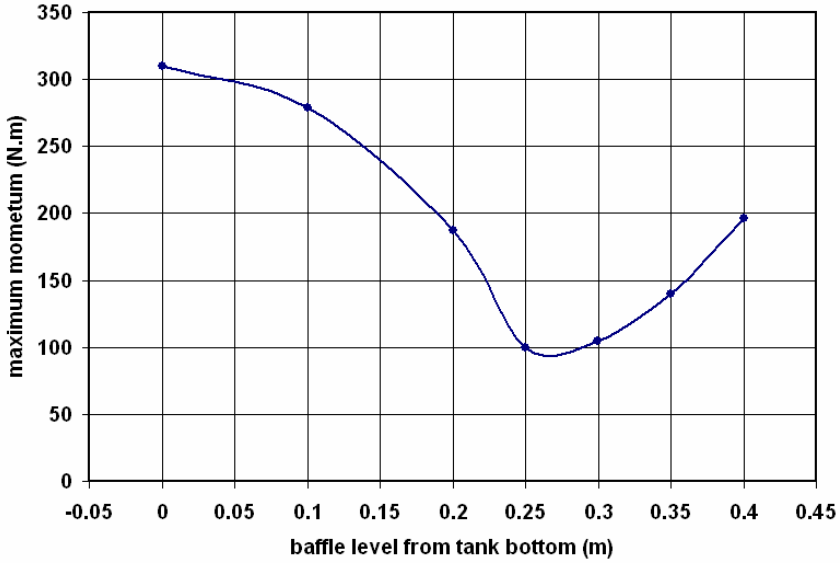

Fig.8. Maximum momentum on tank

5. References

1. Graham, E.W., *The forces produced by fuel oscillation in rectangular tank*, Douglas Aircraft Company Report, SM 13748, (1951).
2. Verhagen, H.G. and Wijngaarden, L.V., *Nonlinear oscillation in a fluid container*, J. of Fluid Mechanics, Vol.22, p.738-751, (1965).
3. Abramson, H.N., *The dynamic behavior of liquids in moving containers*, NASA SP-106, (1966).
4. Faltinsen, O.M., *A nonlinear theory of sloshing in rectangular tanks*, J. Ship Research, Vol.18(2), p.224-241, (1974).
5. Rhee, S.H., *Unstructured grid based Reynolds-Averaged Navier-Stokes method for liquid tank sloshing*, Transaction of ASME, Vol.127, p.572-582, (2005).
6. Liu, Z. and Huang, Y., *A new method for large amplitude sloshing problems*, J. Sound Vibration, Vol.175(2), p.185-195, (1994).
7. Kim, Y., Shin, Y.S., Lin, W.M. and Yue, D.K.P., *Study on sloshing coupled with ship motion in waves*, Proc. 8th Int. Conf. on Numerical Ship Hydrodynamics, Busan, Korea, (2003).
8. Okamoto, T. and Kawahara, M., *3-D sloshing analysis by an arbitrary Eulerian-Lagrangian finite element method*, Int. J. of Computational Fluid Dynamics, Vol.8(2), p.129-146, (1997).
9. Kim, J.W., Shin, Y. and Bai, K.J., *A finite-element computation for the sloshing motion in LNG tank*, Proc. 12th Int. Offshore and Polar Engineering Conf., Fukuoka, Japan, (2002).
10. Guillot, M.J., *Application of a discontinuous Galerkin finite element method to liquid sloshing*, J. of Offshore Mechanics and Arctic Engineering, Vol.128, p.1-10, (2006).
11. Kim, Y., *Numerical simulation of sloshing flows with impact loads*, Applied Ocean Research, Vol.23, p.53-62, (2001).
12. Celebi, M.S. and Akyildiz, H., *Nonlinear modeling of liquid sloshing in moving rectangular tanks*, Ocean Engineering, Vol.29, p.1527-1553, (2002).
13. Iglesias, A.S., Pavon, C.L. and Fraysse, B., *SPH simulation of free surface movement of passive stabilizing tanks for fishing vessels*, Proc. 8th Int. Conf. on Numerical Ship Hydrodynamics, Busan, Korea, (2003).
14. Su, T.C., Lou, Y.K., Flipse, J.E. and Bridges, T.E., *A numerical analysis of large amplitude liquid sloshing in baffled containers*, US Department of Commerce, Final Report, MA-RD-940-82046, (1982).
15. Spalding, D.B., *A method for computing steady and unsteady flow possessing discontinuities of density*, CHAM Report 910/2, (1974).
16. Panahi, R., Jahanbakhsh, E. and Seif, M.S., *Comparison of Interface Capturing Methods in Two Phase Flow*, Iranian Journal of Science & Technology, Transaction B: Technology, Vol.29, No. B6, (2005).
17. Ubbink O. and Issa, R.I., A *method for capturing sharp fluid interfaces on arbitrary meshes*, J. of Computational Physics, Vol.153, p.26-50, (1999).
18. Gaskell, H. and Lau, A.K.C., *Curvature-compensated convective transport: SMART, a new boundedness-preserving transport algorithm*, Int. J. of Numerical Methods in Fluids, Vol.8, p.617-641, (1988).
19. Leonard, B.P., *The ULTIMATE conservation difference scheme applied to unsteady one dimensional direction*, Computational Methods in Applied Mechanics and Engineering, Vol.88, p.17-74, (1991).
20. Jasak, H., *Error analysis and estimation for finite volume method with application to fluid flows*, PhD Thesis, University of London, (1996).
21. Jahanbakhsh, E., Panahi, R. and Seif, M.S., *Multi-dimensional free surface flow simulation using two-phase Navier-Stokes solver*, Proceeding of 8th Numerical Towing Tank Symp. (NuTTs), Varna, 2-4 October, (2005).
22. Brown, D.L., Cortez, R. Minion, M.L., *Accurate projection methods for the incompressible Navier-Stokes equations*, J. of Comput. Phys., Vol.168, p.464-499, 2001.
23. Zang, Y., Street, R.L. and Kossef, J.R., *A non-staggered grid, fractional step method for time-dependent incompressible Navier-Stokes equations in curvilinear coordinates*, J. of Computational Physics, Vol.114, p.18-33, (1994).
24. Raad, P.E., Chen S. and Johnson, D.B., *The introduction of micro cells to treat pressure in free surface fluid flow problems*, J. of Fluids Engineering, Vol.117, p.683-690, (1995).
25. Akyildiz, H. and Unal, E., *Experimental investigation of pressure distribution on a rectangular tank due to the liquid sloshing*, Ocean Research, Vol.32, p.1503-1516, (2005).

MODELLING THE CAVITATING FLOW AROUND A 3-DIMENSIONAL WING SECTION USING LARGE EDDY SIMULATION

Tobias Persson[†], **Göran Bark**[†], **Rickard Bensow**[†], **Nabila Berchiche**[†] and **Christer Fureby**[†,‡]
[†]Dept. of Shipping and Marine Technology
Chalmers University of Technology, SE 412 96 Göteborg, Sweden
[‡]Div. of Weapons & Protection, Warheads & Propulsion
The Swedish Defense Research Agency, FOI, SE 147 25 Tumba, Sweden

INTRODUCTION

Cavitation can occur in a wide range of liquid flows and this physical process is of particular interest for the marine and hydropower industries. Most applied research is performed experimentally in cavitation tunnels, limiting the knowledge to measurable quantities. Present computer models for cavitating flow, which is presently used in the marine industry, is usually based on the Boundary Element Method (BEM). BEM seriously limits the physical knowledge about the flow field, but have the advantage that the method is very fast. To involve more physics into the cavitation prediction, the Navier-Stokes Equations (NSE) have to be incorporated.

It is commonly accepted that the NSE describe what is observed as turbulence. Unfortunately, despite the steady advance in computing power and computational technology, attempts at the Direct Numerical Simulation (DNS) of the NSE have been limited to simple geometries and low Reynolds (Re) numbers. By using turbulence models based on time or ensemble-averaged quantities, i.e. Reynolds Averaged Navier-Stokes (RANS) models, the virtually impossible task of DNS have been approximated, though often crudely. The RANS approach has also been extended to incorporate unsteady modes, Unsteady RANS (URANS). Large Eddy Simulation (LES), [16], used here, is a method with lower level of approximation than RANS and URANS, but need to be examined further, especially in conjunction with cavitation.

The advantage of RANS and URANS is that it is relatively fast compared with LES. The main drawback, however, is that much of the physics is incorporated into turbulence model, leaving results which can have a very low accuracy, [13]. More accurate predictions are offered by LES, founded on separation of scales within the flow, accomplished by low-pass filtering of the NSE. Large, energy containing, structures that can exist on the computational grid are kept in the LES calculations, whereas the smaller, more isotropic structures are modelled. This gives LES a much higher generality than RANS and URANS, in which the complete spectrum of turbulent motions is modelled, and gives more physics which are needed in the cavitation prediction.

In this study the cavitating flow around a wing section is used to test the model presented in this paper. This flow includes many of the cavitating features that the presented model is supposed to handle, e.g. a tip vortex cavity and a large sheet cavity on the suction side of the wing.

GOVERNING EQUATIONS

The governing equations of an incompressible flow consist of the balance equations of mass and momentum for a linear viscous (or Newtonian) fluid, [11],

$$\begin{cases} \nabla\cdot\mathbf{v}=0, \\ \partial_t(\rho\mathbf{v})+\nabla\cdot(\rho\mathbf{v}\otimes\mathbf{v})=-\nabla p+\nabla\cdot\mathbf{S}+\mathbf{f}. \end{cases} \quad (1)$$

where $\mathbf{v}$ is the velocity, p the pressure, $\mathbf{S}=2\nu\mathbf{D}$ the viscous stress tensor with ν the kinematic viscosity, $\mathbf{D}=\frac{1}{2}(\nabla\mathbf{v}+\nabla\mathbf{v}^T)$ the rate-of-strain tensor and $\mathbf{f}$ the external forces. We must also add initial and boundary conditions to complete the mathematical description. As mentioned in the introduction the numerical simulation of turbulent flows of practical or engineering interest will require too fine computational meshes for present-day computers to handle. Consequently some level of approximation needs to be introduced into the equations. In LES a low pass filtering technique is introduced, using a kernel $G=G(\mathbf{x},\Delta)$, where Δ is the filter width, such that,

$$\begin{cases} \nabla\cdot\bar{\mathbf{v}}=m^\rho, \\ \partial_t(\rho\bar{\mathbf{v}})+\nabla\cdot(\rho\bar{\mathbf{v}}\otimes\bar{\mathbf{v}})=-\nabla\bar{p}+\nabla\cdot(\bar{\mathbf{S}}-\mathbf{B})+\bar{\mathbf{f}}+\mathbf{m}^v. \end{cases} \quad (2)$$

Equation (2) introduces three new terms when compared to the unfiltered NSE (1); the unresolved transport term $\nabla\cdot\mathbf{B}$, where $\mathbf{B}=(\overline{\mathbf{v}\otimes\mathbf{v}}-\bar{\mathbf{v}}\otimes\bar{\mathbf{v}})$ is the subgrid stress tensor and the commutation error terms, arising since differentiation and filtering generally do not commute, $\mathbf{m}^v=[G*,\nabla](\mathbf{v}\otimes\mathbf{v}+p\mathbf{I}-\mathbf{S})$ and $m^\rho=[G*,\nabla]\mathbf{v}$, where $[G*,\nabla]f=\overline{\nabla f}-\nabla\bar{f}$ defines the commutation operator and $\mathbf{I}$ is the identity tensor. Although both types of terms contribute to the closure problem, it is customary to neglect the

influence of the commutation error terms, since they are usually expected to be smaller than the effect of the unresolved transport. The subgrid stress tensor **B** can be modeled in a numerous of different ways e.g. [16]. Examples of subgrid models are the Smagorinsky model, [18], the One Equation Eddy Viscosity Model (OEEVM), [17], and the Mixed Model (MM), [3]. An alternative to explicit LES is *implicit* LES (ILES), originally proposed by Boris, [2], under the name of Monotone Integrated LES (MILES). In ILES and MILES the subgrid modelling is performed by the numerical scheme (see [4, 5] for recent surveys) and the ILES approach is used in this study. The main objective for using ILES is that the relationship between the subgrid kinetic energy equations used in e.g. OEEVM and MM and the free surface is not fully understood.

When cavitation is included in the flow, different phases will occur simultaneously in the flow field, giving a challenging task for the flow solver. Two different aspects need to be handled, the ability to describe sharp interfaces with complex topology changes between gaseous and liquid phases and the ability to compute the interaction of the phases, i.e. vaporisation, condensation and possible diffusion of inert gases. A complete description should also include glassy cavities with sharp interfaces as well as clouds of bubbles with changing bubble distribution and transition between these states, a difficult but important problem in several engineering applications.

The interface between liquids and gases can be handled in different ways, e.g. level set, [10], and volume of fluid (VOF), [6]. In this study VOF is used for the interface capturing. VOF is an Eulerian interface capturing technique where a scalar field, advected by the velocity field, describes the ratio of gas to liquid at every position in the flow. The volume fraction field $\gamma=\gamma(\mathbf{x},t)$, is a step function, defining the flow properties by the linear relations for the mixture of bulk density ρ and molecular viscosity μ,

$$\begin{cases} \rho = \gamma\rho_l + (1-\gamma)\rho_v, \\ \mu = \gamma\mu_l + (1-\gamma)\mu_v, \end{cases} \tag{3}$$

where the indexes l and v denotes liquid and vapor respectively. This convection relates a value of $\gamma = 1$ to pure liquid and $\gamma=0$ to pure vapor. The volume fraction γ is advected by the velocity field $\bar{\mathbf{v}}$, thus the equation system solved for the continuous varying mixture of the two phase flow is,

$$\begin{cases} \nabla\cdot\bar{\mathbf{v}}=S_\rho, \\ \partial_t(\rho\bar{\mathbf{v}})+\nabla\cdot(\rho\bar{\mathbf{v}}\otimes\bar{\mathbf{v}})=-\nabla\bar{p}+\nabla\cdot(\bar{\mathbf{S}}-\mathbf{B})+\bar{\mathbf{f}}_\sigma, \\ \partial_t\gamma+\bar{\mathbf{v}}\cdot\nabla\gamma=S_\gamma. \end{cases} \tag{4}$$

Here, where the gravitation is neglected, the external force $\bar{\mathbf{f}}_\sigma$ is computed from the interfacial surface tension, evaluated as $\bar{\mathbf{f}}_\sigma = \sigma_{surf}\nabla\cdot\hat{\mathbf{n}}$, where $\hat{\mathbf{n}}=\nabla\gamma^*/|\nabla\gamma^*|$ is the normal vector at the interface and σ_{surf} is the surface tension. In the evaluation of $\hat{\mathbf{n}}$, γ is filtered to generate a smoother normal vector field, hence the $\gamma^*=F(\gamma)$, where F is a so-called Laplacian filter. The source terms appearing in equation (4), i.e. S_ρ and S_γ, are usually zero, but when the flow is subject to a phase change, like in cavitation, these terms are nonzero as described in the following section.

The modeling of the phase change in the flow is one of the most challenging tasks in cavitation modeling and there are some different approaches developed. A common starting point for engineering problems is the Rayleight-Plesset equation, where this equation is solved at each time step for a large number of cavitation nuclei. The total volume changes of the nuclei in a control volume define the mass transfer between vapor and liquid. In this paper a different method is used, based on the work by Kunz *et al.* [7,8]. Here proportionality between the liquid volume fraction and the amount by which the pressure is below the vapor pressure is used to model the transformation from liquid to vapor. This model, described below, is based on a theory of phase transitions referred to in [9].

The source terms appearing in (4), S_ρ and S_γ, incorporates the vaporization and condensation processes. For a volumetric source representation, S_ρ can be expressed as,

$$S_\rho = \dot{m}(\rho_l^{-1}-\rho_v^{-1}), \tag{5}$$

where $\dot{m}$ is the specific mass transfer rate and $(\rho_l^{-1}-\rho_v^{-1})$ handles the bulk volume change when mass is transferred from one phase to the other. The bulk density for liquid and vapor, ρ_l and ρ_v, are kept constant throughout the computation. The source term in the volume fraction transport equation, S_γ, can be estimated from the mass transfer from vapor to liquid at a rate $\dot{m}$. The bulk density change rate can be represented as,

$$D_t(\rho) = \partial_t(\rho) + \bar{\mathbf{v}}\cdot\nabla\rho = -\dot{m}\rho(\rho_l^{-1}-\rho_v^{-1}). \tag{6}$$

By substituting equation (3_1) into (6), gives,

$$D_t(\rho) = (\rho_l-\rho_v)D_t(\gamma). \tag{7}$$

Substituting equation (6) into equation (7) gives,

$$\begin{aligned} &D_t(\gamma) = \partial_t(\gamma) + \bar{\mathbf{v}}\cdot\nabla\gamma = \\ &= -\dot{m}\rho(\rho_l^{-1}-\rho_v^{-1})(1/((\rho_l-\rho_v))) \\ &= -\dot{m}(\gamma\rho_v-\gamma\rho_l-\rho_v)/(\rho_l\rho_v), \end{aligned} \tag{8}$$

and, accordingly, the source term S_γ can be identified as,

$$S_\gamma = -\dot{m}(\gamma\rho_v - \gamma\rho_l - \rho_v)/(\rho_l\rho_v). \quad (9)$$

The mass transfer term $\dot{m}$, included in the source terms, is calculated in accordance with Kunz *et al.,* [7], where $\dot{m} = \dot{m}^+ + \dot{m}^-$ and,

$$\begin{cases} \dot{m}^- = 2C_{dest}\rho_v\gamma\min[0, \bar{p} - p_v]/\rho_l U_\infty^2 t_\infty, \\ \dot{m}^+ = C_{prod}\rho_v\gamma^2(1-\gamma)/t_\infty. \end{cases} \quad (10)$$

Here C_{dest} and C_{prod} are constant parameters, t_∞ and U_∞ are reference quantities preferably related to the largest velocity and time scales of the flow and ρ_v is the vapor pressure. The model is implemented in accordance with the studies [19,20].

COMPUTATIONAL CONFIGURATION

Results presented in this report are produced with a NACA0015 wing with an aspect ratio of 2. The wing is wall mounted at a fixed angle of attack of α=10º. The computational domain consists of a part of a cavitation tunnel, with streamwise, cross-stream and spanwise extends of 13L/2, 10L/3 and 10L/3, respectively, where L is the chord length of the wing section, see figure 1.

At the outer walls symmetry planes with slip boundary condition for the velocity are used and at the inner wall both a symmetry plane, case A, and a wall boundary condition, case B, is used. The pressure is set at the outlet boundary, whereas zero gradient boundary conditions are used for the pressure at the remaining boundaries. At the inlet the volume fraction γ is set to unity, indicating pure liquid at the inlet and for the remaining boundaries zero gradient is used for the volume fraction. The computational domain is filled by a block-structured grid containing 0.9 million cells for case A, figure 1a, and 1.3 million cells for case B, figure 1b. The cells are concentrated in the wing region and along an assumed tip vortex trajectory. In case B the extra cells are located close to the inner wall.

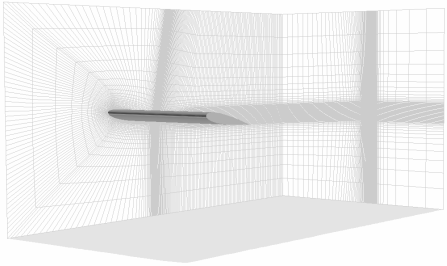

(a)

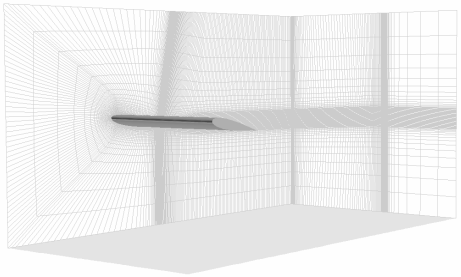

(b)

Figure 1. Computational mesh. (a) Case A with slip boundary condition on the inner wall. (b) Case B with wall boundary condition on the inner wall.

The aim of this particular work is to investigate the possibilities of studying the interaction between cavitation and separation. To illustrate certain behavior in this interaction two cavitation numbers $\sigma=2(P_{out}-P_v)/\rho_l U_{in}^2$ are used, σ_1=1.07 and σ_2=0.69.

At the inlet boundary the velocity is set to $U_{in,cav}$=12m/s for both cavitation cases, yet the Re-number $\mathrm{Re} = \rho_l U_{in,cav} L_{chord}/\mu_l$ is slightly altered between the two conditions. For condition 1 the chord length is set to L_{chord}=1.0m and in condition 2 the chord length is set to L_{chord}=0.10m, giving Re-numbers of $\mathrm{Re}_1 \approx 10^7$ and $\mathrm{Re}_2 \approx 10^6$, respectively. The coefficients in the cavitation model are given the following values $C_{prod}=C_{dest}$=1000 and $t_\infty = L_\infty/U_\infty$ where U_∞ and L_∞ are the inlet velocity and the chord length. These settings give two specific cases demonstrating the interaction between cavitation and separation. Cavitation condition 1 produces a cavity that interacts with the separation and makes separation virtually disappear. The cavity is in this case located close to the surface of the wing and the risk of erosion is consequently high if a fast collapse develops. In cavitation condition 2 the cavity travels above the separation and is located far from the wing and the risk of erosion is accordingly smaller. The cavitation conditions are summarized in table 1.

Cavitation Condition	Cavitation number, σ	U_{in} [m/s]	L_{chord} [m]	Reynolds number, Re
1	1.07	12	1.0	10^7
2	0.69	12	0.10	10^6

Table 1. Conditions in the cavitation simulations.

RESULT

There are no validation data available for this specific geometry, yet the LES solver are earlier validated for several different geometries, [14], and the implementation of the cavitation model has been validated for a similar configuration, [19]. Based on the observations made in the EUROCAV project, [1], it is legitimate to use this configuration to test the cavitation model.

CAVITATION SIMULATIONS

The first computation, cavitation condition 1 with geometry from case A, is performed at stationary inflow conditions with $Re \approx 10^7$, $\alpha = 10^o$ and $\sigma = 1.07$, but with the cavitation source, i.e. the vaporization initially set to zero. When the flow field is fully developed, the sources are gradually turned on to initiate the cavitation, here this is referred to as time t=0. Figure 2 shows a two dimensional plane located at z/H=0.5, where H is the span of the wing section and z=0 is at the tip of the wing. In the non-cavitating case there is a clear separation and recirculation bubble on the suction side of the wing, figure 2a. When the cavity grows, in this case remaining close to the wing surface, the recirculation region is affected and the separation point moves downstream. When the cavity, which in this case is located close to wall, is incepted, the recirculation region is affected and the separation point moves downwards in the flow direction. When the cavity grows the whole recirculation region virtually disappears, figure 2b. The cavity is developed along the wing surface, until a structure similar to a re-entrant jet form which travels under the sheet until it finally cuts off the cavity. When the cavity travels along the wing surface, as in this case, the risk of erosive collapses are impending.

The second computation, cavitation condition 2, is performed on the two cases A and B, and the settings are $Re \approx 10^6$ and $\sigma = 0.69$. As in the first cavitation condition, the flow field is started from quiescent conditions. When the flow is fully developed, the sources are gradually turned on to initiate the cavitation. Also at this condition there exists a recirculation region, figure 2c. The cavity starts from the leading edge and, as in contrast to cavitation condition 1, the cavity does not significantly influence the recirculation zone. Instead it leaves the wing surface and travels on top of this zone, figure 2d. Because the cavity is located above the separation zone and not so close to the wing surface, the risk of erosion is here smaller than in cavitation condition 1. There is no visual difference between case A and case B in this view.

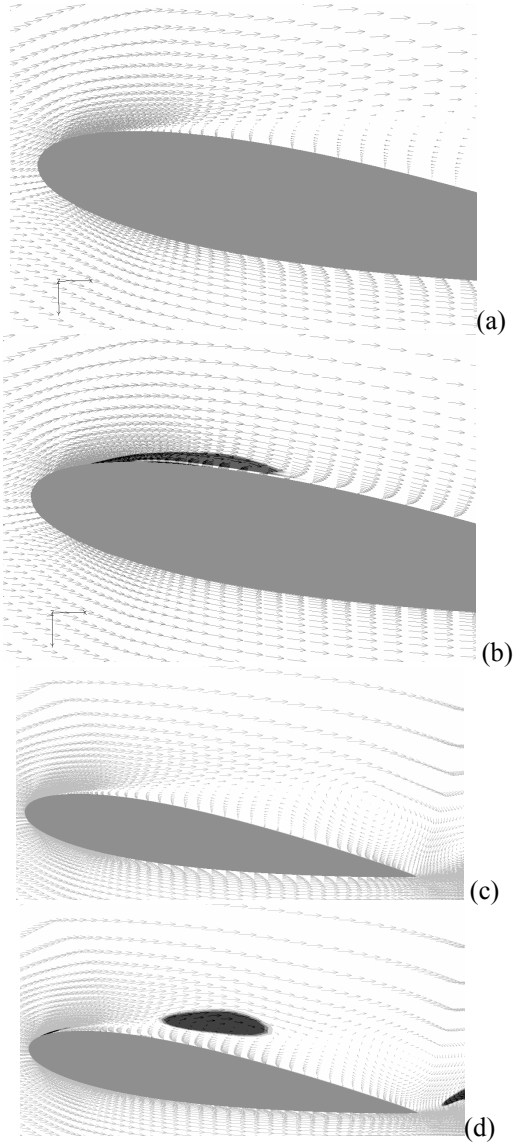

Figure 2. Volume fraction γ, at z/H=0.5, (a) cavitation condition 1 σ=1.07 and t=0, (b) cavitation condition 1 σ=1.07 and t=0.15, (c) cavitation condition 2 σ=0.69 and t=0 and (d) cavitation condition 2 σ=0.69 and t=0.01

Seen from above, the early development of the cavity close to the leading edge, in cavitation condition 1, is very two dimensional and structured. The cavity keeps the bi-dimensional shape from the tip of the wing to the inner wall as it is expanded and transported along the suction side of the wing, figure 3a. The tip vortex cavity is in this case very stable but also very short.

In cavitation condition 2, on case A, the structure of the first cavitation cycle is clearly two dimensional from the inner slip wall z/H=1.0 to about z/H=0.2. In the region far from the wing tip the recirculation is mainly bi-dimensional, directed normal to the inflow, as a true re-entrant jet would be. In the tip region, where the downstream edge of the cavity is

not normal to the inflow, a possible re-entrant jet does not move upstream and cut off the sheet along a cut normal to the leading edge, as occurs further inwards from the wing tip, due to the separation. Instead a re-entrant jet here gains a transverse velocity component. The development of the separated zone in the tip region is not yet studied but the resulting behavior of the cavity approaches the behavior in a non-separated flow, i.e. a reduced tendency of cut-off in the tip region see figure 3b.

In case B the cavity remains attached to the leading edge close to the inner wall, see figure 3c, giving a more reasonable overall appearance of the cavity. Between the tip and approximately *z/H=0.8*, the structure, size and behavior of the cavity are very similar to the cavity in case A.

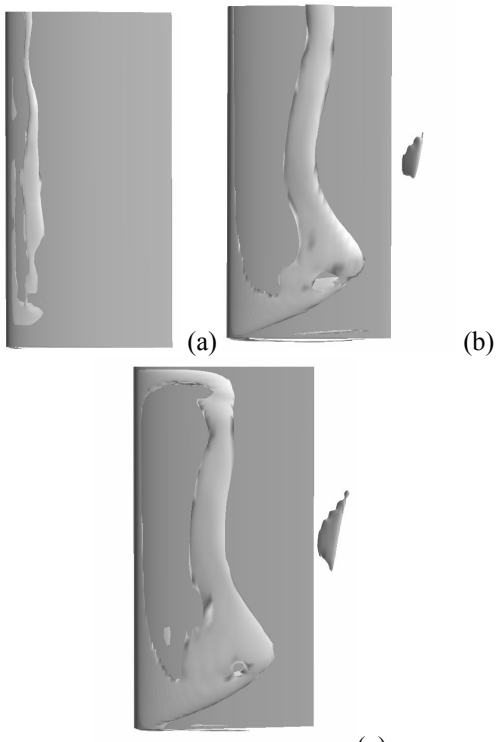

Figure 3. Suction side of the wing as seen from above. Iso-surfaces the volume fraction γ=0.25. (a) Cavitation condition 1 σ=1.07 and t=0.1, (b) cavitation condition 2 σ=0.69 and t=0.01 and (c) cavitation condition 2 σ=0.69, on case B with a wall boundary condition on the inner wall, t=0.01.

In cavitation condition 2, a strong and stable tip vortex cavity is created, figure 4. The tip vortex cavity in this region is created by different interacting cavitating vortices. Two smaller vortex cavities, one on the tip, and one on the suction side of the wing can be distinguished. Because the detailed behaviour of vortex cavitation close to blade tips can be crucial for the erosion risk it is interesting to notice that the simulation resolves the two interacting vortex cavities. In a earlier work, see [12], it is found that the surprisingly small, but still existing, numerical dissipation implies that the cavity will be somewhat underpredicted further downstream the of wing.

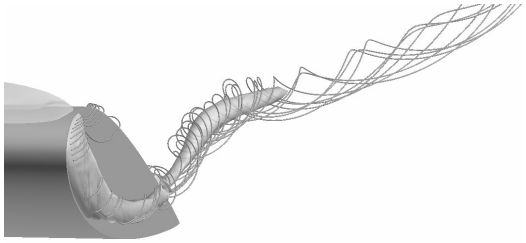

Figure 4. Tip vortex cavity at cavitation condition 2 σ=0.69 on case A with a slip boundary condition on the inner wall, t=0.035.

CONCLUSIONS

From general experiences of for example cavitation on the pressure side of propellers it is known that the distance of the cavities from the body surface significantly influences the risk of erosion, [1]. It is further demonstrated above a possibility to predict this distance of shed cavities for supporting the assessment of the erosion risk. Qualitative comparisons with the preliminary data used in [19] and other studies confirm that the simulated general cavitation behavior corresponds reasonably well with experimental observations. No data were however available for validation of the separation and the resulting distance between the cavities and the wing surface. A detailed validation of the cavitation kinematics in the separated region is complicated but perhaps the present numerical simulation may be used to support the design of a proper experiment.

Tracing the simulated cavitation development revealed that at cavitation condition 1 the cavity interacts with the separation in such a way that the separation virtually disappears as the cavity grows. The cavity then travels very close to the surface of the wing and the risk of erosion can consequently be high. At cavitation condition 2 the cavity and the separation do not interact in the same way. Instead the cavity travels on top of the separation bubble. Because the cavity in this case is located further from the wing surface, the risk of erosion is smaller than at condition 1.

Extending the observations summarized above about separation and cavitation it is concluded that at certain conditions there seems to exist a subtle interplay between separation and cavitation growth, and if this is true also in the physical world, it is important to predict this behavior at assessment of the erosion risk.

Concerning settings that influence the results

it is noted that when the wall of the cavitation tunnel is added, case B, the overall appearance of the cavity becomes more reasonable, although it does not change the interaction between the cavity and the separation.

An aspect that was not investigated is the influence of resolution, especially in the spanwise direction, which has been seen to be of great importance in earlier simulations of non-cavitating flows, [14]. Further remaining efforts are sub grid modelling and wall handling as well as testing of different cavitation models for cavitating flow. Although it has been demonstrated that even some behaviour critical for cavitation erosion may in a future be simulated by LES it has to be concluded that many things need to be improved before the physical cavitation laboratory can be replaced by CFD.

ACKNOWLEDGMENT

This work is performed within the EU project VIRTUE under grant 516201.

REFERENCES

[1] Bark, G., Berchiche, N. and Grekula, M. 2004, Application of principles for observation and analysis of eroding cavitation - The EROCAV observation handbook. Ed. 3.1, Dept. of Naval Architecture and Ocean Engineering, Chalmers Univ. of Technology, Göteborg, Sweden.

[2] Boris, J.P.; 1992, "On Large Eddy Simulations Using Subgrid Turbulence Models", in Wither Turbulence, Turbulence at the Crossroads, Lumly J.L. (ed), Lecture Notes in Physics, **357**, Springer Verlag, Berlin, p 344.

[3] Fureby C, Bensow R.E., and Persson T., 2005, Scale Similarity Revisited in LES, *TSFP 4, Williamsburg, Virginia.*

[4] Grinstein F.F. and Fureby C.; 2004, "From Canonical to Complex Flows: Recent Progress on Monotonically Integrated LES", Computing in Science and Engineering**, 6**, p 37.

[5] Grinstein F.F., Margolin L. and Rider W., 2005, Implicit Large Eddy Simulation: Computing Turbulent Fluid Dynamics, *Cambridge University Press.*

[6] Hirt C. and Nicols B., 1981, Volume of Fluid (VOF) Method for the Dynamics of Free Boundaries, *Journal of Computational Physics*, **39**(1), p. 201.

[7] Kunz R.F., Boger D.A., Stinebring D.R., Chyczewski T.S. and Gibeling H.J., 1999, A Preconditioned Navier-Stokes Method for Two-Phase Flows with application to Cavitation Prediction, *AIAA Paper 99-3329.*

[8] Kunz R.F., Boger D.A., Stinebring D.R., Chyczewski T.S. and Gibeling H.J., 1999, Multi-Phase CFDAnalysis of Natural and Ventilated Cavitation about Submerged Bodies, *3rd ASME/JSME Joint Fluids Engineering Conference,* San Francisco, California.

[9] Lindau J.W, Boger D.A., Medvitz R.B. and Kunz R.F. 2005, Propeller Cavitation Breakdown Analysis, *Journal of Fluids Engineering*, **127,** pp. 995.

[10] Osher S. and Sethian J., 1988, Fronts propagating with curvature dependent speed: Algorithms based on Hamilton-Jacobi formulations. *Journal of Computational Physics,* **79**(1), p 12.

[11] Panton, R.L., 1996, *Incompressible flow,* New York: John Wiley & Sons.

[12] Persson T., Bark G., Bensow R., Berchiche N. and Fureby C., 2006, Large Eddy Simulation of the Cavitating flow around a Wing Section, *International symposium on cavitation CAV2006,* Wageningen, The Netherlands

[13] Persson T., Liefvendahl M., Bensow R.E. and Fureby C., 2006, Numerical Investigation of the Flow over an Axisymmetric Hill using LES, DES and RANS, *Journal of Turbulence 7*(4)

[14] Persson T., 2005, Numerical Simulation of High Reynolds Number Wall Bounded Flow, *Licentiate Thesis,* Chalmers University of Technology.

[16] Sagaut P., 2001, *Large Eddy Simulation for incompressible flows,* (Berlin: Springer Verlag)

[17] Schumann U., 1975, Subgrid scale model for finite difference simulation of turbulent flows in plane channels and annuli, *J. Comp. Phys.*, **18**, p 376.

[18] Smagorinsky J., 1963, General circulation experiments with the primitive equations. I. The basic experiment, *Month. Wea. Rev.,* **91**, p 99.

[19] Wikström N., 2005, Modeling of Cavitating Flow Around a Stationary/Moving Wing Profile, *AIAA Paper 2005-1287.*

[20] Wikström N, Bark G. and Fureby C.. 2003, Large Eddy Simulation of Cavitating Submerged Objects, *The 8th International Conference on Numerical Ship Hydrodynamics,* Busan, Korea.

RANS Analysis of the Interference Effect in Catamarans

A. Pinto, R. Broglia, E.F. Campana, A. Di Mascio, D. Peri [1]

INSEAN – Italian Ship Model Basin
Via di Vallerano 139, 00128 Rome, Italy

Abstract

In this paper the study of the turbulent flow past a fast catamaran is presented with focus on the fluid-dynamic interference between the demihulls. The flow is investigated analyzing numerical results obtained with the Reynolds Averaged Navier-Stokes code χnavis. The interference between the demihulls increases the catamaran resistance with respect the monohull case, and both pressure and viscous drag components are influenced by the demihulls separation. Comparison between monohull and catamaran flow fields is first shown. Then, the influence of both Reynolds number and demihulls separation on the interference effect, and the multihull resistance is presented. Even though, preliminary results show the complexity of the flow features and the relevance of the analysis for design purposes. According to these results, there is a remarkable scale effect on the multihull resistance.

INTRODUCTION

The goal of this paper is to present the analysis of the flow past a fast catamaran. The focus is on the study of the multihulls interference by investigating Reynolds Average Navier-Stokes (RANS) numerical results. The analyzed multihull geometry (Fig. 1) is the HSSL-B catamaran (displacement at 6.50*m* of 12000*Mtons*, length 170.00*m* and beam 40.00*m*), selected as a possible solution to the design requirements posed by the US Navy of a high-speed displacement ship with limited length and draft. HSSL-B has been also recently adopted as parent hull for an optimization study and results presented at the 26th Symposium on Naval Hydrodynamics are the outcome of a strong effort among the code developers, in the framework of projects funded by the ONR and ship designers (Bath Iron Works - General Dynamics). A number of optimization problems aimed at the enhancement of the hydrodynamic performance were discussed and elaborated in Campana et al., 2006.

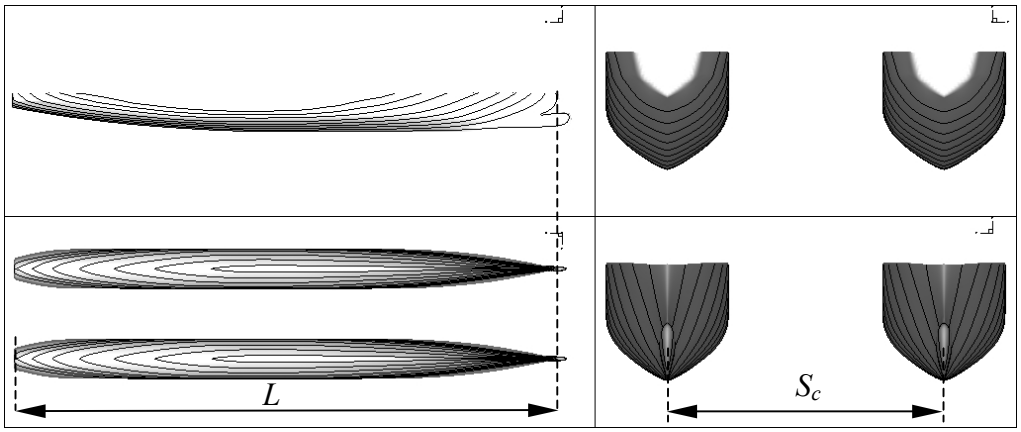

Fig. 1 - The catamaran HSSL-B

The literature about the analysis of the viscous flow past catamarans is very limited and most of the previous works devoted to multihulls adopt potential flow models (e.g. Doctors and Scrace, 2003) to predict the wave interference effect and select the optimal separation between the demihulls. Nonetheless, the use of RANS solvers has revealed the extension of the flow distortion induced by the proximity of the hulls (Campana et al., 2006). Compared to the monohull (demihull) case, distorted streamlines, altered pressure distributions from bow to stern, zones of flow separation, and vortex shedding are easily detected. Each of these effects, which could not be possibly captured by potential flow solvers, alters the resistance characteristics of the multihull.

[1] e-mail: (a.pinto, r.broglia, e.campana, a.dimascio, d.peri) @insean.it

In the next sections, a brief description of the numerical solver is given, comparisons between monohull and catamaran flow fields are shown, and the influence on the multihull resistance of both Reynolds number, *Re*, and demihulls separation is presented. The influence of the interference factor on the drag is finally highlighted.

Actually, results are preliminary and no numerical uncertainty is provided: nevertheless, the relevance of the viscous analysis, with respect to past works potential flow-based, is clear. Moreover, they indicate that the interference effect is strongly dependent by the model scale (in the typical scale range adopted in the towing tanks) that the ranking can be altered.

FLOW SOLVER

The code *χnavis* is a general purpose, finite volume, second-order solver, based on a pseudo-compressibility formulation of the Navier-Stokes equations (Broglia and Di Mascio, 2003). *χnavis* includes multi-block overlapping grid capabilities, one-phase Level-set approach for the simulation of free surface flows and the possibility of using different turbulence models. Unsteady flows are resolved with a dual-time technique.

The numerical algorithm is based on the non-dimensional integral form of governing equations of incompressible viscous fluids. Numerical solutions of the governing equations are computed by means of a second order finite volume solver. The turbulent viscosity has been calculated by means of the Spalart-Allmaras turbulence model (Spalart and Almaras, 1992). For the simulation of free surface effects an one–phase level set algorithm is adopted, i.e. only the liquid phase of the fluid is computed (Di Mascio et al., 2005). The volume discretization is made by a Chimera algorithm. The fluid domain is partitioned into structured blocks and each block is subdivided into disjoint hexahedrons. Conservation laws are then applied to each finite volume.

Derivatives are computed by means of a finite volume approximation. Computation of convective fluxes and surface velocity integral velocity included in the continuity equation requires evaluation of pressure and velocity at the face center. To this aim, a second order ENO-type scheme is adopted (Harten et al., 1987). In this scheme, the flux vector at cell interface is computed as the solution of a Riemann problem, whose left and right states are given in a way such that second order accuracy and oscillation-free of the discrete solutions are ensured.

Pressure-velocity coupling is obtained by the introduction of a dual (or pseudo) time-derivative in the discrete system of equations and the solution is iterated to steady state with respect to the pseudo time, for each physical time step. The time derivative is approximated by means of a second order accurate three-points backward finite difference approximation formula, whereas the integration with respect to the pseudo time is carried out by means of an implicit Euler scheme. Local dual time step and a multi-grid technique have been used for improving the convergence rate of the sub-iteration algorithm. Finally, MPI (Message Passing Interface) procedures are used in order to reduce the computational time solving the problem on several parallel processors.

COMPARISON BETWEEN MONOHULL AND CATAMARAN

Numerical results have been obtained with a quite coarse grid, even if $y^+ < 1$. Only 3 blocks were used, one as background (64*56*32) and two for the demihulls (80*48*32) for a total number 0.36 Mpoints. In this respect, they should be regarded as preliminary and a finer grid has been prepared now for a deeper analysis that is an on-going work.

Comparison between the viscous flow field generated by the monohull geometry of HSSL-B and the catamaran ($S_c / L = 0.16$, $Fr = 0.541$, $Re = 1.2x10^7$) is presented in this section. The flow field of the catamaran completely differs from that of a monohull ship. In particular, in the case of multihulls grossly distorted streamlines are present, the wave pattern is altered, the pressure distributions along the hull is considerably changed, the boundary layer is modified, and zones of flow separation are present. All these aspects vary the resistance of multihulls with respect individual hulls.

In Fig. 2a the wave pattern correspondent to the different configurations is reported. In the case of the catamaran, due to the blocking effect, the bow wave generated in the starboard is bigger than in the monohull case. For the catamaran, the interference between the hulls produces a great acceleration of the flow in the aft part of the ship and a corresponding increase of the wave pattern. Even if this acceleration is stronger in the inboard region, the outboard flow is also influenced and the height of the wave elevation is increased also in the outer field. The pressure distribution is also largely influenced by the twin hull (Fig. 2b). The pressure distribution is qualitatively the same in the fore region. Differences start to $x/L > 0.3$ and the pattern is drastically changed for $x/L > 0.6$. The catamaran shows an asymmetric pressure distribution on the two demihulls and, as a consequence, a transversal pressure gradient is present.

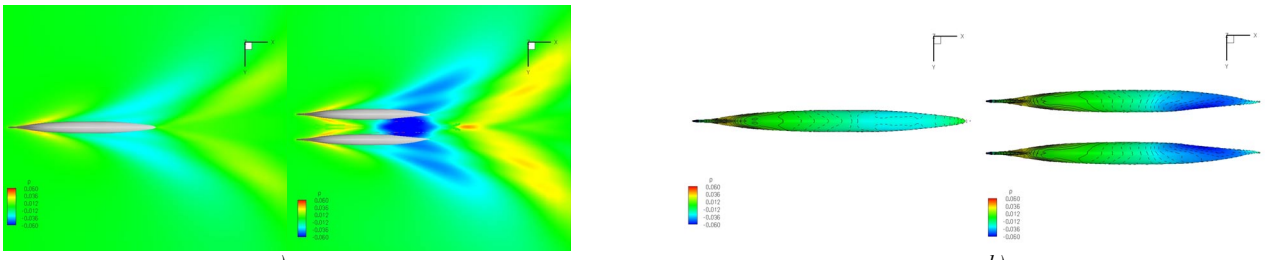

a) b)

Fig. 2 – a) Monohull and catamaran wave pattern. b) Pressure distribution (S_c/L = 0.16, Re = 1.2x10^7)

In Fig. 3a, the mean flow deflection is highlighted by plotting the streamlines in the proximity of the hull. In contrast with the monohull case, the streamlines converge toward the inner region of the catamaran. The streamlines modification is also shown in Fig 3b, where the transversal velocity component, *v*, across the symmetry plane of one demihull is reported; the maximum outboard value seems to be located at amidships, whereas for *x/L > 0.75* the flow is pushed inboard, toward the center plane of the catamaran.

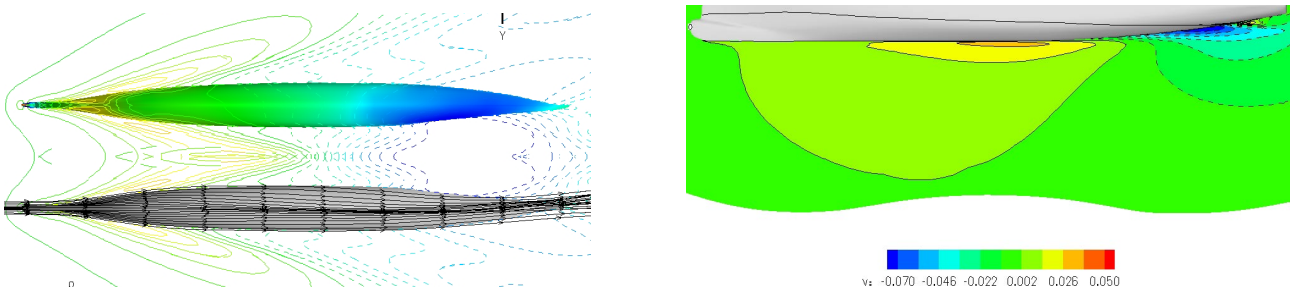

a) b)

Fig. 3 – a) Streamlines and pressure distribution for the catamaran; b) color contours of the transversal velocity component, v, across the longitudinal plane of one demihulls (s/L = 0.16, Re = 1.2x10^7)

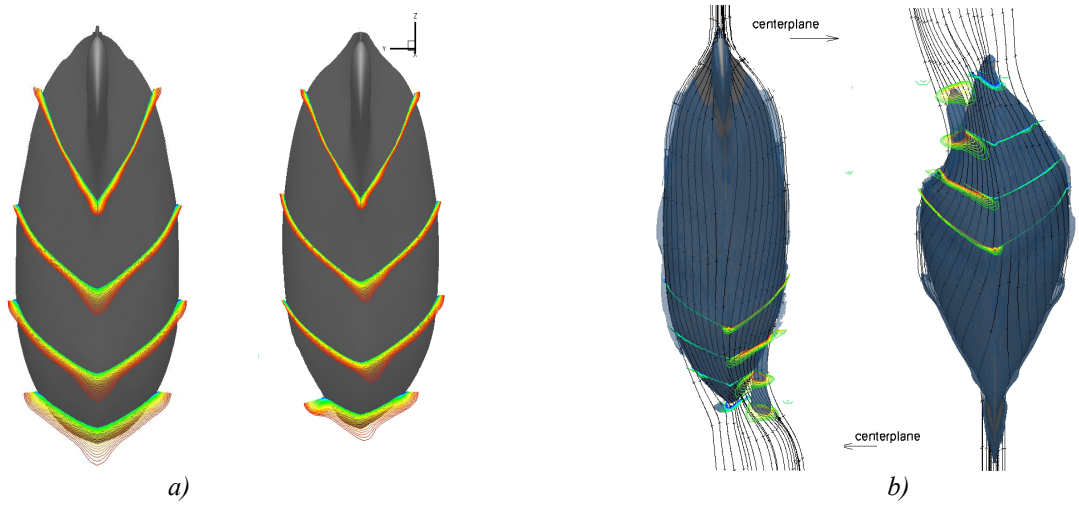

a) b)

Fig. 4 – a) Color contours of the axial velocity for the monohull (left) and on a demihull of the catamaran (right); b) fore and aft views of the streamlines, axial vorticity contours and a Q invariant iso-surface distribution (s/L=0.16, Re = 1.2x10^7)

The boundary layer is also influenced by the hulls interference (Fig. 4a). In particular, for *x/L* < 0.65 the inner boundary layer thickness is smaller in the case of the catamaran due to the stronger flow acceleration. For *x/L* > 0.65 the adverse gradient of pressure increases the boundary layer. In Fig. 4b, axial vorticity contours are plotted with an iso-surface of the *Q* invariant (Jeong and Hussain, 1995) defined as $Q=1/2\,tr(S_{ij}^2)$, where S_{ij} is the strain rate tensor: a large vortex is shed into the inner wake of the catamaran.

ANALYSIS OF THE INTERFERENCE EFFECT

The resistance of a multihull composed by n demihulls is substantially greater than *n-times* the resistance of one hull in isolation. This added resistance is typically considered to be part of residuary resistance and attributed to the interference effect, a term that relates the demihull (or monohull) drag to the multihull drag. A quite general definition of the interference factor I_x of a given resistance component x, is as follows:

$$I_x = (C_x^{multihull} - 2 * C_x^{monohull}) / (2 * C_x^{monohull})$$

where $C_x^{multihull}$ indicates a resistance coefficient (i.e. total, C_t, pressure, C_p, or viscous C_f) of the catamaran, whereas $C_x^{monohull}$ indicates a resistance coefficient of the monohull. It is clear that the added drag is due to both (i) the interaction of the wave trains from the individual demihulls (i.e. wavemaking interference), and (ii) to distortions in the viscous flow caused by the proximity of the other demihulls. Even though traditional studies are focused on wave interference, the pressures induced on each hull by the presence of the other demihull(s) significantly distorts the flow over each demihull in ways that affect viscous resistance as well as wavemaking.

A considerable amount of towing tank work has been done to measure multihull interference drag associated with variations in demihull longitudinal and transverse positions. However, to the author's knowledge, little experimental data exists to provide insight into interference effects between hulls in the absence of the free surface. Fortunately, two experimental data set are available with systematic variation in the demihull separation for both a ship model in a towing tank (Molland et al.,1996) and a double model of the hull in a wind tunnel (Armstrong, 2003). Data shows that the altered flow due to the proximity of two hulls results in significant interference effects in both the wind tunnel and the towing tank.

In Armstrong (2003) pressure distribution and drag were measured during double model wind tunnel tests. The total viscous drag C_v was decomposed into a skin friction component C_f and a viscous pressure component C_{vp} ($C_v = C_f + C_{vp}$) and the variation of C_v with *Re* was reported. He observed that while C_v of the isolated hull agrees very well with the ITTC friction line C_f, the C_v of catamaran is significantly greater than the ITTC C_f and that this difference varies with both hull spacing and *Re*. Relatively large differences occur at the lower speeds tested while the sensitivity of C_v to hull separation decreases with *Re*. Furthermore, being the experimentally derived skin friction resistance C_f was substantially insensitive to hull separation, he concluded that the C_v of catamaran is influenced by the viscous pressure drag term C_{vp} by both *Re* and separation effects. Unfortunately he did not test for hull separations as small as those of HSSL-B catamaran. While it is tempting to hope that this added interference drag involves only a simple correction to the viscous drag, the variation of the interference effect with speed indicates a significant *Fr* effect.

In summary, there are significant interference effects between demihulls in the absence of a free surface which are independent of wavemaking interactions. If factors such as wind tunnel blockage effects, model mounting effects, etc. can be neglected, the inescapable conclusion is that there is significant interference of a purely viscous nature between two model scale hulls in close proximity. On the other hand, towing tank tests combine viscous interference effects with wavemaking interference effects. A comparison of Armstrong's wind tunnel data with Molland's towing tank data shows that there is drag interference in addition to the wavemaking interference inherent in the wave profile drag (Campana et al., 2006).

In Fig. 5 the multihull global coefficients obtained with *χnavis* are reported as a function of the separation between the demihulls. Total resistance coefficient at *Froude* number *Fr=0.541* is split into both pressure and viscous resistance components for four different values of *Re*. In analyzing these results, let put aside some evident considerations. The lower is the *Reynolds* number, the larger are the coefficients, whereas the pressure coefficient C_p is substantially *Reynolds* independent; furthermore, C_t and C_p decrease when the separation distance S_c/L increases.

The increase of C_t, observed when reducing the proximity of the demihulls, seems to be largely due to an increase in C_p. Perhaps is more interesting to notice that two different regions - below and above $S_c/L=0.24$ – are clearly visibles in all the three plots. For large separation values, the trend of the coefficients seems smooth and almost less influenced from S_c/L (Fig. 5c), whereas for $S_c/L \leq 0.24$ the demihull interaction plays a key role. The bandwidth of the results obtained with different *Reynolds* number (Fig. 5c) increases as the separation decreases. Also, in the $S_c/L \leq 0.24$ region the coefficient C_f shows an opposite behavior with *Re*, that is, C_f grows for $Re=3.06*10^6$ and decreases for $1.02*10^7$. Thinking in terms of model scale, given that *Fr=0.541*, this corresponds to two models whose length is *1.48 m* and *3.69 m*, respectively.

Continuing in exploring the interference effect between the demihulls, in Fig. 6 the global coefficients are now reported as a function of the *Reynolds* number and compared with the monohull resistance multiplied by two. It is evident (Fig. 6a) the increase of the catamaran resistance – more than twice the monohull drag (i.e. positive interference) – as a result of flow field distortions highlighted in the previous section. Looking at C_f plot (Fig. 6c), it is worthwhile to notice that, when passing from high to low *Reynolds* number, the curve relative to the smallest separation value ($S_c/L=0.16$) crosses all the others. Being the *Froude* number fixed at *0.541*, this results may also be interpreted in terms of model *length*: when passing from the large model (*3.69 m*) to the small one (*1.48 m*), the ranking changes. These results, should be confirmed by a fine

grid computation (now running). Anyway, they indicate that the interference effect is strongly dependent by the model scale (in the typical scale range adopted in the towing tanks) that the ranking can be altered. Summarizing, model tests in towing tank might indicate strongly variable results with the scale of the model and might lead to wrong conclusions: in this respect, even more complex appears the full scale extrapolation process.

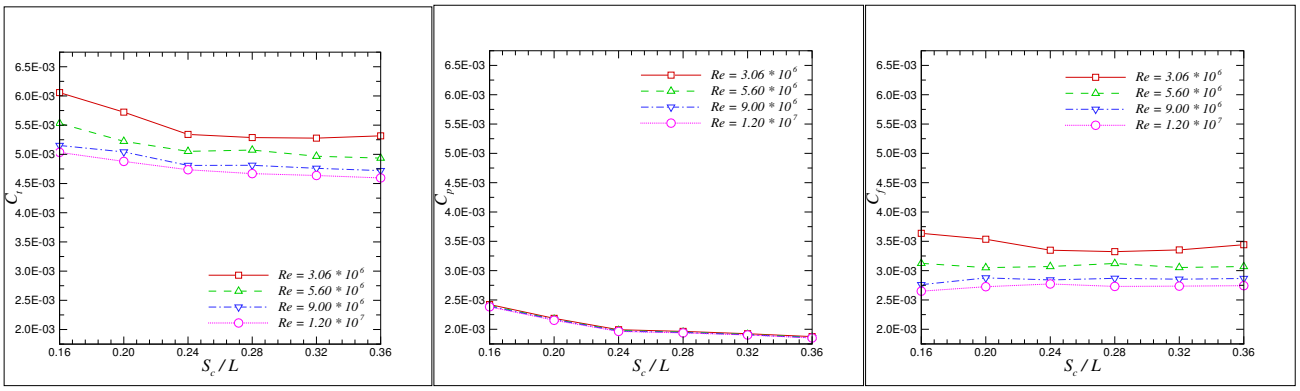

a) *b)* *c)*

Fig. 5 – C_t , C_p and C_f coefficients (a,b and c, respectively) for the catamaran as functions of the demihull separation S_c/L

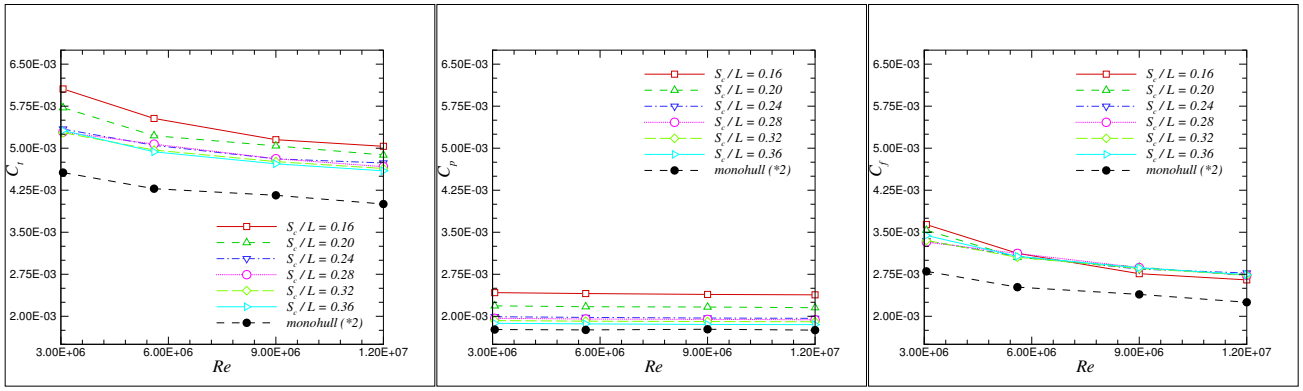

a) *b)* *c)*

Fig. 6 – C_t , C_p and C_f coefficients (a,b and c, respectively) for the catamaran as functions of the Reynolds number Re

Based on the same results, in the next two figures the interference coefficient is reported, split into I_t , I_p and I_f . With the increase of the demihull separation (Fig. 7b, 8b) I_p rapidly collapses from about 37% down to 5% whereas the behavior of I_f is more complex and doesn't show a simple trend. This oscillatory behavior should however be verified on a finer grid. However, in the investigated range of demihull separation, I_f does not show a clear trend toward lower values, so that I_t is decreasing due to the I_p reduction.

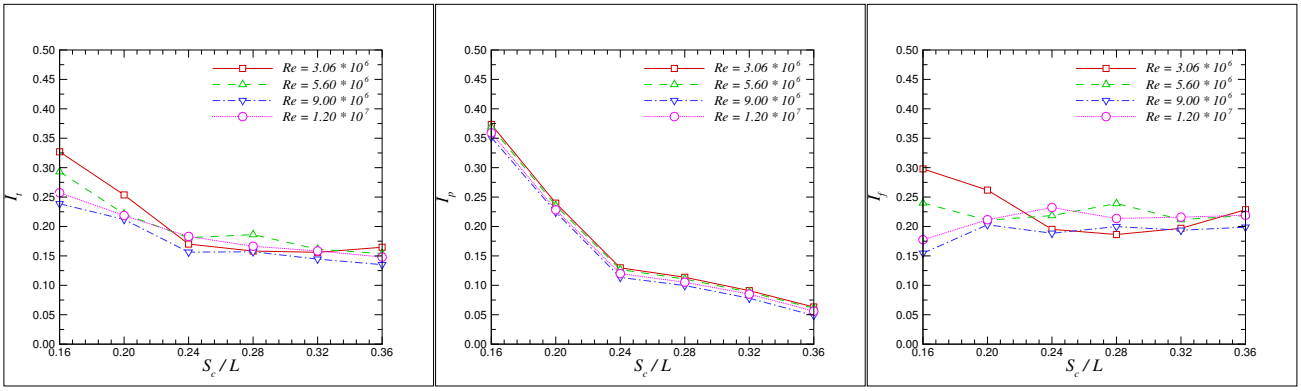

a) *b)* *c)*

Fig. 7 – Interference factor: a) total resistance, b) pressure resistance, and c) viscous resistance as functions of the demihull separation S_c/L

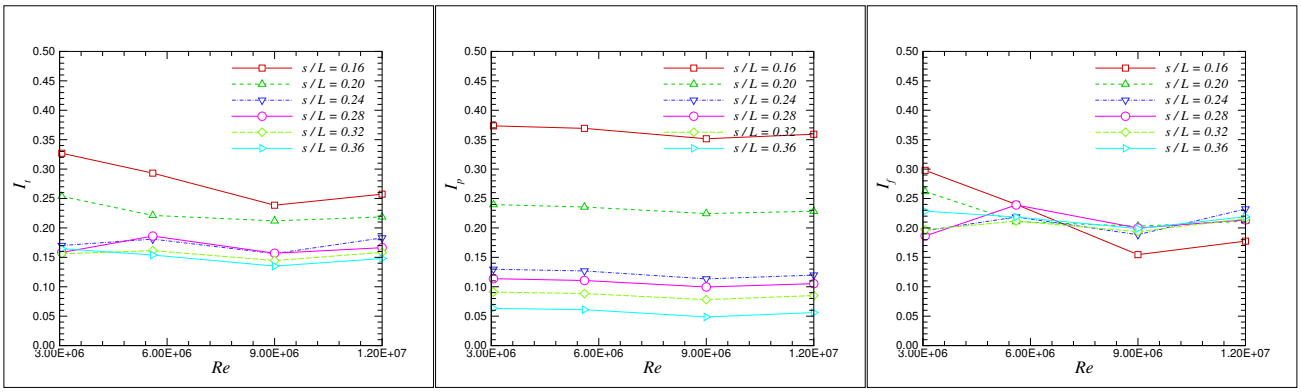

Fig. 8 – Interference factor: a) total resistance, b) pressure resistance, and c) viscous resistance as functions of the Reynolds number Re

CONCLUSIONS

The analysis of the flow past a fast catamaran, and the fluid-dynamic interference between two demihulls have been presented by showing result from Reynolds Averaged Navier-Stokes simulations. Comparison between monohull and catamaran flow fields has been shown, and the influence on the multihull resistance of both Reynolds number and demihulls separation has been addressed. It has also been evidenced that there is a remarkable scale effect on the multihull resistance. Even though the presented results are preliminary, they clearly show the complexity of the flow features and the relevance of the analysis for design purposes.

ACKNOWLEDGMENTS

This work has been partially supported by the U.S. Office of Naval Research under the NICOP grant 000140510617. The authors wish to express their appreciation also to C. Kennell and F. Stern for the useful discussion about the interference effect.

REFERENCES

Armstrong, T, 2003. "The Effect of Demihull Separation on the Frictional Resistance of Catamarans", FAST 2003, Ischia, Italy

Broglia, R. and Di Mascio, 2003, A, "Unsteady RANS Calculations of the Flow Around a Moving Ship Hull", in Proc. 8th Int. Conf. on Numerical Ship Hydrodynamics, Busan, Korea.

Campana EF, Peri D, Pinto A, Tahara Y, Kandasamy M, Stern F, Cary C, Hoffman R, Gorski J, Kennell C, 2006, "Simulation-Based Design of Fast Multihull Ships", in Proc. 26th Symposium on Naval Hydrodynamics, Rome, Italy.

Di Mascio, A., Broglia, R., and Muscari, R., 2005. "On the Application of the One–Phase Level Set Method for Naval Hydrodynamic Flows", submitted to Comp. and Fluids.

Doctors, L.J., Scrace R.J., 2003. "The optimization of trimaran sidehull position for minimum resistance", FAST 2003, Ischia, Italy

Harten, A., Engquist, B., Osher, S., and Chakravarthy, S. R. (1987). "Uniformly High Order Accurate Essentially Non–Oscillatory Schemes". J. Comput. Phys., 71:231–303.

Jeong, J., Hussain, F., 1995. "On the identification of a vortex", J. Fluid Mech. 285, 69-94.

Molland AF, Wellicome JF, Couser PR, 1996. "Resistance Experiments on a Systematic Series of High Speed Displacement Catamaran Forms: Variation of Length-Displacement Ratio and Breadth-Draught Ratio", RINA Transaction, vol. 138, 1996

Spalart P.R. and Allmaras S.R., 1992. "A one-equation turbulence model for aerodynamic flows", in AIAA-92-0439, AIAA 30th Aerospace Sciences Meeting.

Developments on Hydroelasticity of Ships Using RANS

A. Quérard, P. Temarel, S.R. Turnock
Lloyd's Register University Technical Centre
School of Engineering Sciences, University of Southampton, S017 1BJ, U.K.

Nomenclature

C_D	Drag coefficient.	$U_i = (U,V,W)$	Mean velocity components.
C_P	Pressure coefficient.	U_0, V_0, W_0	Free-stream velocity components.
$f_i = (f_x, f_y, f_z)$	Components of external body force.	$\overline{u_i' u_j'}$	Reynolds stresses.
KE_{fluid}	Kinetic energy of the fluid.	$T = \frac{\tau_0}{\rho U_0^2}\sqrt{R_n}$	Skin Friction Coefficient.
M_V	Dimensional added mass coefficient.	y_0	Height of first node of the grid away from the section's wall.
$m_v = \frac{M_v}{\rho \cdot \pi \cdot R^2}$	Reduced added mass coefficient.	ρ	Density.
P	Pressure.	τ_0	Skin friction.
R	Radius of circle encompassing section.		
R_n	Reynolds Number.		

Introduction

One of the role of classification societies such as Lloyd's Register is to make sure that ships are safe to operate with an adequate structure. The ability to predict accurately the dynamic forces and stresses on a ship at sea is thus of prime interest to them.

The first practical method for predicting the ship motions, is the « *strip theory* », developed in 1955 by Korvin-Kroukovsky[1] and later by Korvin-Kroukovsky and Jacobs[2]. The « *strip theory* » reduced the determination of the added mass and damping coefficients to a two dimensional problem. It relied upon the assumption that as long as the ship was slender enough and that surge was not considered, the three-dimensional motion of a ship could be represented by a number of transverse two-dimensional sections experiencing parasitic motion. Hence, for each of these « *strips* » swaying, heaving and rolling harmonically on the free surface at the encounter frequency, the hydrodynamic coefficients can be found. The properties of the entire hull can then be obtained by integration. The two-dimensional coefficients of each strip were obtained using a potential flow solution, satisfying Laplace's equation, the free surface and radiation conditions. The so-called « *intuitive* » strip theory developed by Korvin-Kroukovsky and Korvin-Kroukovsky and Jacobs was the first method to predict ship motion with reasonable accuracy [1][2]. However; one of the major objections voiced against it was that it did not take into account the effects of forward speed. Furthermore, the calculations were performed without any interaction between the strips. To include the solution of the full three-dimensional boundary value problem, the so-called « *rational strip theory* » was developed by Ogilvie and Tuck[3]. Noting that this method was quite computationally intensive, Salvesen et al[4] used a less complex formulation which incorporated forward speed dependent terms in the strip theory. But even though strip theory was giving good predictions for conventional ships, more complex geometries required a fully three-dimensional approach. Garrison[5] and Faltinsen and Mitchelsen[6] used successfully a method with fundamental singularities - pulsating sources - distributed over the wetted surface of the body. Nevertheless, as in the two-dimensional case, forward speed effects caused problems. Wehausen and Laitone[7] proposed the use of translating, pulsating sources instead of standard pulsating sources, but this method was extremely time-consuming. On the other hand, if the three-dimensional boundary value problem is reformulated in the time domain, the computational complexity can be reduced as in the time domain the Green's function is much less complicated, and speed dependence can be tackled implicitly. King et al[8] presented successful results obtained using a linear time domain method which accounted for forward speed effects. Bingham et al[9] applied a time domain method to a Wigley hull, with and without steady forward speed. Their results were found to be in good agreement with experiments and frequency domain methods. They then applied the method to the more realistic Series 60 type hull form[10]. The works presented so far are all modelling the ship as a rigid body. However, in 1971, Bishop[11] brought the theory of hydroelasticity into consideration by suggesting that ship response should be evaluated via hydroelastic analysis.

Bishop and Price[12] presented the concept of "*dry modes*" to perform the modal analysis of the hulls. This comprised two stages : the "in vacuo" analysis where the structural principal modes were first calculated using free-free Euler or Timoshenko beams before the fluid actions were applied using simple orthogonality relations and strip theory. This approach was first applied to symmetric response of beam-like ships by Bishop, Price and Tam[13] and then extended by Bishop, Price and Temarel[14] to model the antisymmetric response of a container ship in regular waves. As the matter of antisymmetric response was taken into consideration, Bishop, Price and Zhang Xicheng[15] studied specifically the problem of torsion with warping using Vlasov beam. Later on, Pedersen studied the torsional response of containerships[16] and developed[17] his one dimensional finite-element procedure for analysis of the coupled torsional-bending response of thin-walled beam structures which could model ship hulls. These studies raised the concern of ships with large deck openings which have then specifically studied by Senjanovic and Fan[18] followed by Hu and Chen[19].

Although hydroelastic theory provides a good approximation to the real physical phenomenon of a ship experiencing stresses in waves, the underlying potential flow model can only predict the fluid-structure interaction in an ideal fluid. Strip theory and three-dimensional panel methods proved to be reliable tools. However, there exist strong linear phenomena for which free-surface viscous-flow computations are necessary. Recent developments of computational power enabled the implementation of viscous-flow simulations using the so-called Computational Fluid Dynamics by solving Reynolds Average Navier Stokes (RANS) equations. Korpus and Falzarano[20] and Chang et al[21] first neglected the influence of the free-surface in their computation. Subsequently, Gentaz et al[22] developed a fully coupled two-dimensional method using exact non-linear free-surface. This method was then applied by Jouette et al[23] to a three-dimensional hull. However, applying a RANS solver to estimate all components of motion is still computationally intensive. Thus, an alternative was proposed by Salui, Sarkar and Vassalos[24] in calculating the moments experienced by a section (square, U and V sections) forced to roll harmonically on a free-surface initially undisturbed. For different frequencies of oscillation, the hydrodynamic coefficients were calculated by extracting the Fourier coefficients of the fundamental frequency via an analysis of the instantaneous hydrodynamic moment. The method improved considerably the prediction of roll damping coefficients, especially in the cases where viscous effects play a more important role – namely V-sections and large amplitude motion. Nevertheless, the gain in accuracy in the prediction of the added moment of inertia was much less pronounced. The authors proposed to apply the methodology to an improved strip theory that would use the hydrodynamic coefficients of each section obtained by RANS. Subsequent examples of a fully three-dimensional RANS analysis of the motion of a ship have shown an improvement in the prediction of the forces, moments and motion coefficients. Weymouth et al[25] have claimed, for example, to obtain less than 2% of uncertainties in the prediction of the symmetric motions of a modified Wigley hull experimentally investigated in 1992 by Journee[26].

The aim of the current study is to investigate the feasibility of using a commercial RANS solver, CFX10, to model the dynamic loads in the time domain. The study focuses on antisymmetric dynamic behaviour (sway, yaw, roll, coupled with twisting and horizontal bending), although symmetric motions (heave and pitch, coupled with vertical bending) are also investigated. Rather than applying Fourier transform to calculate added mass, the method aims to use the global energy of the fluid domain, which is expected to be a more robust approach. The work is divided into a series of objectives. The first one, which is presented here, concerns the study of standard 2D sections, namely circular and squared sections.

Mathematical Theory

Fluid Dynamics

The CFX10 flow solver uses a finite volume formulation of the RANS equations to model fluid flow. In Cartesian coordinates, the continuity and momentum equations in non-dimensional tensor form are :

$$\frac{\partial U_i}{\partial x_i} = 0 \qquad (1)$$

$$\frac{\partial(\rho \cdot U_i)}{\partial t} + \frac{\partial(\rho \cdot U_i \cdot U_j)}{x_j} = -\frac{\partial P}{\partial x_i} + \frac{\partial}{\partial x_j}(\nu \cdot [\frac{\partial U_i}{\partial x_j} + \frac{\partial U_j}{\partial x_i}]) - \frac{\partial(\rho \cdot \overline{u_i' \cdot u_j'})}{\partial x_j} + f_i \qquad (2)$$

Calculation of added mass

By definition, the total kinetic energy of a fluid passing, in this case vertically, over a static two-dimensional section is :

$$KE_{fluid} = \frac{1}{2}\rho \iint [u^2 + (v - V_0)^2] ds \,, \qquad (3)$$

where the domain of integration in taken here as the 0xy plane of the computed domain.

Furthermore, one can express this fluid's kinetic energy in relation with the velocity of the fluid in the free-stream and some coefficient which would have the dimension of mass per unit length, that is to say :

$$KE_{fluid} = \frac{1}{2} M_v V_0^2 \qquad (4)$$

Combining these two equations gives the so-called dimensional added mass coefficient :

$$M_v = \frac{\rho \iint [u^2 + (v - V_0)^2] ds}{V_0^2} \qquad (5)$$

Numerical Modelling

The runs were all performed using CFX10 in parallel on Dual 2.2 GHz 64 bit Opteron with 1.98 GB RAM. Typical clock-time per time-step was 44 seconds.

Mesh generation

CFX uses a fully three-dimensional scheme. The domain used is thus a square box of 50x50x0.1m at the centre of which the section, either a circle or a square, of unit length is positioned. As shown in figure 1, the blocking used a combination of an H and an O grid, splitting the domain into 12 blocks. This combination should enable the eventual capture of both the free surface, particularly close to the section, while giving control upon the boundary layer in the near-wall region of the section. The height of the first node was chosen to get y^+ smaller than 10 so that low Reynolds number models could be applied in the boundary layer. 320 points were distributed uniformly around the section. The distribution was hyperbolic from the edges of the domain towards the section, with 30 nodes from the domain's edges to the edges of the O-grid, and 190 nodes on the diagonals of the O-grid. A total number of 113,768 nodes were used for this study.

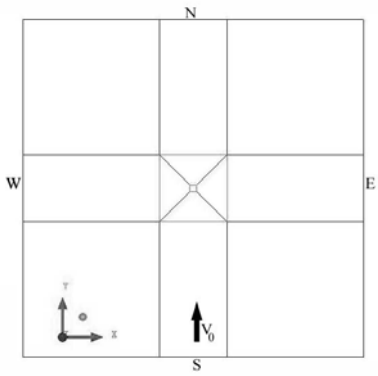

Figure 1: Blocking used

Boundary conditions

For all of the simulations, the two planes encompassing the domain were set as "symmetric" to ensure that no flow could pass through these planes while their presence could not interfere with the flow. The edges of the section were defined as "walls" with "no-slip condition. The bottom edge (S) of the domain was defined as a velocity inlet. The top edge (N) of the domain was set to be a pressure outlet with static pressure equal to the reference pressure. The sides of the domain (W, E) were defined as "freewalls" to ensure no interference with the flow. The inlet turbulence intensity was taken as 1% since this parameter did not seem to affect either the predicted drag, or the added mass due to the large domain. Inlet velocity was chosen to give $Rn=10^5$ or $Rn=3.6x10^6$.

Numerical scheme

A second order advection scheme and a second order backward Euler transient scheme were applied. An adaptative timestep was performed with a target RMS Courant Number of 1. The convergence criterion for the RMS of the residuals was set to 10^{-7}.

Results and Observations

Drag, added mass, pressure and skin-friction coefficients have been computed in the case of a vertical flow over a submerged static circle at infinite depth. The results were compared to the experiment by Achenbach [27] and classical potential flow analysis. Figures 2 and 4 show that, even though the numerical models are always under-predicting drag compared to the experiment, a converged value is reached. However, added mass diverges rapidly from the expected value. The same type of behaviour has also been noted in the case of a flow past a square.

Laminar model and two turbulence models - namely Shear Stress Transport (SST) and the Reynolds Stress model SSG - have been studied. It can be noted from figures 2 and 4 that while the laminar model is highly unstable, SST predicts a drag coefficient closer to the experimental value than SSG. As seen in figure 3, this difference can be explained by the fact that SSG over-predicts the backflow and generates very strong twin vortices in the wake. As expected, both SSG and SST predict a separation point later than the experiment, leading to a lower form drag.

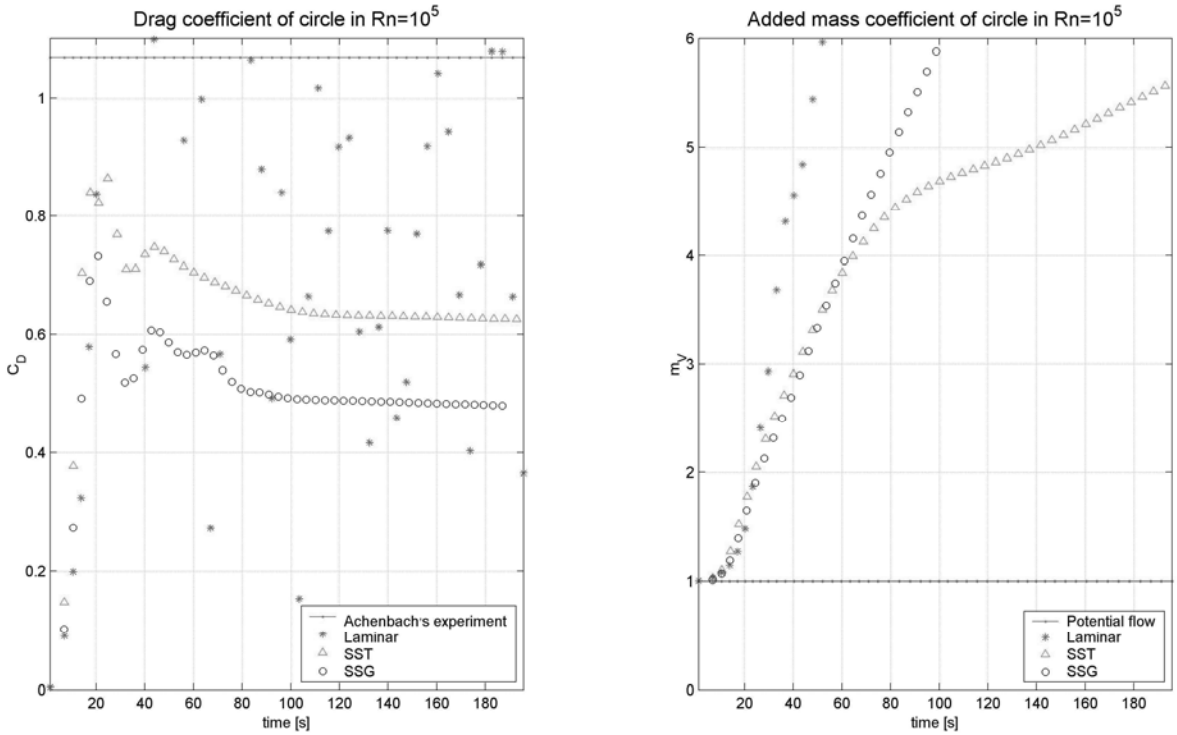

Figure 2 : Influence of turbulence model on drag and added mass coefficients for a flow of Rn=10^5 past a static circle at infinite depth.

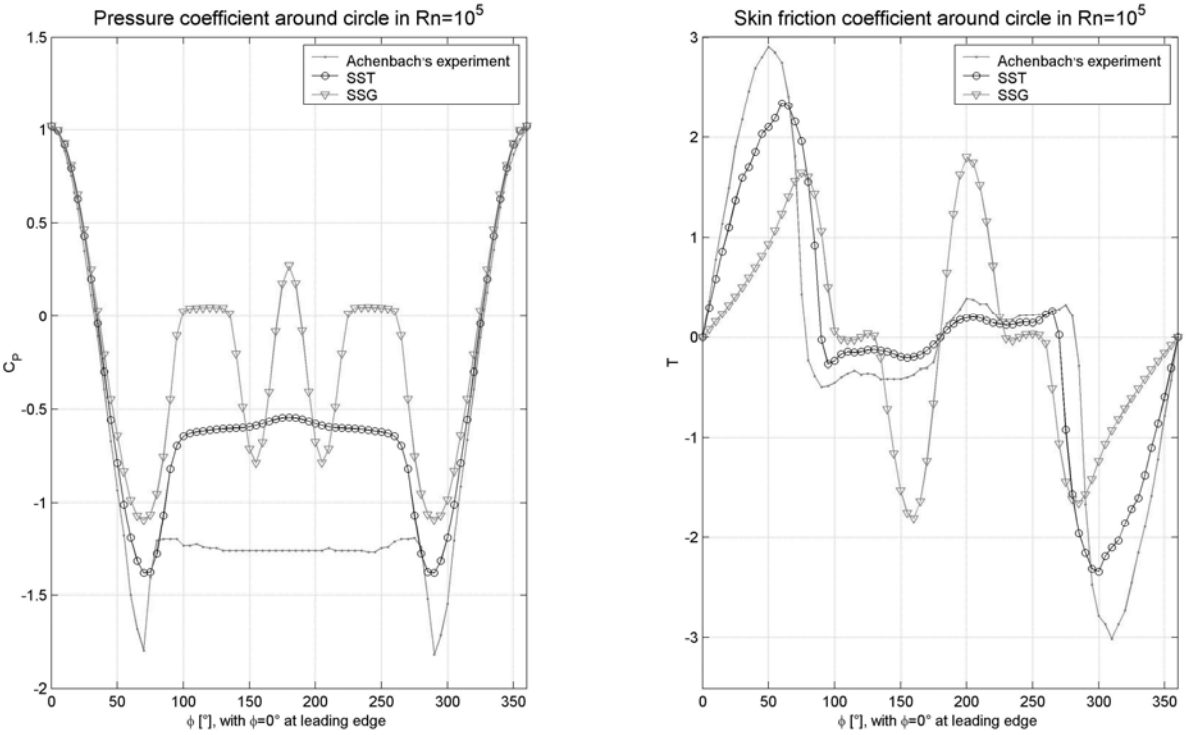

Figure 3 : Influence of turbulence model on pressure and skin friction coefficients at the section's wall for a flow of Rn=10^5 past a static circle at infinite depth.

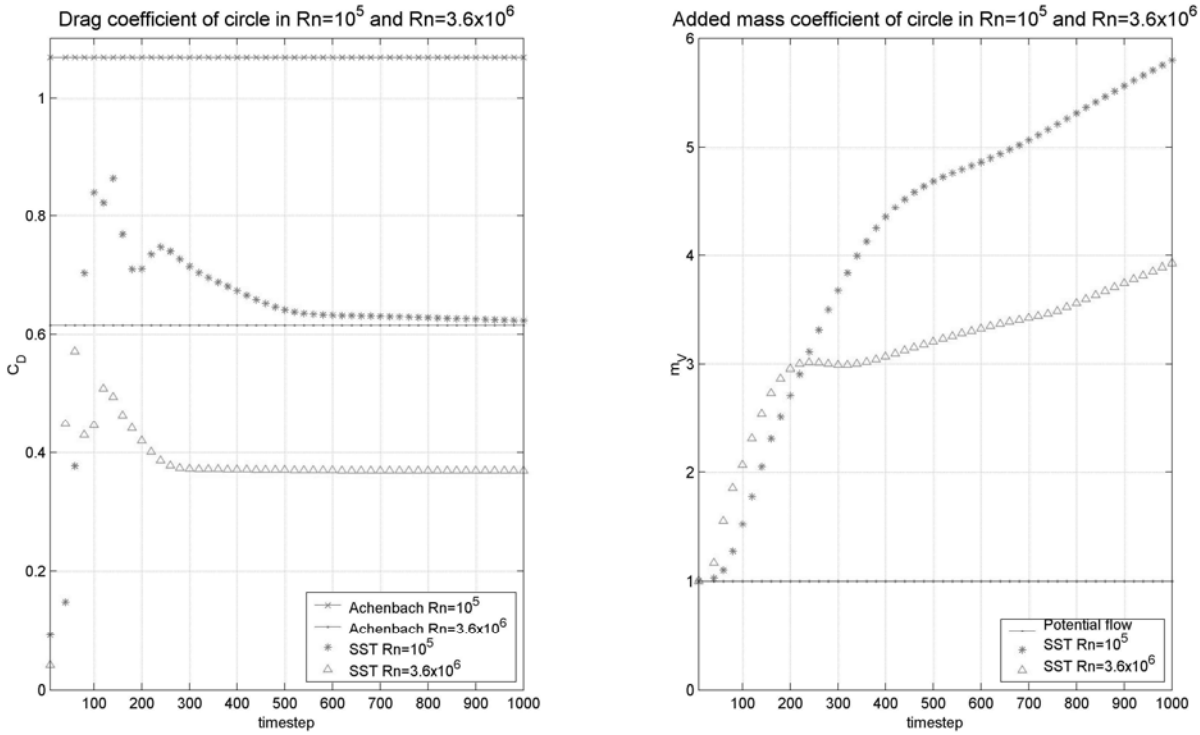

Figure 4 : Influence Reynolds Number on drag and added mass coefficients predicted with SST model for a flow past a static circle at infinite depth.

Added mass as expressed here relies on an energy formulation. Therefore, the total energy of the fluid domain has been calculated to check whether the unexpected divergence of added mass might be due to a violation of the principle of energy conservation. However, the difference of total energy between two consecutive time-steps was only of 0.05%, while the increase in kinetic energy, which is directly linked to added mass, reaches 0.20%*. According to figure 4, the added mass obtained here seems to be sensitive to Reynolds number. In fact, the lower the Reynolds Number, the quicker the divergence in added mass.

* Values calculated both directly within the CFX environment and by analysis of the exported output file.

Conclusion

The study aimed to validate a methodology for obtaining the hydrodynamic coefficients. Drag, pressure and skin friction coefficients reach converged values. However, added mass coefficient diverges quickly. Laminar model leads to highly unstable results. Turbulence models would be expected to stabilise the numerical scheme but will be done at the expense of the introduction of artificial turbulence when the physical flow is below transition. SST seems to give the best results in terms of drag, pressure and skin friction coefficients since SSG delays separation, over-predicts the backflow as well as the twin vortices in the wake.

The next stage in this work is to resolve the numerical difficulties evident in the increase of added mass. The expectation is that this is associated with the current poor mesh quality in the downstream wake. It is a considerable challenge to balance the extra computational cost, especially as the current model is already an expensive calculation with 1,000 time-steps for 113,768 grid nodes.

Acknowledgements

The authors would like to gratefully acknowledge the financial support from *Lloyd's Register U. T.C. in Hydro-dynamics, Hydroelasticity and Mechanics of Composites*.

References

[1] V. Korvin-Kroukovsky, Investigation of ship motions in regular waves, SNAME,63, pp. 386–435, 1955

[2] B. V. Korvin-Kroukovsky and W. R. Jacobs, Pitching and heaving motions of a ship in regular waves. SNAME,65, pp.590–631, 1957

[3] T.F. Ogilvie and E. O. Tuck, A rational strip theory for ship motions, Report013, Uni of Michigan, 1969

[4] N. Salvesen, E. O. Tuck, and O. M. Faltinsen, Ship motions and sea loads, SNAME,78, pp.250–280, 1970

[5] C.J. Garrison, Hydrodynamics of large objects in the sea part 1: Hydrodynamic analysis, Journal of Hydronautics,8, pp.5–12, 1974.

[6] O.M. Faltinsen and F. C. Michelsen, Motions of large structures in waves at zero Froude number, In R. E.D. Bishop and W. G. Price, editors, Int Symp on the Dynamics of Marine Vehicles and Structures in Waves, pp. 91–106, London, UK, April 1974. IMechE.

[7] J.Y. Wehausen and E.V. Laitone, Surface waves, In Encycl of Phys,9, pp 446–778, Springer Verlag, 1960

[8] B.K. King, R.F. Beck, and A. R. Magee, Seakeeping calculations with forward speed using time-domain analysis, In 17th Symp on Naval Hydrodynamics, pp. 577–596, The Hague, The Netherlands, 1988

[9] H. Bingham, F. T. Korsmeyer, J. N. Newman, and G. E. Osborne, The simulation of ship motions, In Proc 6th Int Conf on Num ShipHydrodynamics, pp. 561–579, 1993

[10] H. Bingham, F. Korsmeyer, and J. N. Newman, Prediction of the seakeeping characteristics of ships, In 20th Symposium on Naval Hydrodynamics, pp. 27–47, Santa Barbara, California, USA, 1994

[11] R.E.D Bishop, On the strength of large ships in head seas, The South African Mech Eng,21, pp1-20, 1971

[12] R.E.D. Bishop and W.G. Price, On the modal analysis of ship strength, Pro. Royal Soc. London, A341, pp.121-134, 1974

[13] R.E.D. Bishop, W.G. Price and P.K.Y Tam, A unified dynamic analysis of ship response to waves, Trans RINA,119,pp.363-390, 1977

[14] R.E.D. Bishop, W.G. Price and P. Temarel, A unified dynamic analysis of antisymmetric ship response to waves, Trans RINA,122, pp.349-365, 1980

[15] R.E.D. Bishop, W.G. Price and Zhang Xicheng, On the structural dynamics of a Vlasov beam, Proc. R. Soc. London, Vol A388, pp.49-73, 1983

[16] P.T. Pedersen, Torsional response of containerships, Journal of Ship Research,29-3, pp.194-205, 1985

[17] P.T. Pedersen, Beam theories for torsional-bending response of ship hulls, Journal of Ship Research,35-3, pp.254-265, 1991

[18] I. Senjanovic, Y. Fan, Pontoon torsional strength analysis related to ships with large deck openings, Journal of Ship Research,35-4, pp.339-351, 1991

[19] Y. Hu and B. Chen, Limit state of torsion of ship hulls with large hatch openings, Journal of Ship Research,45-2, pp.95-102, 2001

[20] R.A. Korpus and J.M. Falzarano, Prediction of viscous ship roll by unsteady Navier-Stokes techniques, OMAE, Trans. ASME 119, pp. 108-113, 1997

[21] H.X. Chang, G.P. Miao, Y.Z. Lu, Numerical study on roll damping of ship by solving incompressible N-S equations in hydrodynamics, Balkema Publ., 1996

[22] L. Gentaz, B. Alessandrini, G. Delhommeau, Motion simulation of a two-dimensional body at the surface of a viscous fluid by a fully coupled solver, 12th WWWFB, pp.85-89, 1997

[23] C. de Jouette, O. Laget, J.M. Le Gouez, Vers la tenue à la mer des navires par une formulation en fluide visqueux, 7^{e} Journées de l'Hydrodynamique, ISSN 1161-1847, Marseille, 1999

[24] K.B. Salui, T. Sarkar and D. Vassalos, An improved method for determining hydrodynamics coefficients in roll motion using CFD techniques, Ship Technology Research, 47, pp. 161-174, 2000

[25] G. D. Weymouth, R. V. Wilson, F. Stern, RANS computational fluid dynamics prediction of pitch and heave ship motions in head seas, Journal of Ship Research,49, No 2, pp 80-97, June 2005

[26] J.M.J Journee, Experiments and calculations on four Wigley hull forms, Delft Univ of Tech, Ship Hydrodynamic Laboratory, Report 909, February 1992

[27] E. Achenbach, Distribution of local pressure and skin friction around a circular cylinder in cross-flow up to Re=5x10^{6}, J. Fluid Mech., Vol 34, pp. 625-639, 1968

Investigation of Scale Effects in Exhaust-Gas Tests using RANS Solver FreSCo

Daniel Schmode, d.schmode@tu-harburg.de
Jan Henning Günther , Jan Kaufmann, Thomas Rung
AB 3-13 of TU Hamburg-Harburg, D-21071 Hamburg
Dieke Hafermann
HSVA, Bramfelder Str. 164, D-22305 Hamburg

1 Introduction

To access the performance of ship funnels wind tunnel tests are common practice. The aim of such tests is to check if the passengers were disturbed by the smell of exhaust gas, or if the inlets of ventilation were contaminated. Wind tunnels allow experiments at Reynolds numbers around 10^3 to 10^4. Full scale Reynolds numbers are around three orders of magnitude larger. It is usually believed that the scale effect is negligible, but this has not been proved yet. This study aims to assess the scale effects on wind tunnel tests. It was carried out within an student project with an limited amount of time allocated. Thus this paper presents quite preliminary results.

2 Mathematical Model

The section briefly outlines the governing equations refering to the conservation of mass, momentum and the the transport equation for the exhaust gas.

2.1 Momentum & Continuity

The computational approach is based on the conservative form of the Navier-Stokes equations for solenoidal velocity fields, viz.

$$\frac{\partial}{\partial t}\int_V \rho dV + \int_S \rho \mathbf{v}\cdot\mathbf{n}dS = 0\,, \tag{1}$$

$$\frac{\partial}{\partial t}\int_V \rho \mathbf{v} dV + \int_S \rho \mathbf{v}\mathbf{v}\cdot\mathbf{n}dS = \int_S \mathbf{T}\cdot\mathbf{n}dS. \tag{2}$$

with

$$\mathbf{T} = 2\mu\mathbf{D} - \mathbf{I}\left(\frac{2\mu}{3}\nabla\cdot\mathbf{v} + p\right) \tag{3}$$

and

$$\mathbf{D} = \frac{1}{2}\left(\nabla\mathbf{v} + \mathbf{v}\nabla\right)\,. \tag{4}$$

Here V denotes the observed control volume and S its respective surface, represented by the face normal vector $\mathbf{n}$. The velocity vector and pressure are denoted by $\mathbf{v}$ and p. The properties of the fluid are described by the density ρ and the dynamic viscosity μ.

2.2 Two-Phase Flow Approach (Volume-of-Fluid, VoF)

In the present study, the fluid is deemed to be a homogeneous mixture. The respective volume fraction (concentration) of each phase i is defined by $C_i = V_i/V$, where V_i is the volume associated to the phase i and V is the sum of all phase volumes, i.e. $V = \sum V_i$. Accordingly, the transport equation for a concentration reads

$$\frac{\partial}{\partial t}\int_V C_i dV + \int_S C_i \mathbf{v}\cdot\mathbf{n}dS = 0\,. \tag{5}$$

The density ρ and viscosity μ of the mixture are reconstructed via

$$\rho = \sum_{i=1}^{n}\rho_i C_i \quad , \quad \mu = \sum_{i=1}^{n}\mu_i C_i\,. \tag{6}$$

Diffusion is usually set to zero in VoF computations. In laminar cases this may be justified due to the very small molecular motion. In strongly turbulent flows it may have considerable influence. We do not treat this turbulent mixing effect in our VoF computations here.

2.3 Turbulence Modeling

In this study we apply the Standard k-ϵ. As described in [4].

3 Numerical Method

The numerical procedure FreSCo consists of an unstructured, cell-centred finite-volume method. The algorithm approximates the fully conservative formulation of the governing equations like proposed e.g. in [1]. FreSCo is based on an unstructured grids using arbitrary polyhedral cells and a co-located variable storage arrangement. The governing equations are solved in a segregated manner, utilizing a volume-specific pressure-correction scheme to satisfy the continuity equation. To avoid an odd-even decoupling of pressure and velocity, a third-order pressure smoothing is employed along a route outlined by Rieh & Chow [2].

The fully-implicit algorithm is second-order accurate in space and time. Integrals are approximated based on the mid-point rule. Diffusion terms are approximated using 2nd-order central differences, whereas advective fluxes are approximated based on blends between high-order upwind-biased schemes (e.g. QUICK), 1st-order upwind and 2nd-order central differences schemes.

The resulting linear equation systems are solved iteratively using Krylov subspace methods. The respective solvers are provided by the PETSc library.

4 Generic RoPax

In an preceding study we have investigated the flow around an fast RoPax ferry including many geometrical details using tetrahedron-grids [3]. This study concluded that the strong numerical diffusion related to the tetrahedron-grids spoils the results considerable.

Thus we use a simple generic geometry without filigree details like antennas, rails, etc. in this study. Hexahedron-grid generation for this geometry is straight forward. There are no wind tunnel tests available at present, but we intend do this in the future and the simple geometry reduces the costs for the model. The main dimensions are similar to the modern fast RoPax ferry used in [3]. They are given in Table 1.

Hull	length	200.0	m
	width	25.0	m
	height	10.0	m
Superstructures	length	125.0	m
	width	20.0	m
	height	10.0	m
Funnel	length	10.0	m
	width	4.0	m
	height	5.0/7.5/10.0	m
Box(Radar mast)	length	2.0	m
	width	2.0	m
	height	5.0	m
Pipe	diameter	2.0	m
	height	2.0	m

Table 1: Main dimensions of generic superstructures

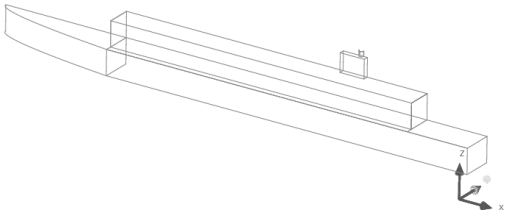

Figure 1: Generic Ship Superstructure without radar mast

We investigate 6 slightly modified geometries. There are 3 different funnel heights (5.0m,7.5m,10.0m) which should simulate an good performing funnel (10.0m), a bad performing funnel (5.0m) and an crucial case (7.5m). And to investigate how sensible the flow is to obstacles upstream of the funnel we investigate all three funnels with and without an generic radar-mast (simply a box) upstream. This yields in six different geometries. Two geometries are given in Figure 1 and 2.

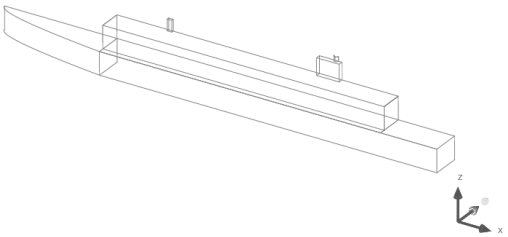

Figure 2: Generic Ship Superstructure with radar mast

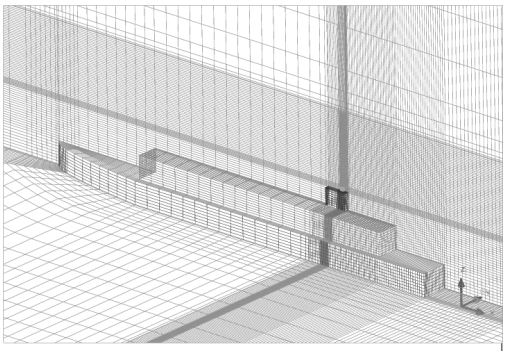

Figure 3: Grid for 7.5m funnel without radar mast

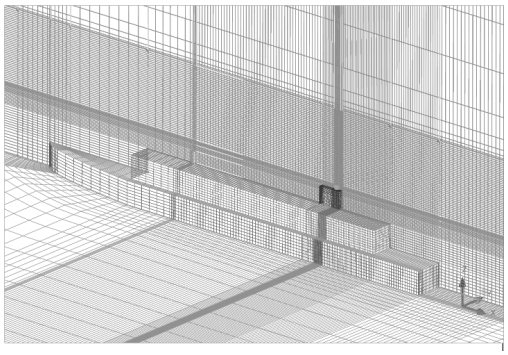

Figure 4: Grid for 7.5m funnel with radar mast

Rn	3.310^3	1.710^4	5.010^6
L_{ship}	$1.3m$	$1.3m$	$200.0m$
v_{ship}	$3.0m/s$	$15.0m/s$	$30.0m/s$
$v_{exhaust}$	$3.0m/s$	$15.0m/s$	$30.0m/s$
μ	$1.8\ 10^{-5}Pas$	$1.8\ 10^{-5}Pas$	$1.810^{-5}Pa\ s$
ρ	$1.1kg/m^3$	$1.1kg/m^3$	$1.1kg/m^3$
dt	$0.051/s$	$0.011/s$	$0.11/s$
turb. model	k-ϵ	k-ϵ	k-ϵ

Table 2: Main parameters

5 Grids

The computational domain reaches one ship length ahead, abeam and atop, and two ship length astern. It includes the inner part of the pipe. The grids were generated using ICEM-cfd Hexa. We only investigate headwind cases here, thus we apply symmetry boundary-condition. The grids with generic radar mast have 770k cells and the cases without have 610k cells (Figure 3 and 4).

6 Computational Parameters

The aim of this study is to investigate scale effects. Thus we have investigated three different Reynolds numbers ($Rn = v_{ship}L_{oa}/\nu$). One for full scale ($Rn = 5.010^6$) one for model scale ($\lambda = 150$) with the wind tunnel speed $v = 3.0m/s$ which is usually used at TUHH ($Rn = 3.310^3$) and one for for model scale ($\lambda = 150$) with a wind tunnel speed $v = 15m/s$ which is the larges possible for the new TUHH wind tunnel in "Eiffel" mode ($Rn = 1.710^4$)). We carried out all computations transient. In real life the exhaust gas has a Temperature of 300^oC, while the gas in the wind tunnel tests have ambient temperature. Here all computations were carried out with exhaust gas on ambient temperature.

7 Results

The results presented here were obtained within an student project and the time allocated to this projects is limited. Thus they were quite preliminary and maybe they suffer from some unconcerns. E.g. we assume that boundary-layer effects do not dominate the flow, thus we did not take much care resolving the boundary-layer. Furthermore the distribution of the grid-density could be improved and the

discretisation error should be assessed by grid studies. Another unaddressed question is exhaust gas propagation in oblique flow. Experimental experience show that this cases are usually more crucial.

In Figure 5 to 6 the species concentrations are given. Typical exhaust gas from ship engines could be visually noticed from an concentration of 8ppm, but the human nose noticed it already by 3ppm. The color map reaches from 0ppm to 10ppm. The limits in the concentration of the gas used in model tests is not known by the authors and may be differ by the different facilities. In each figure the left column shoes results for the geometries without, the right one with radar mast. The funnel height is increasing from top ($h = 5.0m$) to bottom ($h = 10.0m$).

Comparing the full scale and model scale results reveals some unexpected difference. The model scale computations without radar mast Figure 6 left column) show similar behaviour for the different funnel heights. The model scale computations with radar mast Figure 6 right column) show an dependency on the funnel height. For the full scale computation it is the other way round: computations without the mast Figure 5 left column) do depend on funnel height, while the ones with mast Figure 5 right column) do not. Furthermore a very unexpected result can be seen in the full scale computations without mast Figure 5 left column). Here the lower funnel performs best, while the higher one do it worse. This is quite strange and unexpected. Another unexpected result is the influence of the radar mast. It was anticipated that the mast spoils the funnel performance, but is looks like it catalysed it. But at least the comparison between the two model scale computation show the anticipated similarity. Thus the plots are not printed here.

With respect to the mentioned weaknesses of this results, and the quite unxepected results we feel that some more extensive work has to be done.

8 Conclusion

Considering scale effects in wind tunnel tests for exhaust gas propagation, there are still open questions. In the present study we made an first step, and revealed alt least some unexpected behavior. We will continue our work and hope to motivate others to do so as well. We also think about the unaddressed topic of turbulent mixing outlined in 2.2.

References

[1] J.H. Ferziger and M. Peric. *Computational Methods for Fluid Dynamics*. Springer Verlag, 3^{rd} edition, 2002.

[2] C.M. Rhie and W.L. Chow. A Numerical Study for the Turbulent Flow past an Isolated Airfoil with Trailing Edge Separation. *AIAA Journal*, 17:1525–1532, 1983.

[3] D. Schmode. Aerodynamische RANSE-Simulation für eine schnelle Fähre . Master's thesis, Hamburg University of Technology, 2002.

[4] D. C. Wilcox. *Turbulence Modeling for CFD*. DCW Industries, 2^{nd} edition, 1998.

a) Funnel $5\,m$ height without radar mast

b) Funnel $5\,m$ height with radar mast

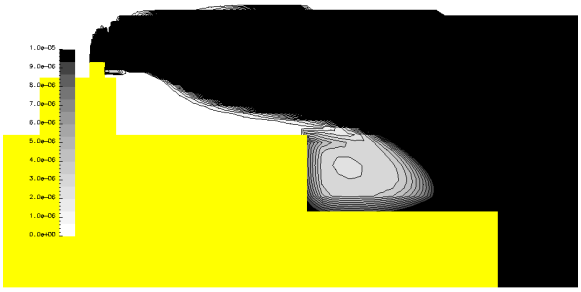

c) Funnel $7,5\,m$ height without radar mast

d) Funnel $7,5\,m$ height with radar mast

e) Funnel $10\,m$ height without radar mast

f) Funnel $10\,m$ height with radar mast

Figure 5: Species concentration for full scale at $Rn = 5.010^6$ ($s_{ship} = 30m/s$ and $v_{exhaust} = 30m/s$)

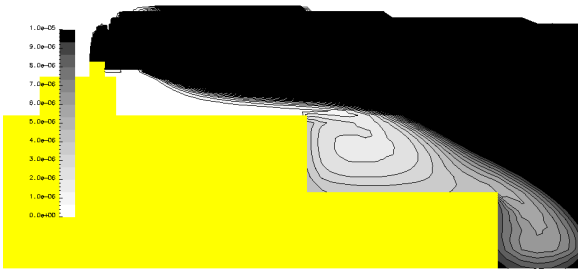

a) Funnel $5\,m$ height without radar mast

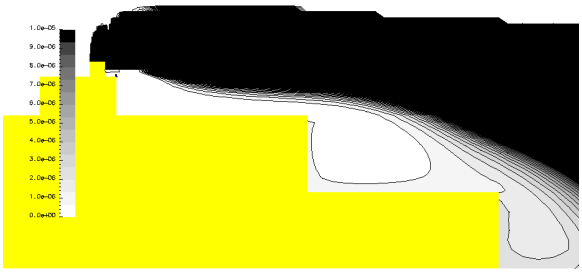

b) Funnel $5\,m$ height with radar mast

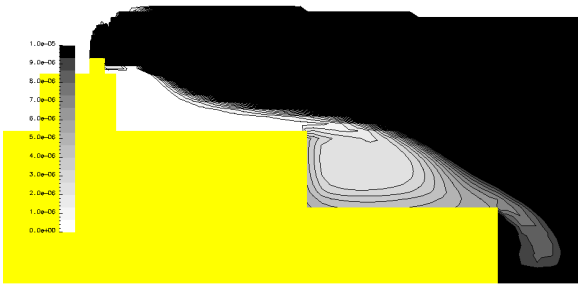

c) Funnel $7,5\,m$ height without radar mast

d) Funnel $7,5\,m$ height with radar mast

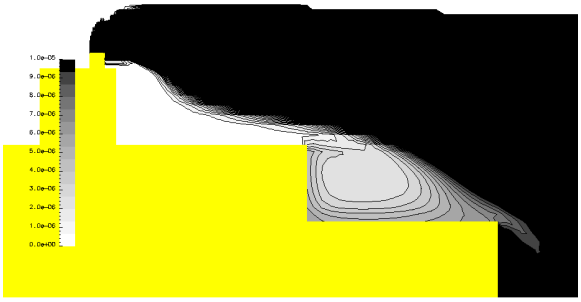

e) Funnel $10\,m$ height without radar mast

f) Funnel $10\,m$ height with radar mast

Figure 6: Species concentration for model scale at $Rn = 3.310^3$ ($\lambda = 150$, $v_{ship} = 3m/s$ and $v_{exhaust} = 3m/s$)

Obvious techniques towards adjoint CFD

Arthur Stück, arthur.stueck@tu-harburg.de
Thomas Rung, thomas.rung@tu-harburg.de
Institut für Fluiddynamik und Schiffstheorie, Hamburg University of Technology, Germany

1 Introduction

In CFD-based shape design computational costs quickly become prohibitive. When many design parameters are involved, it is mostly impossible to vary all influential parameters systematically. Usually, only some preselected parameter variations are investigated instead. Inevitably, many design parameters remain unstudied and rely on the designer's experience.

Gradient-based shape optimisation can facilitate a design process efficiently, provided that reliable sensitivity information is available at low computational effort. It is particularly attractive in terms of local optimisation, coming from a sound reference design: For example in ship design, when a reference hull form is distorted according to a smooth shape parametrisation, such as Söding (2002) or Veelo (2004).

Taking into account sensitivity information, a designer will know the direction of steepest descent of a cost function with respect to the shape parametrisation in a design point. However, he must be aware of being led towards a local optimum. He also has to consider a lot of practical design constraints when modifying the design. But provided the gradients can be obtained efficiently and are sufficiently accurate, he will have a very helpful design tool at hand – such as suggested by Söding (2001) in the context of resistance reduction in ship hull design.

Generally, sensitivity information can be obtained in two ways:

- In a *direct* approach, the sensitivity of the flow variables to a shape perturbation, i.e. the flow change corresponding to a shape modification, is calculated first. Subsequently, the cost function variation has to be calculated from the perturbed flow variables. The flow perturbation can be obtained using different techniques, such as finite differencing, complex variable methods or by solving the linearised flow equations.

- Using an *adjoint* approach, it is possible to compute directly the sensitivity of a cost functional with respect to source terms owing to shape perturbations in the linearised flow equations. This technique is adopted in the present approach.

In the former case, the computational effort scales with the number of design parameters, as the flow field perturbation needs to be calculated for each shape perturbation. In the latter case, computational costs increase with the number of cost functions: The adjoint problem has to be solved once per cost function, independent of the number of design parameters. Therefore, when the number of design parameters exceeds the number of cost functions, the adjoint approach will usually be more efficient.

In conjunction with industrial shape optimisation, a huge set of design parameters is often necessary to allow for a sufficiently fine shape representation. Especially in 3D shape optimisation, the number of parameters quickly exceeds the number of cost functions and the computation of sensitivities should be carried out in adjoint mode.

This paper addresses the construction of adjoint CFD-code for existing CFD solvers. Adjoint code is derived on the basis of the discretisation used in associated primal flow solver. The

approach is known as *discrete adjoint* method and provides consistency between the primal and the sensitivity code (Nadarajah, 2003). It also allows for developing the adjoint code closely to the primal solver so that coding effort can be reduced by using big portions of the original solver. This technique is exemplified for an elementary potential flow code based on the patch method. Subsequently, an incompressible Navier-Stokes solver is considered, using the SIMPLE algorithm on collocated, cell-centred grids.

2 Discrete adjoint formulation

In accordance with Giles and Pierce (2001), the discrete adjoint approach is briefly introduced using Einstein's summation convention. A scalar hydrodynamic cost function $f(z_j(\alpha_i), x_j(\alpha_i))$, e.g. the lift of an airfoil, is considered which depends on the flow field $z_j(\alpha_i)$ and the grid coordinates $x_j(\alpha_i)$, both of which depend on the design parameters α_i. The flow field z_j is subject to the governing flow equations

$$N_m(z_j(\alpha_i), x_j(\alpha_i)) = 0. \tag{1}$$

We are interested in the variation of the cost function δf^k corresponding to a shape perturbation $\delta\alpha_i^k$, which can be obtained by linearising about a base solution z_{0i}:

$$\delta f^k = \frac{\partial f}{\partial z_i}\delta z_i^k + \frac{\partial f}{\partial x_i}\frac{\partial x_i}{\partial \alpha_j}\delta\alpha_j^k = \underbrace{g_i\,\delta z_i^k}_{\delta f_I^k} + \underbrace{\frac{\partial f}{\partial x_i}\frac{\partial x_i}{\partial \alpha_j}\delta\alpha_j^k}_{\delta f_{II}^k} \quad \text{with} \quad \delta z_i^k = \frac{\mathrm{d}z_i}{\mathrm{d}\alpha_j}\delta\alpha_j^k. \tag{2}$$

The direct sensitivity of the cost function to the shape perturbations δf_{II}^k only depends on geometric grid variations and is easy and cheap to evaluate.

The term δf_I^k depends on the flow variation δz_i^k which is subject to the linearised governing flow equations

$$\frac{\partial N_i}{\partial z_j}\delta z_j^k + \frac{\partial N_i}{\partial x_j}\frac{\partial x_j}{\partial \alpha_l}\delta\alpha_l^k = 0 \quad \text{or} \quad A_{ij}\,\delta z_j^k = -\frac{\partial N_i}{\partial x_j}\frac{\partial x_j}{\partial \alpha_l}\delta\alpha_l^k. \tag{3}$$

Using Eq. (3), δf_I^k can be expressed as

$$\delta f_I^k = g_i\,\delta z_i^k = \underbrace{g_i\,A_{ij}^{-1}}_{z_j^*}\left(-\frac{\partial N_j}{\partial x_l}\frac{\partial x_l}{\partial \alpha_m}\right)\delta\alpha_m^k, \tag{4}$$

which yields the discrete adjoint equation

$$A_{ij}^T z_j^* = g_i. \tag{5}$$

As Eq. (5) is independent of the shape variation k, it needs to be solved only once per cost function for an arbitrary number of shape parameters. Then, each cost function increment δf_I^k, corresponding to the shape perturbation $\delta\alpha_i^k$, can efficiently be calculated according to

$$\delta f_I^k = z_i^*\left(-\frac{\partial N_i}{\partial x_j}\frac{\partial x_j}{\partial \alpha_l}\right)\delta\alpha_l^k. \tag{6}$$

When field methods are applied, the interior grid is linked smoothly to the variation of the surface geometry via grid adaptation techniques. Then, $\frac{\partial x_i}{\partial \alpha_j}$ is usually non-zero at both interior and surface grid points.

3 Adjoint code construction

Adjoining a potential flow code

An elementary potential flow solver (Söding, 1999), based on the patch method, is used to exemplify the discrete adjoint approach introduced above. A symmetric NACA0020 section in free stream conditions is considered as a test case. The flow potential is superimposed from parallel flow, sources and a vortex distribution along the chord line. The boundary conditions along the foil contour are $\frac{\partial \phi}{\partial x_i}\, n_i = 0$ and a Kutta condition at the trailing edge. These boundary conditions form a linear equation system (LES), that needs to be solved for the unknown source and vortex strengths.

A shape variation $\delta\alpha_i^k$ is realised using small displacements of the boundary nodes along the foil contour (as shown in Fig. 1 and 2). These are directed outwards, normal to the contour.

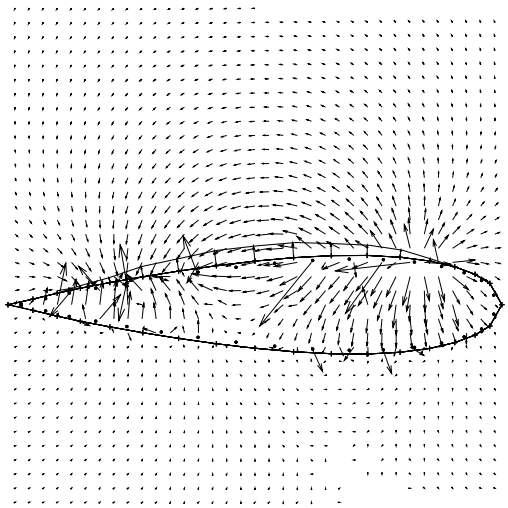

Figure 1: Flow change corresponding to the shape perturbation of the NACA0020. The foil operates in potential flow at 5° angle of attack. Eq. (3) has been solved for the changes in source and vorticity strengths to give the potential change $\delta\phi^k$. The velocity changes have been calculated analytically – therefore very high velocities are induced close to the singularities.

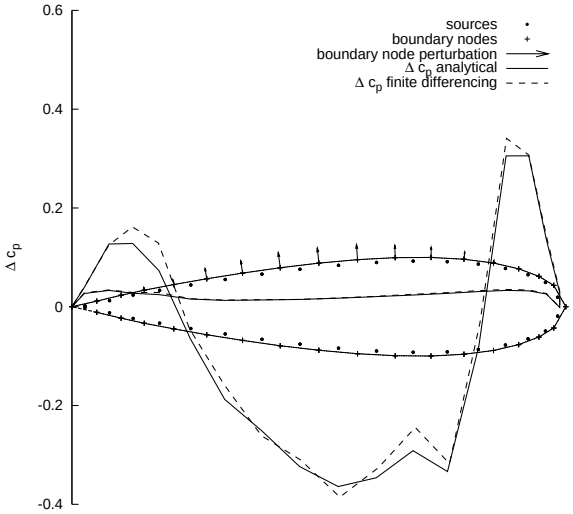

Figure 2: Change in pressure distribution due to the shape perturbation for a NACA0020 at 5° angle of attack. The negative, non-dimensional value of the bracketed expression of δf_I^k [Eq. (7)], labelled "analytical", is plotted over the chord-line of the foil section. It shows good agreement with the change in pressure distribution obtained by finite differencing.

The discrete adjoint equation is constructed for a hydrodynamic cost function f, say the lift force:

$$f = \int p\, n_\alpha \,\mathrm{d}S, \quad \text{with} \;\; p = -\frac{\rho}{2}\left[\left(\frac{\partial \phi}{\partial x_i}\right)^2 - U_0^2\right] .$$

n_α is the component of the surface unit vector normal to the free flow U_0; ϕ represents the superimposed flow potential.

The linear variation of the cost function corresponding to the shape variation $\delta\alpha_i^k$ is devised according to Eq. (2):

$$\delta f^k = \underbrace{-\rho \int \left(\frac{\partial \phi}{\partial x_i}\frac{\partial\, \delta\phi^k}{\partial x_i}\right) n_\alpha \,\mathrm{d}S}_{-\delta f_I^k} \underbrace{- \frac{\rho}{2}\int \left[\left(\frac{\partial \phi}{\partial x_i}\right)^2 - U_0^2\right] \delta(n_\alpha \,\mathrm{d}S)^k}_{-\delta f_{II}^k} \tag{7}$$

It consists of δf_I^k, i.e. the flow variation acting on the unperturbed (labelled "old") geometry and δf_{II}^k which can be interpreted as the "old" flow acting on the geometry change $\delta(n_i \, \mathrm{d}S)^k$. δf_I^k contains the potential variation $\delta\phi^k$ corresponding to shape perturbation k. Instead of solving the linearised potential flow problem (3) for every shape variation, the adjoint approach is applied to transform δf_I^k according to Eq. (4):

$$\delta f_I^k = -\rho \int \left[\frac{\partial \phi}{\partial x_i} \frac{\partial \, \delta\phi^k}{\partial x_i} \right] n_\alpha \, \mathrm{d}S = \overbrace{\underbrace{-\rho \int \frac{\partial \phi}{\partial x_i} \left[n_\alpha \, \mathrm{d}S \, b_{ij} \right]}_{g_j} (A^{-1}_{jm}}^{z^*_m} \left(-\frac{\partial N_m}{\partial x_n} \frac{\partial x_n}{\partial \alpha_l} \right) \delta\alpha_l^k)] \qquad (8)$$

A_{ij} is identical to the coefficient matrix of the original potential flow solver. Also b_{ij} has already been assembled in the primal solver – it is used to calculate $\frac{\partial \phi}{\partial x_i}$ along the contour from the strengths of the singularities, which are the variables in the primal solver. The adjoint equation (5) is independent of $\delta\alpha_i^k$ and has to be solved only once per cost function for the adjoint variables z_i^*. Subsequently, f_I^k can cheaply be evaluated according to Eq. (6) for every shape modification k.

Computing δf_{II}^k only requires geometric operations based on the "old" flow; the computational effort is comparable to that of a force integration in post-processing.

1. Obtain a reference potential flow solution for the unperturbed geometry. Evaluate the cost function for the current design point.
2. Calculate $g_i = \frac{\partial f}{\partial z_i}$.
3. Solve the discrete adjoint problem $A^T_{ij} z^*_j = g_i$.
4. Vary the shape by a small perturbation $\delta\alpha_i^k$.
5. Compute the cost function variation $\delta f_I^k = z_i^* \left(-\frac{\partial N_i}{\partial x_j} \frac{\partial x_j}{\partial \alpha_l} \right) \delta\alpha_l^k$ and δf_{II}^k for shape perturbation k.
6. Repeat (4) and (5) for each perturbation k.

Figure 3: Algorithm for adjoint computation of cost function variations (potential flow)

Navier-Stokes based sensitivity analysis

The incompressible, SIMPLE-based Navier-Stokes solver CAFFA (Peric, 1996) is used in the current study. It is based on a finite volume discretisation on collocated cell-centred grids, assuming steady flow of constant density and viscosity.

The Navier-Stokes equations (NSE) are linearised with respect to a shape perturbation k to yield Eq. (3). Therefore, a perturbed or "new" flow field z is obtained by superimposing an "old" reference solution z_0 and a perturbation δz^k corresponding to shape modification k

$$z(\underline{x}) = z_0(\underline{x}) + \delta z(\underline{x})^k.$$

Using a Taylor expansion, the flow variables at the "new" grid position $\underline{x} = \underline{x}_0 + \delta\underline{x}^k$ can be expressed as

$$z(\underline{x}) = z(\underline{x}_0) + \nabla z(\underline{x}_0) \cdot \delta\underline{x}^k + \mathrm{HOT}.$$

Neglecting HOTs, this yields the "new" variable values at the "new" grid locations $\underline{x}$:

$$z(\underline{x}) \approx z_0(\underline{x}_0) + \nabla z_0(\underline{x}_0) \cdot \delta\underline{x}^k + \delta z^k(\underline{x}_0) \tag{9}$$

As the NSE need to be satisfied by the "new" flow on the "new" grid, the approximation (9) is substituted for the corresponding flow variables in the NSE, i.e. for the pressure and the velocity variables. The surface and volume integrals have to be evaluated on the "new", i.e. perturbed grid – that is $n_i\,\mathrm{d}S + \delta(n_i\,\mathrm{d}S)^k$ for the surface integrals. These expressions are introduced into the momentum equations and the pressure correction equation. Neglecting nonlinearities and terms that are independent of k (these can be neglected when the NSE are satisfied by the unperturbed reference solution), we obtain the linearised momentum and pressure correction equations, corresponding to Eq. (3). These are solved by the SIMPLE algorithm. The calculated velocity perturbations $\delta\underline{u}^k(\underline{x}_0)$, corresponding to shape variation k, are presented in Fig. 4 and 5.

In the subsequent step, the SIMPLE algorithm has to be adapted for solving the adjoint equation system (5); this is currently being developed.

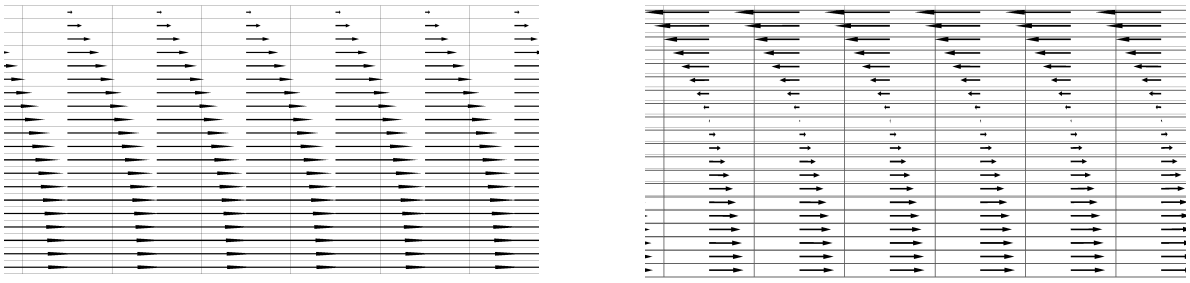

Figure 4: Fully developed laminar flow ($Re = 4$) between a slip-wall at the lower side and a no-slip wall at the upper side (left). On the right, the width is reduced keeping the mass flux fix – the corresponding velocity change $\delta\underline{u}^k(\underline{x}_0)$ calculated on the "old" grid is scaled up by factor 20. The "new" flow on the "new" grid can be calculated according to Eq. (9). Analytical validation is possible for very low Reynolds numbers.

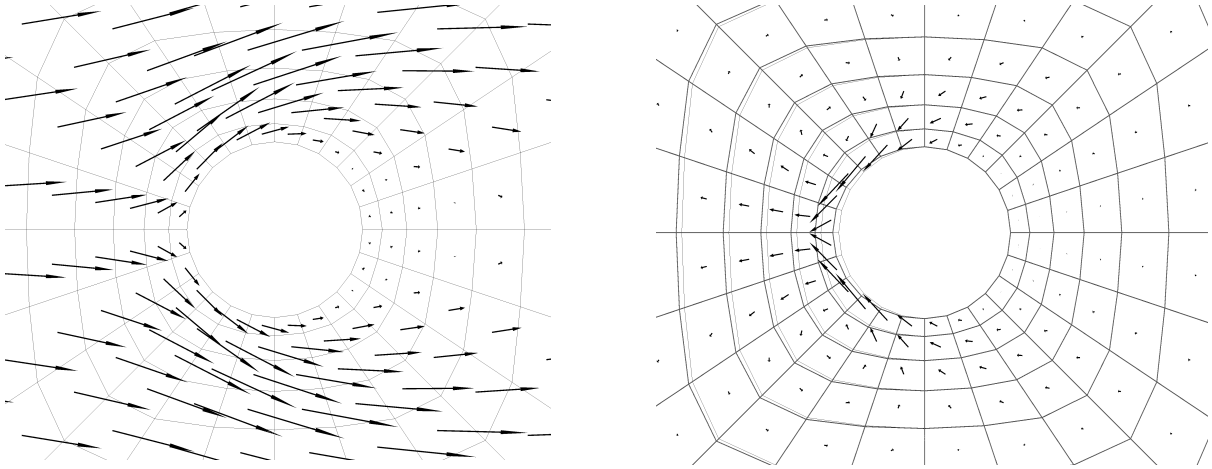

Figure 5: Laminar flow around a cylinder ($Re = 20$). On the right, the front has slightly been extruded – the corresponding velocity change $\delta\underline{u}^k(\underline{x}_0)$ calculated on the "old" grid is scaled up by factor 6. The "new" flow on the "new" grid can be calculated according to Eq. (9).

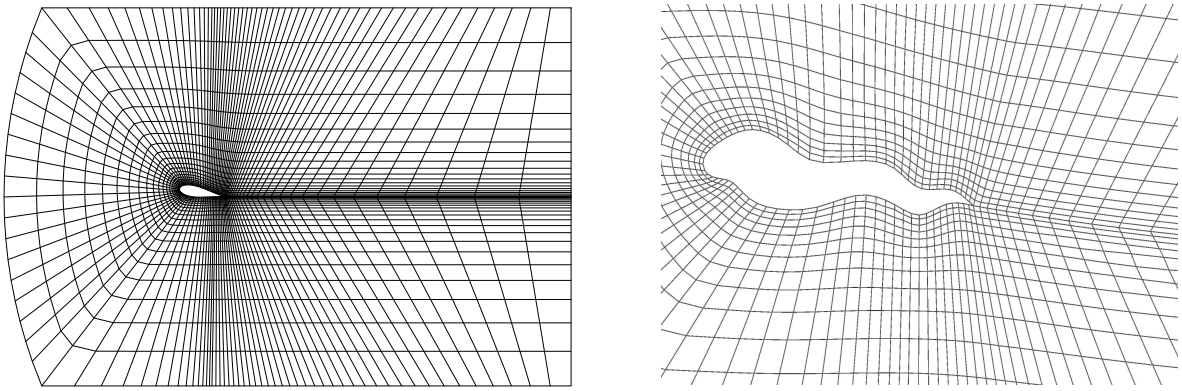

Figure 6: The interior grid is adapted to the variation of the surface geometry using an explicit grid deformation approach based on Green functions, see Laporte and Tallec (2003), to obtain $\frac{\partial x_i}{\partial \alpha_j}$.

4 Conclusions

Exemplarily, the discrete adjoint approach has been introduced for a potential flow solver. As the adjoint code has been developed closely to the primal solver, only moderate coding effort was necessary. The gradients obtained by the adjoint algorithm show good agreement with gradients calculated by finite differences for small shape perturbations.

Subsequently, the momentum equations and the pressure correction equation, used in a SIMPLE-based Navier-Stokes solver, have been linearised with respect to the shape modifications. Elementary solutions to the linearised flow equations have been presented. In the next step, the adjoint equation system corresponding to the linearised NSE has to be solved. Due to the segregated approach, adapting the SIMPLE algorithm to the adjoint problem is more challenging than adjoining the basic potential flow code.

References

M. B. Giles and N. A. Pierce. An introduction to the adjoint approach to design. *Flow, Turbulence and Combustion*, 65:393–415, 2001.

E. Laporte and P. L. Tallec. *Numerical Methods in Sensitivity Analysis and Shape Optimisationa*. Birkhäuser, 2003.

S. K. Nadarajah. *The Discrete Adjoint Approach to Aerodynamic Shape Optimization*. PhD thesis, Stanford University, Jan. 2003.

M. Peric. Computer aided flow analysis (CAFFA ver. 1.2). Institut für Schiffbau der Universität Hamburg, Oct. 1996. URL `ftp://ftp.springer.de/pub/technik/peric`.

H. Söding. Hull shape design for reduced resistance. *Ship Research Technology*, 48:135–144, 2001.

H. Söding. *Beschreibung des Programms Press zur Variation von Schiffsformen*, February 2002.

H. Söding. Numerische Berechnung inkompressibler Potenzialströmungen, 1999.

B. N. Veelo. Shape modification of ship hulls in H-Rep. *Ship Research Technology*, 51(4): 162–184, Oct. 2004.

Validation Study of a Particle Method for Violent Free Surface Flow

Makoto SUEYOSHI
sueyoshi@riam.kyushu-u.ac.jp
RIAM, Kyushu University, Japan

Introduction

In the field of marine engineering, numerical simulation of violent free surface problems is one of the most interesting technical challenges. There are many kinds of numerical scheme to simulate free surface problems. In particular, for violent free surface problems, particle methods are considered as a hopeful technique. MPS(Moving particle Semi-implicit) method is one of them. It was introduced by Koshizuka in the field of nuclear engineering. It is well known that they are suitable for numerical simulations of free surface motions. On the other hand, in order to apply particle methods to simulation for engineering problems, we need to know not only surface shape and flow field but also forces acting on structures. In this paper, a numerical code that is based on the MPS method is validated through comparison of impulsive pressure of sloshing and motions of floating body problems.

Numerical Scheme

The MPS method is a fully Lagrangian scheme to solve equations of fluid motion. The basic equation is

$$\frac{D\mathbf{u}}{Dt} = -\frac{1}{\rho}\nabla P + \mathbf{g} + \nu\nabla^2\mathbf{u} \,. \tag{1}$$

These equations are solved by a fractional step method that is shown in Fig.1. It is similar to ordinary grid type schemes except for the equation for pressure computing. It uses particle number density, n in the source term of the pressure Poisson equation, which is described by

$$\nabla^2 P_i^{n+1} = -\frac{\rho}{\Delta t^2}\frac{(n_i^* - n_{\mathrm{const}})}{n_{\mathrm{const}}} \,. \tag{2}$$

This is the first feature of the MPS method. The gradient of the calculated pressure field works as a kind of repulsive forces between particles where n is higher than the initial value, n_{const}. This procedure gives us a suitable particle arrangement for spatial discretization and natural treatment to incompressible fluid.
The second feature of the MPS method is the formulation of spatial discretization models. They are called as particle interaction models. For example, the gradient of scalar quantity Φ is described by

$$\nabla\Phi_i = \frac{d}{\sum_{j\neq i}^{N} w(|\mathbf{r}_j - \mathbf{r}_i|)} \sum_{j\neq i}^{N} w(|\mathbf{r}_j - \mathbf{r}_i|)\frac{\Phi_j - \Phi_i}{|\mathbf{r}_j - \mathbf{r}_i|}\frac{\mathbf{r}_j - \mathbf{r}_i}{|\mathbf{r}_j - \mathbf{r}_i|} \tag{3}$$

where $\mathbf{r}_i$ is position vector of particle i, d is number of dimension and w is function of distance between particle i and j. This is an average of inclination vector of Φ among particles with weight of distance. The second order difference model, diffusion of Φ is described by

$$\nabla^2\Phi_i = \frac{2d}{\lambda}\sum_{j\neq i}^{N} w(|\mathbf{r}_j - \mathbf{r}_i|)(\Phi_j - \Phi_i) \tag{4}$$

where λ is a parameter to adjust discrete model to analytical solution. All of differential operators in equation (1) is described by using equation (3), (4) and combination of them.

Results and Discussions

(i) Sloshing

2D sloshing simulation in a rectangular tank is carried out and compared with experimental results. Fig. 2 shows the schematic of the problem. The rectangular tank is forcedly oscillated in horizontal direction.

Comparison of free surface profiles is shown in Fig.3. Comparison of time histories of the pressure acting on the sidewall of the tank at point P1 is shown in Fig.4. In these cases, numerical scheme is modified from original MPS method to reduce numerical oscillation of the pressure. The details of the numerical method are shown by author and Naito. Profiles of the pressure time history give reasonable agreement. Comparison of snapshots of the free surface profile is shown in Fig.4. Numerical results show the feature of surface motions in each period with qualitative agreement with experimental results.

(ii) Floating Body Problem

Numerical simulation of motions of a 2D body in waves is carried out. Fig. 5 shows the setup for experiment. There is a plunger type wave maker at the end of the tank. The floating body is moored by the carriage and heaving rod system. In this case, the horizontal motion is weakly moored by soft spring. The heaving and rolling motions are almost freely movable. In computation of motions of the floating body, equations of motions are solved by explicit finite-difference procedure. The algorithm is shown in Fig. 6. All of components of force from fluid are treated as pressure integration together at each time step. The integration for translational force, **F** is described by

$$\mathbf{F} = \sum_{i}^{\text{on the hull}} \mathbf{p}_i \Delta S_i \tag{5}$$

where $\mathbf{p}_i$ is stress vector and ΔS_i is area of the particle on the hull surface. The integration for rotational moment, **M** is described by

$$\mathbf{M} = \sum_{i}^{\text{on the hull}} (\mathbf{r}_i - \mathbf{r}_g) \times \mathbf{p}_i \Delta S_i \tag{6}$$

where $\mathbf{r}_g$ is position vector of the center of gravity of the hull. They are treated as total external forces from fluid in computation procedure of motions.

The motion of wave maker is given as the velocity of particles on the surface of the plunger type wave maker.

Fig. 7 shows snapshots of surface profiles around the body in experiment and computation. Fig. 8 shows time histories of motions of the floating body when the period of vertical motion of the plunger is 1.0sec and the amplitude is 3.0cm. In this case, each numerical result shows qualitative and quantitative agreements with the experimental result. The result of longer time period case is shown in Fig. 9. In this case, discrepancy of swaying motion is larger than the case of 1.0 sec. period. The calculated amplitude of cyclic motion of swaying is not so different from experimental result. But drift motion is completely different. Therefore, it suggests that there are some problems in accuracy of drift force estimation.

Conclusion

Validation study of numerical simulations by the MPS method is carried out through several cases of 2D problems including large deformation of surfaces. In the most of the cases, reasonable results are shown in both of sloshing and floating body simulations.

Refferences

(1) S. Koshizuka and Y. Oka, “Moving-Particle Semi-Implicit Method for Fragmentation of In-compressible Fluid,” Nuclear Science and Eng- eneering, 123 (1996), pp421-434.

(2) Makoto Sueyoshi, Shigeru Naito, “An Improvement on Pressure Calculation Scheme of MPS Method”, J. Kansai Soc. N. A., Japan, 242 (2004), pp53-60.

(3) Makoto Sueyoshi, “Numerical simulation of extreme motions of a floating body by MPS method,” TECHNO-OCEAN'04 CD-Rom Proceedings (2004), pp566-572.

(4) Hu, C, Kishev, Z. "Numerical Simulation of Violent Sloshing by CIP-CSL3 Method," Proc. Symp. RIAM on Hydro dynamic Analyses of Moving Boundaries and Ambient Fluid, No.15 ME-S7(2004), pp 39-43.

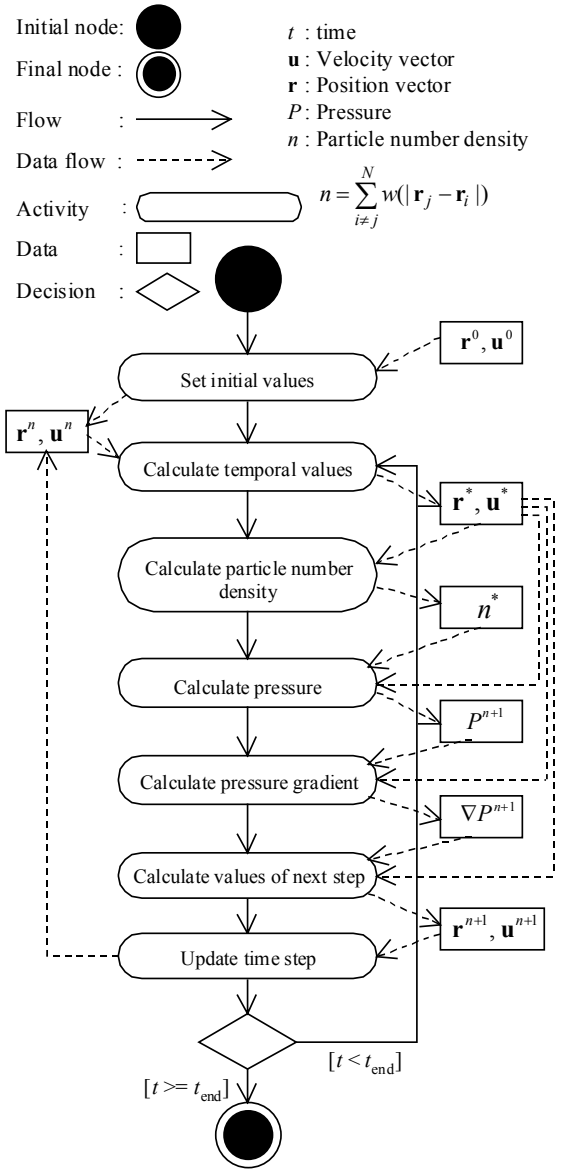

Fig. 1 UML activity diagram of MPS method

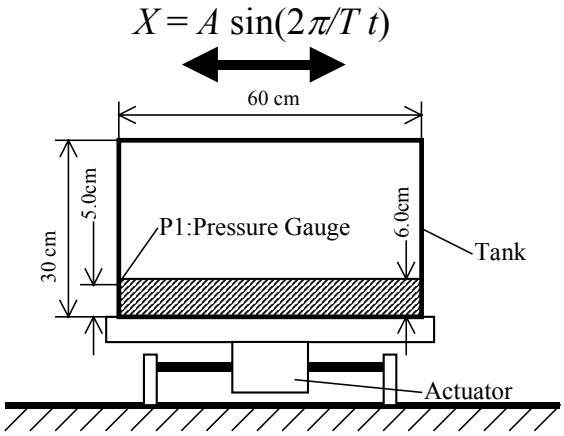

Fig.2 Schematic of set up for sloshing experiment and computation.

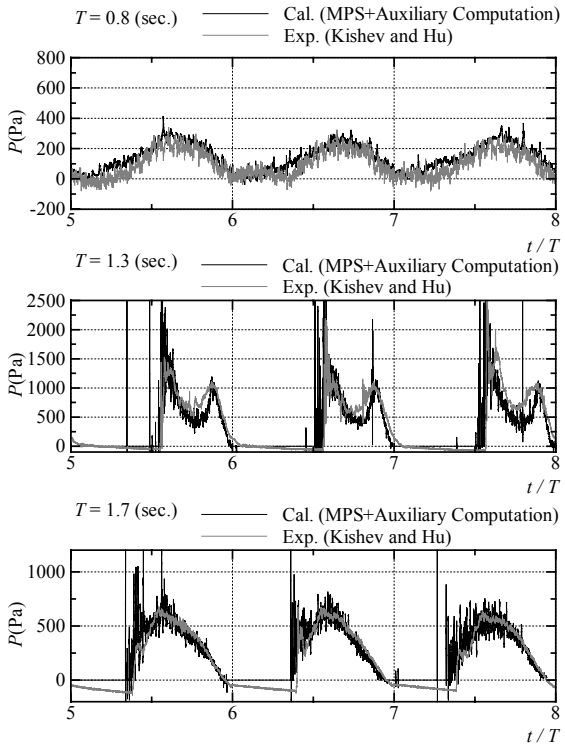

Fig. 3 Time histories of pressure acting on the side wall of the tank. In the numerical cases, initial minimum length between particles l_0 = 2.5(mm), total number of particles N=6,456.

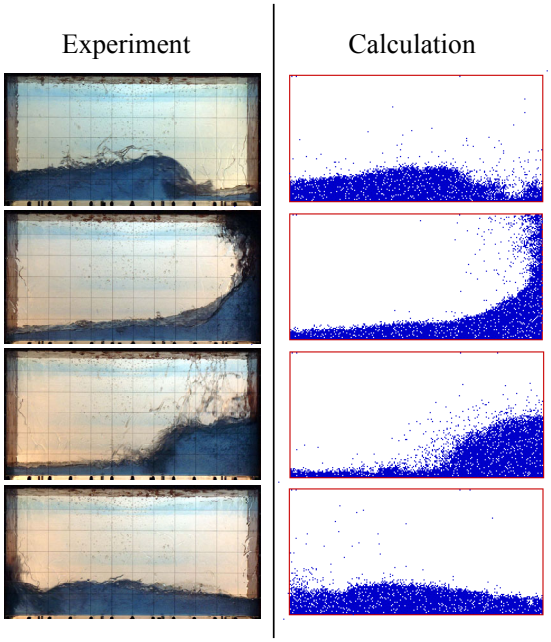

Fig.4 Free surface profiles at period of forced oscillation T=1.3(sec.), amplitude A=6.0(cm). l_0 = 2.5(mm), N=6,456.

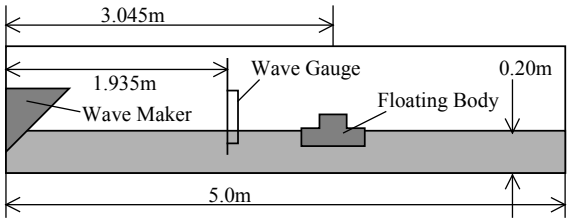

Fig.5 Setup for floating body problem

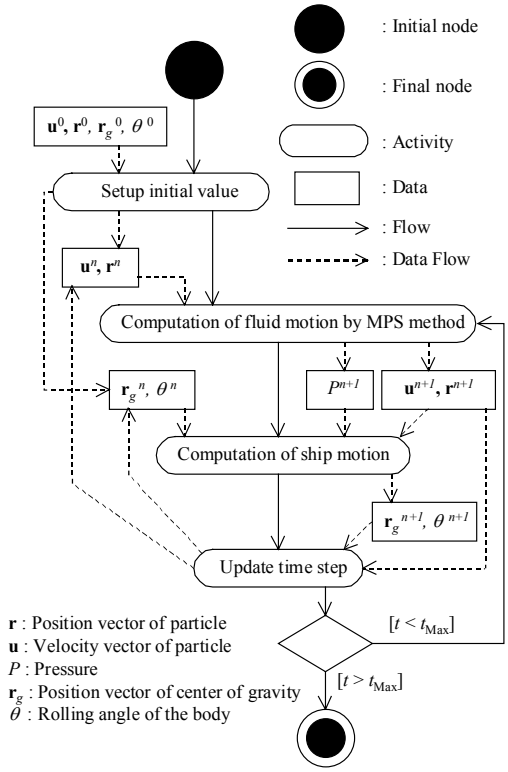

Fig.6 Diagram of simulation of the body motions

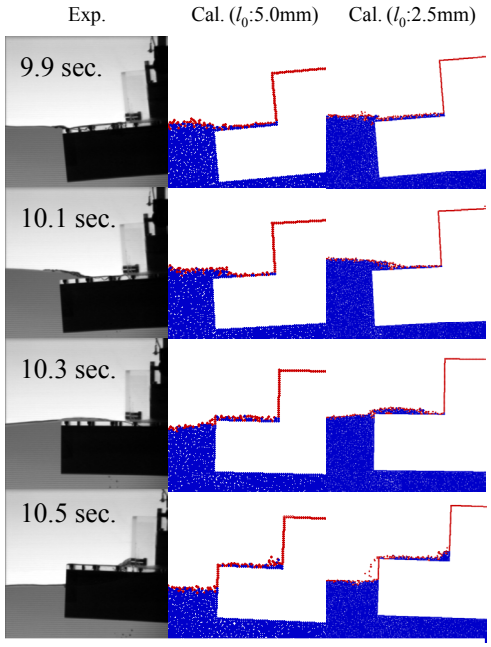

Fig. 7 Comparison of free surface profiles

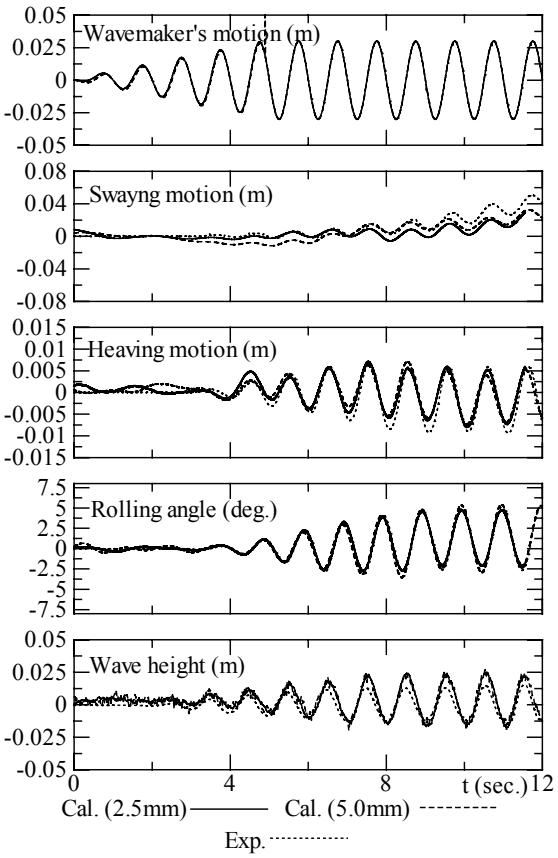

Fig.8 Time histories of motions, T=1.0(sec.)

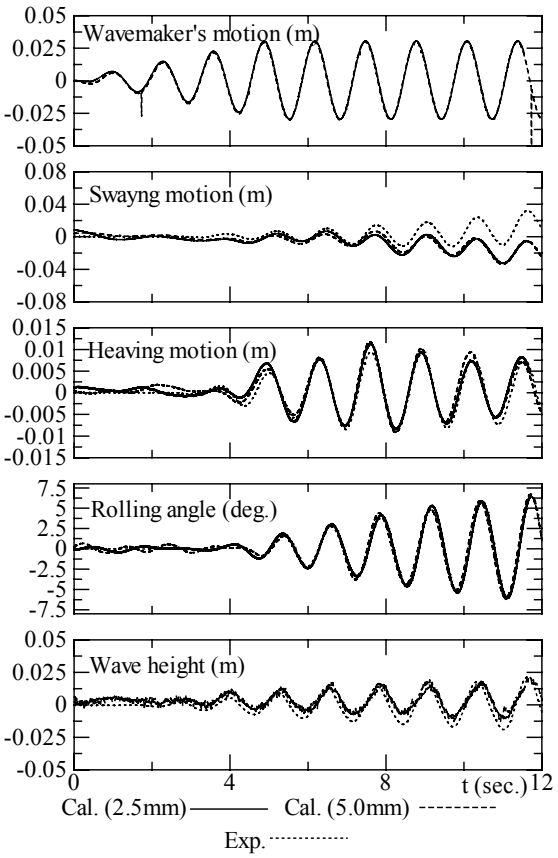

Fig.9 Time histories of motions, T=1.3(sec.)

Evaluation of slamming loads on V-shape ship sections with different numerical methods

M. Viviani – tel. +39 010 3532547 – fax +39 010 3532127 – mail viviani@dinav.unige.it
L. Savio – tel. +39 010 3532386 – fax +39 010 3532127 – mail luce.lux@tiscali.it
S. Brizzolara – tel. +39 010 3532386 – fax +39 010 3532127 – mail brizzolara@dinav.unige.it

Università degli Studi di Genova – Dipartimento di Ingegneria Navale e Tecnologie Marine (DINAV), Via Montallegro 1, 16145 Genova, Italy

INTRODUCTION

This work deals with the application of different numerical methods for the evaluation of slamming loads on V-shape sections, namely a commercial CFD VOF program and Smoothed Particles Hydrodynamics Method (SPH) currently under development at DINAV; preliminary results from both methods are presented, together with a comparison between the two methodologies, stressing their relative merits and shortcomings.

The problem of slamming impact on ship has been investigated for a long time (see for instance Wagner 1932 , Chuang 1967, Stavoy and Chuang 1976, Zhao and Faltinsen 1993), both theoretically and experimentally.

Nevertheless, this problem is still under investigation, due to the intrinsic difficulties which arise from the high non-linearities involved and to the complex interactions between free-surface, hull sections and air; difficulties can be further increased in correspondence of some typical hull shape characteristics, such as hard-chines, spray-rails and so on.

One of the most important problems related to slamming impact is linked to the strong variations of free surface, with development of sprays and consequent high non-linearity, which make free surface treatment more difficult with conventional methods, in which a certain mesh is adopted (both potential and ranse methods).

Meshless methods, like SPH, with their Lagrangian approach allow to overcome this problem, with a much faster generation of the input data for the problem and their intrinsic ability to treat free surfaces.

The problem analysed in this paper is the "traditional" 2D flow resulting from the impact between a triangular wedge and water surface at a certain constant speed. For the study presented in this paper a flare angle of 25° (with respect to the horizontal) has been selected and a speed of 2 m/s has been chosen. These values to reproduce rigid wedge impact tests chosen within MARSTRUCT thematic network as a benchmark case for different theoretical methods.

In order to compare numerical results to other previous results, the following has been taken from literature:

1. Wagner and Chuang give same results for maximum impact pressure and for impact pressure at keel; considering values involved in the present analysis, these result in:

   p_{max} = 27500 Pa p_{keel} = 14500 Pa

   Moreover the value of nondimensional vertical force $f_v = F_3/\rho V^3 t$, as computed using Wagner assumptions, is equal to (Faltinsen 2005) f_v = 35.65
2. More recently, Zhao and Faltinsen (1993) presented different results based on the similarity solution by Dobrovol'skaya (1969), leading to the typical distribution of pressure presented in figure 1.

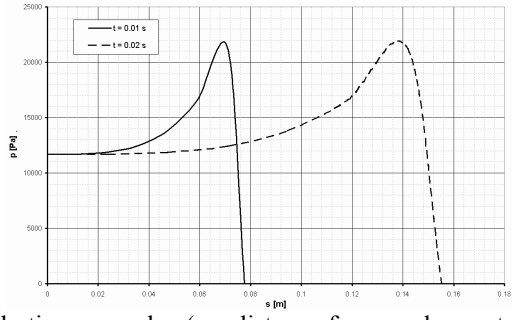

Figure 1: Pressure distribution on wedge (s = distance from wedge vertex, t = time from impact)

These distributions are characterised by lower values of a peak pressure and a width of the peak which increases with time. The overall result is a lower value of the generated vertical impact force on the wedge, in numbers:

p_{max} = 22000 Pa $\qquad$ f_v = 23.657

1 SPH METHOD

1.1 *Brief description of methods adopted*

Smoothed Particle Hydrodynamics is a relatively novel Lagrangian meshless CFD method.

The method, initially developed for compressible fluids (Lucy, 1977; Gingold and Monaghan, 1977), must be adapted and 'corrected' for hydrodynamic problems (Monaghan et al, 1994, Liu and Liu, 2003).

The continuum is discretised in a number of particles, each one representing a certain finite volume of fluid, which are followed (in a Lagrangian way) during their motions induced by internal forces between nearby interacting particles and external mass forces or boundary forces.

Internal forces derive from the usual Navier-Stokes and continuity equations made discrete in space by means of a kernel formulation.

Moreover, an equation of state (reported hereunder) which relate density to pressure for each particle is adopted, thus considering the fluid flow as compressible:

$$p = \frac{c_0^2 \rho_0}{\gamma}\left[\left(\frac{\rho}{\rho_0}\right)^{\gamma} - 1\right]$$

The value of sound speed c_0 cannot in general be set to its effective value for practical reasons (time steps become too small), thus it is usually set in order to limit the Mach number to a value below 0.1 (Monaghan 1994) and consequently density variations in the incompressible flow to acceptable values (usually less than 1%).

Space integrals of a hydrodynamic variable over the fluid domain are discretised by means of a 'kernel estimate' of the field variable (Libersky et al, 1993, Liu and Liu 2003). By means of the kernel function it is possible to weigh the contribution of neighbour fluid particles on every single particle, thus solving the problem; in general, if A is a field variable and W is the kernel function, following equations (already in their discretised form) are adopted:

$$\langle A(r)\rangle = \sum_{j=1}^{N} \frac{m_j}{\rho(r_j)} \cdot A(r_j) \cdot W(r - r_j, h)$$

The term *h* represents the smoothing length, which determines the extent to which a certain particle has influence on the others. Different kernel functions may be utilized (Liu and Liu 2003); in particular, in the present work, Gaussian kernel and Spline kernel have been adopted in calculations reported in 1.2 and 1.3 respectively; it is believed, anyway, that this difference does not affect the results.

The resulting formulas, in the particles approximation, for the continuity equation and the momentum equation are :

$$\partial\rho_i/\partial t = \Sigma_j\, m_j(v_i - v_j) \bullet \nabla W(r - r_j, h) \qquad \partial v_i/\partial t = -\Sigma_j\, m_j(p_i/\rho_i^2 + p_j/\rho_j^2)\nabla W(r - r_j, h) + g$$

Moreover, since SPH can be affected by a lack of stability, during past years various authors have developed different methods which can help in reducing it:

1. Artificial Viscosity: This term is added to the momentum equation (Monaghan 1992) and its effect help to convert sharp variations in the flow kinetic energy into thermal energy and to limit particle interpenetration at high Mach Number. This term is to be added in the momentum equation.
2. XSPH (Monaghan 1992), in which each particle moves in the following way:

$$\frac{dx_i}{dt} = v_i - \varepsilon \sum_j \frac{m_j}{\rho_j} v_{ij} W_{ij}$$

   Application of XSPH results in making particles move with a velocity closer to the one of neighbouring ones
3. Density renormalization (as presented in Colagrossi & Landrini 2003)
4. RKPM (reproducing kernel particle method), as presented in Liu and Liu 2003

In the present work both artificial viscosity and XSPH have been adopted to some extent, while density renormalization has not been used; RKPM has been tested widely. Finally it was decided to avoid this method because it leads to unphysical values of some field variables (here density was overestimated), although it restores mathematical consistency.

For what regards boundary treatment, two different approaches have been considered:

1. Virtual particles on the boundary have a predetermined law motion and are not used for various integrations; their effect results only in a repulsive force (Monaghan 1994) dependent to inverse of the distance between fluid and boundary particles according to the formulation of Lennard-Jones for molecular force, as follows:where $p_1=12$ and $p_2=6$ and r_0 is the cutting off distance, approximately

$$f(r)=\begin{cases} D\frac{r}{r^2}\left(\left(\frac{r_0}{r}\right)^{p_1}-\left(\frac{r_0}{r}\right)^{p_2}\right), & when\ \ r<r_0 \\ 0, & elsewhere \end{cases}$$

   equal to the smoothing length
   This formulation has been further modified in order to let the force act in the direction normal to the surface and to avoid discontinuity of forces along the wedge itself
2. Use of ghost particles which are generated in correspondence to real particles which are near to the boundary according to the following scheme:
   - particles are mirror images of real ones with respect to the boundary surface
   - particles have equal values of all state variables, except for velocity, which is opposite to the one of the real particle.
   - in order to avoid particles from penetrating the boundary, especially when a shock occurs as in this case, a geometrical treatment of the velocity of the particles is performed. This technique is used only when a particle moves too close to the solid boundary.

   Moreover, this second calculation includes also a kernel normalization technique. This is adopted in order to overcome the so called particle inconsistency, which arises from a free surface or a disordered set of particles. This point is important in order to keep the computation more stable

Finally, in order to evaluate pressure an approach similar to the one presented in (Oger et al. 2005) is adopted, somehow simplified since pressure is evaluated as a mean of pressures of real particles in proximity of the boundary particle (namely in a rectangular region with width parallel to boundary surface and height perpendicular to boundary surface which are multiples of the smoothing length).

1.2 *Results – First method: boundary condition with repulsive force*

SPH computations adopting repulsive force only as boundary condition have been performed: in particular, a half wedge (for symmetry reasons) with a length of 0.3 m and a "pool" of 0.6 x 0.6 m composed by about 120000 particles (diameter 1.75 mm) have been studied, with a time step for integration equal to 5×10^{-6} seconds.
In following figures 2 and 3, main results are presented in terms of the time history of the total normal force to half wedge and the pressure distribution along the wedge, after 0.02s from the first impact. The results obtained by SPH method are compared to the analytical results presented by Zhao/Faltinsen (1993) and with original method of Wagner (1932). Figures 4 and 5 represent particle distribution at the same time.

As it can be seen, qualitatively the described method allows to predict pressure distribution and time history of total force; in particular, values of total force lie between those computed using coefficient form Wagner and from Zhao/Faltinsen and still have significant oscillations (it has to be noted that in this case XSPH is set to a very low value, while artificial viscosity coefficients are set to 0.3 to obtain realistically ordered particle trajectories. From the kinematics point of view, the method seem to capture the most important phenomena, as it can be seen from figures 4 and 5.

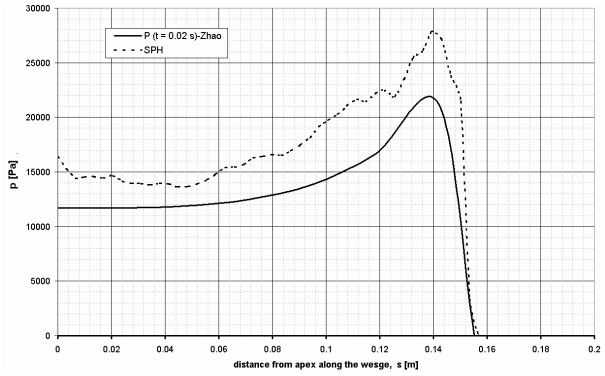

Figure 2: Pressure distribution on a 25 degree rigid wedge at t = 0.02 s

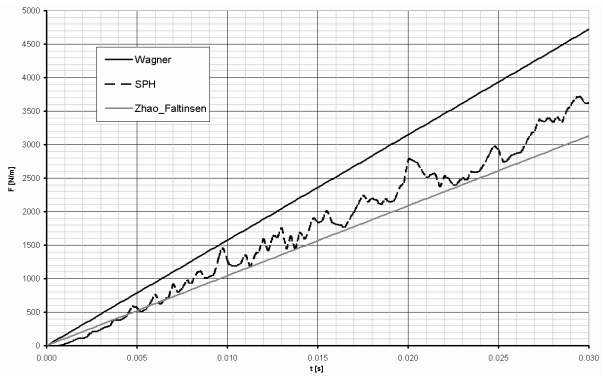

Figure 3: Time history of Normal Force on half-wedge, comparison of SPH with theoretical methods

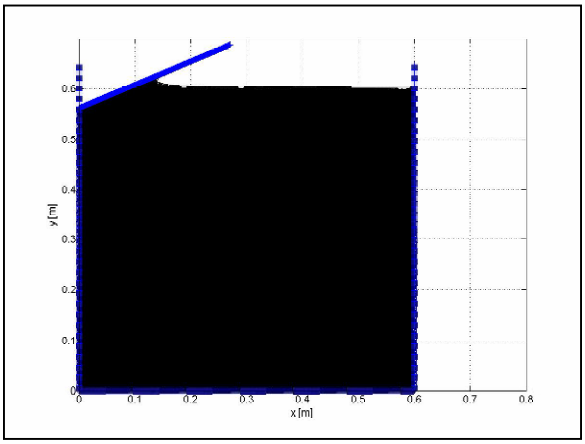

Figure 4: Wedge entry – complete range (t=0.02 s)

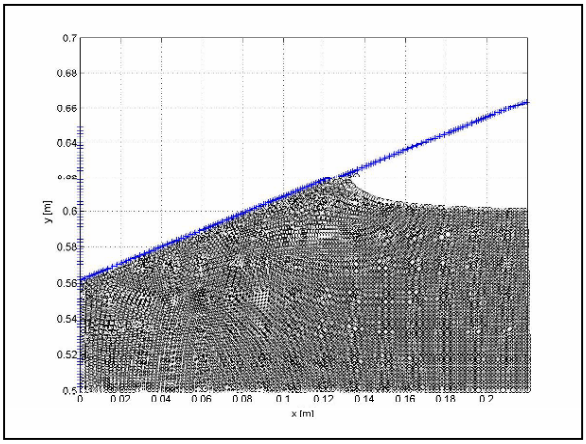

Figure 5: Zoom on free surface at impact (t=0.02 s)

1.3 *Results – Alternative method: boundary condition with ghost particles*

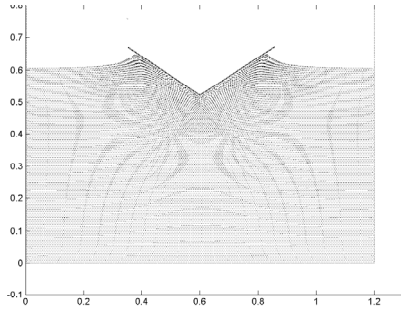

SPH computations adopting ghost particles for simulation of boundary condition have been performed: in particular, a complete wedge with a length of 0.6 m and a "pool" of 1.2 x 0.6 m composed by about 23000 particles (diameter 6 mm) have been studied, with a time step for integration equal to 1 x 10^{-5} seconds.
In following figures 6 and 7, pressure distribution on wedge and the total vertical force acting on the wedge vs time are presented and compared to analytical results from Zhao/Faltinsen and with previous results by Wagner.

As it can be seen, also with this second procedure it is possible to predict pressure distribution and time history of total force; in particular, despite the lower number of particles computed forces are similar to those obtained by Zhao and Faltinsen (at least for 0.025 sec); for a high step number, method tends to diverge, probably due to pressure waves reflected by the tank's walls travelling in the fluid domain. Concerning this last point it can be easily seen that, with the sound speed of 70 m/s, after 0.025 second a sound wave is able to come back to the wedge after being reflected by the tank's walls. For the reason mentioned above it is recommended to pay great attention to the extent of the computational domain. The pressure distribution is not symmetric as one should expect, but peak value is correct and similar on both side. The lack in symmetry is mostly due to the low number of particles, but this problem will be further investigated.

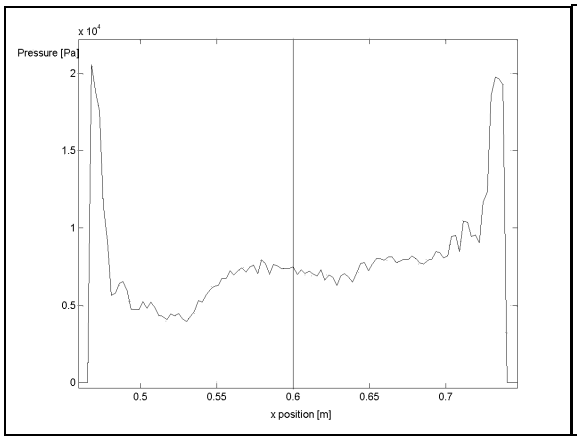

Figure 6: Pressure distribution on wedge (t = 0.02 s)

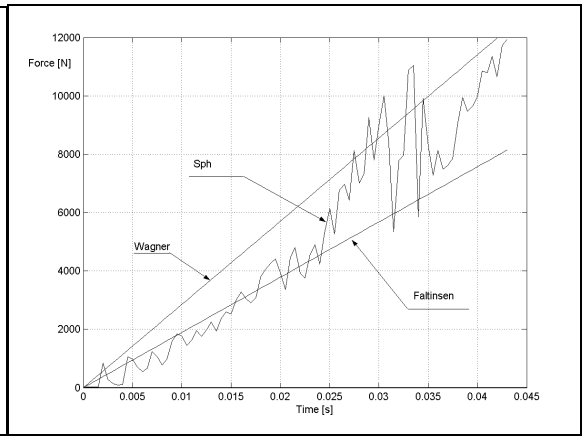

Figure 7: Time history of Normal Force on the wedge

2 RANSE SOLVER

2.1 *Brief description of method adopted and set-up of the model*

The RANSE solver used to perform this study is the commercial code Flow-3D®, developed by Flow Science, Inc.. The algorithm solves the fully 3-D transient Navier-Stokes equations by a finite-volume-finite-differences method in a fixed Eulerian rectangular grid. A distinctive feature of the procedure is the Fractional-Area-Volume-Obstacle-Representation (FAVOR) technique (Hirt and Sicilian, 1985). Such techniques allows for the definition of solid boundaries within the Eulerian grid. FAVOR$_{TM}$ determines fractions of areas and volumes (open to flow) in partially blocked volumes, for the computation of flows correspondent to those boundaries. In this way, the process of defining boundaries and obstacles is done independently of grid generation, avoiding saw-tooth representation or the use of body fitted grids. In fact, the geometry can be either defined using a built-in 'solid modeler', which includes quadratic functions representing objects, or it can be externally provided through STL formats. Once the geometry has been defined, the computational mesh is constructed independently, with the possibility of densification in zones of the domain of particular interest.

The grid (a typical transverse section is represented in figure 3) has been refined along the transversal and vertical directions close to the wedge bottom in order to accurately capture the development of inner and outer domain of the flow, i.e. the local rising up of the free surface and the jet-flow. Only half symmetric wedge with a length of 0.3m has been described, as pictured in figure 8. The mesh extends transversally from the symmetry to a plane at 1.5m aside, and vertically the bottom of the tank is placed 1.1m below the wedge apex. A final structured Cartesian grid of about 350,000 cells, refined in the proximity of the wedge, has been used.

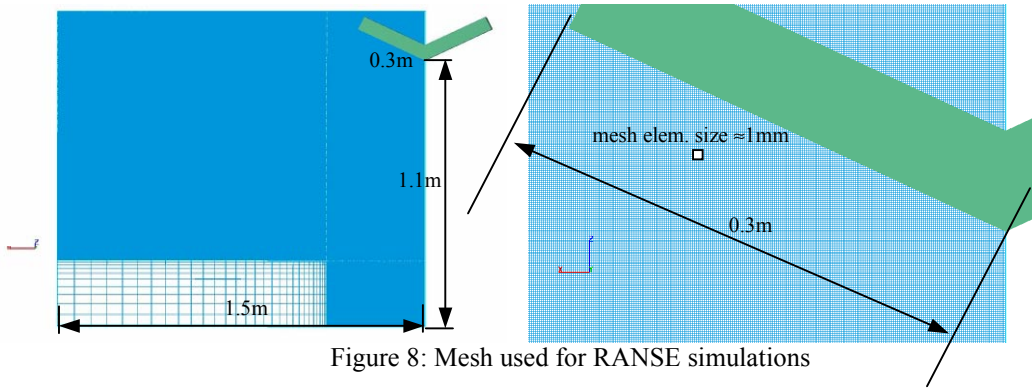

Figure 8: Mesh used for RANSE simulations

The following conditions at the boundaries of the parallelepipedal mesh have been assigned:

- the wedge has been set as a moving object with a constant vertical velocity of 2m/s;
- the wedge bottom has been defined as a sippling wall condition;
- the bottom, the symmetry plane and the right side of the fluid domain has been all assigned a symmetry boundary condition

All the calculations were performed in a non-stationary mode, up to a time of about 0.6 sec, corresponding to the wedge chine deeply submerged under the undisturbed free surface. The method has been used with a variable time step, automatically refined by the code to obtain a good convergence of the residuals and satisfy a set of stability criteria

2.2 *Results obtained with RANSE solver*

Impacts of rigid wedges having a wide range of flair angles have been simulated and the same vertical constant impact speed of 2.0m/s. In general a good agreement with the maximum pressure values predicted with the generalised Wagner theory developed by Zhao and Faltinsen (1993) or the similitude theory of Dobrolov'skaya has been found, but a more accurate analysis of the wide results database has still to be completed. For this study only the 25 degree has been used as a reference for the SPH validation.

The kinematic of the flow is very well captured by the VOF RANSE solver, as illustrated at different time steps in figure 9. The jet flow is growing as expected up to about t= 0.04s when the spray root is just near the wedge chine. The spatial pressure distribution is in agreement with the previously mentioned theories, showing a peak at the spray root and rapidly decreasing pressure away from the peak (towards the wedge apex) attaining on a nearly uniform pressure value of about 11 kPa. The last time frame t=0.05s shows a completely different pressure distribution with maximum pressure level dropped to about 5 kPa. This is due to the different flow set-up: the jet flow disappeared

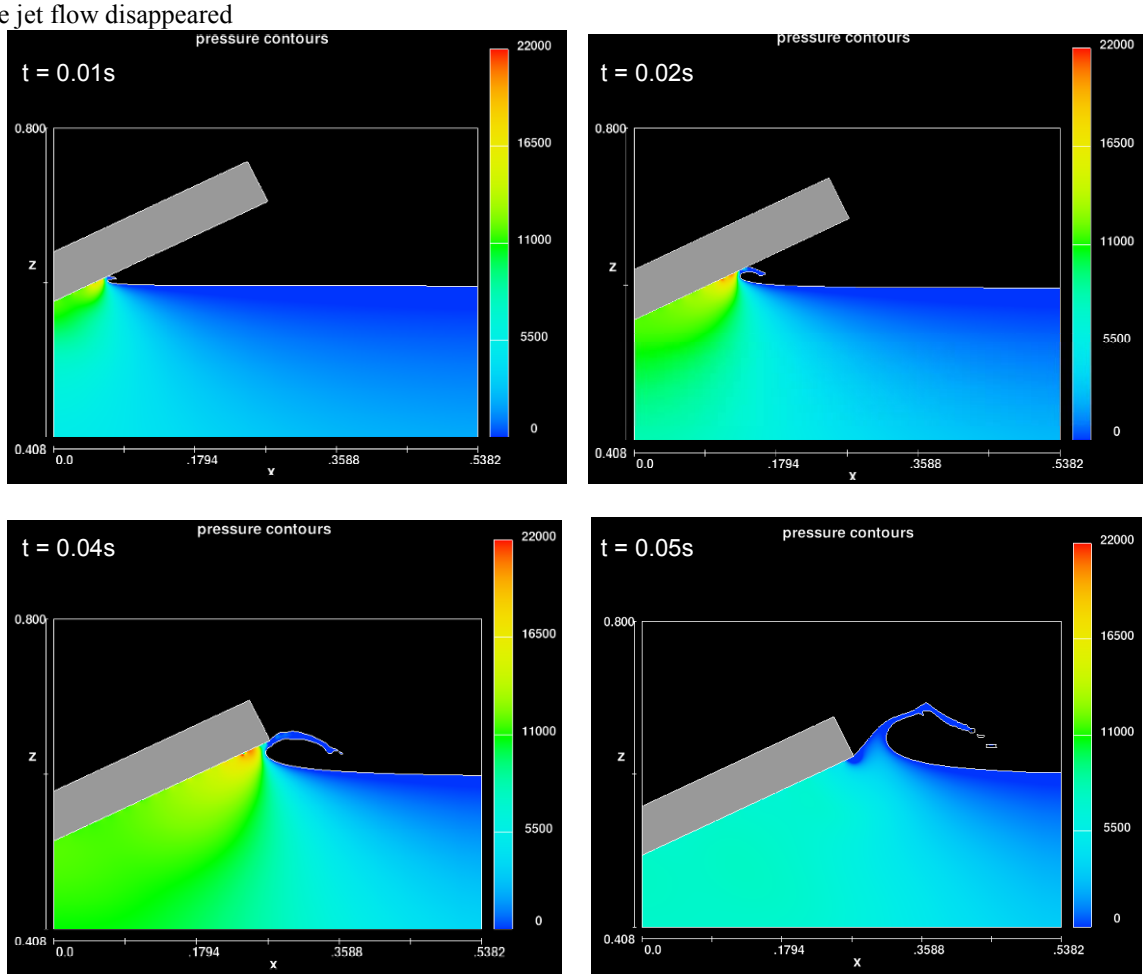

Figure 9: RANSE results: Pressure contours (measured in N) under the wedge at different time steps.

The pressure time histories on different points along the wedge are presented in figure 10. As evident the pressure history has large fluctuations. It is believed that this problem is due to the interpolation method followed to create these time histories: the point on which the pressure is interpolated from the finite size cells of the mesh is infinitesimally small, while the pressure should be averaged, each time step on a certain sensor length along the wedge. In fact, if the integration time step of the RANSE solver is increased just below the stability limit, the point pressure time histories show less fluctuations. Anyhow, it is true that time histories of point pressure are less relevant for sake of comparison with experimental results and for the structural strength analysis. Use of averaged pressure over wedge length space (sensor length or distance between bottom plate stiffen-

ers) and/or in time (impulse of the force) should be used. It is not easy, though, to obtain these results from a commercial RANSE code.

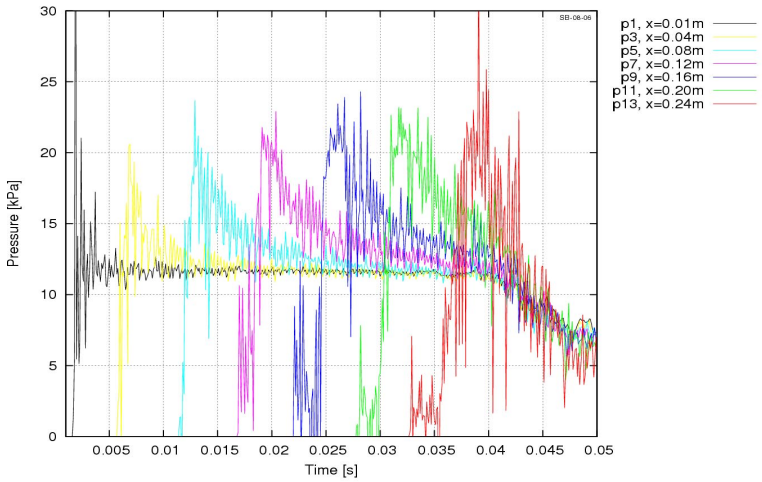

Figure 10: Pressure time history, RANSE with refined time step. V=2 m/s, wedge half breadth: b=0.2719m

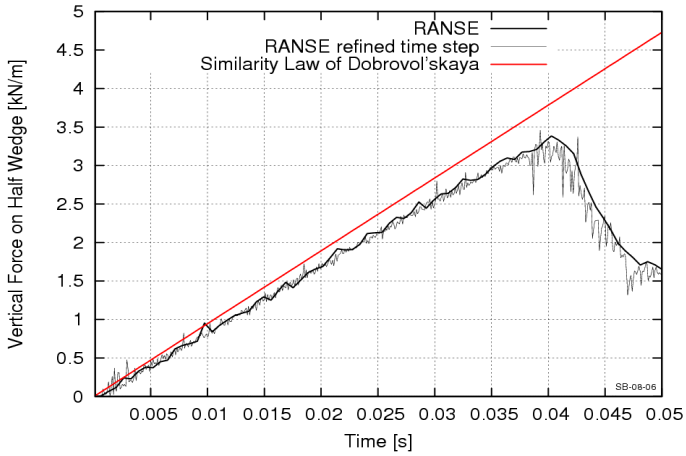

Figure 11: Time history of Vertical Force predicted by RANSE solver on a 2D half-wedge

Results are better in terms of integral parameter, i.e. hydrodynamic force on the wedge. The time history of the vertical force is represented in figure 11.

The level of force is in line with the Dobrovol'skaya method as presented by Zhao & Faltinsen (1993) and well capture also sudden drop of the force when the spray root has passed the wedge chine. From this time on (see figure 10), the pressure distribution along the wedge is completely different not showing the peaked shape and being more uniform along the width, finally resulting into a lower total force.

3 CONCLUSIONS

As presented in the above pages, two different methods (Lagrangian SPH and Eulerian VOF RANSE) have been adopted in order to analyse the problem of slamming of a 2D wedge surface.

In general, both methods seem to be capable of capturing the physics of this phenomena, even if more efforts are required to correctly tune SPH calculations ("smoothing coefficients", number of particles adopted, time step, speed of sound, etc.). The SPH calculations made until now seem to overestimate the pressure distribution on the wedge and consequently the total vertical force on the wedge. RANSE method used, on the contrary, shows a very good correlation of the peak pressure values and the total vertical force on the wedge, although obtained point pressure time histories shows very high fluctuations in time.

SPH methods present significant advantages, which make them very interesting for future developments:

- Free surface capturing is inherent in the nature of this method; hence, no special effort is required (contrary to RANSE methods). There is also a good capturing of sprays and cavities and, in general, of complex kinematics.
- Velocity field and free surface disturbances can be rather accurately predicted.

- From the computational point of view, algorithms to be implemented are much simpler than those adopted in RANSE methods

Most important problems related to SPH which need further study are the following:

- Prediction of internal pressures in the fluid has some evident shortcomings, which in general derives from the 'idealised' equation of state; moreover, the fluid/boundaries interaction evaluation is rather difficult; accurate tuning of all parameters involved in SPH calculations is needed to overcome both problems.
- Turbulence phenomena are difficult to simulate, and certainly will need further efforts in future.
- The computational time is still rather long. The main way to overcome this seems to be a parallel version of the code, whose implementation seems to be rather straightforward for this method.

It will be interesting to check if, once a correct tuning of SPH is reached for this particular problem of the rigid wedge impact, the SPH method can be extended to other similar impact problems (with different 2D sections and/or 3D cases) to obtain similarly good correlation as in this case with RANSE methods.

Regarding boundary conditions to be used in SPH method, there is not a final conclusion; it seems that repulsive force method is more straightforward, while ghost particles method can be more problematic, especially when moving to more complex shapes (e.g. with hard-chines or similar); nevertheless, it has proved to be feasible with the presence of a vertex, and it seems to be almost unavoidable in case of necessity to compute tangential forces and viscosity, which currently has been neglected in SPH calculations.

REFERENCES

Chuang, S.L., 1967, "Experiments on Slamming of Wedge-Shaped Bodies", Journal of Ship Research, 190-198

Colagrossi, A. and Landrini, M., 2003, "Numerical simulation of interfacial flows by smoothed particle hydrodynamics", Journal of Computational Physics 191, 448-475

Faltinsen, O.M., 2005, "Hydrodynamics of High Speed Marine Vehicles", Cambridge University Press

Gingold, R.A. and
Monaghan, J.J., 1977, "Smoothed particle hydrodynamics: theory and application to non-spherical stars", Royal Astronautical Society, 181, 375-389.

Libersky, L.D., Petschek, A.G., Carney, T.C., Hipp, J.R. and Allahdadi, F.A., 1993, "High strain Lagrangian hydrodynamics: a 3D SPH code for dynamic material response", J. Computational Physics, 109, 67-75.

Liu, G.R., Liu M.B., 2003, "Smoothed Particle Hydrodynamics – A Meshfree Particle Method", World Scientific Publishing Co. Pte. Ltd.

Lucy, L.B., 1977, "A numerical approach to the testing of the fission hypothesis [close binary star formation]", Astronomical Journal, 82, 1013-1024.

Monaghan, J.J., 1992 "Smoothed Particle Hydrodynamics" Annual Rev. Astron. Astrophysics 30, 543-574

Monaghan, J.J, Thompson, M.C. and Hourigan, K., 1994, "Simulation of Free-Surface Flows with SPH", ASME Advances in Comp. Methods in Fluid Dynamics, 196, 375-380.

Monaghan, J.J. , 1994, "Simulating free surface flows with SPH, Journal of computational Physics, 110, 399-406

Oger, G., Doring, M., Alessandrini, B., Ferrant, P., 2006, "Two-dimensional SPH simulations of wedge water entries", Journal of Computational Physics 213 (2006) 803-822

Stavoy, A.B. and Chuang, S.L., 1976, "Analytical Determination of Slamming Pressures for High Speed Vehicles in Waves", Journal of Ship Research, 20-4, 190-198

Wagner, V.H., 1932, "Über Stosz und Gleitvorgange an der Oberflache von Flüssigkeiten", Zeitschrift für Angewandte Mathematik und Mechanik, 193-215

Zhao, R. and Faltinsen, O.M., 1993, "Water entry of two-dimensional bodies", Journal of Fluid Mechanics 246, 593-612

Implementation of Cavitation Modeling in FreSCo

Hendrik Vorhölter, hendrik.vorhoelter@tu-harburg.de
Daniel Schmode, d.schmode@tu-harburg.de
Thoma Rung, thomas.rung@tu-harburg.de
Fluid Dynamics and Ship Theory of TU Hamburg-Harburg, D-21073 Hamburg

1 Introduction

Cavitation phenomena are of high interesst for fluid dynamics. Therefore CFD-methods are needed which are able to deal with cavitation. Today many potential-flow codes include cavitation models, which allow a reliable prognosis of steady sheet cavitation. But potential flow methods are not able to capture rotational effects and flow separation. Further more the re-entrace jet aft of a sheet cavitation cannot be predicted. Thus other models are needed which don't base on potential flows. The most promising approach is to use RANS-methods. Cavitation models have been implemented in various RANS-Codes. But the performance has not been validated satisfactorily, although some validation work has been done by [1], [10], [5], [2], [4] and [**?**]. In the following a cavitation model for RANS-methods is described. The model was implemented within the RANSE-solver FreSCo. It is validated with experiments for a cavitating hydrofoil.

2 Mathematical Model

The section briefly outlines the governing equations refering to the conservation of mass, momentum and the evolution of the vapor phase.

2.1 Momentum & Continuity

The computational approach is based on the conservative ALE-form of the Navier-Stokes equations for solenoidal velocity fields, viz.

$$\frac{\partial}{\partial t}\int_V \rho dV + \int_S \rho\left(\mathbf{v}-\mathbf{v}_s\right)\cdot\mathbf{n}dS = 0\ , \qquad (1)$$

$$\frac{\partial}{\partial t}\int_V \rho\mathbf{v}dV + \int_S \rho\mathbf{v}\left(\mathbf{v}-\mathbf{v}_s\right)\cdot\mathbf{n}dS = \int_S \mathbf{T}\cdot\mathbf{n}dS. \qquad (2)$$

$$\text{with} \qquad \mathbf{T} = 2\mu\mathbf{D} - \mathbf{I}\left(\frac{2\mu}{3}\nabla\cdot\mathbf{v}+p\right)$$

$$\text{and} \qquad \mathbf{D} = \frac{1}{2}\left(\ \nabla\mathbf{v}+\mathbf{v}\nabla\right)\ .$$

Here V denotes the observed control volume and S its respective surface, represented by the face normal vector $\mathbf{n}$. The velocity vector and pressure are denoted by $\mathbf{v}$ and p, whereas $\mathbf{v}_s$ indicates the velocity associated with the surface of the moving volume. The porperties of the fluid are described by the density ρ and the dynamic viscosity μ.

2.2 Two-Phase Flow Approach (Volume-of-Fluid, VoF)

In the present study, the fluid is deemed to be a homogeneous mixture. The respective volume fraction (concentration) of each phase i is defined by $C_i = V_i/V$, where V_i is the volume associated to the phase i and V is the sum of all phase volumes, i.e. $V = \sum V_i$. Accordingly, the transport equation for a concentration reads

$$\frac{\partial}{\partial t}\int_V C_i dV + \int_S C_i\left(\mathbf{v}-\mathbf{v}_s\right)\cdot\mathbf{n}dS = \int_V \mathbf{Q}_{\mathbf{C_i}}dV\ . \qquad (3)$$

Here $\mathbf{Q}_{\mathbf{C_i}}$ denotes a source term to be defined in the subsequent section. The density ρ and viscosity μ of the mixture are reconstructed via

$$\rho = \sum_{i=1}^{n}\rho_i C_i \quad , \quad \mu = \sum_{i=1}^{n}\mu_i C_i\ . \qquad (4)$$

2.3 Cavitation Model

The present study employs the cavitation model reported by [1]. The latter is based on a combination of the VoF methodology - which is the preferred approach of hydrodynamic free-surface computations - and a traditional pressure-correction approach to model the influence of cavitation. The fluid is decomposed into a vapor phase and a water phase. Using the VoF methodology to model the cavitation is slightly more complex than a free-surface VoF model, since transient phase changes between vapor and liquid need to be resolved. The latter is addressed by an additional source term in both, the VoF-transport equation and the pressure-correction equation.

The cavitation model computes the amount of vapor in a control volume from the number of nesting vapor bubbles $N_{Bubbles}$ and an average radius of these bubbles R. Defining a volume-specific bubble density $n_0 = N_{Bubbles}/V$, the vapor concentration can be determined by

$$C_v = \frac{V_v}{V} = \frac{N_{Bubbles}\frac{4}{3}\pi R^3}{V_l + V_v} = \frac{n_0 V_l \frac{4}{3}\pi R^3}{V_l + n_0 V_l \frac{4}{3}\pi R^3} = \frac{n_0 \frac{4}{3}\pi R^3}{1 + n_0 \frac{4}{3}\pi R^3} , \quad (5)$$

where V_l (l=liquid) and V_v (v=vapor) denote the liquid and vapor volumes. According to equation (5), the material derivative d/dt of the vapor concentration C_v reads

$$\frac{\mathrm{d}C_v}{\mathrm{d}t} = \frac{(1-C_v)n_0}{1 + n_0 \frac{4}{3}\pi R^3} \frac{\mathrm{d}}{\mathrm{d}t}\left(\frac{4}{3}\pi R^3\right) = 4\pi R^2 \frac{(1-C_v)n_0}{1 + n_0 \frac{4}{3}\pi R^3} \frac{\mathrm{dR}}{\mathrm{d}t} . \quad (6)$$

which can be casted into the respective Eulerian expression

$$\frac{\mathrm{d}C_v}{\mathrm{d}t} = \frac{\partial C_v}{\partial t} + \mathbf{v} \cdot \nabla C_v . \quad (7)$$

Adding $C_v \nabla \cdot \mathbf{v}$ on both sides, we arrive at

$$\frac{\mathrm{d}C_v}{\mathrm{d}t} + C_v \nabla \cdot \mathbf{v} = \frac{\partial C_v}{\partial t} + \nabla \cdot (C_v \mathbf{v}) . \quad (8)$$

The right-hand side of eq. (8) represents the VoF-transport equation (3) in differential form, the left-hand side denotes the source term which can be used for the transition of the phases.
The continuity equation (1) can be rearranged as follows

$$\nabla \cdot \mathbf{v} = -\frac{1}{\rho}\frac{\mathrm{d}\rho}{\mathrm{d}t} . \quad (9)$$

Substituting the density from expression (4) into equation (9) yields

$$\begin{aligned} \nabla \cdot \mathbf{v} &= -\frac{1}{\rho}\frac{\mathrm{d}}{\mathrm{d}t}[C_v\rho_v + (1-C_v)\rho_l] \\ &= -\frac{1}{\rho}\frac{\mathrm{d}}{\mathrm{d}t}[C_v(\rho_v - \rho_l) + \rho_l)] \\ &= -\frac{\rho_v - \rho_l}{\rho}\frac{\mathrm{d}C_v}{\mathrm{d}t} - \frac{C_v}{\rho}\frac{\mathrm{d}(\rho_v - \rho_l)}{\mathrm{d}t} - \frac{1}{\rho}\frac{\mathrm{d}\rho_l}{\mathrm{d}t} . \end{aligned} \quad (10)$$

The latter is further simplified by assuming $\rho_v \simeq$ const. and $\rho_v \ll \rho_l$, viz.

$$\begin{aligned} \nabla \cdot \mathbf{v} &\simeq -\frac{\rho_v - \rho_l}{C_v\rho_v + (1-C_v)\rho_l}\frac{\mathrm{d}C_v}{\mathrm{d}t} \\ &\simeq \frac{1}{1-C_v}\frac{\mathrm{d}C_v}{\mathrm{d}t} . \end{aligned} \quad (11)$$

Combining expressions (11) and (8) yields

$$\begin{aligned} \frac{\partial C_v}{\partial t} + \nabla \cdot (C_v \mathbf{v}) &= \frac{\mathrm{d}C_v}{\mathrm{d}t} + C_v \nabla \cdot \mathbf{v} \\ &\simeq \frac{\mathrm{d}C_v}{\mathrm{d}t} + C_v \frac{1}{1-C_v}\frac{\mathrm{d}C_v}{\mathrm{d}t} \\ &= \frac{1}{1-C_v}\frac{\mathrm{d}C_v}{\mathrm{d}t} . \end{aligned} \quad (12)$$

Substituting the material derivative by expression(6), we finally arrive at the desired transport equation

$$\frac{\partial C_v}{\partial t} + \nabla \cdot (C_v \mathbf{v}) = 4\pi R^2 \frac{n_0}{1 + n_0 \frac{4}{3}\pi R^3}\frac{\mathrm{dR}}{\mathrm{d}t} , \quad (13)$$

or

$$\begin{aligned} &\frac{\mathrm{d}}{\mathrm{d}t}\int_V C_v \mathrm{d}V + \int_S C_v(\mathbf{v} - \mathbf{v}_s)\cdot \mathrm{d}\mathbf{s} \\ &= \int_V 4\pi R^2 \frac{n_0}{1 + n_0 \frac{4}{3}\pi R^3}\left[\frac{\mathrm{dR}}{\mathrm{d}t}\right]\mathrm{d}V . \end{aligned} \quad (14)$$

The transient term in equation (14), which describes the velocity of the bubble-growth, needs to be modelled. Vitually all models refer to a simplification of the Rayleigh-Plasset equation, viz.

$$R\frac{\mathrm{d}^2 R}{\mathrm{d}t^2} + \frac{3}{2}\left(\frac{\mathrm{d}R}{\mathrm{d}t}\right)^2 = \frac{p_B - p_\infty}{\rho_l} - \frac{2\tau}{\rho_l R} - 4\frac{\mu_l}{\rho_l R}\frac{\mathrm{D}R}{\mathrm{D}t} . \quad (15)$$

In equation (15), p_B denotes the saturation pressure and p_∞ represents the reference pressure of the ambient fluid. The density and the dynamic viscosity of the liquid are respresented by ρ_l and μ_l and τ denotes the surface tension. Neglecting the inertia- and the viscosity-term as well as the surface tension yields

$$\left(\frac{\mathrm{d}R}{\mathrm{d}t}\right)^2 \simeq \frac{2}{3}\frac{p_B - p_\infty}{\rho_l} . \quad (16)$$

The consequences of supressing the viscous and inertia effects are discussed by [1]. In view of maritime applications, the related inaccuracies are primarily associated with the supression of non-negligible inertia effects during the bubble collapse. Such effects can approximately be captured through the introduction of minor empirical corrections.

3 Numerical Method

The numerical procedure FreSCo consists of an unstructered, cell-centred finite-volume method. The algorithm approximates the fully conservative formulation of the governing equations [6]. FreSCo is

based on an unstructered grids using arbitrary polyhedral cells and a co-located variable storage arrangement. The governing equations are solved in a segregated manner, utilizing a volume-specific pressure-correction scheme to satisfy the continuity equation. To avoid an odd-even decoupling of pressure and velocity, a third-order pressure smoothing is employed along a route outlined by Rieh & Chow.

The fully-implicit algorithm is second-order accurate in space and time. Integrals are approximated based on the mid-point rule. Diffusion terms are approximated using 2nd-order central differences, whereas advective fluxes are approximated based on blends between high-order upwind-biased schemes (e.g. QUICK), 1st-order upwind and 2nd-order central differences schemes.

The resulting linear equation systems are solved iteratively using Krylov subspace methods. The respective solvers are provided by the PETSc library [8].

3.1 Cavitation Model

The numerical treatment of convective terms in the vapor-concentration eq. (14) follows the usual approach. Diffusion terms are neglected, the approximation of the source term in eq. (14) is obtained from a mid-point rule, viz.

$$\begin{aligned}\int_V 4\pi R^2 \, \frac{n_0}{1+n_0\frac{4}{3}\pi R^3}\left[\frac{\mathrm{dR}}{\mathrm{d}t}\right]\mathrm{d}V \\ \simeq \frac{n_0}{1+n_0\frac{4}{3}\pi R^3}\left(4\pi R^2\right)\frac{\mathrm{dR}}{\mathrm{d}t}V \\ = \frac{n_0}{1+n_0\frac{4}{3}\pi R^3}\left(4\pi R^2\right)\sqrt{\frac{2}{3}\frac{|p_B-p|}{\rho_l}}V\,. \qquad (17)\end{aligned}$$

Mind that R is reconstructed depending on the value C_v as indicated by equation (5). The same source term is used to account for the density change in the pressure-correction equation.

Unfortunetly the model is unstable in this form. In order to stabilize the model, the absolut value of the source term in eq. (17) must be limited. Therefore R in eq. (17) is limited by R_{max}.

4 Results

Results are reported for three different flow cases. Note, that convective fluxes were approximated by central differences with some small amount of 1st-order upwind diferencing (around 10%). The specific bubble density n_0 was assigned to a value of $n_0 = 10^8 \frac{1}{m^3}$.

4.1 NACA0015 at Re=$1.56 \cdot 10^6$ and 6° incidence

The flow over a submerged, two-dimensional NACA0015 hydrofoil centred in a channel at 6° incidence is a prominent validation case for computational cavitation models. The Reynolds number based on the chord lenght c of the profile is $Re = 1.56\ 10^6$. The height of the channel is $H = 2.3c$, the length of the computational domain spans $L = 4.6c$. Slip-flow boundary conditions are applied at the walls. The computational grid has a C-type topology with approximately 5000 cells. The computations were done without modeling of the turbulence. Figure 1 displays the grid and the physical domain.

The test case has been investigated experimentally by Keller and Arndt. Results of the experimetal work are summarised by [1]. The cavitation number of the investigated test case is $\sigma = 1.0$. The time step was assigned to $\Delta t = T/108$, where $T = c/U_\infty$ is an appropriate convective time.

Unfortunately, pressure measurements are not published, thus the validation is restricted to visual comparisons. The results depicted by Figure 3 illustrate four time steps during one shedding cycle. Sheet cavitation is initiated in the vicinity of the suction peak (a) and convected downstream (b). Being exposed to adverse pressure gradients (c) the cavitation cloud forms a detached vortex and collapses (d). The predicted non-dimensional primary frequencies $f \cdot c/U_\infty$ are at $St = 0.087$ and 0.174, which is in line with experimental observations.

4.2 NACA66-mod airfoil at $Re = 1.85 \cdot 10^6$ and 4° incidence

The NACA66-mod is of particular relevance for marine applications since it is typical for propeller profiles. The investigated example refers to a chord-based Reynolds number of $Re = 1.85\ 10^6$ at $\alpha = 4°$ incidence. The cavitation number reads $\sigma = 1.00$. The computational grid has a C-type topology with also approximately 5000 cells (c.f. Figure 2). The physical domain refers again to an airfoil centred in a channel ($H = 5c$, $L = 8c$). Slip-flow boundary conditions are applied at the walls. The time step was assigned to $\Delta t = T/1250$. Turbulence was modeled with the k-ε-model. The specific choice of the test case is motivated by the available experimental and computational data. In [9] time-averaged pressure measurements along the suction side are published. In [10] computational results obtained by CFX5 are presented. For $\alpha = 4°$ a steady sheet cavitation at the leading edge was observed [9]. Figure 4(a) compares computed and measured normalised time-mean pressure coefficients. The computations with FreSCo

were done with three different maximum bubble radii R_max. Despite remaining uncertainties about the details of the numerical approach inherent to the CFX5 result, the agreement is considered to be fair, especially for the largest maximum Radius.

4.3 NACA66-mod airfoil at $Re = 1.85 \cdot 10^6$ and 1° incidence

The second example of the NACA66-mod airfoil refers to a chord-based Reynolds number of $Re = 1.85\ 10^6$ at $\alpha = 1^\circ$ incidence. The cavitation number reads $\sigma = 0.34$. The computational grid has again a C-type topology with also approximately 5000 cells. The boundary conditions and other parameter are the same as above. Figure **??**(b) compares computed and measured normalised time-mean pressure coefficients. For this case in [9] an oscillating mid-chord cavitation was observed. This was captured by the computations for a greater R_{max}. The results of computations with a smaler R_{max} yield to a steady mid-chord cavitation sheet. But the match of the pressure distribution is better for the smaler R_{max}.

5 Conclusions

First validation steps for the described cavitation model have been presented. The results are encouraging and demonstrate the capabilities of RANS based cavitation modelling. Comparisons with commercial competitives and experiments show good agreement, even for the pressure distribution. Nevertheless the results also show, that the influence of some model parameter is not clear. Furthermore it should be discussed whether a different formulation for the phase change is needed. Therefore more validation work is worthwhile, but reliable experimental data especially for pressures is rare.

References

[1] Sauer, J.(2000): Instationär kavitierende Strömungen - Ein neues Modell, basierend auf Front Capturing (VoF) und Blasendynamik. Universität Karlsruhe

[2] Lindenau, O.(2002): Simulation einer kavitierenden Ströung mit einem RANSE-Löser und ihre Visualisierung durch Virtual Reality Techniken. Hamburg University of Technology

[3] Vorhölter, H.(2006): Implementierung und Validierung eines VoF basierten Kavitationsmodells in FreSCo. Hamburg University of Technology

[4] Hympendahl, O.(2003): Simulation einer kavitierenden Strömung um moderne Propeller mit Feldmethoden. Hamburg University of Technology

[5] Lindenau, O./ Bertram, V.(2003): RANSE Simulation of Cavitating Flow at a Foil. Ship Technology Research. Vol.50 pp51-65

[6] Ferziger, J.H./ Peric, M.(2002):Computational Methods for Fluid Dynamics. Springer Verlag. Berlin. 3rd edition

[7] Rhie, C.M./ Chow, W.L.(1983): A Numerical Study for the Turbulent Flow past an Isolated Airfoil with Trailing Edge Separation. AIAA Journal. Vol. 17 pp 1525-1532

[8] Satish Balay/ Kris Buschelman/ William D. Gropp/ Dinesh Kaushik/ Matthew G. Knepley/ Lois Curfman McInnes/ Barry F. Smith/ Hong Zhang: PETSc Web page. 2001. http://www.mcs.anl.gov/petsc

[9] Shen, Y.T./ Dimotakis, P.E (1989): The Influence of Surface Cavitation on hydrodynamic Forces. 22nd American Towing Tank Conference. pp 44-53

[10] Zwart, P.J./ Gerber, A.G./ Belamri, T.(2004): A Two-Phase Flow Model for Predicting Cavitation Dynamics. International Conference on Multiphase Flow. Yokohama Japan

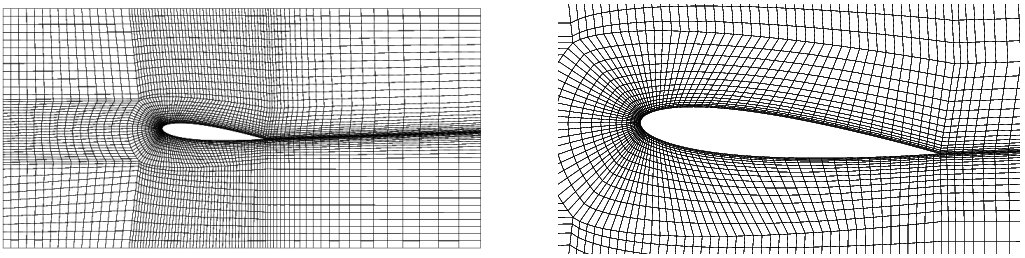

Figure 1: Computational grid for the NACA0015 case.

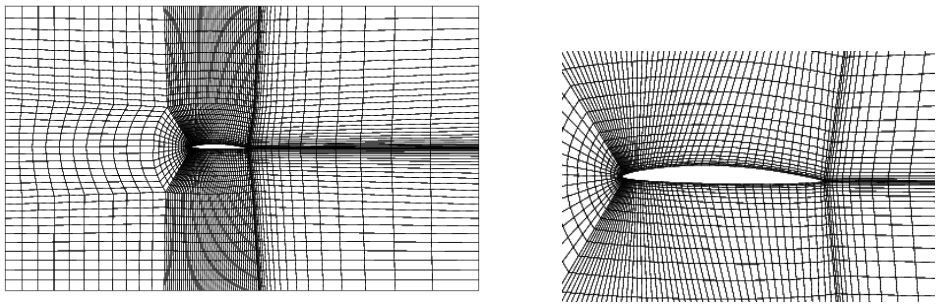

Figure 2: Computational grid for the NACA66-mod case.

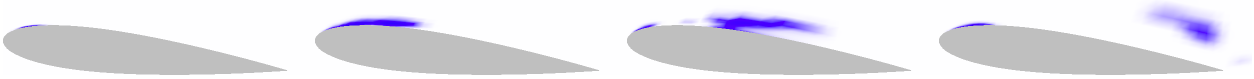

a) b) c) d)

Figure 3: Cavitation pattern ($C_v \in [0, 1]$) for NACA0015 during one period, photographs from experiments were published by [1].

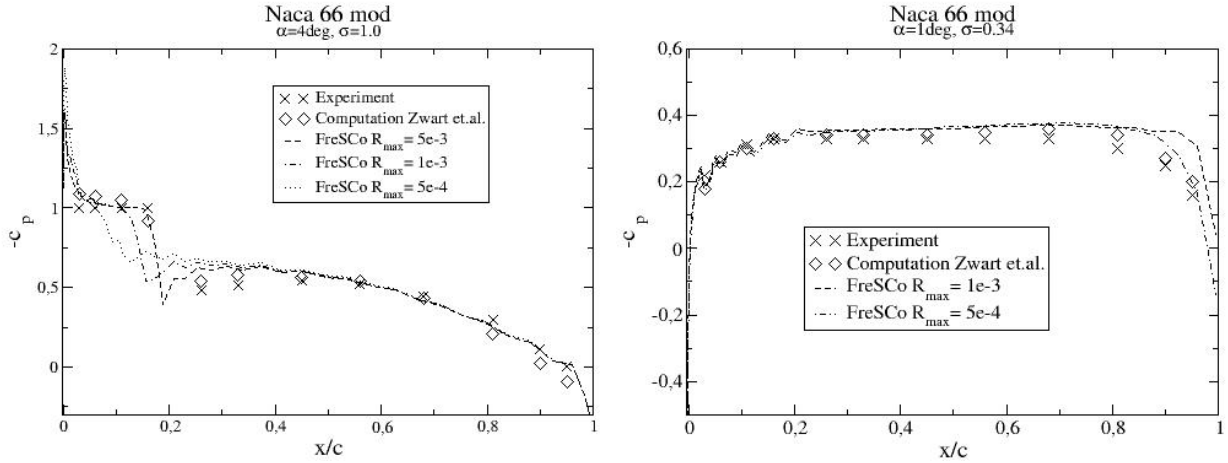

a) $\sigma = 1.00$ and $\alpha = 4°$ b) $\sigma = 0.34$ and $\alpha = 1°$

Figure 4: Pressure coefficent $c_p = \frac{(p-p_{inlet})}{\frac{\rho}{2} v_{inlet}^2}$ over the suction side of the NACA66mod hydrofoil.

CFD validation for a yacht keel

Sofia Werner[1], Alessio Pistidda[2], Lars Larsson[1], Björn Regnström[1,3]

[1] Dept. of Shipping and Marine Technology, Chalmers University of Technology, Sweden,
sofia.werner@chalmers.se
[2] Dept. of Mechanical Engineering, University of Cagliari, Italy
[3] Flowtech International AB, Sweden

1 Introduction

The design and optimisation of keels for advanced sailing yachts are often performed with Computational Fluid Dynamics (CFD), either by using the fast and easy panel codes or the more time consuming RANS codes. There are different opinions about which of these methods that can give sufficiently accurate results. Comparisons of computations from different types of codes with experimental results for fin/bulb/winglets keels would help to clarify the question. For confidentiality reasons, very few studies of that kind have been published.

In the present work we compare wind tunnel results of a winglet keel with CFD results from one RANS code and one panel code, with various set-ups of each code. The test case consists of a set of geometrically different configurations, such that force trends can be extracted. The goal is is to study:

1. which methods are able to accurately predict forces, trends and flow fields.
2. how the methods should be used in the best possible way.
3. how accurately the over-all forces of the keel can be predicted with CFD.

This extended abstract is a shortened version of a paper that will be published in the autumn of 2006.

2 Test model

The test case was a 1:4 model of an America's Cup yacht keel with a bulb and two winglets, as shown in Figure 1. The winglets can rotate $\pm 2^\circ$ around their span-wise axis (i.e. variable pitch). In order to avoid laminar separation zig-zag tape was used to trip the boundary layer. The experiment results

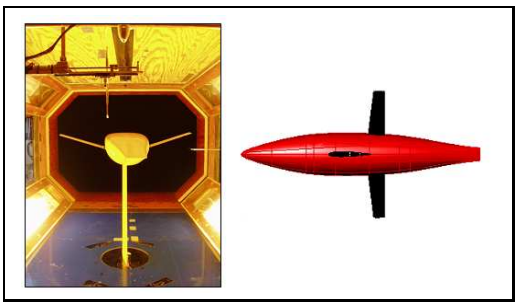

Figure 1: Wind tunnel set-up. (Model is upside down compared to the real case.

and the test model set-up have been described in detailed in [13]. The model geometry as well as the results are available on request from the first author of the present paper.

3 Estimation of tape drag

The tape used to trip the boundary layer of the wind tunnel model caused a significant drag, which cannot be neglected when comparing the experimental and computational results. The CFD simulations of the keel did not include the tape, as this would increase the computational cost too much. Instead, the drag values of the computations were corrected for the extra drag of the tape.

An estimate of the tape drag was obtained by carrying out 2D RANS simulations of a wing section, with and without the tape. For both cases, the flow was laminar ahead of the tape position and turbulent aft of it. The drag of the tape was assumed to be the difference in total drag between the case with and without tape.

The tape drag estimate in this way differed considerably depending on the turbulence model used for the evaluation. Therefore, a separate validation study was carried out using the experimental data for 2D rectangular disturbances on a flat plate due to Wieghardt [14] and reported in [2].

Figure 2 shows the drag coefficient against the width to height ratio of the rectangular disturbance for the experiments of Wieghardt as well as the results of our 2D RANS simulations with various turbulence models. The wall cell size was around y+=1. In both cases the drag coefficient was obtained by comparing the total drag of the plate with and without tape and non-dimensionalising with the x-momentum integrated over the tape height.

It is clear that the $k-\omega$ model with realisability constraint predicted the drag more accurately than the SST $k-\omega$, the realisable $k-\epsilon$ and the Spalart-Allmaras models. The tape used on the keel model had a width to height ratio of around 10, which is in the region where the predictions with $k-\omega$ gave small errors. Based on this result we concluded that the $k-\omega$ model was the best model available for estimating the tape drag. The values used for correcting the drag of the CFD simulations were 0.07 N for the case without winglets and 0.13 N for the case with

winglets, corresponding to 1.5% and 3% of the experimental values of the total drag.

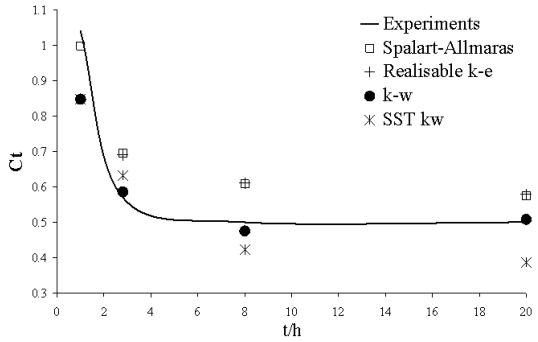

Figure 2: Validation of 2D tape drag estimation against the experimental data of Wieghardt [14].

4 Numerical methods

4.1 RANS method

The RANS simulations were carried out with the CFD code Fluent 6.2.16 on structured grids. The complete wind tunnel test section was modelled. In order to economise with grid points, slip conditions and large cells were used on the wind tunnel walls. No-slip condition and wall functions were employed on the keel surface, where the wall cell size was around y+=30. The total number of cells for the finest grid used in this study was 3.6 million, which was the limit of the available computer resources.

As mentioned above, the real wind tunnel model was equipped with tape to trip the transition. In Fluent this was modelled by defining so called laminar zones from the leading edges and back to the positions where the trip tape was placed on the real model, as shown in Figure 3. In the laminar zones no production or dissipation of turbulent kinetic energy takes place but the upstream turbulence properties are transported through the zones.

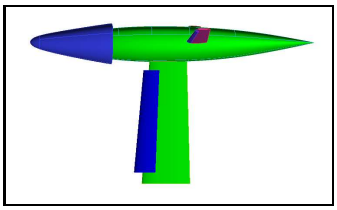

Figure 3: Test case with laminar zones.

4.2 Potential flow method

The potential flow simulations were performed with the XPAN module of the CFD code SHIPFLOW from Flowtech International. XPAN is a panel method for thick bodies and lifting surface based on the formulations of Hess [4] and described in detailed in [5]. For the trend predictions, the bulb was modelled as a non-lifting body and the fin and winglets as lifting surfaces with wake panels. The wake panels were aligned with the free stream. For accurate predictions of the forces it was necessary to also model the bulb as a lifting surface. The wake panels had then to be aligned with the keel symmetry plane, either-wise the wake panels crossed bulb lifting panels, which gave large errors. A Trefftz plane integration [3] was used to extract the lift and induced drag.

4.3 Boundary layer integration

The boundary layer code SHIPFLOW XBOUND was used in conjunction with SHIPFLOW XPAN for calculation of the skin friction. XBOUND integrates the boundary layer integral equations along streamlines from the velocity field computed by XPAN. There is no coupling back to the panel code after the boundary layer integration is done. The skin friction is computed along each streamline and integrated over the surface to get the total friction drag.

5 Computational times

The computational time for the case with winglets and wind tunnel was 20 minutes for the panel code and boundary layer solution and 80 hours for the RANS solution with 3.6M cells, both on a single 3.0GHz CPU and with 2Gb RAM.

6 Results - forces

6.1 Effect of grid size

Grid dependence studies in CFD is a problematic issue, especially for complicated geometries. With a non-automatic meshing tool such as ICEM CFD, which was used in the current work, it is very problematic to create systematically refined grids that are geometrically similar. For this reasons, we turned to a simpler approach. The effect of grid size was investigated by performing simulations on a number of grids that differed both in size and in distribution of grid points. The scatter in the force values obtained on these grids was taken as a measure of the uncertainty associated with grid dependency.

Five different grids from 1 million to 2.8 million cells with various cell distributions were created for the case without winglets. All grids had similar values of y+, around 30. The simulations were performed with the $k-\omega$ model with realisability constraint and wall function.

The results showed a precision (2σ) in the lift of 1.1% and in drag 1.8%. We cannot connect these values directly to an uncertainty estimation, but it shows that the effects of grid size and distributions are smaller than the differences between the computed and the experimental force values. Moreover, as will be seen later, the effect of grid size is considerably smaller than the effect of turbulence models.

6.2 Effect of turbulence model

In order to study the effect of turbulence models a series of simulations of the test case without winglets were carried out for five different turbulence models: the Spalart-Allmaras [12], the standard $k-\epsilon$ [6], the realizable $k-\epsilon$ [11], the standard $k-\omega$ [15] and the SST $k-\omega$ [7].

A well-known problem with the standard $k-\epsilon$ and the standard $k-\omega$ models is the so called stagnation point anomaly. In both models the production of turbulent kinetic energy is modelled as being proportional to the strain-rate tensor squared. In a real flow the production is close to zero in the vicinity of a stagnation point. However, since the strain-rate is large, the modelled production term is large too, and the turbulent kinetic energy and turbulent viscosity may obtain un-physically high values. A common way to fix this problem is to apply the realisability constraint due to Durbin [1]. Since this constraint is not included in Fluent 6.2.16 by default, it was implemented for the standard $k-\omega$ simulations in the present work with a user-defined function, as described in [9]. For the $k-\epsilon$ model the realisability version included in Fluent takes care of this problem. The effect of neglecting the stagnation point anomaly is described in section 6.3.

All turbulence models were tested on the same grid of 2.6 million cells and wall cell y+ values around 30. Wall functions were used for all models. The errors of the lift and drag prediction of each turbulence model compared to the experimental data are presented in Table 1. The drag data was corrected for the tape drag.

Model	Error in lift	Error in drag
S-A	-2%	-12%
SST $k-\omega$	-3%	-6%
$k-\omega$ with constraint	-2%	-5%
standard $k-\epsilon$	-0.4%	4%
realizable $k-\epsilon$	-1%	-4%
standard $k-\omega$	-2%	-0.3%

Table 1: Effect of turbulence model on force result for the no-winglet case.

From Table 1 it is clear that the lift values are rather independent on turbulence model, whereas the drag predictions, as expected, differ considerably. The lift values are all within the experimental error margin and it is therefore not possible to rank the tested models with respect to lift. Considering the drag values, we can say that the S-A model gave an inaccurate prediction, clearly out of the experimental error range. Moreover, the standard $k-\omega$ model without constraint appears to have given an accurate result. However, as it will be shown in section 6.3, this model used without the realisability constraint showed some unphysical flow features. The remaining four models gave quite similar results. Considering the fact that the models are only tested on one grid and that the "precision" in grid variations was found to be around 2%, the difference are not large enough to show a clear ranking of the models. The only conclusion drawn from this test was that the S-A model was not suitable for the current case.

6.3 Stagnation point anomaly

As mentioned in the previous section, the effect of applying a realisability constraint together with the $k-\omega$ model to avoid the stagnation point anomaly was studied. In most of the domain, the stagnation point anomaly did not appear anyway, due to the laminar zones around the leading edges. Since no production of kinetic energy takes place in those zones, the problem is cured automatically. In the root and tips of the fin, however, there were no laminar zones and without the constraint turned on the anomaly was clearly present, as shown in the plots of turbulent viscosity ratio in Figure 4. Without the constraint (b) the turbulent viscosity is high around the leading edge, which is physically incorrect. Instead, the turbulent viscosity should start to grow in the boundary layer aft of the leading edge, which is the case when the constraint is active (a).

A noticeable effect on the over all drag was observed. The drag changed by 4.7%, even though the anomaly was present in a relatively small part of the domain. An effect of the flow field could also be noticed. The junction vortices of the bulb-fin intersection were weaker when the constraint was not applied.

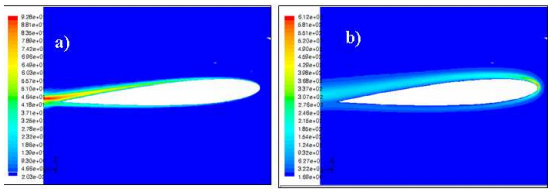

Figure 4: Turbulent viscosity ratio in the junction between the fin and the bulb a) with constraint b) without constraint.

6.4 Skin friction calculations

The presence of laminar flow on the leading edges of the keel affects the amount of skin friction. Neglecting the laminar zones in the RANS calculations and treating the boundary layer as all turbulent resulted in a drag increase of 14%.

The way the transition to turbulent boundary layer is treated influences on the resulting skin friction drag. The skin friction distribution differed considerably between the methods used in this work. Therefore, 2D computations of a wing section from the ERCOFTAC database [8] were carried out. The boundary layer of this model was tripped with a wire at x/chord=0.16. Figure 5 compares the skin friction computed with 2D

RANS $k-\omega$ with resolved (wall cells up to y+=2) and under-resolved boundary layer (wall cells up to y+=30), as well as with SHIPFLOW XBOUND in 3D. In all computations the flow was assumed to be laminar up to x/chord=0.16. Wall functions were used for the RANS calculation with wall cells of y+30. This is the wall resolution that was later used in the 3D computations of the fin/bulb/wing keel.

We note first that with y+=30 in RANS the skin friction close to the leading edge is under-predicted compared to the other computations. As the boundary layer is very thin so close to the stagnation point, the wall cell size is too large to resolve the flow well in this area.

The two RANS simulations show over-predicted skin friction values compared to the experiments in the aft half of the wing, with the largest values for the y+=30 simulations. The result of SHIPFLOW XPAN-XBOUND correspond better with the measurements, but the error is still up to 10%.

The largest differences between the three computational results appear in the start of the turbulent part of the boundary layer (x/chord≈0.16). Unfortunately, there are no measurements in this area.

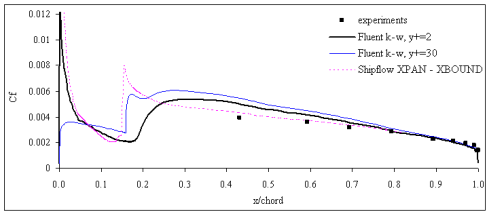

Figure 5: Skin friction coefficient of the upper side of a wing. Experiments from [8].

6.5 Summary of force results

Table 2 summarises the results concerning the force predictions with RANS. We see that the important issues for accurate force predictions are to select a suitable turbulence model, pay attention to laminar parts and fix the stagnation point anomaly.

The errors of the forces computed with the $k-\omega$ model with realisability constraint on the finest grids are given in Table 3, together with the errors of the panel/boundary layer code. Both codes predicted the lift and drag with accuracies close to the experimental error.

7 Results - trends

7.1 Trends with constant surface area

The wind tunnel measurements included lift and drag forces for different winglet pitch angles. These results enabled validation of trend predictions with constant surface area. Figure 6 shows the drag force increment relative to the drag of the case of pitch 0°.

Issue	Effect on lift	Effect on drag
Turbulence model (2σ, based on 6 models)	0.9%	5.8%
Grid sizes 1M-2.8M (2σ, from 5 grids, $k-\omega$)	0.6%	0.9%
Inlet turbulence length scale, 0.1-10mm ($k-\omega$)	0.1%	0.01%
Neglecting laminar zone	5%	14%
Stagnation point anomaly	0.3%	4.7%

Table 2: Effects of simulation set-up on force result

	Error in lift	Error in drag
RANS $k-\omega$	-3%	-5%
Panel/BL code	-2%	-2%

Table 3: Errors compared to experimental forces corrected for tape drag. $k-\omega$ model with realisability constraint, finest grid and panel/boundary layer code. With winglets, pitch 0°.

Fluent $k-\omega$ predicts the trends fairly well, but with less accuracy than the panel code, which is within the experimental uncertainty for all tested pitch angles. The drag minimum at pitch 1° is correct for both methods.

The panel code results in Figure 6 were obtained with the bulb modelled as a non-lifting body and the friction drag was not included. The fact that these inviscid calculations predict the trends well shows that they are governed by the lift-induced drag.

Included in Figure 6 is also the result of simulations carried out by Team Shosholosa using CFX with the SST $k-\omega$ model on a structured grid of 3.8 million cells [10]. It is interesting to note how similar the CFX and the Fluent results are in spite of the fact that two different codes and different grids were used.

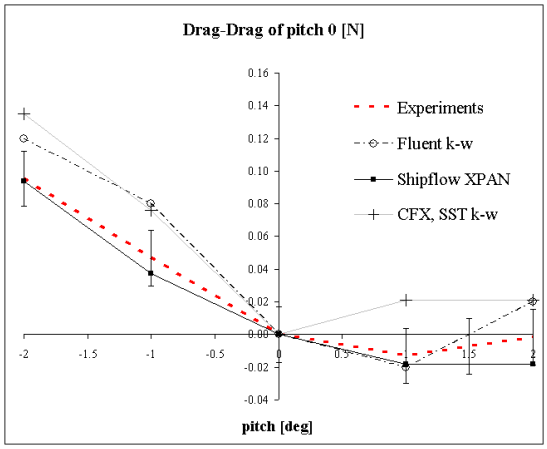

Figure 6: Drag forces trends with winglet pitch angle.

7.2 Trends with varying wetted surface

By adding winglets to the fin-bulb configuration, the drag force changes in two ways: the induced drag is decreased and the viscous drag, including junction separation, is increased. Figure 7 compares the ability of the tested numerical methods to predict the difference in drag for the keel with and without winglets.

The ability to predict force trends is important when the code is used in design optimisations. The size of the error in drag differences indicates the possible step size in the optimisation procedure. For example, the error in drag difference obtained with Fluent $k-\omega$ is 0.25 N or 5% of the total drag. This means that in an optimisation procedure we can not compare design alternatives that differs in drag with less than 5%. The corresponding number for $k-\epsilon$ was 2%, for SHIPFLOW without lifting panels on the bulb 1% and SHIPFLOW with lifting panels 0.5%. Of course a larger number of trend validations is needed in order to state these limits with any confidence. Also, adding winglets is probably one of the more difficult design variations to simulate. As we saw in the previous section, trends with constant wetted surface were predicted well even for drag difference of around 1%. Nevertheless, this comparison indicates the minimum drag differences that is sensible to use for design ranking.

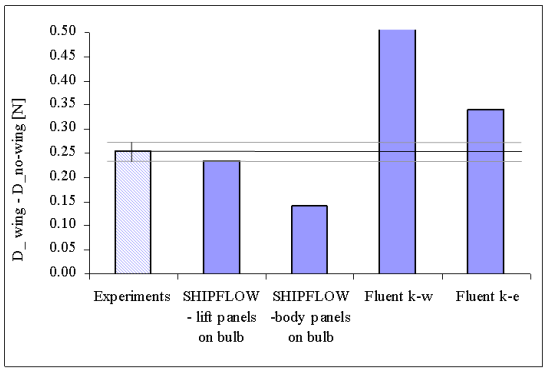

Figure 7: Difference in drag with and without winglets

8 Results - wake flow field

A wake survey is an easy way to get information about the flow over a body when more detailed measurements such as surface pressure and velocities on the body cannot be obtained. Many important features of the flow over a body will leave their footprints in the wake field, for example the formation of large vortices or separation. For this reason, validation of a CFD code using wake field data gives information about the ability of the code to capture some of the large flow features of the body, as well as to simulate a free wake.

The wake behind the keel consists of a system of large-scale vortices. Therefore, it is interesting to study the field of x-vorticity. In Figure 8a, showing the x-vorticity from the experimental data, we can identify two separate vortices in the wake of the bulb. The left one (in position y=0.72 m , z=-0,04 m) comes from a strong vortex created on the tip of the bulb. The other one (position y=0.67 m, z=0 m) is the trace of a vortex created on the rounded corner on the bulb suction side, about half a bulb-length forward of the bulb tip. Other areas of vorticity to mention is the traces of the fin-bulb junction separation in positions y=0.65 m, z=-0.03 m and z=-0.05 m.

The results from the simulations with Fluent for various turbulence models are given in Figure 8b-f. The $k-\omega$ model gives the best predictions of the wake. The right vortex is visible with this model only, and the fin junction vorticity, which is under-predicted for all turbulence models, is strongest for the $k-\omega$ model. Detailed studies of the vorticity field around the bulb show that the right vortex after being created quickly moves out of the bulb boundary layer and travels along the bulb. The Spalart-Allmaras, the $k-\epsilon$ and the SST $k-\omega$ (which is basically a $k-\epsilon$ in the outer region and outside of the boundary layers) all damp out this vortex more than the $k-\omega$ model did.

9 Conclusions

A validation study of the RANS code Fluent and the panel/boundary layer code SHIPFLOW XPAN/XBOUND has been carried out using experimental data of a fin/bulb/winglet yacht keel. The goal was to compare the accuracy that can be achieved with the different codes and to study how they should be used in the best way.

The main conclusions in the study were:

RANS code

- The $k-\epsilon$ and $k-\omega$ models predicted the drag with 5% error and the lift with 3% error on a grid of 2.6 milion cells..
- The Spalart-Allmaras model under-predicted the drag by 12%.
- Using laminar flow calculations in areas known to be laminar was essential for accurate drag predictions.
- It was found to be important to use a realisability constraint to avoid the stagnation point anomaly in the $k-\omega$ model. If it was not applied the junction separation as well as the drag force was affected significantly. This constraint is *not* included in Fluent 6.2.16.
- The $k-\omega$ model predicted trends fairly well. The correct drag minimum was detected.
- Out of the tested turbulence models, the wake flow field was best calculated with the $k-\omega$ model.

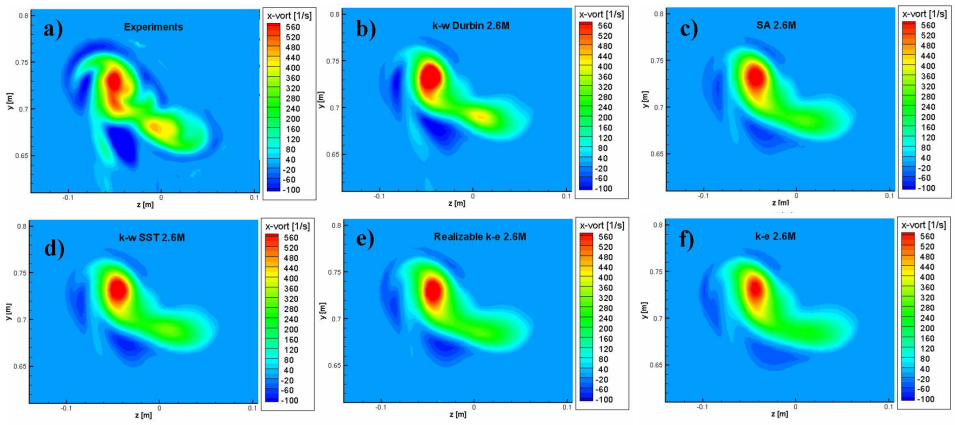

Figure 8: x-vorticity in the wake plane for the case without winglets. a) Experiments, b) $k-\omega$ SST, c) SA, d) $k-\omega$ with restraint, e) realisable $k-\epsilon$, f) $k-\epsilon$.

Panel/boundary layer code

- With SHIPFLOW XPAN/XBOUND the errors of both lift and drag were smaller than the experimental uncertainty.

- It was necessary to model the bulb as a lifting surface for accurate drag results. With the bulb as a non-lifting surface the drag error was -8%.

- The drag predictions were very sensitive to the panelisation. A suitable grid could only be created after careful inspections of the flow field on the body.

- Very good predictions of the trends with constant surface were obtained if the wakes of the fin and winglets were aligned with the free-stream. The bulb did not have to be modelled as a non-lifting body for the trend predictions.

In a comparison between the panel code and the RANS code both methods showed satisfactory accuracy in force predictions but the panel code proved to be better in trend predictions. The large difference in computational time, 20 minutes versus 80 hours, is of course an advantage of the panel code. A weakness of the panel code is the sensitivity to panelisation, which makes the code less reliable.

10 Discussion

In the current case the friction and induced drag turned out to be the dominating drag components. For a keel with larger amount of separation, for example in the junctions, the panel/boundary layer code would not perform as well as it did in this study.

Our conclusions regarding the accuracy of the computations might have been influenced by the amount of computational resources that we had available. It is possible that with more computer power a higher accuracy could have been obtained with the RANS code.

References

[1] P.A. Durbin. On the k-e stagnation point anomaly. *Int. J. Heat and Fluid Flow*, 17:89–90, 1996.

[2] M. C. Good. The form drag of two-dimensional bluff-plates immersed in turbulent shear flows. Master's thesis, University of Melbourne, 1965.

[3] D.S. Greeley and J.H. Cross-Whither. Design and hydrodynamic performance of sailboat keels. *Marine Technology and SNAME News*, 26, 1989.

[4] J.L. Hess. Calculation of potential flow about arbitrary three-dimensional lifting bodies. In *Douglas Report No MDC J5679-01*, 1972.

[5] C-E. Janson. *Potential Flow Oanel Methods for the Calculation of Free-surface Flows with Lift*. PhD thesis, Chalmers University of Technology, 1997.

[6] B. E. Launder and D. B. Spalding. *Lectures in Mathematical Models of Turbulence*. Academic Press, London, England, 1972.

[7] F. R. Menter. Two-equation eddy-viscosity turbulence models for engineering applications. *AIAA Journal*, 32:1598–1605, 1994.

[8] A. Nakayama. Characteristics of the flow around conventional and supercritical airfoils. *J. Fluid Mech.*, 160, 1985.

[9] A. Ooi and M.E. Young. Turbulence models and boundary conditions for bluff body flow. In *15th Australasian Fluid Mechanics Conference*, 2004.

[10] C. Pashias. Private communication, 2006.

[11] T.-H. Shih, W.W. Liou, A. Shabbir, Z. Yang, and J. Zhu. A new eddy-viscosity model for high reynolds number turbulent flows - model development and validation. *Computers Fluids*, 24:227–238, 1995.

[12] P. Spalart and S. Allmaras. A one-equation turbulence model for aerodynamic flows. *Technical Report AIAA-92-0439*, 1992.

[13] S. Werner, L. Larsson, and B. Regnström. A CFD validation test case - wind tunnel tests of a winglet keel. In *2nd High Performance Yacht Design Conference, New Zealand*, 2006.

[14] K. Wieghardt. Erhöhung des turbulenten veibungswiderstandes durch oberflächenströrungen. *Forshungshefte fur schiffstechnik*, 65, 1953.

[15] D. C. Wilcox. *Turbulence Modeling for CFD*. DCW Industries, Inc., La Canada, California, 1998.

CALL FOR PAPERS

10th Numerical Towing Tank Symposium (NuTTS'07)

Hamburg, Germany, 23.9.-25.9. 2007

Topics:

- Nonlinear flows around marine structures (LES, RANSE, Euler with or w/o free surface)
- Free-surface flows around marine structures (3-d ship seakeeping, free-surface viscous flows)
- Related topics (validation experiments, numerical techniques, grid generation, etc)

Deadlines:

Early feedback :	30 April 2007
Extended Abstracts received :	28 July 2007
Last possible update :	1 September 2007

You are invited to participate in the above event. The objective of the event is to provide a forum for informal discussions among experts in the field and to disseminate latest results. Younger workers and Ph.D. students are especially encouraged to participate. The event will be held at Haus Rissen in Hamburg. All participants stay and have meals together to maximize interaction and discussion.

The extended abstracts of the proposed talk will be directly reproduced in the proceedings. Proceedings will be in black and white. Work in progress, encountered problems, etc. should be discussed in an open, informal atmosphere (no ties!) among colleagues. The first page of the extended abstract should be headed with the title and authors' names and address (incl. email) in a compact form to economize on space. Academic titles and page numbers shall be omitted. The extended abstract shall neither contain an abstract of the abstract, nor keywords, nor further headers. Font size shall not be less than 10pt Times New Roman. Extended abstracts should be limited to 6 pages in A4 format with 2.5 cm margin. An early reply will help us in organizing the event better. For the early feedback, a tentative title or topic will suffice.

Following the tradition of previous NuTTS events, the fees will be kept low to allow a maximum number of scientists to attend. The fees including accommodation (3 nights) and meals during the symposium will be :

250 Euro PhD candidates and students (expected to share double)
300 Euro authors (in single room)
350 Euro others (in single room)

50 Euro surcharge for updates after 28 July 2007

The day after NuTTS, the German STG will organize a one-day ship hydrodynamics conference in Hamburg-Harburg. Contact for this: moustafa.abdel-maksoud@uni-duisburg-essen.de

Contacts :
Volker Bertram, **volker.bertram@ensieta.fr**
Heinrich Söding, **h.soeding@tu-harburg.de**

Sponsors : CD-Adapco, Numeca